University of Oxford



Institute of Biomedical Engineering
Department of Engineering Science

Computational modelling of brain transport phenomena: Application of multicompartmental poroelasticity

Dean Chou

St. Cross College

Supervised by

Professor Yiannis Ventikos

A thesis submitted for the degree of Doctor of Philosophy

Michaelmas 2016

To Cristina and Hayley

獻給我永遠最愛的家人

Abstract

The global population is predicted to increase to around 11 billion by 2100. By 2050, the average age in the most populous age group will be over sixty. The ageing population (over sixty-five) is projected to exceed the number of children by 2047. These demographics imply that as the ageing population section increases, there will be a greater need for long-term care services. In order to adequately prepare against this trend, medical experts and evidence-driven policymakers are realising that personalised healthcare can help alleviate the burden related to the planning and commissioning of services allied to long-term care.

Central to this picture is conditions that affect the brain – the most important organ of the human body. Dementia, stroke, and other conditions have a tremendous impact on loss of life, quality of life and healthcare cost. The challenge regarding brain disease is exacerbated further due to the difficulty regarding accessibility of this organ, but also due to the immense complexity regarding its morphology and functionality. In this context, advanced biophysical modelling is considered a promising option for studying brain pathophysiology and becomes a priority investment regarding routes for brain research. Simulations offer the promise of improved, clinically relevant, predictive information, acceleration for the pipeline of drug discovery/design and better planning of long-term care for patients.

Within this paradigm, a particular model of water transport in the cerebral environment is essential. Numerous brain disorders arise from water imbalance in the cerebral environment, such as hydrocephalus (HCP), oedema and Chiari malformations to name a few. In this research, a novel multiscale model of fluid regulation and tissue displacement in the cerebral environment is developed, arising from the use of Multiple-network Poroelastic Theory (MPET). Characteristics of a four-network poroelastic model (4MPET) are first explored. Then, this model is extended to a fully dynamic (transient) six-network model (6MPET) via the addition of two new compartments, namely the glial cells compartment and the glymphatic system compartment. The introduction of these two compartments in the MPET paradigm reflects recent seminal findings in cerebral physiology, namely the extent and importance regarding transport/clearance of the perivascular spaces of the brain vasculature. We develop and present a numerical implementation of the 6MPET model, and we utilise this framework to analyse acute HCP and cerebral oedema in a variety of settings, in order to show the enhanced capability of the proposed 6MPET model compared to the classical 4MPET.

Investigations of acute hydrocephalus through the fully dynamic 6MPET reveal compensatory trans-ependymal pressure behaviour in the glymphatic compartment. It was also shown that aquaporin-4 (AQP4) deficient expression exaggerates ventriculomegaly, and this too is demonstrated in acute hydrocephalus. Additionally, using the 6MPET model, one is able to witness three mitigating factors for cytotoxic oedema. Specifically, these are: reducing water mobility in the glial cells compartment, increasing the compliance of the glial cells compartment and finally AQP4-deficient expression.



Statement of Originality

I hereby declare that this submission is my own work and to the best of my knowledge it contains no materials previously published or written by another person, or substantial proportions of material which have been accepted for the award of any other degree or diploma at the University of Oxford or any other educational institution, except where due acknowledgement is made in the thesis.

Any contribution made to the research by others, with whom I have worked at the University of Oxford or elsewhere, is explicitly acknowledged in the thesis.

I also declare that the intellectual content of this thesis is the product of my own work, except to the extent that assistance from others in the project's design and conception or in style, presentation and linguistic expression is acknowledged.

Dean Chou

30th March 2016

Acknowledgements

Without the insight from Professor Yiannis Ventikos, I would not have had this great opportunity to enjoy such an incredible journey at the University of Oxford. All of these amazing experiences will be profoundly rooted in my memory including his real management style and warm encouragement in the mental; the rigorous manner with critical comments and in-depth knowledge to deal with the innovative research. Hence, I offer my sincerest gratitude and respect to him. Besides my D.Phil. advisor, my sincere thanks has to go to the rest of my dissertation committee: Prof. Ian Sobey as my internal examiner and Prof. Vartan Kurtcuoglu as my external examiner. With your insightful comments and encouragement makes this dissertation more elegant.

Moreover, I would like to thank my colleagues in the Fluidics and Biocomplexity Group, especially, Dr Ioannis C. Vardakis who gave me a lot of moral and technical support and Dr Li-wei Kuo who show his great friendship and enthusiasm to share his knowledge in FEM. Outside the lab, I would like to thank all of my friends who ever supported me in any form, especially Prof. Kuo-Ching Chen as my mentor and Prof. Yu-Chen Shu as my best friend over three-decade friendship. Regardless of any angle, to ascend the final point at the University of Oxford is difficult and arduous. Without all of these friends, I definitely could not make this achievement. Therefore, since my family along the way, pursuing this D.Phil. degree, behind me, I finish up with appreciating my family in Taiwan for their unconditional love and incentive.

Dean

30th March 2016

Contents

Chapter 1 Motivation, Physiology & Disease 1

1.1 Motivation 1

1.2 Cerebral Anatomy, Physiology & Disease 5

1.2.1 Cerebrospinal Fluid 8

1.2.2 Aquaporins 10

1.2.3 The Glymphatic System 14

1.2.4 Diseases of the Cerebral Environment 17

Chapter 2 Literature Review in Modelling & Experimental Works in Cerebromechanics 30

2.1 Cerebromechanics *in silico* 31

2.1.1 Electrical Analogue Models for Brain 31

2.1.2 Porous Parenchyma Models using Poroelasticity 33

2.1.3 Viscoelastic Parenchyma Models 38

2.1.4 Cerebral Models incorporating Computational Fluid Dynamics 40

2.2 Pertinent Cerebral Experimental Work 47

2.2.1 Cerebromechanical Properties Measurement 47

2.2.2 Cerebral Diseases Measurement 50

Chapter 3 Poromechanics 56

3.1 Poroelasticity 56

3.1.1 Poroelastic Constitutive Relations 58

3.1.2 Poroelastic Governing Equations 62

3.1.3 The Simplified Governing Equations 65

3.1.4 Multiple-network Isotropic Linear Poroelastic Theory 67

3.2 Four-compartmental Multiple-network Poroelastic Theory 70

3.2.1 General Assumptions 70

3.2.2 Continuity and Directional Water Transfer 72
3.2.3 Methodology in One-Dimension 74
3.2.4 Boundary Conditions at the Ventricular Wall 74
3.2.5 Boundary Conditions at the Skull 76
3.2.6 Initial Conditions 76
3.2.7 Numerical Implementation 77
3.3 Six-compartmental Multiple-Network Poroelastic Theory 88
3.3.1 Continuity and Directional Water Transfer 91
3.3.2 Methodology in One-Dimension 94
3.3.3 Boundary Conditions at the Ventricular Wall 94
3.3.4 Boundary Conditions at the Skull 95
3.3.5 Initial Conditions 96
3.3.6 Numerical Implementation 97
3.4 Parameter Estimation 111
3.4.1 Cerebral Geometry 113
3.4.2 Poroelastic Constants 113
3.4.3 Coefficients in MPET Source Terms 114
Chapter 4 Obstructive Hydrocephalus 118
4.1 Quasi-Static Four-Network MPET 118
4.2 Quasi-Static Six-Network MPET 123
4.3 Comparison & Validation of the MPET template 132
4.3.1 Convergence Analysis for the u-*p* Formulation 133
4.3.2 Comparison 4MPET with various porosities 135
4.3.3 Comparison of the quasi-static 4MPET and 6MPET with various compliances 138
Chapter 5 Acute Hydrocephalus 145
5.1 Fully Dynamic Four-Network MPET 145

5.1.1 Results 145
5.1.2 Discussion 147
5.2 Fully Dynamic Six-Network MPET 151
5.2.1 The water mobility effect in 6MPET 154
5.2.2 The effect of compliance on the fully dynamic 6MPET 156
5.2.3 The AQP4 effect in the fully dynamic 6MPET model 157
5.3 Comparison of the Quasi-static & Fully Dynamic MPET 163
Chapter 6 Cerebral Oedema 171
6.1 The evolution of the brain oedema 178
Chapter 7 Conclusions and Future Work 192
7.1 Conclusions 192
7.2 Future Work 197
7.2.1 Model Improvements 197
7.2.2 Other MPET Applications 201
References 203
Appendices 234
A1 Mathematical Transformations 234
A2 Stress as a Function of Displacement 235
A3 Boundary Condition Derivation at Ventricle Wall, Displacement 235
A4 Boundary Condition Derivation at Ventricle Wall, Glial Cells 236

List of Figures

Figure 1.1 Percentage of the world population over 65 from 1950 to 2050……..2

Figure 1.2 Schematic of the up-to-date microstructures in a human brain……7

Figure 1.3 A schematic of a sagittal plane depicting important structures in the human brain, such as the ventricles and their choroid plexuses……...9

Figure 1.4 Water permeability and AQP 1 in Xenopus laevis oocytes……..11

Figure 1.5 Distribution of different types of water channels in the brain…….……12

Figure 1.6 An illustration of the glymphatic system.……16

Figure 1.7 Hydrocephalus in the cerebroventricular system.....27

Figure 3.1 The sketch of the Dual-MPET system…….....64

Figure 3.2 A 4MPET sketch of the cerebral environment with the directional transfer between different compartments …….....72

Figure 3.3 Schematic spherical representation of the 1D 6MPET model……..88

Figure 3.4 The fluid transfer restrictions place between the six compartments…..…90

Figure 3.5 The fluid transfer Parameters sensitivity for 6MPET by focusing on the compliances and AQP scaling factors……...…116

Figure 4.1 The first order discretised scheme of the quasi-static 4MPET model with aqueductal stenosis of varying levels.……...……120

Figure 4.2 The second order discretised scheme on the quasi-static 4MPET model with aqueductal stenosis of varying level……...…..……..122

Figure 4.3 The evolution of severe stenosis of the aqueduct of Sylvius utilising the second order discretised scheme on the quasi-static 4MPET model....122

Figure 4.4 The first order discretised scheme on the quasi-static 6MPET model with the aqueductal stenosis in different level…….…….....129

Figure 4.5 The second order discretised scheme on the quasi-static 6MPET model with the aqueductal stenosis in different level……130

Figure 4.6 The evolution of severe stenosis of the aqueduct of Sylvius with the second order discretised scheme on the quasi-static 6MPET model…..131

Figure 4.7 The comparison of the first and the second order discretised scheme on the quasi-static 4MPET and 6MPET model with the aqueductal stenosis in the different level……..132

Figure 4.8 Validation results of the first and second discretised scheme with the severe aqueductal stenosis on the quasi-static 4MPET model….....140

Figure 4.9 Validation results of the first and second discretised scheme with the severe aqueductal stenosis on the dynamic 4MPET model……....141

Figure 4.10 Validation results of the first and second discretised scheme with the severe aqueductal stenosis on the quasi-static 6MPET model.……..142

Figure 4.11 Validation results of the first and second discretised scheme with the severe aqueductal stenosis on the fully dynamic 6MPET model……...143

Figure 4.12 Using the different combination porosity to compare the ventricular displacement (LHS) and CSF pressure (RHS) between the quasi-static and dynamic 4MPET model…….……....144

Figure 4.13 Ventricular displacement with various compliances on the quasi-static 4MPET (LHS) and 6MPET (RHS) model…….……144

Figure 5.1 First order discretised fully dynamic 4MPET model with different levels of aqueductal stenosis…….……...149

Figure 5.2 Second order discretised fully dynamic 4MPET model with different levels of aqueductal stenosis…….…….149

Figure 5.3 Evolution of severe stenosis of the aqueduct of Sylvius - second order discretised scheme of the fully dynamic 4MPET model……150

Figure 5.4 Evolution of CSF/ECF fluid content and volume dilation for severe stenosis of the aqueduct of Sylvius with the second order discretised scheme of the fully dynamic 4MPET model…….....150

Figure 5.5 Second order discretised scheme applied on the fully dynamic 6MPET model, with varying degrees of aqueductal stenosis……..159

Figure 5.6 Evolution of severe stenosis of the aqueduct of Sylvius with the second order discretised scheme being applied on the fully dynamic 6MPET model.....160

Figure 5.7 Evolution of the fluid content and volume dilation for severe stenosis of the aqueduct of Sylvius with the second order discretised scheme being applied on the fully dynamic 6MPET model……...…….161

Figure 5.8 Mobility combinations for severe stenosis of the aqueduct of Sylvius with the second order discretised scheme on the fully dynamic 6MPET model…….162

Figure 5.9 Ventricular displacement with various compliances (LHS) and with different AQP4 expression level (RHS) for the severe stenosis of the aqueduct of Sylvius on the fully dynamic 6MPET model…….163

Figure 5.10 Comparison the quasi-static and dynamic model via 4MPET and 6MPET……..…….....167

Figure 5.11 Comparison between the quasi-static and dynamic 6MPET models…..167

Figure 5.12 Comparison of the parenchymal tissue displacement as a function of skull radius for the quasi-static and dynamic 4MPET and 6MPET models…168

Figure 5.13 Comparison of the CSF/ECF pressure as a function of skull radius for the quasi-static and dynamic MPET model with 4MPET and 6MPET……169

Figure 5.14 Comparison the pressure of the glial cells with a function of skull radius for the quasi-static and dynamic 6MPET model……..…..…..……..170

Figure 5.15 Comparison the glymphatic system/PVS/ISF pressure of the evolution of the quasi-static and dynamic 6MPET model……..……...170

Figure 6.1 The progressing oedema level is mainly alleviated by the AQP4-deficient expression, the reducing water mobility and compliance of the glial cells compartment...……...…184

Figure 6.2 Ventricular displacement of the open aqueduct case, using different combinations of two compartmental mobilities and various compliances of the glial cells compartment with the AQP4-deficient expression for the open aqueduct on the fully dynamic 6MPET model……..185

Figure 6.3 CASE (A): Evolution of the open aqueduct with the second order discretised scheme on the fully dynamic 6MPET model……..……186

Figure 6.4 CASE (A): Evolution of the fluid content and volume dilation for the open aqueduct with the second order discretised scheme on the fully dynamic 6MPET model……..…….……187

Figure 6.5 CASE (B): Evolution of the open aqueduct case, with the second order discretised scheme on the fully dynamic 6MPET model……..……188

Figure 6.6 CASE (B): Evolution of fluid content and volume dilation for the open aqueduct with the second order discretised scheme on the fully dynamic 6MPET model.……..……..……..189

Figure 6.7 CASE (C): Evolution of the open aqueduct with the second order discretised scheme on the fully dynamic 6MPET model…….…….190

Figure 6.8 CASE (C): Evolution of the fluid content and volume dilation for the open aqueduct with the second order discretised scheme on the fully dynamic 6MPET model……..…….191

Figure 7.1 The glymphatic hypothesis and conventional understanding of the AQP4 role in brain water movement.……...…200

List of Tables

Table 2.1 Summary of the selected CSF brain models…….46

Table 3.1 List of the parameter values for 4MPET framework……...116

Table 3.2 List of the parameter values for 6MPET framework……..117

Table 6.1 Values of ventricular shrinking corresponding to Figure 6.2.……...….178

Table 7.1 The advantages and disadvantages for the MPET templates……..197

Acronyms

4MPET	four-compartmental Poroelastic Theory
6MPET	Six-compartmental Poroelastic Theory
ADC	Apparent diffusion coefficient
AG	Arachnoid granulation
AQP	Aquaporin
BBB	Blood-brain barrier
BEM	Boundary Element Method
CFD	Computational fluid dynamics
CNS	Central nervous system
CP	Choroid plexus
CSF	Cerebrospinal fluid
CT	Computerized tomography
CV	Control Volume
ECF	Extra-cellular fluid
FDM	Finite difference method
FEM	Finite element method
HCP	Hydrocephalus
H-Tx	Congenital hydrocephalus Texas
ICP	Intracranial pressure
iNPH	Idiopathic Normal pressure hydrocephalus
IoT	Internet of things
ISF	Interstitial fluid
MPET	Multiple-Network Poroelastic Theory
MRE	Magnetic Resonance Elastography
MRI	Magnetic Resonance Imaging
NPH	Normal pressure hydrocephalus
PVS	Perivascular space
SAS	Subarachnoid space
SSS	Superior sagittal sinus
TBI	Traumatic brain injury
VRS	Virchow-Robin spaces
WCP	Water channel protein

Chapter 1 Motivation, Physiology & Disease

The Topic of this Chapter

As technology advances in the twenty-first century, some serious global problems are expected to be solved via computer-integrated bioengineering, such as the personalisation of medical treatments in dementia. The advancement of translational computational technologies may prove to be crucial in achieving patient-specific healthcare provision. This chapter will outline the motivation for this research, and introduce the cerebral anatomy and physiology. Finally, diseases of the cerebral environment, such as hydrocephalus (HCP) and cerebral oedema, will be described.

1.1 Motivation

The world human population has been increasing, and it is projected to increase from 7.3 billion (as of July 2015) to 11.2 billion in the year 2100, as estimated by the United Nations [1]. Over the last fifty years, the total number of children globally has decreased from 34% in 1950 to 30% in 2000. Over the next thirty-four years, the proportion of children is projected to decline by a further one-third [2]. Therefore, the percentage of the ageing population will exceed the number of children to a precedent extent by the year 2050 [2]. Moreover, the proportion of the world ageing population (over 65) is rapidly expanding, as shown in Figure 1.1 according to the United Nations' estimates [3]. Although substantial portions of this ageing group maintain healthy conditions, degenerative issues, such as neurodegenerative diseases, eventually catch up with a critical section. Dementia is probably the most prominent and amongst the most devastating of these neurodegenerative diseases [4].

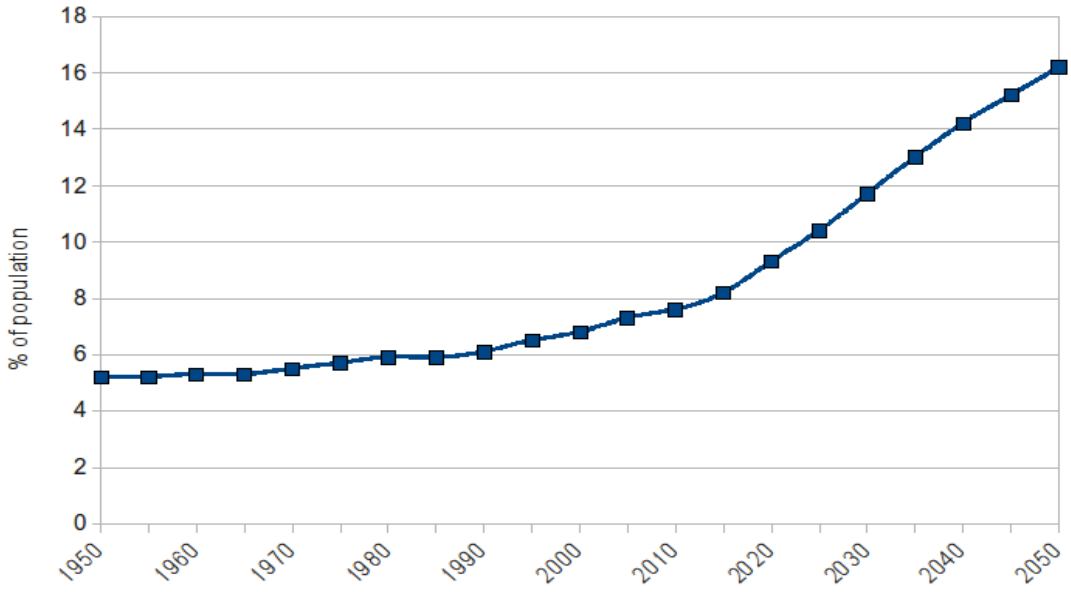


Figure 1.1 Percentage of the world population over 65 from 1950 to 2050 [3].

According to the non-profit organisation *Alzheimer's Disease International* prediction, dementia will approach 130 million cases worldwide by 2050 (44 million cases, 2014) [5]. Likewise, the World Health Organisation (WHO) also predicted that, driven by population ageing in developed countries, neurodegenerative diseases such as Alzheimer's disease and other types of dementia, as well as conditions which affect mainly motor - rather than cognitive - functions, e.g. Parkinson's disease and amyotrophic lateral sclerosis (ALS), will turn into the second leading cause of death after cardiovascular disease instead of cancer [6]. As a consequence of the ageing population worldwide, increasing costs to society arise from later-in-life conditions such as cognitive decline and dementia [7]. Dementia is a public healthcare problem, with an estimated incidence of 26.6 million cases worldwide in 2012 [8]. Around 48 million people were living with dementia worldwide in 2015, whilst the number will increase to around 76 million by 2030, and over 130 million by 2050 [9]. Interestingly, the numbers for dementia in this WHO report are higher than the original report in 2009 [10]. This gap between actual value and estimated value shows that an increasing

proportion of the ageing population is developing, and living with, dementia, as opposed to what is shown in older demographic models. This outcome may be fueled by decreases in fertility and increases in longevity since the global economic downturn (reduced procreant desire) and the advancement in medical technology. It may also result from persistence of the growing trend in obesity and physical inactivity [11]. Hence, this situation creates an inevitable problem at a national level, and subsequently, this extends globally.

In recent years, an increasing number of medical experts and politicians became aware of the significant issue that dementia affects many within the ageing population, and have taken steps to try to address it; mainly driven probably by healthcare cost considerations. It is appreciated that the solutions may be highly linked to the personalisation of treatment for dementia [12, 13]. Personalised treatment can be considered a combination of therapy and comprehensive long-term care, which incorporates diagnostic, continuous monitoring and continuing medical treatment, and family and community care. Among these strategies, the combined treatment will be able to rely on new technologies – an example of those include computer-integrated technology, such as that of the virtual physiological human (VPH), which is a technological framework that will enable collaborative investigation of the human body as a single complex system [14-16].

The evolution of combined treatment protocols in dementia will join the fourth industrial revolution based on the digital revolution, since the combined treatment will utilise advanced technologies, such as the Internet of Things (IoT) for pervasive monitoring of cognitive function and computer-integrated medical diagnostics and treatment (“*theranostics”*). Regarding the IoT, wearable technology can record a

personalised signal to provide an *in-silico* derived diagnosis [17-21]. To provide this type of proper diagnostic service, computer-integrated diagnosis techniques have to be developed simultaneously. Computer-integrated diagnosis utilising simulations is an advanced example of diagnostic technology. It can offer many advantages to improve the current limitations within the clinical domain. For example, the prospect of improved clinically relevant predictive information, enabling more efficient use of resources for designing treatment protocols, risk assessment and urgently needed management, [22-24].

Within this paradigm, we highlight the importance of the cerebrospinal fluid (CSF), as an important component of the cerebral system. Although we shall provide detailed information on its production, exchange and transport in the brain, later on, we need to emphasise two facts here that underpin its importance: first, CSF (CSF-borne metabolites) remains the most reliable biomarker – albeit invasive – of dementia nowadays [25, 26]. Second, recent seminal work has shown a clear connection between CSF and metabolite clearance [27, 28]. The transport of fluids in the brain (CSF and blood), and their exchange processes and mechanisms became a focal point of the investigation, through simulation technologies, such as that proposed by the VPH-DARE@IT project, which intends to assists in the quest to understand the onset and progression of dementia. These early predictive and individualised diagnoses are to be realised via a systematic, multifactorial and multiscale modelling approach [29].

1.2 Cerebral Anatomy, Physiology & Disease

The brain is the most complex organ in the human body. Most of the essential functions in the body are controlled by the brain [30, 31]. Although a gross simplification, one could distinguish three components within the rigid skull (cranium): the brain parenchyma (functional tissue), blood vessels (structural tissue, e.g. stroma), the blood that fills them and finally spaces filled with fluid – interstitial or CSF (the latter two being practically mostly indistinguishable [32, 33]. The brain parenchyma-comprising cells that are surrounded by interstitial fluid (ISF) pervades the matrix and fills the spaces between the cells, the blood vessels, the meninges, and the cerebrospinal fluid (CSF) that fills the cavities within the brain and the space on its outer surface [34]. The main cell types of the cerebral parenchyma are comprised of two types of the cerebral cell, neurones and glial cells [35]. Therefore, the fact that cells are formed by the brain parenchyma and stroma with inter-cell space allows us to think about this as a sponge-like porous medium [30].

Regarding the meninges, there are three membranes to enclose the brain beneath the skull. These three layers of tissue in the meninges are the dura mater, the arachnoid mater and the pia mater [36]. The meninges also play a protective role in the central nervous system (CNS) by encapsulating a fluid-filled space in order to prevent trauma to the brain, since the parenchyma of the brain is very soft, but of course is vital and needs protection [37]. The dura mater is a thick and stiff membrane which is closest to the skull and directly adjacent to the arachnoid mater. The structure of the arachnoid mater resembles a spider web-like pattern [38]; the arachnoid mater cushions the CSF pressure from the subarachnoid space (SAS) which is between the arachnoid mater and the pia mater in the meninges system. The pia mater forms the meningeal envelope

which is adjacent to the gyri and sulci on the surface of the brain. When the pia mater is penetrated by artery blood vessels into the brain parenchyma from the SAS, the sheath of pia mater is carried with artery blood vessels which pass through the subpial space (see Figure 1.2a). According to some studies focusing on the human [39] and mouse [40] brain tissue via electron microscopy, both of these studies revealed no perivascular/Virchow-Robin space shown in the cerebral cortex due to that the glia limitans, pia mater and artery wall are tight (see Figure 1.2a). However, perivascular spaces (PVS) are shown in the basal ganglia and white matter [41, 42]. Regarding the venous blood vessels in the CNS, they do not have a complete wrapping of pia mater, but they do have a covered leptomeningeal cells in the SAS [39].

At the oxygen/nutrients delivery end of the vascular system, the micro-cerebrovascular system (including small arterioles, capillaries and venules) in the brain parenchyma are surrounded by the parenchymal basement membrane and the *end feet* of the glial cells (shown in Figure 1.2b), namely glia limitans. Regarding the blood-brain barrier (BBB), it provides the controlled transport of fluids and solutes into the CNS. The BBB endothelial cells are composed of a basement membrane formed by the fusion of endothelial cells and glia limitans. Moreover, the endothelial cells and parenchymal basement membranes are fused at the capillary BBB [43].

Beyond these microscopic water passages in the parenchyma, the brain also involves spaces filled with CSF, i.e., the *cerebroventricular* system. According to Figure 1.3, four primary structures comprise a pair of lateral ventricles, the third ventricle and the fourth ventricle (which are connected via the aqueduct of Sylvius). These are a series of interconnected, CSF-filled cavities that lie in the core of the forebrain and brainstem. The lateral ventricles are the largest hollows in this ventricular

system (one within each of the cerebral hemispheres). The third ventricle shapes a thin slit-like cavity between the right and left thalamus, and this can allow CSF to communicate with the lateral ventricles via the foramina of Monro. Moreover, the third and fourth ventricles communicate via the aqueduct of Sylvius (cerebral aqueduct), which runs through the midbrain, in the diencephalon. At its caudal end, the fourth ventricle is located in the dorsal pons and medulla oblongata, taking the formation of a much smaller tent-like space, where its apex protrudes into the cerebellum. The fourth ventricle narrows caudally to form the central canal of the spinal cord. Finally, the fourth ventricle connects to the SAS through three foramina: the foramen of Magendie and the foramina of Luschka.

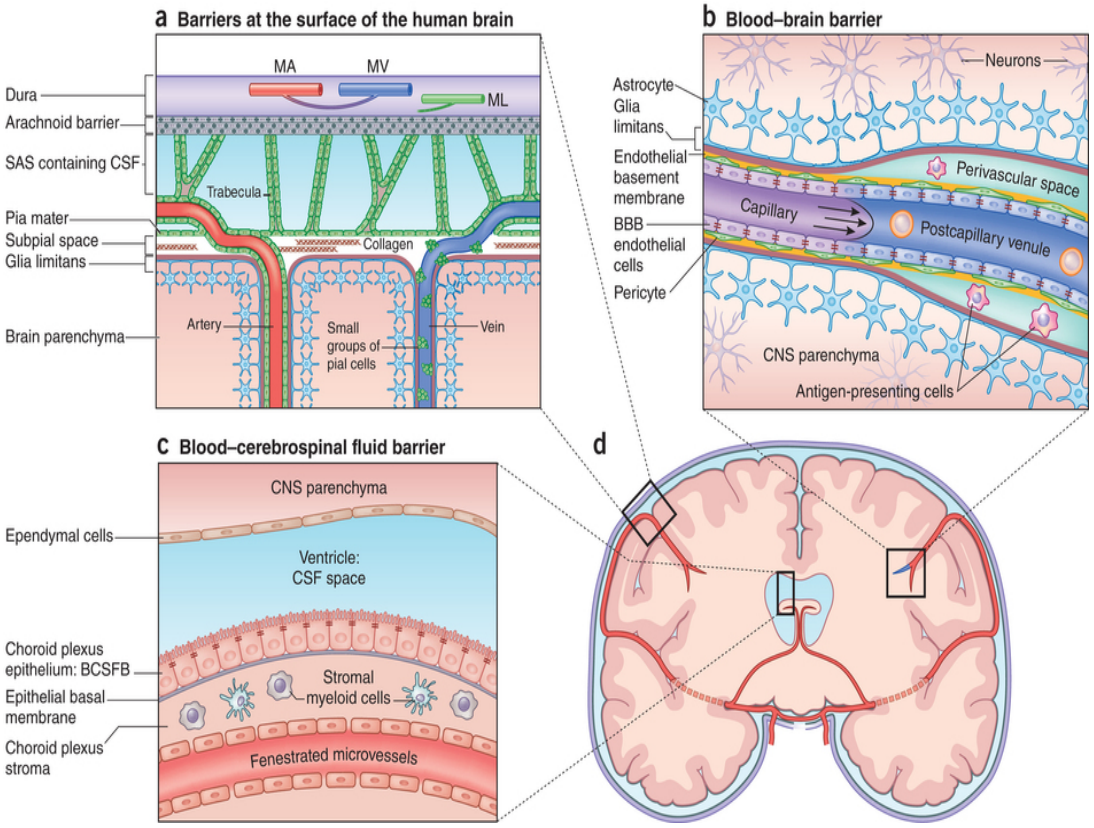


Figure 1.2 Schematic of the up-to-date microstructures in a human brain [43]. (a) Barriers at the surface of the human (b) Blood-brain barrier (c) Blood-cerebrospinal fluid barrier (d) the localisation of the brain barriers depicted via the frontal plan of the brain section

1.2.1 Cerebrospinal Fluid

Cerebrospinal fluid (CSF) is a pellucid fluid existing within the brain and spine. It occupies the SAS, ventricular system and spinal cord. At the microscopic level, the epithelial cells of the choroid plexus (CP) are constructed by parallel running tight junctions and express efflux pumps and form the blood-cerebrospinal fluid barrier (BCSFB), simultaneously (see Figure 1.2c) [44, 45]. The CP stroma which is adjacent to the epithelial basal membrane is made up of dendritic cells and macrophages [43]. According to Dandy's experimental work [46], the CP is responsible for producing CSF within the ventricular cavities. It is composed of granular meningeal protrusions of single layered epithelial cells enclosing fenestrated microvessels and is supplied by a dense microvascular network that does not form a BBB [43]. It distributes within all ventricular cavities. The brain gains buoyancy by and is loosely floating in the CSF [47]. The remaining CSF comes from other compartments, such as the capillary-astrocyte complex in the BBB, as it is an active producer of ISF [48]. The ISF eventually leads to the net formation of CSF and is secreted at the BBB. This is coupled with the transmission of extracellular fluid (ECF) between CSF and brain [49, 50].

Moreover, the fluid pressure in the cerebral environment is governed by the Monro-Kellie doctrine, postulating that the total volume of tissue, blood, ISF and CSF is constant and constrained by the volume of the skull for adult subjects [51, 52]. Within this bound cranial volume, the CSF formation rate in a healthy human may vary from 0.3 to 0.6 *ml/min*, the daily volume of CSF is around 600-650 *ml* and the normal CSF pressure is about 7.355 *mmHg* (980.638 *Pa*) in adults [48, 53]. It is important to note that the ratio of CSF volume to brain volume increases during normal ageing, irrespective of neurodegenerative processes [48, 54-58].

In 1875, Key and Retzius demonstrated the routes of cerebrospinal fluid flow [59]. This work inspired Cushing's research which introduced the concept of the *third circulation*, which suggested that CSF flows through the ventricular system, cisterns and SAS and it is absorbed into the blood stream at the arachnoid granulations (AG) via the venous sinuses [60]. This "bulk" production-mean flow-absorption pathway has been revised in recent years: research argued for a new hypothesis, which describes the cardiac cycle-dependent (systolic-diastolic) bidirectional craniospinal CSF movement [61, 62]. More recently, many in the CSF transport community still assume a dominant classical hypothesis to CSF transport [48, 63, 64]. This may mean that our current understanding of CSF movement (or circulation) seems to be a particular case of a much more complicated process. The classical hypothesis of CSF circulation is assumed here and is used to establish our poroelastic model (and its constitutive boundary conditions) in this thesis.

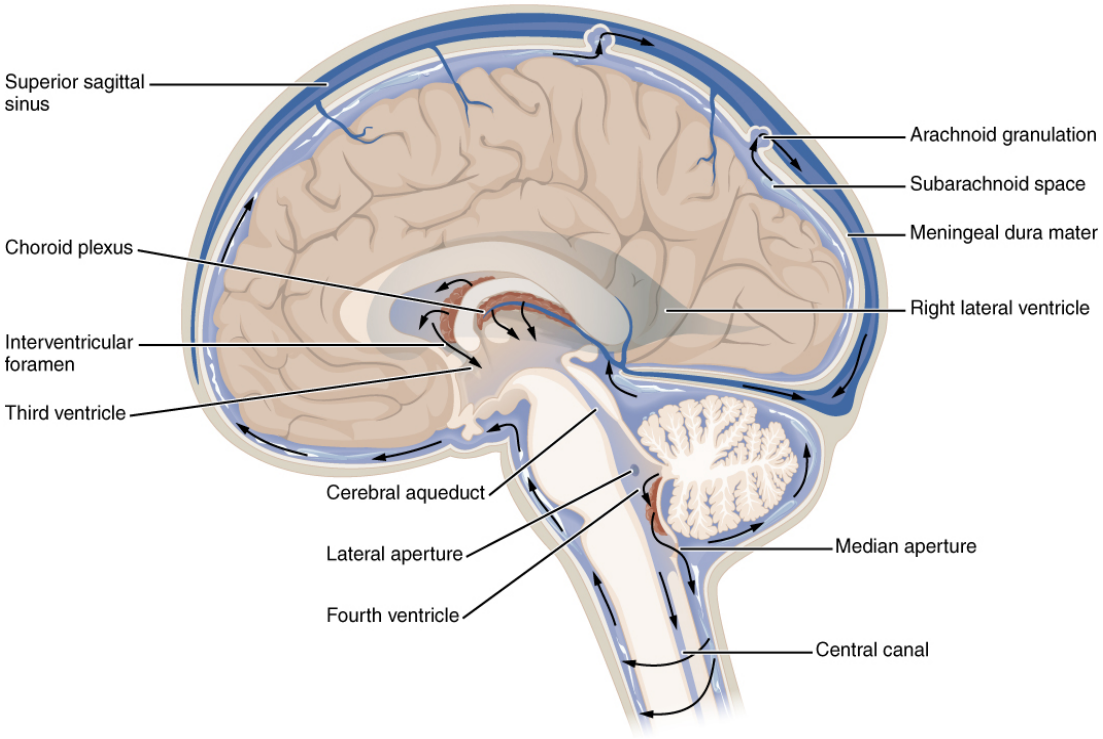


Figure 1.3 A schematic of a sagittal plane depicting important structures in the human brain, such as the ventricles and their choroid plexuses [65].

CSF serves several purposes in the cerebral environment. In the early 20th century, Cushing already proposed the concept of the third circulation, which was the idea that the CSF is similar to the blood and lymph, in addition to possessing functions of support and protection of the parenchyma [60, 63]. With developments in neuroscience, it has been shown that the CSF has additional features, such as the clearance of waste (e.g. soluble proteins) [66]. CSF plays a role in the excretion that is potentially poisoned by clearance waste (the products of cerebral metabolism). It is necessary to ensure that the fluids bathing the brain cells have a well-regulated function for metabolic waste removal because neurones need a harmonious composition of ions in the extracellular space (ECS) [67, 68]. The brain was considered as lacking a lymphatic system, so soluble proteins existed in the cerebral environment mainly leave the cerebral parenchyma via the perivascular spaces and directly diffuse to the SAS through the pia mater [69, 70]. However, the concept of a lacking lymphatic drainage system in the cerebral environment has taken on a new look, as lymphatic vessels in cerebral dura mater were discovered by Louveau A. and his colleagues in 2015 [71, 72].

1.2.2 Aquaporins

In 1877, Pfeffer investigated osmotic behaviour in living cells [73]. He mentioned that “membrane particles” exist in cell membranes and that water may penetrate these structures, a process he refers to as “cell diosmosis and swelling”. Three decades later, the phenomenon that water can penetrate biological membranes was recognised, and Nernst introduced the concept of the “semi-permeable” membrane. [74]. Using biophysical experimentation in the late 1950s, Paganelli and Solomon revisited the idea of fluid travelling through water channels of the membrane [75]. They explained that

erythrocyte cells in mammals were permeable by quite a diverse range of substances and compounds, from water to mercury (as an example of two extremes).

When Peter Agre was studying the biochemical properties of the Rh blood group antigens from the erythrocyte membrane [76], he serendipitously discovered a protein called CHIP28, a new 28 kDa membrane protein which was isolated from both red blood cells and renal tubules [77]. After cloning the full-length cDNA sequence [78] and extracting an N-terminal peptide sequence [79], he discovered the long sought after water channel, which is now known as aquaporin-1 (AQP1) [80], research that led to the Nobel Prize in Chemistry. The function and importance of this channel can be demonstrated with a simple experiment: when the protein is typically expressed in *Xenopus laevis* oocytes, these cells rapidly swell when placed in hypo-osmotic environments, (upper row of cells in Figure. 1.4). When, however, AQP is not expressed, the cells appear impermeable to water, when in the same solution, and maintain their volume, (lower row of cells in Figure. 1.4) [81]. The same phenomenon was observed in rat's kidney cells [82] and again in liposomes [83].

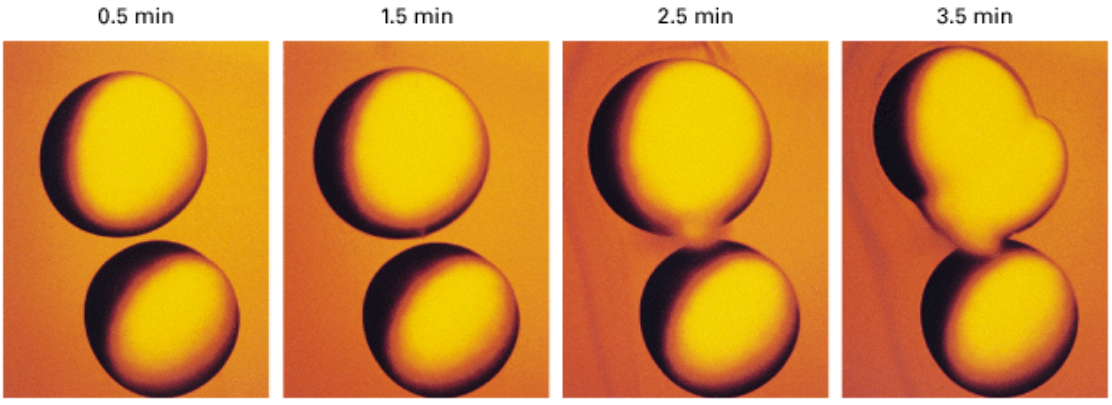


Figure 1.4 Water permeability and AQP 1 in *Xenopus laevis* oocytes [84]. The upper row shows an oocyte where AQP is expressed in a hypotonic salt solution. The lower row shows the same type of cell, in the same solution but without AQP1 expression.

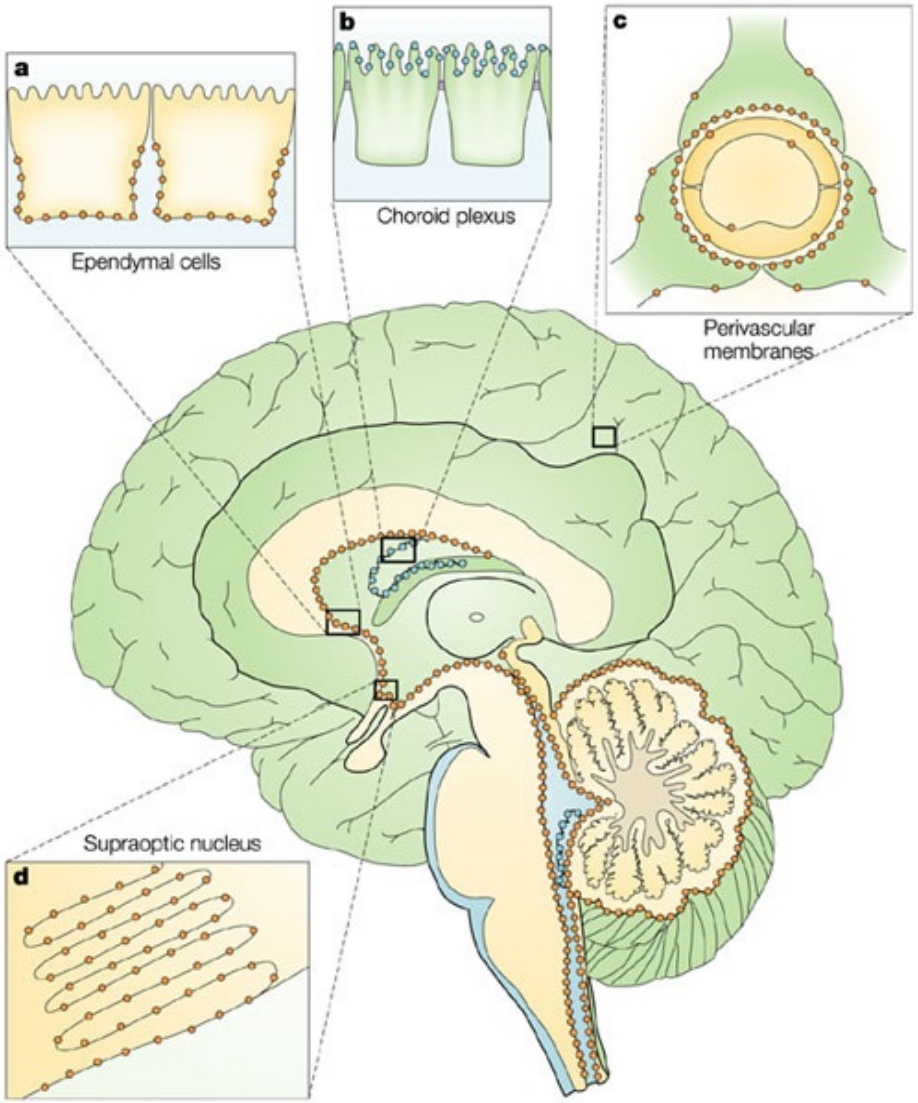


Figure 1.5 Distribution of different types of water channels in the brain (small dots represent AQPs; AQP1: blue dots; AQP4: orange dots) [85].

Since this important discovery, hundreds of homologous proteins have been identified in many species, including invertebrates, vertebrates, microbes, and plants. Thirteen different aquaporins (AQPs) with distinct distributions in various tissue types have been classified in mammals [86]. Furthermore, several regulatory mechanisms for AQPs in humans have been explained, especially distribution and function, and these have been linked to various important diseases [87, 88]. For example, neuroinflammation is usually distinguished from a hypertrophy of the astrocytes, e.g.

astrogliosis [89, 90]. AQP4 is expressed on astrocytes and is involved in water homoeostasis and oedema formation [91]. Besides the water homoeostasis function of AQP4, recent studies show further possible connections to disease, such as neuromyelitis optica (NMO) [92, 93]. In plants, more than thirty-five different AQPs and their molecular physiology have been found, especially in the plant model, Arabidopsis thaliana [94, 95].

In this research we are interested in the development of appropriate mathematical models for AQP-related processes in the brain, to embed into the Multi-network Poroelasticity Theory (MPET) framework. More specifically, given the very high prevalence of AQP4 in cerebral tissue (for example, more AQP4 channels which means a higher density of AQP4 on the end feet of the glial cells than anywhere else in the human body [96]), it is hypothesised that these channels play an important role in brain transport phenomena. Although some (often competing) theories have been proposed, there is little substantial evidence regarding their controlling mechanisms, as far as expression and/or flux regulation is concerned [97, 98], or even actual functionality. The aquaporin family (water channel proteins, WCPs) consists of two subgroups. In the first, AQPs are water-permeable and in the second, aquaglyceroporins are permeable by small neutral solutes, such as glycerol. Most AQPs inhibit the transfer of ions through them but a few AQPs, like AQP6 and AQP8, relax this constraint [99]. The distribution of these AQPs is shown in Figure 1.5. These AQPs play different roles. For example, AQP1 is expressed in the epithelial cells of the choroid plexus, where cerebrospinal fluid (CSF) is produced and plays a role in CSF formation [100]. AQP4, by contrast, is expressed in astrocytes and ependymal cells. It may not only play a role as a predominant brain water channel, but may also be involved in brain oedema formation and in potassium clearance [101, 102]. AQP9 is expressed in astrocytes, but

its distribution and expression in the brain are still controversial. It may play a role in energy metabolism [102].

1.2.3 The Glymphatic System

The lymphatic system, a network of lymphoid organs and lymphatic vessels, is not only part of the circulatory system which runs parallel to the blood circulation system as a secondary circulation, but is also part of the immune system which transports lymph and assists to clear proteins and metabolic waste from the systemic tissues back into the blood in the peripheral organs in the human body [103, 104]. The lymphatic system is not closed and there is no central pump exist in the lymphatic system as the heart in the cardiovascular system. Moreover, the lymph is made when excess ISF is collected via lymph capillaries based on the hydrostatic pressure gradients and subsequently is moved through the lymphatic vessels to lymph nodes before emptying eventually into the right/left subclavian vein [105]. If exaggerated hydrostatic pressure occurs within the lymph vessels, the fluid may backflow (leak) into the interstitial spaces and then cause oedema [106]. Regarding the lymph movement, it depends on peristalsis during constriction and relaxation of the adjacent skeletal muscle and arterial pulsation transports [107].

However, a similar system to the lymphatic system had not been discovered for the brain. In 2015, the cerebral lymphatic system was first identified by two independent studies, namely that by Louveau et al. [71] and Aspelund et al. [108]. Both of these two groups finally took a forward step in ending any speculation on the existence of a lymphatic system that caters for the CNS. Prior to this critical discovery, some studies had demonstrated the ISF movement in brain parenchyma and the constant

interchange between CSF and ISF. Traditionally, it was believed that fluids travel through the interstitial compartment in the brain parenchyma via diffusion. However, the distances between the ISF, and CSF in the ventricular system, and SAS are too far to efficiently remove the metabolic wastes via simple diffusion mechanisms, since large molecules such as albumin spend over 100*hrs* to travel across only 1*cm* of brain parenchyma [109]. Additionally, solute and water movement through the brain parenchyma slows as the extracellular volume fraction decreases and becomes more tortuous [110]. Hence, an alternative explanation to diffusion was pursued. Using “bulk flow of ISF” was favoured by early investigators to describe the mechanism for transporting metabolites and other compounds from the brain into CSF [109]. It was assumed that bulk flow of ISF from the brain to CSF could be an effective mechanism for removing compounds from the brain by analogy with other tissues [109]. Although Jin et al. [111] earlier used a spatial model to claim that the solute transport in the brain extracellular space does not support a "glymphatic" mechanism, Asgari et al. [112] recently published a paper to demonstrate that the mechanism of the solute transport through the glymphatic system may be independent of bulk flow.

The osmotic pressure gradient occurs in the capillary network of the CNS and is essential for regulation of ISF and CSF, which are continuously mixed in pulsatile fluid motion [113]. Regarding CSF and ISF being always interchanged in the parenchyma, this phenomenon is facilitated by convective CSF influx along the PVS [27]. The water channel, AQP4, along the glia limitans facilitates CSF travelling in the PVS [27, 114]. This movement drives convective ISF fluxes within the tissue toward the paravenous space [50, 115]. Finally, the ISF is collected in the paravenous space, from where it drains out of the brain toward the cervical lymphatic system [116-118]. This system, where the convective fluid facilitated to transport via AQP4 channels fluxes with rapid

interchange from CSF and ISF, was named the glymphatic system based on its ability to mimic the lymphatic system in the peripheral tissue in function [27].

Smith et al. [119] utilised the conventional explanation of the cerebral physiology to challenge this glymphatic mechanism (shown in Figure 7.1). In this paper, they insisted that the physiological function of the glial water channel, AQP4 and its contribution to cerebral oedema have been blurred by the glymphatic hypothesis. Although quantitative studies were the failure in discovering the evidence regarding the directional convective flow in the grey matter under normal conditions [120, 121], the current results from Iliff et al. [122] are a consequence of differences between normal (wild type) and AQP4 knock-out mice in the ECS structure. Therefore, one may be required to rely on the application of quantitative imaging methods and biophysically realistic spatial modelling to study the role of AQP4 in diffusive and convective fluid transport in the brain in the future research.

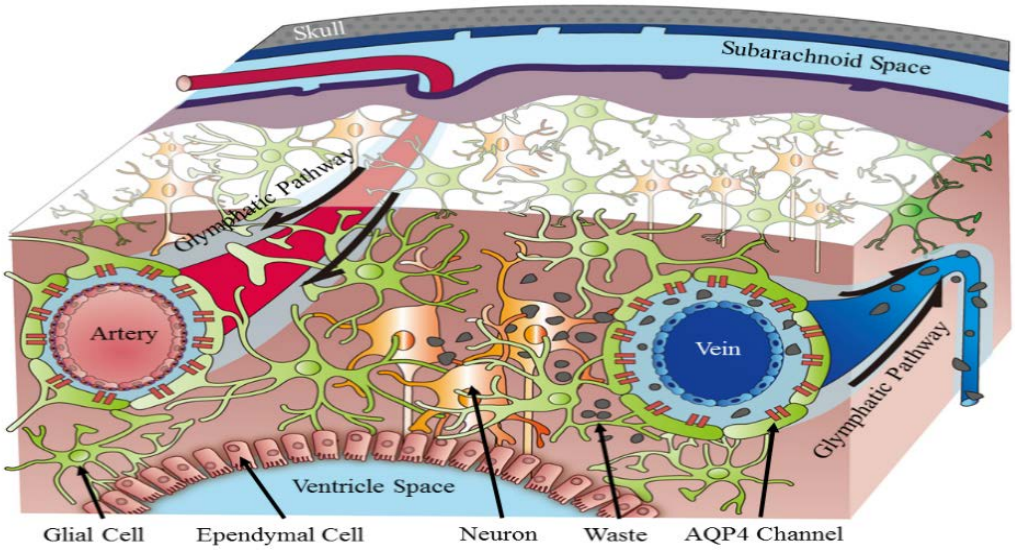


Figure 1.6 An illustration of the glymphatic system. The glymphatic pathway (black arrows) clears waste from the ISF through the brain parenchyma.

1.2.4 Diseases of the Cerebral Environment

Investigate the transport phenomena which regulate the water and ions from microscopic cellular levels to the macroscopic ventricular system, naturally lead to the investigation of cerebral diseases connected to transport, such as cerebral oedema and hydrocephalus, with all their consequent phenomena, like increased fluid content, ventriculomegaly, and abnormal pressure fields.

1.2.4.1 Cerebral Oedema

Cerebral oedema is a common clinical disorder which increases the accumulation of water content in the intra- and/or extracellular space in the brain [123]. Milhorat et. al. stipulate that the ECS oedema is usually categorised into four primary types [123]. Among these types, osmotic oedema is classified as an unbalanced osmotic gradient between the plasma and ISF across an intact BBB. Vasogenic oedema refers to the increased permeability of capillaries. Compressive oedema occurs when there is obstruction of the ISF bulk flow pathways, and hydrocephalic oedema occurs when there is an obstruction of the CSF bulk flow pathways. However, most brain injuries occur from the combination of these types making overall classification challenging. Besides the above classification, Ho and colleagues also give another simple classification; cerebral oedema may be considered as: vasogenic oedema, cytotoxic oedema, interstitial oedema and combined oedema [124].

Vasogenic oedema refers to dysfunction of BBB (formed by the tight endothelial junctions) which include physical disruption (c.f. cytotoxic oedema which keeps BBB intact), such as traumatic brain injury (TBI), intracranial hypertension and inflammatory conditions which make the movement of proteins from the intravascular

space through the capillary wall into the ECS [125-127]. Some studies showed an increased permeability of BBB to high-molecular-weight markers via animal models and suggested the early formation of vasogenic oedema after TBI [128-130]. Holtmannspötter et al. investigated the influence of intracranial hypertension on the resolution of vasogenic brain oedema following intracerebral haemorrhage [126]. They demonstrated vasogenic oedema, induced by an intracerebral hematoma, is cleared into the ventricular system and the resorption of vasogenic oedema is affected by the actual intracranial pressure (ICP). Moreover, this is the most common type of brain oedema in clinical medicine and predominantly affects white matter (lower cell density and numerous unconnected parallel axon tracts) [124, 131]. Interestingly, the early stages of vasogenic oedema may be reversible with the reorganisation of BBB which means reabsorbed excess water via CSF bulk flow and digested extracellular proteins via macrophages or transported back into cells via transmembrane carriers, but it cannot occur in chronic cases [124]. Vasogenic oedema is most frequently seen around brain tumours which are benign and malignant, e.g. meningioma; gliomas and metastases, respectively, and infectious processes like cerebral abscesses [132].

Cytotoxic oedema usually refers to cellular swelling. It results from the accumulated cations of dysregulation via ionic pumps or/and ion channels from ECS into neurones or/and glial cells [124]. When cerebral ischemia or hypoxia occurs, very few new adenosine triphosphate (ATP) molecules (a type of coenzyme for intracellular energy transfer) can be generated due to oxidative phosphorylation rapid reduction [133]. Cells rapidly exhaust their store of ATP and disturb their own regulation of homoeostasis which is maintained by primary active transport, mainly ATP-dependent Na^+/K^+ ATPase that continues consumption of ATP [134]. Whether cells are able to survival or not depends on sodium ions continuously extruded from the intracellular

space [135]. The ATP consumption induces a failure of regulation between intracellular and extracellular via Na^+ transport systems (pumps and channels), and intracellular Na^+ excessively accumulation [136]. This over-accumulation leads to an abnormal fluid movement from extracellular space into cells and further causes cell swelling. Furthermore, evidence shows that AQP4 plays a major role in cytotoxic oedema [137]. This study showed AQP4-deficient mice have much better survival than wild-type mice in a model of brain oedema caused by acute water intoxication. The cytotoxic oedema results, cerebral parenchyma water content and swelling of pericapillary astrocytic foot processes in AQP4-deficient mice, were also significantly reduced in the same study. AQP4-deficient mice are also protected from other models of cytotoxic brain oedema, including bacterial meningitis [138] and early focal cerebral ischemia [139].

Interstitial oedema (hydrocephalic oedema) is witnessed in acute hydrocephalus when the bulk CSF pathway is obstructed, and intraventricular pressure subsequently increases [124]. This leads to the periventricular space being increasingly penetrated by CSF flow into the interstitial space of the parenchyma [131]. During meningitis, interstitial cerebral oedema usually occurs because of the increasing resistance to CSF outflow [131]. The difference between interstitial oedema and vasogenic oedema is that CSF contains almost no protein in interstitial oedema [131]. Besides discovering the aetiology of hydrocephalus regarding ventriculomegaly, the mechanism of interstitial oedema was investigated on the assumption of fluid clearance which the periventricular oedema associated with the hydrocephalic process represented a similar mechanism for clearance of fluid due to the water content in hydrocephalus were limited to models of compensated hydrocephalus [140-142]. Although accumulated CSF and increased ventricular pressure are able to produce interstitial oedema with excess fluid accumulation in the cerebral parenchyma of hydrocephalus [143-145], it is insufficient

that these studies only discovered the hydrocephalic model without AQP4 effect regarding the migration of the fluid content and then dissipation of the gradients as ventriculomegaly occurred. Therefore, the further study with/without AQP4 effect from Bloch et al. showed that $AQP4^{-/-}$ mice had accelerated ventriculomegaly progression in kaolin-induced obstructive hydrocephalus model compared with wild-type mice [146]. They utilised the column gravimetry over the course of hydrocephalus to measure the water content of periventricular parenchyma in order to evaluate the magnitude of CSF flow from the ventricular to the parenchyma. For the results at three and five days, the parenchymal water content did not differ significantly between wild-type and AQP4 null mice. This implies that AQP4 deletion in mice accelerates the progression of kaolin-induced hydrocephalus by decreasing parenchymal ECF clearance. Meanwhile, Papadopoulos et al. also mentioned that the reduced water permeability of the ependymal layer, sub-ependymal astrocytes, and glia limitans via AQP4 knock-out manner ($AQP4^{-/-}$) reduces the elimination rate of CSF across these boundaries into the SAS [147].

Combined oedema is a mixed type of cytotoxic and vasogenic oedema. It results from several disorders including trauma, infection or inflammation, hypoxic-ischemic encephalopathy, osmotic oedema, and hydrostatic oedema [124].

Furthermore, AQPs and the glymphatic system are considered as alternative solutions of oedema treatment [148-150]. Other non-invasive treatments of the brain oedema include osmotherapy [151]. AQPs are widely regarded as critical solutions for the cerebral oedema, owing to their regionally distinct distribution [152-154]. Notably, AQP4 is believed to induce an interrelation between cerebral oedema and neuroinflammation [153, 155].The glymphatic system may be a possible pathway for

oedema therapy since vasogenic oedema is representative of continued increase of glymphatic fluid influx that assists in paravascular leukocyte and cytokine delivery [150].

1.2.4.2 Hydrocephalus

When the pathway of CSF in the ventricular system is obstructed, an abnormal accumulation (imbalance between production and circulation) occurs and the excess fluid increases the size of the ventricles, ventriculomegaly, because of the raised pressure. This medical condition is called hydrocephalus (HCP), depicted in Figure 1.7 [156-159]. HCP is an active dilation of the cerebral ventricle system which is caused by the insufficient passage of CSF from its main point of production (choroid plexuses) to its points of absorption into the systemic circulation [156, 160, 161]. The normal CSF pressure measured by the lumbar puncture method is approximated between 600 to 1800 *Pa* [162]. The root cause of the pathology in HCP may result from a consequence of a variety of congenital (caused by any condition that existed before birth) and acquired (a condition that did not previously exist in the patient) disorders [163].

Moreover, it may be led by the obstructive movement of CSF (e.g. stenosis of the cerebral aqueduct, obstruction of the interventricular foramina), reabsorption (e.g. impaired at the AG), or overproduction of CSF (e.g. choroid plexus papilloma, villous hypertrophy) and therefore increase the pressure in central nervous system (e.g. CSF pressure, ISF pressure) [159]. HCP is traditionally categorised into two forms according to whether obstruction occurs in or outside the ventricular system (e.g. obstructive and communicating HCP, respectively) [157]. In a way, HCP also can be further categorised

into acute HCP which is caused by obstruction of the CSF flow routes, and chronic HCP which is distinguished from the development of prolonged time scales for the unidentifiable flow obstruction when using radiographic techniques [164-166].

Acute Hydrocephalus Acute HCP is caused by the existence of obstructive flow routes during CSF movement, as per the conventional view. It causes different ventriculomegaly patterns which depend on the location of the obstruction.

- **The obstructed foramen of Monro**: it may enlarge one or both lateral ventricles (e.g. colloid cyst [167]).
- **The obstructed aqueduct of Sylvius**: It may be obstructed by a number of genetically or acquired lesions (e.g. atresia, ependymitis which is an inflammation of the ependymal tissue, haemorrhage, tumour) and lead to lateral ventricles and the third ventricle dilation [159].
- **The obstructed Fourth ventricle**: It may cause the cerebral aqueduct, lateral and third ventricle dilation. (e.g., Chiari malformation [168, 169]).
- **The obstructed foramina of Luschka and/or Magendie**: It may be obstructed because of congenital failure opening (e.g. Dandy-Walker malformation [170]).

HCP is induced by the stenosis of the aqueduct of Sylvius, as was originally reported by Bourneville and Noir in 1990 [171]. Although stenosis may be congenital or acquired, there is still some unknown cases that may still occur, such as idiopathic aqueductal stenosis [172, 173]. On the one hand, for the congenital stenosis of the aqueduct of Sylvius, it is usually difficult to extract the exact cause because there are generally numerous factors at play. It may be associated with Chiari malformation type I (herniation of the cerebellar tonsils into the cervical spinal canal) [174], vein of Galen

aneurysmal malformation (VGAM, a venous aneurysm by numerous abnormal branches of the carotid or vertebrobasilar vessels) [175], Dandy-Walker malformation (a continuum of posterior fossa abnormalities) [176], or X-linked recessive gene (L1CAM mutation) [159, 177-182]; on the other hand, the acquired stenosis of aqueduct of Sylvius may be the consequence of hemorrhage, inflammation (from infection), or a nearby tumor or cyst [159, 183, 184].

According to the intricate aetiology of the aqueductal stenosis, it can mainly divide into congenital and acquired classification [185]. Russell argued that an alternative manner to classify the nontumoral aqueductal stenosis is possible [186]. According to histopathological observations, Russell described four types of abnormality from associated aqueductal stenosis: forking, septum formation, gliosis and simple stenosis [186]. In the case of forking, the aqueduct is divided into at least two channels. Some channels can communicate with each other, some channels independently connect to the ventricle, and still other channels are terminated. These channels usually reduce the size of the aqueductal lumen, and/or disturb the laminar flow of CSF [187]. Septum formation is caused by totally or partially obstructive translucent membranes (gliotic membrane) and is usually located at the lower end of the aqueduct [188]. Moreover, Turnbull and Drake explained when glial overgrowth (a small bridging glial occlusion) is obstructive to the aqueduct, it gradually becomes a pellicle which is composed of loose textured fibrillary neuroglia from the sustained pressure and dilatation of the aqueduct of Sylvius [189, 190]. The hyperplastic glial cells which are usually a reaction to irritant, such as haemorrhage, inflammatory or toxic agents, characterise gliosis aqueductal stenosis (gliotic stenosis) [188, 191]. This increased number of cells thus cause the blockage to worsen and then make the increased pressure in the third ventricle [190]. Simple stenosis which is a naturally narrow or close aqueduct may be caused by

the developmental errors which are narrowed from birth (congenital atresia) [190]. It happens with normal ependymal cells which line with ventricles [190].

Chronic Hydrocephalus One of the most representative yet perplexing cases of chronic HCP is normal pressure hydrocephalus (NPH). It has several aliases, such as hydrocephalic dementia, communicating HCP or even "occult" HCP [192-194]. The classic symptom triad, e.g. gaits disturbance, urinary incontinence and dementia, associated with ventricular enlargement (ventriculomegaly) are present, in the absence of elevated ICP or any radiographically visible CSF flow obstruction. The term of NPH was first described by Hakim and Adams in 1965 [194], and it is often misdiagnosed, such as Parkinson's disease (PD), Alzheimer's disease (AD) or dementia, because of its chronic nature and nonspecific presenting symptoms [195]. It is important to note that it is challenging to observe flow via imaging technology, since there is no significantly identifiable flow obstruction [166, 196]. The NPH patients have been observed and measured by using magnified pulse-wave amplitudes of CSF movement via MR imaging technology for several years [197, 198]. However, this technique has failed to correctly identify those patients. It cannot reliably visualise CSF flow within the ventricular spaces or SAS via Time-SLIP [199]. The amount of drainage CSF from the CNS (approximately 20 *mL/hr*) is too little and too widely dispersed to be visualised via MR imaging technique at present [196].

Neuroimaging is this class of techniques and modalities used to create an intracranial visualisation. Hence, it is an important tool for estimating ventriculomegaly. For example, *Evan's Index,* which is the ratio of maximum width of the frontal horns of the lateral ventricles and maximal internal diameter of skull at the same level employed in axial CT and MRI images is considered as a biomarker in the diagnosis of

NPH, when the index value is 0.3 or larger [195, 200-202]. Other key features of NPH are periventricular hyper-intensities, increased CSF flow velocity in the Sylvian aqueduct, thinning and elevation of the corpus callosum on sagittal images, a narrowing of the CSF space at high convexity/midline areas relative to Sylvian fissure size and absence of a visible obstruction to CSF flow [200, 201, 203-205].

When Dr. Salomon Hakim described certain cases of HCP where a triad of neurologic symptoms occurred in the presence of "normal" CSF pressure, this was before continuous pressure monitoring techniques were developed. Therefore, "normal pressure" is a misnomer, since many patients have fluctuations in CSF pressure [195, 206, 207]. However, NPH continues to be the common name for the condition. Although this possibly misleading term, i.e. "normal pressure" hydrocephalus, has been phrased, the characterisation of NPH still generally depends on the same triad of symptoms. These symptoms may not occur all at the same time, and sometimes only one or two symptoms are present.

- **Gait disturbance**: Slow shuffling and short-stepped walking. People with NPH may have trouble with picking up their feet, going up stairs and subsequently frequently resulting in falls. They may also have difficulty turning around (turn very slowly with multiple little steps). Gait disturbance is often the most pronounced symptom and the first to become apparent [208, 209].
- **Urinary incontinence**: This means loss of bladder control. The symptom includes urinary frequency which is the need to urinate more often than usual and urinary urgency which is a strong and immediate sensation of

the need to urinate. In very rare cases, faecal incontinence may occur [210, 211].

- **Dementia**: The symptom shows a lack of interest in daily activities, obliviousness, difficulty dealing with routine tasks and short-term memory loss. Patients with NPH do not usually lose language skills. Not all individuals have an obvious cognitive impairment. In mildly affected cases, conversational skills may be preserved and thinking abilities may be relatively unchanged. In some cases, cognitive changes may only be detectable with formal neuropsychological testing [212-214].

Regarding NPH, it could be separated into two categories, idiopathic normal pressure hydrocephalus (iNPH) and secondary normal pressure hydrocephalus (sNPH). sNPH is probably formed by a subarachnoid haemorrhage, TBI, tumour, CNS infection, or a complication from cranial neurosurgery [195, 215]. The term, idiopathic normal pressure hydrocephalus, was first introduced by Shenkin et al. in 1975 [216]. iNPH occurs mainly for elderly patients with a condition that comes about from normal ICP and ventriculomegaly [159]. The aetiology of iNPH is still ambiguous, and quite different from secondary NPH, which is more comprehensible. Secondary NPH may possess causes such as subarachnoid haemorrhage, bacterial meningitis, head trauma or intracranial surgery [195].

Although the exact pathophysiological mechanism of iNPH remains unknown, some studies have been demonstrated via clinical, autopsy, biopsy and MRI including with/without shunt surgery treatment that there is a correlation between iNPH and cerebrovascular disease which is a vascular disease of the cerebral circulation [204, 217-223]. Furthermore, some arterial related research, including arterial stiffness, the

arterial pulse pressure and intracranial pulsatility have been concerned with iNPH. For example, Bateman proposed that vascular compliance which was measured in the superior sagittal sinus and straight sinus territory by use of MR flow quantification with net systolic pulse volume and arteriovenous delay as markers is significantly different in the brains of healthy subjects as compared with that in patients with ischemia/atrophy or iNPH [224]. After Bateman's research was investigated, vascular compliance of healthy subjects was significantly lower than that of patients with ischemia or atrophy, but was significantly higher than that of patients with iNPH in the superior sagittal sinus (SSS). Bateman also proposed that age-related arterial stiffness and reduced compliance of the brain leads to larger pressure pulsations in the CSF [225]. Moreover, systolic pressure and pulse pressure are associated with ventriculomegaly was concluded by Graff-Radford et al [226]. They also observed intraventricular pulse pressure (systolic-diastolic) results in ventriculomegaly via the animal model. Based on these conclusions, they speculated that high pulse pressure might play a role in the pathogenesis of iNPH. Meanwhile, the correlation between iNPH and arterial hypertension was showed in the research from Krauss et al. and arterial hypertension might be involved in the pathophysiological mechanisms promoting iNPH was proposed as well [227].

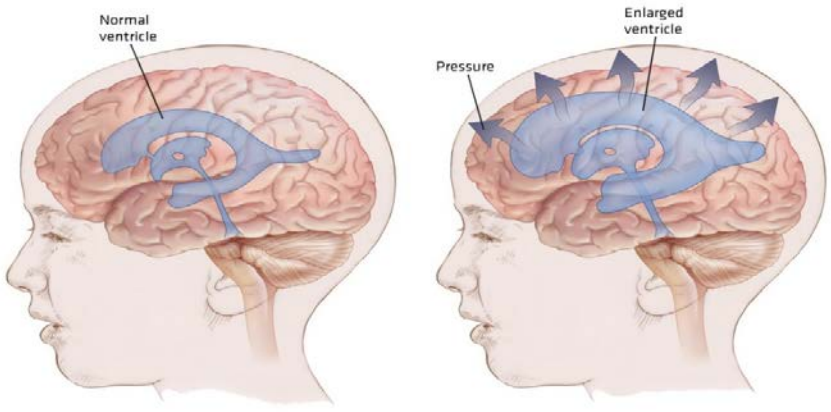


Figure 1.7 Hydrocephalus in the cerebroventricular system. The normal size of the ventricles is shown at the left-hand-side image. The enlarged ventricles at the right-hand-side image are presented because of increased intraventricular pressure [228]

Furthermore, Bateman studied the comparison of blood flow and compliance measures in a cohort study with NPH selected for having arterial inflows above the normal range in order to check whether deep white matter ischemia (DWMI) or superficial hemodynamic changes contribute to the pathophysiology of NPH [229]. He argued that DWMI is not a prerequisite for NPH, or rather an elevation in superficial venous pressure which occurs from both changes, alterations in superficial venous compliance and a reduction in the blood flow returning via the sagittal sinus. However, Bradley insisted that DWMI is a cause of NPH but not the only cause [230]. In terms of his argument, he and his colleagues made a hypothesis that NPH may be a 'two-hit' disease [231]. This two-hit hypothesis interprets that the NPH patient may lead to benign external hydrocephalus (BEH), also known as "benign macrocrania of infancy", in infancy due to reducing resorption of CSF via the "immature" arachnoid villi and granulations and catch up with deep white matter ischemia (DWMI) in agedness. Cumulatively, hydrocephalic infants suffer from the cranial volumes expansion due to the cranial sutures have not amalgamated allowing for swelling. Therefore, BEH shows slightly larger ventricles and cranium (it seems symptom-free) where the cerebral development of patients copes with mechanisms that adjust to the initial change. Afterwards, a vascular change with ageing disorders the balance and then gets NPH results.

Nevertheless, McComb et al. gave some challenges to two hit hypothesis [232]. Firstly, the correlation between body size and head size did not have any data relating body size to head size in the research from Bradley and his colleagues [231]. Infants with enlarged craniums may derive from particular familial gene expression and of course, may also occur from BEH. Moreover, these infants possessing enlarged craniums should also be defined via the correlation with their own body size. Secondly,

it is hard to prove due to a follow-up time spanning at least 50 years to correlate the targets in infancy with those individuals who subsequently develop NPH. Therefore, Tully and Ventikos proposed using Multiple-Network Poroelastic Theory (MPET), to explore NPH as a “two-hit” disease *in silico* [233]. In this study, they assumed that the infant’s brain has an increased congenital compliance (decreasing magnitude of α^c), in addition to mimicking a continual leak of the capillary compartment in older age (increasing magnitude of γ_{ce}).

Chapter 2 Literature Review in Modelling & Experimental Works in Cerebromechanics

The Topic of this Chapter

This chapter discusses the mathematical modelling and experimental works in the study of cerebral dynamics relating to transport phenomena. Although mathematical modelling can provide an efficient and low-cost way to analyse the mechanisms of cerebral fluid transport phenomena, it still has to rely on a multitude of variables which are obtained from experiments in order to inform the models and to verify the simulated results. Therefore, understanding the causal relationship of the cerebral diseases or structural disorders via a predictive manner is important. Knowledge of the cerebromechanical properties of the brain parenchyma when developing the algorithmic tools, such as the finite difference method, finite volume method and finite element method is also a pertinent issue. A selection of cerebromechanical properties and transport parameters which are measured from the relevant experimental works are also collated in this chapter.

Historically, the study of fluid transport phenomena in the human brain takes us back more than two centuries, when Alexander Monro first applied the concepts of physics to intracranial dynamics in 1783 [234]. He mentioned that the brain is enveloped within a rigid skull, the cerebral tissue is considered as the combination of incompressible substances, the blood volume in the cranial cavity is constant or nearly constant, and no excess cerebrovascular, arterial and venous blood exists. After several revisions, this line of thinking resulted in what we know today as the Monro-Kellie doctrine, which states that the total volume of the brain tissue, cerebral blood and the CSF and ISF must remain constant because of the fixed volume within the skull [51, 52]. If the volume of one component increases, it causes an equivalent decrease in the other components, a consequence of fluids and tissues being incompressible. Bulk flow theory was proposed as the “Third Circulation” by Cushing [60]. For the next several decades, the bulk flow of water in the CSF space should be treated as the pulsatile flow through the intracranial

cavity. [235]. Based on the assumption of bulk flow theory, Ransohoff suggested that the bulk flow models are able to apply on all HCP cases because of obstruction [236].

The Monro-Kellie doctrine created a foundation for future developments, as it provided a fundamental theory for creating different approaches to the discovery of pathophysiology and pathogeny within the cerebral environment. Some of these approaches are developed via modelling, and some others are established via experimental work. In the early years, most of the experimental works were mainly focused on ex vivo approaches to observe and record data via animal models or corpses (cadavers) due to technique-centric limitations. However, in order to collect the most practical information from *in vivo* studies, some non-invasive methodologies have thrived in recent years, such as magnetic resonance imaging (MRI), magnetic resonance elastography (MRE), computed tomography (CT) and ultrasound.

2.1 Cerebromechanics *in silico*

Mathematical models describing the environment of the cerebral fluid and the matrix of the parenchyma *in silico* are outlined in this section. Meanwhile, these models are separated into four subsections in the following sections: electrical analogue models, poroelastic models, viscoelastic models and cerebral models coupled with computational fluid dynamics. A summary table with strengths and weaknesses of the brain model is provided at the end of this section.

2.1.1 Electrical Analogue Models for Brain

Besides the porous models which describe the biomechanics problem in the cerebral environment, there are some circuit-based models to depict the cerebral fluid and

pressure in the cerebral environment. For example, one of the first mathematical models was addressed by Guinane [237]. He used a differential equation to describe the CSF dynamics via the idea of the circuit analysis. Marmarou [238] predicted the evolution of pressure as a function of time with the added advantage of incorporating parameters such as intracranial compliance and resistance to absorption. Slight modifications to Marmarou's model was also proposed by Sklar [239, 240]. A circuit based viscoelastic model of a spherical shell (parenchyma) which takes into account available creep compliance data was proposed by Spertell [241]. It evaluates the ventriculomegaly in response to a square-wave pressure pulse within the ventricles. Moreover, Egnor et al. [242] analysed the pulsatile motion within the cranium via an analogue electrical circuit model by applied the mathematical description of a harmonic oscillator. In this research work, the authors not only demonstrate that decreased intracranial compliance connects to a phase lag of the ICP pulse with respect to the vascular pulse, but also showed CSF velocity waveforms have good correspondence with MRI flow studies via their pulsation dynamics analogue electrical circuit model. In the next year, Egnor et al. [243] utilised the model that they had developed to discover communicating HCP. Given the simulation conditions that increased impedance to mimic an obstacle flow of CSF pulsations in the SAS redistributes the flow of pulsations into the ventricular CSF and into the capillary and venous circulation, they remarked that communicating HCP is the result of a redistribution of CSF pulsations in the cranium.

Furthermore, some researchers employ the electrical analogue auxiliary to advocate their hypothesis on "two-hit" disease or to support their supposition on cerebral homoeostasis. For example, Bradley et al. [231] designed an electrical circuit model to demonstrate increasing ventricular volume with increasing resistance to flow through the ECS of the brain and finding than an increased periventricular ADC in order

to support their hypothesis that iNPH is a “two-hit” disease. Asgari et al. [244] revealed that astrocyte networks may contribute to cerebral metabolite clearance. This electrical analogue model illustrates the cerebral water transport phenomena between arteriole and venule via PVS and astrocytes’ network including intra/extracellular spaces and capillary basement membranes which construct low resistance fluid pathways. These allow for water flux exchange through AQP4 on the astrocyte plasma membrane. Meanwhile, they used animal studies to observe the influx from Virchow-Robin space (VRS) into the cerebral parenchyma via a reduction of the applied tracer.

The aforementioned models cannot provide the information in the parenchymal region due to the inability of capturing spatial variations in the mechanical properties of the brain. This insufficient information makes the prospect of clinical treatment applications rather difficult, such as in computer-assisted clinical intervention [245].

2.1.2 Porous Parenchyma Models using Poroelasticity

In the effort to overcome the limitations of these models, an class of models emerged, which proposed the utilisation of consolidation theory [246-249] and the concept of describing the brain parenchyma as either a viscoelastic or a poroelastic porous medium [250]. Nagashima [251] solved the first representative porous biomechanical model, based on Biot’s method with a 2-D finite element method (FEM), and also provided substantial correlative results to those witnessed in clinical HCP cases and vasogenic brain oedema. Kaczmarek demonstrated a steady-state analytical solution of a poroelastic model of both the brain and ventricles [252]. The CSF and the solid matrix of the porous medium were in communication (i.e., permitted CSF exchange) in this model. The aim was to reproduce the features of ventricular dilatation and oedema

when under the influence of obstructive HCP (occlusion of the aqueduct). Levine attempted to sensitise models of this nature, which were effectively macroscopic, with microscopic effects, by describing the transcapillary exchange between ISF and blood networks using Starling's law [253]. This ultimately took into account the net colloid osmotic and hydrostatic pressures. The parenchyma in this paper was modelled as a tri-phasic linear poroelastic structure, incorporating a single solid network representing tissue elements and two fluid networks representing ISF and compressible capillary and venous channels. Levine's model was used to test three theories relating to the physiology of CSF: firstly, the ventricular walls being impermeable to CSF; secondly, the efficient absorption of ventricular CSF leaking through the parenchyma; and finally, the inefficient absorption of ventricular CSF leaking through the parenchyma. He concluded that only the second case accounts for the clinical observations of NPH. In the next year (2000), he also outlined the relationship between the size of the ventricular cavity and the impaired absorption of the CSF in pseudotumor cerebri via the similar representation of the parenchyma as mentioned earlier [254].

Smillie and Sobey developed a model for investigating HCP and the effect of shunting [255]. They developed and utilised a poroelastic model based on a Darcy flow representation of fluid movement, but also included a dual (white and grey matter) representation of the brain. A more realistic and physiologically relevant set of boundary conditions, incorporating effects such as the resistance of drainage pathways and possible deformation of the skull is also introduced here, along with a quasi-steady assumption dictating time dependence. Sivaloganathan et al. defined a single parabolic equation governing uni-directional biphasic displacement and flow which is able to describe consolidation with both a constant and a deformation-dependent permeability [256]. Wirth and Sobey extended their poroelastic framework by representing the

cerebral ventricles as lumped axisymmetric geometries within a spherical skull and in addition a 3-D representation of the lateral and third ventricle geometries within an encapsulated non-spherical skull [257]. They are both modelled via a non-linear strain-dependent permeability, linear elasticity and an embedded CSF source/sink within the parenchyma. Later in the same year and journal, Sobey and Wirth extended their poroelastic model to include the effects of non-linear permeability in models depicting communicating HCP [258]. This ultimately enabled a qualitative appreciation of the macroscopic poroelastic properties when applied on the vascular system. The skull was treated as inelastic, and in addition, the CSF absorption in the parenchyma was also investigated. Moreover, based on their previously demonstrated methodology, they showed an analysis of a multi-poroelastic model in detail, whilst excluded the interaction between the fluid compartments when modelling the infusion test [259].

Clatz et al. described the communicating HCP via a coupling of a scalar description of CSF production and resorption, along with the ventricular representation of the biphasic (CSF and parenchyma) parenchyma in a three-dimensional patient-specific cerebroventricular system and claimed the CSF flux is induced by the boundary condition of the imposed trans-parenchymal pressure [260]. Momjian and Bichsel utilised their model to capture the ventricular dilation in acute and chronic HCP [261]. They applied the hydraulic permeability as a function of void ratio to deal with this nonlinear poroelastic framework and combined with FEM from the commercial software package, COMSOL Multiphysics (COMSOL Ltd, Cambridge, UK). Narsilio et al. studied acute HCP with the incorporation of patient-specific MRI via the simplified porous medium model (not poroelastic) [262]. They used the similar manner to solve their model (by using FEM within COMSOL Multiphysics) and considered the white and grey matter as two separately entities with different permeability values.

Linninger et al. compared their fluid-tissue coupled (Navier-stokes equations and Darcy's law) poroelastic model with *in vivo* CINE-MRI measurements of CSF flow for healthy and communicating HCP patients [263]. Liu et al. also tried to use a poroelastic model to describe the ventriculomegaly and applied it to the cat brain to study obstructive HCP which is induced by kaolin [264]. By using the FEM, these equations from the poroelastic model can be solved with the adjoint equations method (AEM) to incorporate the intraoperative measurements that the displacement data was extracted from pre-drainage and post-drainage MRI. Tully and Ventikos succeeded in adapting Smillie's poroelastic model by coupling it with a multidimensional representation of the aqueduct of Sylvius in order to investigate the impact of relative degrees of stenosis in 2009 [265]. After one year, the same authors introduced a novel representation of Multiple-Network Poroelastic theory (MPET) [233]. This allowed, for the first time, the individual investigation of the multi-scalar and spatiotemporal properties dictating the transfer of fluid between the cerebral blood network, CSF and brain parenchyma. The MPET extension was specifically used to interrogate the clinical markers of NPH. However, they only demonstrated the steady-state results of the system equations by using quasi-steady boundary conditions to close the system in these two papers. This process is similar to the process that is adopted in Smillie and Sobey's paper [255]. Moreover, a spherically symmetric two-fluid poroelastic model including a CSF compartment and a single blood compartment with no exchange of fluid between the CSF and blood compartments was utilised by Sobey et al. to apply an infusion test that the apparent rate of CSF production is temporarily increased through injection of fluid directly into the CSF system with the result in CSF pressure rise [266]. They studied the blood pressure fluctuations and the spatial dependence of this model. The limitation of their model does not consider the exchange phenomena of the compartments. Wirth

et al. examined the steady state poroelastic system for the elastic models and permeability-strain relations and considered solutions for the resulting constant strain and fluid flow [267]. They proposed there is no steady solution existing when the permeability can reduce to zero and the solid matrix become impermeable in porous media flow, and a sufficient condition on the functional form of the permeability–strain relation for solutions to existing for the applied pressure. Mokhtarudin and Payne used the poroelastic model and the osmotic filtration, Starling equation, to study the effect of reperfusion on the formation of vasogenic oedema and cerebral microvessel collapse [268]. They showed the tissue displacement and interstitial pressure are increased after reperfusion, and some specific conditions may lead the vessel collapse, such as the high reperfusion pressure, low blood osmotic pressure, high cerebral capillary permeability and low cerebral capillary stiffness. Chou et al. proposed the implementation of a fully dynamic four-network poroelastic model which is underpinned by MPET, in order to account for the effects of varying stages of aqueductal stenosis and atresia during acute HCP [269]. The fully dynamic MPET implementation avoids the commonplace assumption of quasi-steady behaviour; instead, it incorporates all transient terms in the casting of the equations and the numerical solution of the resulting discrete system.

In 2010, Shahim et al. utilised a combination of data including MRI and DTI for the computational domain (parenchyma), CSF content and permeability to apply on a poroelastic model which is discretised by the FEM, and demonstrated results which depicted pressure distribution and CSF streamlines highly dependent on ventriculomegaly when considering inhomogeneous CSF content and anisotropic permeability [270]. In the next two years, they also tried to predict the onset of NPH via one-dimensional analytical poroelastic model which was based on a spherical skull and ventricles [271]. A large deformation problem is considered in this model. A similar

method was shown by Kaczmarek et al. [252]. The primary focus of this paper was CSF seepage towards brain parenchyma and the equilibrium position of the ventricular wall. A spherical geometry was recently applied by Wilkie et al. to solve the one-dimensional poroelastic problem via a convection-diffusion model which included the antibody concentration in the brain parenchyma [272]. They utilised this model to speculate that the influence of an AQP4-β1 integrin relationship and the water absorption of the capillary may play a pivotal role in the generation of pressure gradients in their HCP model.

2.1.3 Viscoelastic Parenchyma Models

To describe the physical behaviour of the brain parenchyma, most of the pertinent articles are divided into viscoelastic and poroelastic models. Some of the relevant poroelastic models are discussed in the above paragraphs; other appropriate simulation models and viscoelastic models will be subsequently outlined.

In 1944, the modelling of traumas in a biomechanical brain-tissue context was pioneered by Holbourn by employing the elasticity theory [273]. Sivaloganathan et al. applied linear viscoelasticity theory to predict the ventricular wall configuration in shunted HCP [274]. They used the elastic viscoelastic analogy (EVA) to obtain analytic solutions which consider the brain to be composed of a viscoelastic solid. In the same year and same journal, they presented a more physically relevant viscoelastic model which obtained explicit solutions for the displacement and stresses [275]. They solved the boundary value problems corresponding to adult HCP and the general case where both dilatational and deviatoric responses are assumed to be viscoelastic. A quasi-linear viscoelastic model was proposed by Drapaca et al. to apply it on HCP [276]. Due to the

high failure rate of the shunting treatments and the misplacement of the proximal catheter's tip, which can be remedied if the healed configuration of the ventricular space can be predicted, they showed the inwardly moving speed of the ventricular walls via their quasi-linear viscoelastic model and revealed that it will become practically usefulness as soon as more experimental results become available.

Regarding the high strain-rate dependence of the brain mechanical behaviour, Libertiaux and Pascon described the brain as a viscoelastic medium which assumed that the constitutive law was based on the Caputo fractional derivation operator [277]. The model that they presented was calibrated using experimental data on simple compression tests performed by Miller and Chinzei [278, 279]. Miller et al. attempted to simulate surgical procedures via their previously proposed brain tissue model, hyper-viscoelastic constitutive model and developed it as a three-dimensional non-linear finite element model [280]. An *in vivo* indentation experiment was described and applied on their model in order to complement the previous deficiency which the mechanical properties of brain tissue were measured *in vitro* [281-285]. Hence, Miller gave a technical note to emphasise that the constitutive model of brain tissue should be suitable for FEM during surgical procedures analysis after two years [286]. He showed the performance results of the neurosurgical procedures via ABAQUS with a large deformation, linear viscoelastic model to promote his statements. Kohandel et al. studied several constitutive equations for the brain based on the strain energy density function [287]. They used the polynomial function and hyper-elastic Ogden model for the strain energy and included the energy dissipation by a Prony series expansion. Davis et al. considered the fractional Zener model (four-parameter model) to study both the relaxation function and creep compliance [288]. They compared the non-fractional Zener model and four-parameter Burgers model with their results and indicated that the

fractional Zener model gives a substantially better fit to the experimental data. Mehrabian and Abousleiman gave the general solution of the poroviscoelastic model for HCP in spherical symmetry human brain tissue [289]. The poroviscoelastic constitutive model could represent the effects of the time dependence of mechanical properties of soft tissues and fluid flow hydraulics. A generalised Kelvin model was considered for the rheological properties of brain tissues. They also used numerical analysis to show the sensitivity of the solution to various factors such as aqueduct blockage level and trabeculae. Results indicated that only severe occlusion of the aqueduct could cause a significant increase in the ventricle and extracellular fluid pressure of the brain.

2.1.4 Cerebral Models incorporating Computational Fluid Dynamics

Fin and Grebe utilised the anatomical shape of the cerebral aqueduct as a fluid-structure interaction (FSI) problem to discuss the difference between deformable and rigid aqueduct [290]. They found that the deformability of the walls has a strong influence on the pressure drop for a given flow. Kurtcuoglu et al. used patient-specific data which obtained via segmentation of MRI brain anatomy scans to reconstruct CSF velocity and pressure fields in the third ventricle and the aqueduct of Sylvius via the computational fluid dynamics (CFD) [291], and outlined a CFD model to describe the behaviour of the CSF-containing spaces, within the impermeable ventricular walls in the same year [292]. Later, Kurtcuoglu et al. again used the same methodology which combined the reconstruction of the patient-specific MRI data and CFD simulations which set the boundary conditions from the brain motion scans and CSF flow velocity via magnetic resonance velocimetry (MRV) to outlined the three most important flow features

witnessed in the third ventricle and aqueduct of Sylvius, such as jets and recirculation zones [293]. He also published a review paper which mentioned the use of CFD models in the SAS, ventricles and perivascular space regarding modelling the CSF flow via CFD [294].

Linninger et al. [295] utilised canine based mathematical models to examine Hakim's hypothesis [296], which asserts that transmural pressure gradients (between ventricles and SAS) across the parenchyma might be associated with describing ventriculomegaly. Moreover, the FSI model based on fluid mechanics showed flows and pressures throughout the cerebral ventricular pathways consistent with both animal ICP measurements and human CINE phase-contrast MRI data. Regarding the animal model, they injected kaolin into six canines' brain to induce HCP. However, they did not observe the large transmural pressure gradients via the animal model. According to the results of their experimental data, there is no transmural pressure difference in these canines' brain. They also mentioned that the minimum sensitivity of their equipment that they used the ICP monitors is around 1-2 mmHg (133-267 Pa). Therefore, even if the pressure differences exist, it should be below 1-2 mmHg. Furthermore, they utilised fluid mechanics to explain that the large transmural pressure differences cannot be developed with open ventricular pathways via the simulation manner. Regarding the FSI model, the periventricular tissue lining the ventricles was modelled by linear elastic springs and the pulsatile motion of the cerebrospinal flow was linked to arterial blood flow in the choroid plexus. They also gave an explanation regarding CSF flow reversal and showed that increased ICP is a result of increased fluid because of lowered absorption of CSF via their hydrodynamics model. A homogenous isotropic porous medium was assumed to represent brain tissue and bulk CSF flow boundary conditions including the CSF generation of CP in the lateral ventricles by Linninger et al. as well

[297]. They assumed that CP continues to generate CSF and produce the pulsating flow of CSF during the cardiac cycle. In this research, large ICP variations in amplitude between normal and hydrocephalic human brain were also witnessed. They tried to compare experimental results of flow velocities and flow patterns to two and three-dimensional CFD simulation results in the normal and hydrocephalic human brain.

Howden et al. used CFD simulations to describe a geometrically accurate three-dimensional patient-specific ventricular system constructed from MRI [298]. They investigated the pulsatile CSF movement via their CFD model which provided the time varying pressure data for the outlets of the ventricular system. A nesting approach to account for the pressure boundary conditions at the outlets was employed. Gupta et al. presented a three-dimensional subject-specific model to assess the CSF dynamics in the inferior cranial SAS, superior spinal SAS and fourth ventricle through the use of an anisotropic porous media model [299]. This has the benefit of taking directional variations in permeability within the trabecular SAS into consideration. They assumed that CSF production in the fourth ventricle is around 5% of the overall CSF production [300] which was calculated by superimposing volumetric flow rates at the outlet boundaries and calculating the net flow rate over a cardiac cycle. They also assumed that there is no seepage of CSF through the ventricular or subarachnoid walls and that 95% of CSF is produced in the lateral and the third ventricles.

The CP in the third and lateral ventricles (which accounted for 95% of the CSF production) were not independently considered. For boundary conditions, velocity profiles were obtained through MRV and implemented accordingly. Sweetman et al. presented a three-dimensional flow model of the intracranial space and used it to predict CSF flow patterns and ICP as a consequence of brain tissue displacement in normal and

hydrocephalic cases [301]. The ventricular system and the entire cranial SAS were included in this paper. Arterial expansion and contraction were represented by volumetric expansion terms (source terms). They proposed to treat brain tissue as poroelastic in order to foster a better understanding of pathological brain dynamics as part of their future model refinement. Bouzerar et al. developed the dynamics of HCP model with the laws of thermodynamics to show that the dynamical instabilities lead to dilation of the ventricles [302]. They also claimed that the development of a unified view of these complex intracranial conditions along with a classification via their dynamical approach may be clinically relevant.

Vardakis et al. used the MPET model coupled with a finite-volume CFD technique for the purpose of exploring the efficacy of endoscopic ventriculostomy for HCP Treatment [303]. They proposed the amalgamation of anatomically accurate choroid plexuses with their feeding arteries and a simple relationship relaxing the constraint of a constant permeability for the CSF compartment with AQP4 mediated swelling characteristics. They not only investigated the impact of aqueductal stenosis and fourth ventricle outlet obstruction but also considered the implications of treating such a clinical condition with the aid of endoscopic third (ETV) and endoscopic fourth (EFV) ventriculostomy. Later, Vardakis et al. also utilised MPET via two formats, a one-dimensional finite difference–CFD coupling framework, as well as a two-dimensional FEM formulation to investigate the role of endoscopic fourth ventriculostomy in alleviating oedema formation due to fourth ventricle outlet obstruction (1D coupled model) in addition to observing the capability of the FEM template in capturing important characteristics allied to oedema formation, like for instance in the periventricular region (2D model) [304].

To provide a more comprehensive, as well as critical, perspective on available models, an attempt to tabulate some important efforts and to list the respective strengths and weaknesses is shown below. Table 2.1 shown below, is based on the work that considered CSF (fluid) and parenchymal mechanics (solid) is the summary of the selected categorisation effort.

Ref.	Strong Points	Weak Points
Chou [269]	• 4MPET model with fully dynamic implementation	• 1-D linear mathematical model • Simplified geometry
Kurtcuoglu [305]	• Using CFD to simulate and couple all four ventricles and their connecting pathways	• Approximation and idealization of geometrical representation • Assuming rigid ventricle walls
Kurtcuoglu [306]	• Using patient-specific geometries of the cerebral aqueduct and the third ventricle from MRI data • Boundary conditions obtained from MRI	• Neglected the choroid plexuses
Kaczmarek [252]	• Providing analytical solution for a poroelastic model of both the brain and ventricles • Considering the communication between CSF and the solid matrix of the porous medium • Including strain dependent permeability • Utilizing the experimental data via the edema of hydrocephalic cats to compare the simulation results	• Using an idealised cylindrical geometry • Using rough estimates of material properties • Ignored material non-linearities of the solid matrix
Levine[253, 254]	• Varying the Biot parameter as a measure of the relative roles of blood and interstitial fluid in changing the parenchymal volume • Using Starling law to describe the transcapillary exchange between interstitial fluid and blood networks • Treat the tissue as a deformable porous medium • Account for hydrodynamic coupling between ventricles. This allow for quantitative statements to be made on the flow and pressure	• Model in 1-D • Using a simplified spherical geometry
Linninger [307]	• Confirming the existence of pulsatile ICP via canine experiments • A hydraulic experiment to obtain better insight into the asymmetric expansion of the lateral ventricles	• 2-D CFD geometry analysis • 1-D fluid-structure interaction model
Linninger [308]	• Using homogenous isotropic porous medium to represent brain tissue and bulk CSF flow boundary conditions • The first systematic procedure for conducting a detailed CFD flow analysis for individual patients based on MRI data • Clinical *in vivo* flow measurements are utilised to validate the proposed computational model • Integrated MRI-CFD approach for studying intracranial dynamics	• No account of the exchange of CSF with the spinal SAS and the influence of spinal SAS compliance on intracranial dynamics • No account of displacement of brain tissue • No account of the spinal cord • Does not account for deformations of the parenchyma

Linninger [309]	• Giving a good interpretation of their previous work on acquiring CSF flow, pressure and brain tissue displacement based on fluid dynamics and poroelasticity theory	• Many comparisons between normal and hydrocephalic simulation were conducted within 2-D • Do not fully create a spatially accurate model of the cerebral vasculature
Loth [310]	• Using N-S equations coupling 1-D model (Circular Annulus) and 2-D model (Ellipitic Spinal Cavity and Circular Spinal Cavity)	• 2-D geometries • Simplifying and not considering nerve roots and compliant boundaries
Miller [311]	• Using non-linear theory of continuum mechanics • Considering the Ogden-based hyper-viscoelastic constitutive model • Applying FEM procedures for the numerical solution of the proposed models • Coupling FEM and meshless method with explicit time-marching procedures	• Expensive calculations • Only take account for brain tissue-not including CSF • Assuming pressure boundaries without including the fluid • Require to know the full strain history and state of stress of the tissue
Sivaloganathan [256]	• Including a permeability that varies with deformation of the ventricular wall • Giving the solutions for the spatial and temporal variability	• Single 1-D parabolic equation governing displacement and flow
Sivaloganathan [274]	• Assume parenchyma is a viscoelastic solid • Yields explicit and analytical solutions to provide benchmark solutions for numerical procedures capable of handling more complex geometries	• Parenchyma is impermeable • Simplify the ventricular cavity as a thick walled cylinder • CSF at a fixed pressure
Smillie [255]	• Two-layer (white & grey matter), Two-phase (CSF & brain tissue), Spherical poroelastic model • Provide a new set of boundary conditions with a more realistic representation of the physical system and quasi-steady time dependence • A review of the parameters to be used in describing the poroelastic properties of the brain tissue	• 1-D linear mathematical model • Simplified geometry • Quasi-static implementation
Sobey [258]	• Applying non-linear permeability in a small strain poroelastic framework • Exploring a number of quantitative consequences for CSF circulation and absorption • Noted that including non-linear permeability should increase the relevance to clinical observations • Extension of the model to communicating HCP	• Using the geometric simplicity of a spherical model • Theoretical results not validated with clinical results • Without viscoelastic effects • Idealised the SAS as an infinitesimally thin layer • Ignored any effects from oscillations of pressure and flow on the time-scales of heartbeat or breathing
Tully [265]	• Using fluidic-poroelastic coupling (SPET coupled with CFD) implementation to study acute HCP • Investigating the impact of physically relevant stenosis patterns on ventricular enlargement	• 1-D linear mathematical model • Artificial geometry
Tully [233]	• Using MPET to investigate NPH • allow a detailed investigation of spatiotemporal transport of fluid between the cerebral blood, cerebrospinal fluid (CSF) and brain parenchyma across scales	• 1-D linear mathematical model • Simplified geometry • Quasi-static implementation

Ursino [312]	• Using reduced mathematical complexity to describe the craniospinal compartment by non-linear pressure-volume relationship • The physiological reliability • Directly usable in neurosurgery intensive care units (ICU's)	• Neglected the role of venous blood volume changes • Cannot simulate the rapid effect of perturbations arising in extracranial venous drainage pathways • Cannot distinguish between the action of the mechanisms working on large pial arteries and those working on small arterioles • Cannot study ICP pulsating waves synchronous with the cardiac beat or with respiration.
Vardakis [303]	• Using MPET combined with CFD to explore the efficacy of endoscopic ventriculostomy for HCP treatment • The implications of treating such a clinical condition with the aid of ETV and EFV	• 1D MPET coupled 3D CFD • Simplified geometry in MPET as a lumped model
Vardakis [304]	• One-dimensional finite difference–CFD coupling framework • Investigated the role of endoscopic fourth ventriculostomy in alleviating oedema formation • Extend MPET to 2D FEM model	• 1D MPET coupled 3D CFD • Simplified geometry in MPET as a lumped model
Wirth [257]	• 3-D poroelastic model • Applied on axisymmetric non-spherical ventricle model • Including non-linear strain-dependent permeability & a gravitational term in the governing equations • Providing the spatial distribution of physical variables (pressure, fluid velocity & fluid content)	• Only considering lateral and third ventricle geometries • No connecting pathways (Aqueduct of Sylvius)
Wirth & Sobey [313]	• Multi-poroelastic model (between CSF, arterial & venous blood) • Considering the spatial and temporal structure of the solution • Providing an analytic solution to validate and calibrate numerical methods	• Using a spherically symmetric model of the brain • Requires the enhanced accuracy of the constitutive laws • Investigation is required for the numerical solutions for these analytic solutions • Considering isotropies of the tissue • The arterial pulse is not synchronous all over the brain • Neglected the cerebrospinal system

Table 2.1 Summary of the selected CSF brain models.

2.2 Pertinent Cerebral Experimental Work

In the following section, experimental research in cerebromechanical properties, processes and cerebral diseases are considered. In particular, HCP and cerebral oedema will be focused upon.

2.2.1 Cerebromechanical Properties Measurement

Regarding cerebromechanical properties, there are some common methods that are used for investigating cerebral parenchyma, such as shear, compression, indentation and tensile testing. Shear testing is one of the most common types of mechanical tests performed on brain tissue. It is commonly conducted in the brain because of the high shear strain of the primary mechanism behind traumatic brain injury (TBI) [314]. The dynamic complex shear modulus of *in vitro* samples of the human brain have been measured by Fallenstein et al. [315]. Eight specimens of brain tissue were subjected to a sinusoidal shear stress input under resonant conditions on an electro-mechanical test device. All tests were conducted to determine the effects of time after death, refrigeration of material and shear strain dependence. The intracranial expansion of brain tissue for live (under anaesthesia), dead and fixed (fixation with formalin) were measured and compared by Metz et al. [316]. The materials that they analysed kept the assumption of elasticity. The results indicated that the elastic modulus increases with strain and varies between the ranges of strain tested.

Although the shear modulus of death and fixation (with formalin) of brain tissue are increased as well, it does not appear to change the manner in which it varies with strain tested. Donnelly and Medige also demonstrated the shear properties of human brain tissue [317]. These shear tests were performed on 125 tissue samples taken from

twelve fresh cadaver brain specimens. They examined a relationship between shear stress and strain by performing transient, single-pulse, shear displacement tests via the equipment which generated constant rate shear strains in cylindrical tissue samples mounted between the shear plates. Galford and McElhaney showed the stress relaxation (or creep response) on the scalp, brain and dura from both human and monkey under compression [318]. An empirical expression for the observed creep curves was developed and a four parameter Maxwell-kelvin fluid model was proposed to fit the creep data. They also presented a free vibration test using the same equipment as the creep and relaxation experiments. For the tensile testing, there are few researches to present it for cerebral parenchyma [279, 319]. This may come from two sources: it is technically difficult and is less important than shear in TBI.

Recently, the dynamic behaviour of porcine brain tissue was analysed with the aid of a large strain, nonlinear, viscoelastic constitutive model by Prevost et al. to capture the observed complexities of the material response during loading, unloading and relaxation over the entire range of strain rate [320]. The model was further verified by comparing model predictions with the tissue response in unconfined compression at higher strain rate and with data from the literature during uniaxial tension. Later, Sanborn et al. showed the inertial effects on the characterisation of the dynamic response of brain tissue [321]. They used fresh bovine brain tissue to study its mechanical response via two modified Kolsky bar techniques and examined radial deformation behaviour of annular specimens. The results presented that the annular specimen geometry aimed at reducing inertia induced stress components for high rate soft materials uniaxial-compressive testing may still possess a significant component of radial inertia induced radial stress which consequently caused the observed inhomogeneous deformation in brain tissue test samples. Li et al. developed a three-

dimensional FEM model using linear poroelasticity to study the mean ICP response during constant rate infusion [322]. They provided the main poroelastic constants via the parametric study (artificial neural network was used to obtain the best parameter fitting with the experimental data) and showed their influence on the mean ICP infusion curve. They also pointed out an important parameter, the specific storage coefficient, for future consideration.

Moreover, there are also a lot of non-invasive methods to be developed to study the properties of brain parenchyma, such as ultrasound and MRE. The concept behind ultrasound is that an ultrasound device transmits and receives ultrasonic waves through the tissue, and so one may estimate the stiffness of the tissue from the attenuation and speed of propagation of the waves through this tissue. The advantage of this method is that it could be used to investigate brain properties *in vivo* (non-invasive detection). However, some drawbacks to this method make it difficult for widespread use. For example, there are difficulties in achieving ultrasound wave penetration through the skull, and the tissue region that is accessible to the ultrasound waves may be limited because of the attenuation at high frequencies. Using shear wave elasticity imaging via a quantitative ultrasound technique to obtain the shear modulus of the porcine brain tissue *in vivo* was demonstrated by Urbanczyk et al. [323]. For *in vitro* measurement of brain tissue properties, Nicolas et al. proposed a shear wave inducing system for brain ultrasound elastography [324]. They validated their system *in vitro* on a tissue mimicking phantom by doing shear wave velocity measurements. Another MRE technique has been developed to characterise the mechanical properties of soft tissues *in vivo* using a magnetic resonance (MR) scanner [325]. This technique uses an external source of cyclic excitation (or vibration) to produce and propagate waves in the tissue, and then an MR scanner is used to visualise and quantify the propagating strain waves

for computation of viscoelastic properties. In a similar way to the ultrasound technique, MRE analysis is based on shear wave propagation as these have a lower attenuation at high frequencies. One of the advantages of MRE over ultrasound is that magnetic field gradients can penetrate the skull and be easily superimposed along any desired axis, thus making MRE more appropriate for investigating the anisotropic mechanical properties of brain tissue [326, 327].

2.2.2 Cerebral Diseases Measurement

Some experimental work of cerebral diseases, HCP and cerebral oedema, will be introduced here. In 1976, Marlin et al. studied the fluid movement through the hydrocephalic brain in felines' model [328]. They examined the effects of changes in serum osmolality on the bulk flow through the cerebral ventricles and on water content in the feline's brain with kaolin-induced HCP. According to their calculation for the filtration coefficient, they inferred that the water flows from serum through the brain and into CSF is limited by the resistance of fluid flow through the brain. Two years later, Collins also published an experimental obstructive HCP model in the rat [329]. He injected the kaolin suspension into twelve days old rats and observed the anatomy of these rats via scanning electron microscopy. The ependymal damage occurred in half of these twelve rats. Two of the remainder possessed fibres on the ependymal surface, and the others had tears covered with small round cells. He believed that these four cases are responsible for the repair of the ependyma. The periventricular regions present in the third and fourth ventricles were not damaged by ventriculomegaly, even during severe HCP.

Aarabi and Long studied the dynamics of cerebral oedema in felines, with a focus on the role of an intact vascular bed in the production and propagation of vasogenic brain oedema [330]. They utilised the standard brain oedema generation procedure, a standardised cortical freezing lesion to study a single removed piece (injured cortex) either immediately after induction or at two, four, or eight hours after lesion production. They reached certain conclusions after their experimental work: Firstly, the formation of the expected vasogenic brain oedema can be completely reversed when the lesion is removed immediately after production. Secondly, the replacement of the frozen brain, therefore, is unable to increase the permeability of the surrounding BBB or the amount of brain oedema. Thirdly, the amount of cerebral oedema is halted no matter when the lesion is removed (2, 4, or 8 hours), with or without replacement. Moreover, an intact vascular bed is necessary for the ECF component of brain oedema. Børgesen and Gjerrris collected and analysed the relationships between ICP, ventricular size and CSF resorption from 230 patients [331]. This study showed a linear relationship between ICP and outflow resistance. Generally, the CSF formation rate tends to decrease with increasing ICP is concluded by their study. They also gave the implication that a small or normal ventricular size in acute or subacute condition does not preclude defective CSF resorption. McCormick et al. studied the time course of intraventricular pressure (IVP) in a canine's brain via a kaolin-induced hydrocephalic condition [332]. They monitored the IVP and obtained that IVP is increased within thirty-six hours after kaolin suspension infusion.

Since some cerebromechanical properties of oedematous brain parenchyma had not been well explained before the research of Kuroiwa et al., they measured regional compliance and swelling level of the cat brain parenchyma during the development of vasogenic and cytotoxic oedema [333]. They marked the differences in basic

cerebromechanical properties between vasogenic and cytotoxic oedema. For the vasogenic oedema results induced by cryogenic injury, they concluded that the white matter has an increase of regional parenchyma compliance in addition to increased water content (swelling). Johnson et al. used the new blockage method which is the surgical occlusion of the fourth ventricle with a cryanoacrylic gel injection to study the development of obstructive HCP in the canine model via MRI [334]. The results showed that the ICP was gradually raised and brain compliance abated. The advantages of this model are less clinical symptoms and without any local compression or general inflammation. Kostopoulos et al. also developed the new method to do an early diagnosis for the brain oedema and verified it using a rabbit model [335]. They concluded that the eigenfrequency spectrum and the modal damping characteristics are the major parameters for measuring a mass increase in the skull.

In 2000, Manley et al. used the AQP4 deletion mice model to observe brain oedema and ischemic stroke [137]. They showed that the AQP4 deficient mice have higher survival rate than wild-type mice for brain oedema induced by acute water intoxication. In AQP4 deficient mice, the brain water content and swelling condition were significantly reduced from their research conclusions. At twenty-four hours, measurement results showed hemispheric enlargement and alleviative oedema in AQP4 deficient mice. These results implicated that AQP4 plays a regulatory role in brain water transport and AQP4 inhibition provide a means of alleviating brain oedema. Mao et al., based on their hypothesis, showed that AQP expression should be increased in the hydrocephalic brains because of their function in facilitating water transport. They used real-time polymerase chain reaction, western blotting and immunohistochemistry in order to examine the expression of AQPs including AQP1, AQP4 and AQP9 in kaolin-induced hydrocephalic rats [336]. In that study, increased immunoreaction

occurred along the perivascular region in severe HCP, at three to four weeks after evocation. Their experimental results inferred that the compensatory behaviour, namely AQP4 up-regulation, may promote water homoeostasis in HCP.

Bloch et al. studied the role of AQ4 in cytotoxic and vasogenic oedema [337]. Regarding cytotoxic oedema, they demonstrated that AQP4 deletion (knock-out) or altered expression (knock-down) plays a protective role which assists to reduce oedema burden and to improve the overall survival in their animal studies. They also had a similar conclusion with previous studies, whereby it was deduced that AQP4 not only plays an important role in cerebral water transport but also crucially facilitates water (formation and resorption) through the brain tissue. Tourdias et al. utilised the measurement of the apparent diffusion coefficient (ADC) to bridge AQP4 expression and severe HCP in the rat brain [338]. They induced communicating inflammatory HCP in rats in order to prove their hypothesis that water movement via AQP4 could alter ADC. They found the periventricular AQP4 up-regulation in the hydrocephalic rats is strongly correlated with CSF volume and periventricular ADC. They observed that the whole astrocyte membrane would switch to hypertrophy in the most severe and chronic hydrocephalic rats. This observation and finding may support the previous studies that the expression of AQP4 keeps a dynamically adaptive pattern in severe HCP and may actually be a protective mechanism. They implied that AD might indirectly reflect quantitative AQP expression as well.

Moreover, Feng et al. showed sporadic obstructive HCP in AQ4 null mice [339]. They reported an unexpected observation in a small (random) subset of AQP4 null mice. This unexpected observation is that encephalomegaly in this subset has a threefold larger size than others. They also reported reduced ventricular size and ependymocytes

disorder are presented in some non-hydrocephalic AQP4 null mice. The development of cerebral aqueduct stenosis in humans may occur from AQP4 polymorphisms is one of the statements that was stipulated. In HCP, a compensatory phenomenon (brain water clearance) is presented when the expression of AQP4 raised. This compensatory phenomenon occurs due to the idea that was proposed by Bloch et al., where it was demonstrated that there was accelerated ventriculomegaly and raised ICP in the kaolin-induced AQP4 null mice [146].

Recently, the research work from Paul et al. actually supported this argument, since they evaluated different AQP expression in AQP1 and AQP4 in congenital hydrocephalus Texas (H-Tx) rat [340]. This H-Tx rat model which is a well-accepted animal model of congenital obstructive HCP was utilised to show the relationship between AQP4 and HCP [341]. Since AQPs' mechanism which mediates water movement has been discovered, it is important to the role of AQP4 in HCP and characterises the spatiotemporal change and distribution of AQP4. Therefore, their research results suggested that a subset of H-Tx rats may have arrested HCP, which is related to the temporal progression and severity of ventriculomegaly because alternative AQP absorption mechanisms have compensated for obstructed CSF pathways.

However, McAllister et al. challenged that their research did not consider the causes for the protracted survival of these rats [342]. They mentioned that the precise aetiology for HCP in the H-Tx rat continues to be investigated and unclear whether ventriculomegaly is because of atresia or stenosis. Furthermore, Skjolding et al. demonstrated that AQP4 expression levels are significantly influenced by the spatiotemporal dependent (dynamic) manner in the kaolin-induced hydrocephalic rats

[343]. In this research, they showed that ventriculomegaly occurs at lateral ventricular volume over control at all the time points after induced and the periventricular ADC value is apparently increased after one and two weeks of HCP. Relative AQP4 density is clearly decreased in both cortex and periventricular region after two days and normalised after one week and periventricular AQP4 expression is significantly increased after two weeks. They also concluded that relative periventricular AQP4 density is significantly correlated with the lateral ventriculomegaly and AQP4 levels are significantly affected by a spatiotemporal dependency in kaolin-induced HCP. The same results were demonstrated by the same author in a recent paper which presents AQP4 expression as being significantly increased in both hydrocephalic human and rat brain [344].

Chapter 3 Poromechanics

The Topic of this Chapter

The formerly basic theory of deformable porous media was demonstrated by Biot's linear constitutive equations, coupled with fluid flow via Darcy's law, in 1941. However, the term poroelasticity was coined by J. Geertsma work in 1966 (as a footnote in his paper) [345]. During this half-century, poroelasticity theory has been applied to many scientific fields, such as geomechanics, hydrogeology, petroleum engineering and biomedical engineering. The aim of this chapter is to present the spatiotemporal multiple-network poroelastic theory and extend it to describe the multiscale cerebral transport phenomena using six-compartments specifically. The discretisation procedure via the finite difference method and the associated parameter estimation will be shown in this chapter.

3.1 Poroelasticity

Many natural materials are considered as porous media, such as rocks, soil (e.g. sand and clay), and biological tissues. These different porous media vary significantly in underlying structure. For example, sand consists of solid particles and pore spaces to form a granular type structure, micro/nanofabricated materials are constructed by a regular array of cylindrical pores, and polymeric gels are mainly composed of a fibre matrix. For complex biological tissues, several of these structures may exist simultaneously. All of these porous media are assembled by considering a solid matrix (small material volumes or particles) and the void space (pores), including penetrable and isolated pores. Describing the deformation of the solid matrix in porous media and the flow of the pore fluid is the subject of the theory of poroelasticity, also known as poromechanics.

The theory of consolidation was developed by Terzaghi [346]. He derived the consolidation equation for his one-dimensional laboratory experiments to be the diffusion equation for excess pore water pressure. The theory for the time rate of one-dimensional consolidation was based on some underlying assumptions in the derivation of the mathematical equations:

- The clay layer is saturated and homogeneous;
- Darcy's law valid;
- Both of the pore fluid and the soil particles are incompressible;
- One-dimensional flow;
- Small strains;
- Linear relationship between volume change and effective stress.

With the above assumptions, the phenomena of a saturated porous medium with the stress created by a specific load are simplified to depict as Terzaghi's one-dimensional consolidation.

Moreover, the general three-dimensional theory of poroelasticity was created by Biot [347] and showed that Terzaghi's one-dimensional consolidation theory is a particular case of his theory. He subsequently extended this theory to present wave propagation in a fluid-saturated (fluid-filled) porous medium [348, 349]. However, the realistic representation of porous media should be in possession of both storage and transport. In classical poroelasticity theory, there is a lack of investigation of the transport phenomena in a porous medium. Hence, poroelasticity theory was extended to multiple-network poroelasticity theory (MPET) to describe natural porous media [249, 350-355], such as fissured rocks [356] or fractured reservoirs [357].

3.1.1 Poroelastic Constitutive Relations

In Biot's poroelasticity theory for an isotropic fluid-saturated porous medium [347], there are two major linear constitutive equations for the case of an isotropically applied stress field, σ. The two linear constitutive equations are expressed as:

$$\varepsilon = \frac{1}{K}\sigma + \frac{1}{H}p \tag{3.1a}$$

$$\zeta = \frac{1}{H}\sigma + \frac{1}{R}p \tag{3.1b}$$

The quantities here are the volumetric strain $\epsilon \equiv dV/V$, where V is the bulk volume, the increment of fluid content ζ, and the fluid pressure p (pore pressure). The fluid pressure greater than atmospheric pressure is positive. The increment of fluid content is positive while fluid is added to the control volume and negative while fluid is moved out the control volume. When the volumetric strain is positive, this represents an expansion. A negative volumetric strain denotes contraction. Regarding the convention for stress, a positive stress is tensile whilst a negative stress is compressive.

The above equations are a statement of the observation that changes in applied stress and pore pressure produce a fractional volume change (the volumetric strain) and require fluid be added to or moved out from storage (the pores), respectively. The poroelastic constants are defined as ratios of field variables while maintaining various constraints on the elementary control volume. For each coefficient in Eqn. (3.1a) and Eqn. (3.1b), the physical meaning will now be addressed. The coefficient $1/K$ is defined from measuring the volumetric strain due to change in applied stress while maintaining a constant pore pressure (referred to as the drained condition). The concept of holding a constant pore pressure can be explained to be enforced by inserting a tube

into a porous medium and connecting it to a fluid reservoir at the same pressure or vented to atmospheric pressure. Hence, $1/K$ can be defined as the compressibility of the material measured under drained conditions, and K is the drained bulk modulus. The coefficient $1/H$ is obtained by measuring the bulk volume changes due to a pore pressure change while maintaining a constant applied stress. The coefficient $1/R$ is the unconstrained specific storage coefficient measured under conditions of constant applied stress and describes the rate of change in the volume of water storage per unit permeable volume with respect to changes in the pore pressure. The unconstrained specific storage coefficient is denoted as S_σ:

$$S_\sigma \equiv \frac{1}{R} = \frac{\alpha}{KB} \tag{3.2}$$

Where α is the Biot-Willis coefficient and B is Skempton's coefficient, which is the ratio of the induced pore pressure to the change in applied stress for undrained conditions (which means that no fluid is exchanged with the control volume ($\zeta = 0$)), hence:

$$B \equiv -\left.\frac{dp}{d\sigma}\right|_{\varsigma=0} = \frac{R}{H} \tag{3.3}$$

Skempton's coefficient is nearly naught ($1/K_f \rightarrow 0$) when air fills the pore volume, whereas it is typically between 0.5 to 1.0 for fluid-saturated grains-like solid matrix and close to 1.0 for a fluid-saturated soft solid matrix (e.g. biological tissue or soil) [358]. Furthermore, Biot introduced the coefficient $1/M$ at a constant strain in addition. It is called the constrained specific storage coefficient and designated S_ε:

$$S_\varepsilon \equiv \left.\frac{d\zeta}{dp}\right|_{\varepsilon=0} = \frac{1}{M} = \frac{\alpha}{K_u B} \tag{3.4}$$

where ε is the volumetric strain and K_u is undrained bulk modulus. Its definition and relationship to coefficients in the compliance formulation are

$$K_u \equiv \left.\frac{d\sigma}{d\varepsilon}\right|_{\zeta=0} = \frac{K}{1-\alpha B} \tag{3.5}$$

By solving Eqn. (3.1a) for σ and substitute this into Eqn. (3.1b), one can show the relating S_ε to the aforementioned coefficients. The increment of fluid content is then indicated as a function of volumetric strain and pore pressure:

$$\zeta = \frac{K}{H}\varepsilon + \left(\frac{1}{R} - \frac{K}{H^2}\right)p \tag{3.6}$$

Moreover, the ratio K/H is known as the Biot-Willis coefficient α, which is the ratio of increment of fluid content to volumetric strain while maintaining a drained condition (constant fluid pressure):

$$\alpha \equiv \left.\frac{d\zeta}{d\varepsilon}\right|_{p=0} = \frac{K}{H} \tag{3.7}$$

It is equal to unity when the solid matrix is incompressible. It is less than unity for a compressible solid matrix because the change in bulk volume is larger than the change in pore volume [358].

Eqn. (3.4) and Eqn. (3.5) with Eqn. (3.3) and Eqn. (3.7) show that

$$S_\varepsilon = S_\sigma - \frac{K}{H^2} = S_\sigma - \frac{\alpha^2}{K} = \frac{1}{R} - \frac{K}{H^2} \tag{3.8}$$

Eqn. (3.8) shows that the unconstrained specific storage coefficient is larger than the constrained specific storage coefficient due to the constrained condition, where the bulk volume remains constant.

Now, Eqn. (3.6) can be rewritten as

$$\zeta = \alpha\varepsilon + \frac{1}{M} p = \alpha\varepsilon + S_{\varepsilon} p \tag{3.9}$$

The ratio K/K_u is same as the expression of the ratio S_ε/S_σ of the constrained to unconstrained specific storage coefficients which divide Eqn. (3.4) by Eqn. (3.2). Therefore, taking the ratio K/K_u with Eqn. (3.7) and substituting into Eqn. (3.8), one can obtain another relation of the constrained storage coefficient with Biot-Willis coefficient, undrained, and drained bulk modulus,

$$S_{\varepsilon} = \frac{\alpha^2}{K_u - K} \tag{3.10}$$

Moreover, the drained and undrained Poisson's ratios, ν and ν_u, are related to the moduli G (shear modulus), K, and K_u for the representation of the linear poroelastic theory.

$$\begin{aligned} \nu &= \frac{3K - 2G}{2\left(3K + G\right)} \\ \nu_u &= \frac{3K_u - 2G}{2\left(3K_u + G\right)} \end{aligned} \tag{3.11}$$

There are two limiting cases to notice. Firstly, when $\alpha = 1$ and $\nu_u = 0.5$ imply the strongest poroelastic effect, some researchers call it as the incompressible constituents

model [359, 360]. Secondly, when $\nu \cong \nu_u$, this is an uncoupled model situation which means both Skempton's, and poroelastic effects are neglected [359].

3.1.2 Poroelastic Governing Equations

Before introducing the poroelastic governing equations, the concept of effective stress, which for soil is well approximated to be the difference between the applied stresses and pore pressure (since the solid matrix part is incompressible relative to the soil) shall be presented. It was first stated by Karl von Terzaghi, who studied both volumetric deformation and shear failure in the soil [346]. The effective principal stresses are approximated by the differential principal stresses. This is also known as the Terzaghi effective stress:

$$\sigma'_{ij} = \sigma_{ij} + \alpha p \delta_{ij} \tag{3.12}$$

where δ_{ij} represents the Kronecker delta and σ_{ij} is the total stresses. For an isotropic and linearly elastic medium, the effective stress can be shown as a stress-strain relation equation with the shear modulus G and Poisson's ratio ν, yielding:

$$\sigma'_{ij} = 2G\varepsilon_{ij} + \frac{2G\nu}{1-2\nu}\varepsilon_{kk}\delta_{ij} \tag{3.13}$$

Meanwhile, the strain-displacement relationship is given by

$$\varepsilon_{ij} = \frac{1}{2}\left(\mathbf{u}_{i,j} + \mathbf{u}_{j,i}\right) \tag{3.14}$$

The poroelastic governing equations can be presented in momentum equilibrium and mass conservation [361-364] in the saturated domain:

3.1.2.1 Momentum Equilibrium Equations

Considering that static equilibrium leads to the momentum balance for the solid-fluid ensemble by a unit volume, we have

$$\sigma_{ij,j} + \rho\left(\mathbf{b}_i - \ddot{\mathbf{u}}_i\right) = \rho_f \ddot{\mathbf{w}}_i \tag{3.15}$$

where σ_{ij} is the stress in the solid matrix, $\mathbf{b}_i$ is the body force per unit mass, $\mathbf{u}_i$ is the displacement of the solid matrix, $\mathbf{w}_i$ is the displacement of the fluid phase relative to the solid matrix, and ρ is the assembly density (total density) written as

$$\rho = \phi\rho_f + \left(1-\phi\right)\rho_s \tag{3.16}$$

The left-hand-side of Eqn. (3.15) can be rewritten in a manner that the Lagrangian coordinate system moves with the solid phase and the right-hand-side of Eqn. (3.15) can be rewritten that the fluid acceleration terms (convective acceleration in terms of relative velocity applies on the fluid phase) are described in a Eulerian frame relative to the solid matrix (refer to Zienkiewicz et al. [363]):

$$\sigma_{ij,j} + \rho\left(\mathbf{b}_i - \ddot{\mathbf{u}}_i\right) = \rho_f \left(\frac{\partial \dot{\mathbf{w}}_i}{\partial t} + \dot{\mathbf{w}}_j \dot{\mathbf{w}}_{i,j} \right) \tag{3.17}$$

where $\dot{\mathbf{w}}_i = d\mathbf{w}/dt$ is the average relative seepage velocity. Moreover, the second governing equation describes the momentum equilibrium for the pore fluid.

$$\rho_f \left(\mathbf{b}_i - \mathbf{u}_i\right) - p_{,i} - \mathbf{R}_i = \frac{\rho_f}{\phi}\left(\frac{\partial \dot{\mathbf{w}}_i}{\partial t} + \dot{\mathbf{w}}_j \dot{\mathbf{w}}_{i,j} \right) \tag{3.18}$$

where $\mathbf{R}_i$ represents the viscous drag force (units of force per volume, e.g. N/m^3). The validity of the Darcy seepage law is assumed here and is given by

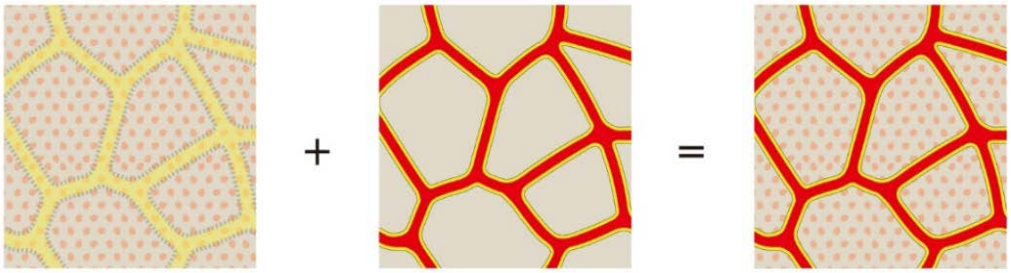


Figure 3.1 The sketch of the Dual-MPET system, e.g. pores (LHS) and fissures (middle), the concept used in geotechnical engineering.

$$\kappa_{ij} R_j = \dot{\mathbf{w}}_i \tag{3.19}$$

where κ_{ij} represent the fact that anisotropic mobility is used with dimensions of [length]^3[time]/[mass] (units of area square per force per time, e.g. m^4/Ns). If the isotropic case is considered, these shall be replaced by a constant κ value. The permeability is defined in units of area (e.g. m^2), which relates to the area of the pore space in the cross section that is perpendicular to the direction of flowing fluid. The mobility is defined as the permeability of the porous media divided by the dynamic viscosity of the fluid flowing through the porous media. Moreover, hydraulic conductivity is defined as the discharge velocity of fluid flow through the porous medium which is equal to the volumetric flow rate (fluid flux) divided by the cross-sectional area. The hydraulic conductivity has units with dimensions of [length]/[time] (e.g. *m/s*).

3.1.2.2 Equation for the Fluid Phase

Mass conservation equation applied to the fluid phase:

$$\dot{p}/M + \alpha \dot{\varepsilon}_{ii} + \dot{\mathbf{w}}_{i,i} = \overline{s} \tag{3.20}$$

where $\bar{s}$ is the source term which represents the rate of volume changes of the fluid. The first term of the LHS introduces a constant M which denotes the storage due to the compressibility of the solid and fluid phases. The second term of the LHS shows the additional storage caused by the expansion of the solid matrix.

3.1.3 The Simplified Governing Equations

Eqns. (3.17), (3.18), and (3.20) with the ancillary Eqns. (3.12) – (3.14), and (3.19) point to a well-defined closed problem, various solutions of which have been demonstrated in the literature [361-363]. However, this highly non-linear system of equations makes the framework computationally expensive. Hence, a simplified system of equations should be considered in practice. Before simplifying the assembled system of equations, some conditions should be set up.

Considering to deal with the majority of geomechanical low-frequency problems, the solution of the full equations is possible to reduce and the new simplified system of equations leads to major computational economies. Therefore, the low-frequency range has to be pondered. Firstly, according to Biot's hypotheses in the low-frequency range are [365]:

- the wavelength of the perturbations is large in comparison with the diameter of the pores and the same as the representative macroscopic volumes;
- the amplitudes of the perturbations are small;
- the elastic (isotropic) matrix is fully saturated in a single fluid phase.

Meanwhile, he gave a valid relationship to express the range of the low-frequency [366]. The low-frequency in Biot theory is adequate for the harmonic wave of frequency $f <$

$0.15f_c$ where characteristic frequency, $f_c = \mu\phi/2\pi\lambda\kappa\rho_f$ (μ: dynamic viscosity, λ: tortuosity).

Secondly, when the low frequencies of acceleration occur in the motion of an earthquake, the right-hand-side term addressed in the Eulerian reference frame in Eqns. (3.17) and (3.18) does not play a significant role [367, 368]. Moreover, the terms of the Eulerian reference frame in Eqns. (3.17) and (3.18) are involved the relative acceleration of the fluid, so these three terms are omitted when dealing with the low-frequency range problem. Hence, the relative fluid displacement $\mathbf{w}_i$ can be excluded from the system equations, and $\mathbf{u}$ and p are preserved as the two primary variables. Subsequently, the simplified governing equations (system equations) will be outlined accounting for the above assumptions.

Since the second assumption is the condition that we will deal with, the Eqns. (3.17) and (3.18) can be converted to:

$$\sigma_{ij,j} + \rho\left(\mathbf{b}_i - \ddot{\mathbf{u}}_i\right) = 0 \tag{3.21}$$

and

$$\rho_f\left(\mathbf{b}_i - \mathbf{u}_i\right) - p_{,i} - \mathbf{R}_i = 0 \tag{3.22}$$

respectively. Due to the first assumption above, Eqn. (3.20) is rewritten as

$$\dot{p}/M + \alpha\dot{\varepsilon}_{ii} + \dot{\mathbf{w}}_{i,i} = \overline{s} \tag{3.23}$$

Combining Eqn. (3.19) and (3.22), one obtains:

$$\dot{\mathbf{w}}_i = \kappa_{ij}\rho_f\left(\mathbf{b}_j - \ddot{\mathbf{u}}_j\right) - \kappa_{ij}p_{,j} \tag{3.24}$$

and substituting Eqn. (3.24) into Eqn. (3.23),

$$\dot{p}/M + \alpha\dot{\varepsilon}_{ii} + \left[\kappa_{ij}\rho\left(\mathbf{b}_j - \ddot{\mathbf{u}}_j\right) - \kappa_{ij}p_{,j}\right]_{,i} = \overline{s} \tag{3.25}$$

Furthermore, substituting Eqn. (3.12) and (3.13) into Eqn. (3.21),

$$\left(\sigma'_{ij} - \alpha p\delta_{ij}\right)_{,j} + \rho\left(\mathbf{b}_i - \ddot{\mathbf{u}}_i\right) = 0 \tag{3.26}$$

Therefore, the final simplified governing equations of the **u**-*p* formulation shall be demonstrated in vector notation as (the details for converting Eqn. (3.26) to Eqn. (3.27a) is available in Appendix, A2):

$$\rho\left(\frac{\partial^2\mathbf{u}}{\partial t^2} - \mathbf{b}\right) = G\nabla^2\mathbf{u} + \frac{G}{1-2\nu}\nabla\left(\nabla\cdot\mathbf{u}\right) - \alpha\nabla p \tag{3.27a}$$

$$\frac{1}{M}\frac{\partial p}{\partial t} + \alpha\frac{\partial\left(\nabla\cdot\mathbf{u}\right)}{\partial t} + \kappa\rho\left[\left(\nabla\cdot\mathbf{b}\right) - \frac{\partial^2\left(\nabla\cdot\mathbf{u}\right)}{\partial t^2}\right] = \kappa\nabla^2 p + \overline{s} \tag{3.27b}$$

3.1.4 Multiple-network Isotropic Linear Poroelastic Theory

The concept of the MPET system utilises the description of natural porous media, which is comprised of the solid matrix permeated by porosity elements (e.g. pores and fissures) that are communicating with each other (fluids transfer between them) (see Figure 3.1). Within this system, a solid matrix is permeated by different fluid networks ($\Omega = \Omega_1, \ldots, \Omega_m$). Moreover, MPET is a system model assembled by considering mass conservation, momentum equilibrium, a porous seepage law, stress-strain relationship, and the Terzaghi effective stress principle. This system model can be showed in the following way:

3.1.4.1 Terzaghi effective stress with Multiple Fluid Network

When the Terzaghi effective stress Eqn. (3.12) is applied to multiple fluid networks (Ω), it is rewritten as:

$$\sigma'_{ij} = \sigma_{ij} + \sum_{\Omega=\Omega_1}^{\Omega_m} \alpha^{\Omega} p^{\Omega} \delta_{ij} \tag{3.28}$$

3.1.4.2 Momentum Equilibrium Equations with Multiple Fluid Network

While the momentum equilibrium equations Eqn. (3.17) and Eqn. (3.18) are applied to multiple fluid networks, they can be expressed as:

$$\sigma_{ij,j} + \rho\left(\mathbf{b}_i - \ddot{\mathbf{u}}_i\right) = \sum_{\Omega=\Omega_1}^{\Omega_m} \rho_f^{\Omega} \left(\frac{\partial \dot{\mathbf{w}}_i^{\Omega}}{\partial t} + \dot{\mathbf{w}}_j^{\Omega} \dot{\mathbf{w}}_{i,j}^{\Omega} \right) \tag{3.29}$$

and

$$\rho_f^{\Omega}\left(\mathbf{b}_i - \mathbf{u}_i\right) - p_{,i}^{\Omega} - \mathbf{R}_i^{\Omega} = \sum_{\Omega=\Omega_1}^{\Omega_m} \frac{\rho_f^{\Omega}}{\phi^{\Omega}} \left(\frac{\partial \dot{\mathbf{w}}_i^{\Omega}}{\partial t} + \dot{\mathbf{w}}_j^{\Omega} \dot{\mathbf{w}}_{i,j}^{\Omega} \right) \tag{3.30}$$

where ϕ^{Ω} and ρ_f^{Ω} represent the porosity and fluid density of the Ω compartment, respectively. Meanwhile, the total density is extended from Eqn. (3.16)

$$\rho = \sum_{\Omega=\Omega_1}^{\Omega_m} \phi^{\Omega} \rho_f^{\Omega} + \left(1 - \sum_{\Omega=\Omega_1}^{\Omega_m} \phi^{\Omega}\right) \rho_s \tag{3.31}$$

3.1.4.3 Mass conservation in the Fluid Phase with Multiple Fluid Networks

Eqn. (3.20) can be extended to multiple fluid networks in the following way:

$$\dot{p}^{\Omega}/M + \alpha\dot{\varepsilon}_{ii} + \dot{\mathbf{w}}^{\Omega}_{i,i} + \left(\dot{\rho}_f/\rho\right)\dot{\mathbf{w}}^{\Omega}_{i} = \sum_{\Lambda=\Omega_1,\Lambda\neq\Omega}^{\Omega_m} \overbrace{\gamma_{\Lambda\Omega}\left(p^{\Omega} - p^{\Lambda}\right)}^{\bar{s}_{\Lambda\to\Omega}} \tag{3.32}$$

In Eqn. (3.32), the mass conservation of the equations includes the sum of all interporosity fluxes $\bar{s}_{\Lambda\to\Omega}$, from network Λ to Ω. Here, the transfer is considered to be driven by a hydrostatic pressure gradient, and $\gamma_{\Lambda\Omega}$ is the transfer coefficient scaling the flow from network Λ to Ω. Following the conditions mentioned in the section 3.1.3, the final field equations, Eqn. (3.27a) and Eqn. (3.27b), are presented as,

$$\rho\left(\frac{\partial^2\mathbf{u}}{\partial t^2} - \mathbf{b}\right) = G\nabla^2\mathbf{u} + \frac{G}{1-2\nu}\nabla\left(\nabla\cdot\mathbf{u}\right) - \sum_{\Omega=\Omega_1}^{\Omega_m}\alpha^{\Omega}\nabla p^{\Omega} \tag{3.33a}$$

$$S^{\Omega}_{\varepsilon}\frac{\partial p^{\Omega}}{\partial t} + \alpha^{\Omega}\frac{\partial\left(\nabla\cdot\mathbf{u}\right)}{\partial t} + \kappa^{\Omega}\rho^{\Omega}\left(\nabla\cdot\mathbf{b}\right) - \kappa^{\Omega}\rho^{\Omega}\frac{\partial^2\left(\nabla\cdot\mathbf{u}\right)}{\partial t^2} = \kappa^{\Omega}\nabla^2 p^{\Omega} + \sum_{\Lambda=\Omega_1,\Lambda\neq\Omega}^{\Omega_m}\bar{s}_{\Lambda\to\Omega} \tag{3.33b}$$

3.2 Four-compartmental Multiple-network Poroelastic Theory

In section 3.1.4, the interaction of multiple intercommunicating fluid networks in a deformable solid matrix was outlined. Before showing the adaptation of the MPET system to the cerebral environment, some simplified assumptions will be mentioned.

3.2.1 General Assumptions

The MPET framework has been described independently of the coordinate system. For this thesis, we employ a spherically symmetric geometry to describe the parenchyma of the healthy adult brain when developing the boundary conditions and applying this direct representation to the 1D system presented herein. The body force term can be ignored in this 1D system. The fluid acceleration terms, described in an Eulerian reference frame relative to the solid matrix (on the right-hand-side of the Eqn. (3.17) and Eqn. (3.18)), can be neglected due to the acceleration frequencies being low in biological flows according to Tully et al. [164, 233, 265]. Although Tully did not specifically mention the definition of the lower-frequency range [164, 233], the lower-frequency range may consider the Biot's investigation [365]. Meanwhile, Bukhman et al. [369] investigated the spectral and topographic features of the vibrations generated on the surface of the human body at rest. They concluded that low-frequency spectra of the vibrations are excited by the internal organs on the surface of the human body and several specific features are found in the spatial distribution of the spectra in the frequency range from 0.1 to 100 Hz.

For the mechanical properties in the cerebral environment, the material properties of the parenchyma will be taken to be isotropic and homogenous (ignoring

white/grey matter region, white matter tracts, etc.), and the CSF is treated as incompressible. Furthermore, to adapt this MPET modelling framework in order to capture the transfer phenomena of fluid through the brain parenchyma, we propose that the solid porous matrix represents the brain parenchyma, accompanied by the communicating fluid phases of arterial blood (*a*), arteriole/capillary blood (*c*), venous blood (*v*) and the CSF/ISF (*e*) space. Now, extending Eqns. (3.33a) and (3.33b) to represent four-network poroelasticity theory (4MPET), the general system equations dictate:

$$\rho\frac{\partial^2\mathbf{u}}{\partial t^2}=G\nabla^2\mathbf{u}+\frac{G}{1-2\nu}\nabla\left(\nabla\cdot\mathbf{u}\right)-\alpha^a\nabla p^a-\alpha^c\nabla p^c-\alpha^v\nabla p^v-\alpha^e\nabla p^e$$

$$S_\varepsilon^a\frac{\partial p^a}{\partial t}+\alpha^a\frac{\partial\left(\nabla\cdot\mathbf{u}\right)}{\partial t}-\kappa^a\rho^a\frac{\partial^2\left(\nabla\cdot\mathbf{u}\right)}{\partial t^2}=\kappa^a\nabla^2p^a+\overline{s}_{a\to c}+\overline{s}_{a\to v}+\overline{s}_{a\to e}$$

$$S_\varepsilon^c\frac{\partial p^c}{\partial t}+\alpha^c\frac{\partial\left(\nabla\cdot\mathbf{u}\right)}{\partial t}-\kappa^c\rho^c\frac{\partial^2\left(\nabla\cdot\mathbf{u}\right)}{\partial t^2}=\kappa^c\nabla^2p^c+\overline{s}_{c\to a}+\overline{s}_{c\to v}+\overline{s}_{c\to e} \qquad (3.34a\text{-}e)$$

$$S_\varepsilon^v\frac{\partial p^v}{\partial t}+\alpha^v\frac{\partial\left(\nabla\cdot\mathbf{u}\right)}{\partial t}-\kappa^v\rho^v\frac{\partial^2\left(\nabla\cdot\mathbf{u}\right)}{\partial t^2}=\kappa^v\nabla^2p^v+\overline{s}_{v\to a}+\overline{s}_{v\to c}+\overline{s}_{v\to e}$$

$$S_\varepsilon^e\frac{\partial p^e}{\partial t}+\alpha^e\frac{\partial\left(\nabla\cdot\mathbf{u}\right)}{\partial t}-\kappa^e\rho^e\frac{\partial^2\left(\nabla\cdot\mathbf{u}\right)}{\partial t^2}=\kappa^e\nabla^2p^e+\overline{s}_{e\to a}+\overline{s}_{e\to c}+\overline{s}_{e\to v}$$

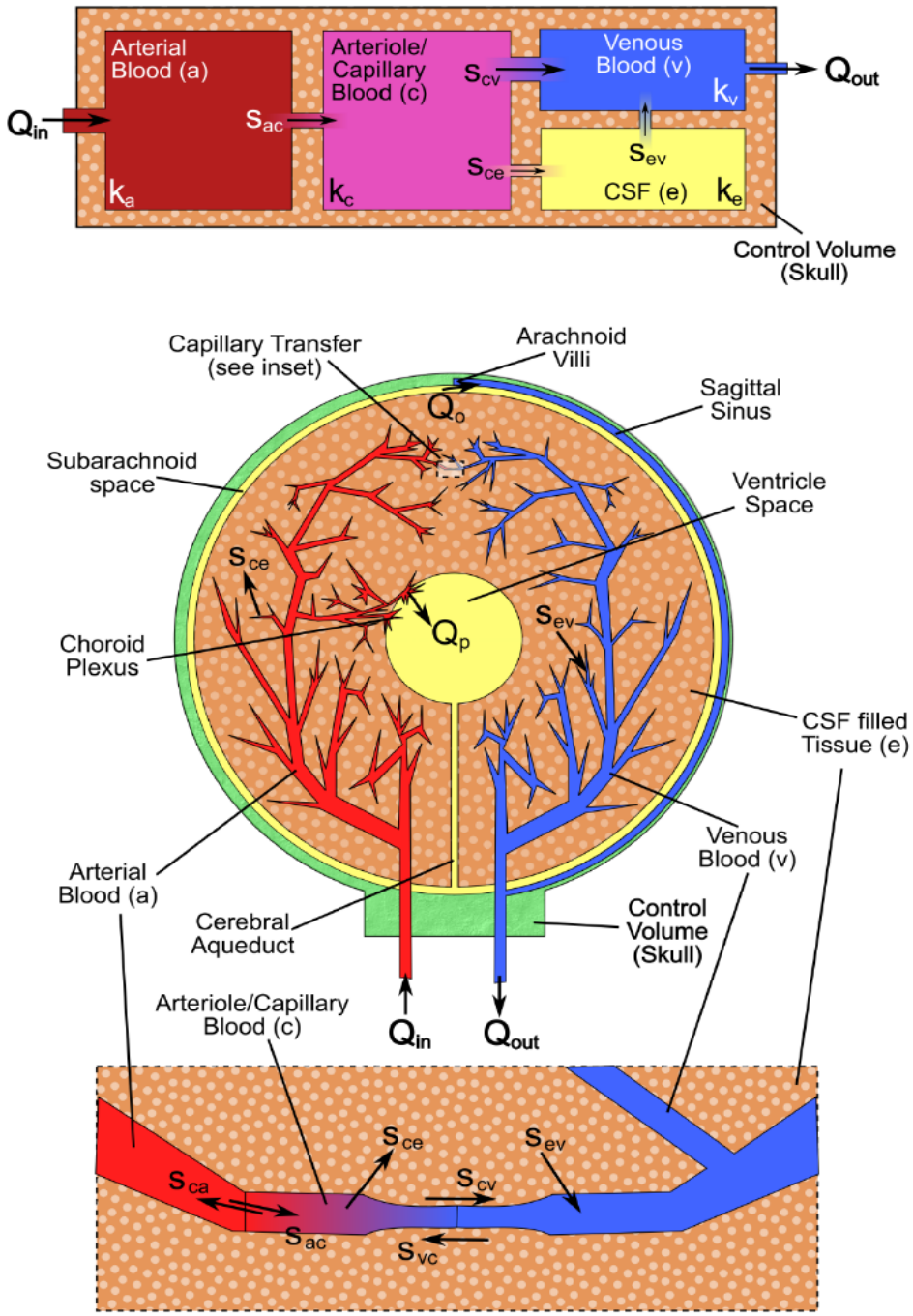


Figure 3.2 A 4MPET sketch of the cerebral environment with the directional transfer between different compartments [233].

3.2.2 Continuity and Directional Water Transfer

The transfer of fluid among four fluid networks is required to obey the law of continuity for the entire system, but also mimic human cerebral physiology as closely as possible. Hence, directionality amongst the fluid compartments must be accurately specified. A

summary of the directional fluid restrictions is shown in schematic Figure 3.1 for a reduced model, and by extending this to four fluid compartments, the constraints are illustrating in the following:

$$\begin{aligned} Q_{in} + Q_{acc} &= Q_{out} \\ Q_{acc} &= Q_a + Q_c + Q_v + Q_e \\ Q_a &= -Q_{in} + \overline{s}_{a\to c} \\ Q_c &= \overline{s}_{c\to a} + \overline{s}_{c\to e} + \overline{s}_{c\to v} \\ Q_v &= \overline{s}_{v\to c} + \overline{s}_{v\to e} + Q_{out} \\ Q_e &= \overline{s}_{e\to c} + \overline{s}_{e\to v} \end{aligned} \tag{3.35a-f}$$

where Q_{in} and Q_{out} are the flux of fluid in and out of the control volume, Q_{acc} is the net fluid accumulated in the control volume, and finally, Q_a, Q_c, Q_v, Q_e represent the fluid accumulation in each individual fluid network, namely: arterial/arteriole blood (a), capillary blood (c), venous blood (v) and the CSF/ISF (e) network. $\bar{s}_{\Lambda\to\Omega}$ represents the interporosity fluxes from network Λ to Ω which have been described in Eqn. (3.32), and it can be both positive and negative. Meanwhile, Q_{acc} is equal to zero when averaged over time in the healthy brain, but fluid accumulates in the CSF and ISF space or in the individual blood networks in the symptomatic brain. Based on the physiological observations of the system, there are some assumptions in detail:

i. Directional Fluid transport always occurs from the arterial network to the arteriole/capillary network ($\bar{s}_{a\to c} = -\bar{s}_{c\to a} \geq 0$).
ii. Fluid transport from the arteriole/capillary network will go to either the CSF/ISF network ($\bar{s}_{c\to e} = -\bar{s}_{e\to c} \geq 0$) or the venous network ($\bar{s}_{c\to v} = -\bar{s}_{v\to c} \geq 0$).
iii. CSF egress flows from CSF compartment into the venous compartment ($\bar{s}_{e\to v} = -\bar{s}_{v\to e} \geq 0$) which allows CSF movement along the dura of the superior sagittal sinus (arachnoid villi outflow system).

According to the physiology, there is no direct transfer of fluid from the arterial network to either the CSF/ISF network or venous networks ($\bar{s}_{a\to e} = \bar{s}_{a\to v} = 0$).

3.2.3 Methodology in One-Dimension

Here, the 1D system equations in the *r*-direction of the spherical coordinate reduce from Eqns. (3.34a-e) to:

$$\rho\frac{\partial^2 u_r}{\partial t^2} = \frac{2G(1-\nu)}{1-2\nu}\left(\frac{\partial^2 u_r}{\partial r^2}+\frac{2}{r}\frac{\partial u_r}{\partial r}-\frac{2}{r^2}u_r\right)-\alpha^a\frac{\partial p^a}{\partial r}-\alpha^c\frac{\partial p^c}{\partial r}-\alpha^v\frac{\partial p^v}{\partial r}-\alpha^e\frac{\partial p^e}{\partial r}$$

$$S_\varepsilon^a\frac{\partial p^a}{\partial t}+\alpha^a\frac{\partial}{\partial t}\left(\frac{\partial u_r}{\partial r}+\frac{2}{r}u_r\right)-\kappa^a\rho^a\frac{\partial^2}{\partial t^2}\left(\frac{\partial u_r}{\partial r}+\frac{2}{r}u_r\right)=\kappa^a\frac{\partial^2 p^a}{\partial r^2}+\bar{s}_{a\to c}$$

$$S_\varepsilon^c\frac{\partial p^c}{\partial t}+\alpha^c\frac{\partial}{\partial t}\left(\frac{\partial u_r}{\partial r}+\frac{2}{r}u_r\right)-\kappa^c\rho^c\frac{\partial^2}{\partial t^2}\left(\frac{\partial u_r}{\partial r}+\frac{2}{r}u_r\right)=\kappa^c\frac{\partial^2 p^c}{\partial r^2}+\bar{s}_{c\to a}+\bar{s}_{c\to v}+\bar{s}_{c\to e} \qquad (3.36a\text{-}e)$$

$$S_\varepsilon^v\frac{\partial p^v}{\partial t}+\alpha^v\frac{\partial}{\partial t}\left(\frac{\partial u_r}{\partial r}+\frac{2}{r}u_r\right)-\kappa^v\rho^v\frac{\partial^2}{\partial t^2}\left(\frac{\partial u_r}{\partial r}+\frac{2}{r}u_r\right)=\kappa^v\frac{\partial^2 p^v}{\partial r^2}+\bar{s}_{v\to c}+\bar{s}_{v\to e}$$

$$S_\varepsilon^e\frac{\partial p^e}{\partial t}+\alpha^e\frac{\partial}{\partial t}\left(\frac{\partial u_r}{\partial r}+\frac{2}{r}u_r\right)-\kappa^e\rho^e\frac{\partial^2}{\partial t^2}\left(\frac{\partial u_r}{\partial r}+\frac{2}{r}u_r\right)=\kappa^e\frac{\partial^2 p^e}{\partial r^2}+\bar{s}_{e\to c}+\bar{s}_{e\to v}$$

where u_r is the displacement in the *r*-direction of the spherical coordinate.

3.2.4 Boundary Conditions at the Ventricular Wall

Due to the spherically symmetric shell geometry and assuming the stress must be continuous across the ventricular wall ($r = r_1$),

$$(1-\nu)\frac{\partial u_1^t}{\partial r}+2\nu\frac{u_1^t}{r_1}=\frac{1-2\nu}{2G}\sum_{\Omega=a,c,v,e}\left(\alpha^\Omega-1\right)p_1^{\Omega,t} \qquad (3.37)^1$$

The production of CSF from the blood leads to a pressure drop in the capillary blood network,

[1] The derivation of Eqn (3.37) is available in Appendix (A3).

$$\frac{\partial p_1^{c,t}}{\partial r} = \frac{Q_{prod}}{R_{c\to vent}^{CP}} \tag{3.38}$$

where $R_{c\to vent}^{CP}$ is the resistance of the flow from the capillary network to the ventricles via the choroid plexuses (CP) and Q_{prod} is the production rate of the fluid, assumed constant. There is no flow moving in/out the arterial and venous blood networks because of wall-thickness arguments,

$$\frac{\partial p_1^{a,t}}{\partial r} = 0 \quad ; \quad \frac{\partial p_1^{v,t}}{\partial r} = 0 \tag{3.39a-b}$$

The mass of fluid is conserved in the ventricles,

$$\overbrace{\frac{\pi d^4}{128\mu^e L}\left(p_1^e - p_N^e\right)}^{\text{Poiseuille flow}} \overbrace{-4\pi\left(r_1+u_1\right)^2\kappa^e\frac{\partial p_1^e}{\partial r}}^{\text{Seepage flow}} + \overbrace{4\pi\left(r_1+u_1\right)^2\frac{\partial u_1}{\partial t}}^{\text{Solid Matrix Dilation}} = Q_{prod} \tag{3.40}$$

where d and L is the diameter and length of the cerebral aqueduct, respectively; μ^e is the viscosity of the CSF, κ^e is the mobility in the CSF compartment. In the LHS of Eqn. (3.40), the first term of the left-hand-side of the Eqn. (3.40) implies the Poiseuille flow is driven by the CSF pressure difference between the ventricles (p_1^e) and the SAS (p_N^e), since the cylindrical tube is assumed to describe the cerebral aqueduct. The second term represents the flow of fluid penetrating the inner spherical surface of the ventricle walls into the parenchyma via seepage motion (corresponding to Darcy's law). Regarding the second term, the negative sign is necessary because the fluid flows from high pressure to low pressure. The third term describes the inner spherical surface of the ventricular displacement change rate with respect to time.

3.2.5 Boundary Conditions at the Skull

Since we are investigating the adult brain, the displacement at the skull ($r = r_N$) is zero,

$$u_N^t = 0 \tag{3.41}$$

The blood pressures are given by physically relevant arterial and venous blood pressures,

$$\begin{aligned} p_N^{a,t} &= p_{ABL} \\ p_N^{v,t} &= p_{VBL} \end{aligned} \tag{3.42a-b}$$

There is no flow into or out of the arteriole/capillary blood network at the skull,

$$\frac{\partial p_N^{c,t}}{\partial r} = 0 \tag{3.43}$$

The CSF pressure at the skull equals to sum of pressure in venous network and CSF absorption,

$$p_N^{e,t} = p_{VBL} + \mu^e R_{abs}^{AG} Q_o \tag{3.44}$$

where R_{abs}^{AG} is the resistance to outflow via the AG and Q_o is the rate of CSF egress at the skull.

3.2.6 Initial Conditions

The initial displacement (u_r^0) and velocity (V_r^0) are given as,

$$u_r^0 = 0 \quad ; \quad \frac{\partial u_r^0}{\partial t} = V_r^0 = 0 \tag{3.45 a-b}$$

Additionally, setting the steady-state results of the pressure compartments as the initial conditions for the transient model,

$$\begin{aligned} p_r^{a,0} &= \bar{p}^a \\ p_r^{c,0} &= \bar{p}^c \\ p_r^{v,0} &= \bar{p}^v \\ p_r^{e,0} &= \bar{p}^e \end{aligned} \tag{3.46a-d}$$

where $\bar{p}^a$, $\bar{p}^c$, $\bar{p}^v$, and $\bar{p}^e$ are the steady-state results in arterial blood compartment, arteriole/capillary blood compartment, venous blood compartment and the CSF/ISF compartment, respectively.

3.2.7 Numerical Implementation

The 4MPET model is described as a boundary value problem, and finite differences are used to discretise the system equations. The central difference scheme is employed for spatial discretization for the equations of motion, and the Crank-Nicolson method is applied to deal with temporal discretization. Moreover, the second order forward or backward difference schemes are implemented as appropriate for estimating spatial derivatives in the boundary conditions. Finally, we write a FORTRAN 90 in-house code for the MPET model by using the following discretised system equations and solve this linear system via the LU decomposition method [370].

3.2.7.1 Displacement Equation

Eqn. (3.36a) becomes,

$$\frac{u_i^{t+1}-2u_i^t+u_i^{t-1}}{\Delta t^2}=\frac{2G(1-\nu)}{\rho(1-2\nu)}\left(\frac{1}{2}\right)\left[\frac{u_{i+1}^{t+1}-2u_i^{t+1}+u_{i-1}^{t+1}}{\Delta r^2}+\frac{2}{r_i}\left(\frac{u_{i+1}^{t+1}-u_{i-1}^{t+1}}{2\Delta r}\right)-\frac{2}{r_i^2}u_i^{t+1}\right]$$

$$+\frac{2G(1-\nu)}{\rho(1-2\nu)}\left(\frac{1}{2}\right)\left[\frac{u_{i+1}^{t}-2u_{i}^{t}+u_{i-1}^{t}}{\Delta r^{2}}+\frac{2}{r_i}\left(\frac{u_{i+1}^{t}-u_{i-1}^{t}}{2\Delta r}\right)-\frac{2}{r_i^{2}}u_{i}^{t}\right]$$

$$-\left(\frac{1}{2}\right)\frac{1}{\rho}\sum_{\Omega=a,c,v,e}\alpha^{\Omega}\left(\frac{p_{i+1}^{\Omega,t+1}-p_{i-1}^{\Omega,t+1}}{2\Delta r}\right)-\left(\frac{1}{2}\right)\frac{1}{\rho}\sum_{\Omega=a,c,v,e}\alpha^{\Omega}\left(\frac{p_{i+1}^{\Omega,t}-p_{i-1}^{\Omega,t}}{2\Delta r}\right)$$

Rearranging for the nodal values,

$$-\left(\frac{1}{2}\right)\Delta t^{2}\frac{2G(1-\nu)}{\rho(1-2\nu)}\left(\frac{1}{\Delta r^{2}}-\frac{1}{r_i\Delta r}\right)u_{i-1}^{t+1}+\left[1+\left(\frac{1}{2}\right)\Delta t^{2}\frac{2G(1-\nu)}{\rho(1-2\nu)}\left(\frac{2}{r_i^{2}}+\frac{2}{\Delta r^{2}}\right)\right]u_{i}^{t+1}$$

$$-\left(\frac{1}{2}\right)\Delta t^{2}\frac{2G(1-\nu)}{\rho(1-2\nu)}\left(\frac{1}{\Delta r^{2}}+\frac{1}{r_i\Delta r}\right)u_{i+1}^{t+1}$$

$$-\left(\frac{1}{2}\right)\frac{\Delta t^{2}}{\rho 2\Delta r}\sum_{\Omega=a,c,v,e}\alpha^{\Omega}p_{i-1}^{\Omega,t+1}+\left(\frac{1}{2}\right)\frac{\Delta t^{2}}{\rho 2\Delta r}\sum_{\Omega=a,c,v,e}\alpha^{\Omega}p_{i+1}^{\Omega,t+1}=$$

$$\left(\frac{1}{2}\right)\Delta t^{2}\frac{2G(1-\nu)}{\rho(1-2\nu)}\left(\frac{1}{\Delta r^{2}}-\frac{1}{r_i\Delta r}\right)u_{i-1}^{t}+\left[2-\left(\frac{1}{2}\right)\Delta t^{2}\frac{2G(1-\nu)}{\rho(1-2\nu)}\left(\frac{2}{\Delta r^{2}}+\frac{2}{r_i^{2}}\right)\right]u_{i}^{t}$$

$$+\left(\frac{1}{2}\right)\Delta t^{2}\frac{2G(1-\nu)}{\rho(1-2\nu)}\left(\frac{1}{\Delta r^{2}}+\frac{1}{r_i\Delta r}\right)u_{i+1}^{t}-u_{i}^{t-1}$$

$$+\left(\frac{1}{2}\right)\frac{\Delta t^{2}}{\rho 2\Delta r}\sum_{\Omega=a,c,v,e}\alpha^{\Omega}p_{i-1}^{\Omega,t}-\left(\frac{1}{2}\right)\frac{\Delta t^{2}}{\rho 2\Delta r}\sum_{\Omega=a,c,v,e}\alpha^{\Omega}p_{i+1}^{\Omega,t} \qquad (3.47a)$$

When $t = 0$, we have $u_i^{-1} = u_i^1 - 2\Delta t V_r^0$ and Eqn. (3.45b), and then substitute into Eqn. (3.47a),

$$-\left(\frac{1}{2}\right)\Delta t^{2}\frac{2G(1-\nu)}{\rho(1-2\nu)}\left(\frac{1}{\Delta r^{2}}-\frac{1}{r_i\Delta r}\right)u_{i-1}^{1}+\left[2+\left(\frac{1}{2}\right)\Delta t^{2}\frac{2G(1-\nu)}{\rho(1-2\nu)}\left(\frac{2}{r_i^{2}}+\frac{2}{\Delta r^{2}}\right)\right]u_{i}^{1}$$

$$-\left(\frac{1}{2}\right)\Delta t^{2}\frac{2G(1-\nu)}{\rho(1-2\nu)}\left(\frac{1}{\Delta r^{2}}+\frac{1}{r_i\Delta r}\right)u_{i+1}^{1}-\left(\frac{1}{2}\right)\frac{\Delta t^{2}}{\rho 2\Delta r}\sum_{\Omega=a,c,v,e}\alpha^{\Omega}p_{i-1}^{\Omega,1}$$

$$+\left(\frac{1}{2}\right)\frac{\Delta t^{2}}{\rho 2\Delta r}\sum_{\Omega=a,c,v,e}\alpha^{\Omega}p_{i+1}^{\Omega,1}=\left(\frac{1}{2}\right)\Delta t^{2}\frac{2G(1-\nu)}{\rho(1-2\nu)}\left(\frac{1}{\Delta r^{2}}-\frac{1}{r_i\Delta r}\right)u_{i-1}^{0}$$

$$+\left[2-\left(\frac{1}{2}\right)\Delta t^2\frac{2G(1-\nu)}{\rho(1-2\nu)}\left(\frac{2}{\Delta r^2}+\frac{2}{r_i^2}\right)\right]u_i^0+\left(\frac{1}{2}\right)\Delta t^2\frac{2G(1-\nu)}{\rho(1-2\nu)}\left(\frac{1}{\Delta r^2}+\frac{1}{r_i\Delta r}\right)u_{i+1}^0$$

$$+2\Delta tV_r^0+\left(\frac{1}{2}\right)\frac{\Delta t^2}{\rho 2\Delta r}\sum_{\Omega=a,c,v,e}\alpha^{\Omega}p_{i-1}^{\Omega,0}-\left(\frac{1}{2}\right)\frac{\Delta t^2}{\rho 2\Delta r}\sum_{\Omega=a,c,v,e}\alpha^{\Omega}p_{i+1}^{\Omega,0} \tag{3.47b}$$

3.2.7.2 Arterial Pressure

Eqn. (3.36b) becomes,

$$\Delta tS_{\varepsilon}^{a}\left(p_i^{a,t+1}-p_i^{a,t}\right)$$

$$+\frac{\Delta t}{2}\alpha^{a}\left[\left(\frac{-1}{2\Delta r}u_{i-1}^{t+1}+\frac{2}{r_i}u_i^{t+1}+\frac{1}{2\Delta r}u_{i+1}^{t+1}\right)-\left(\frac{-1}{2\Delta r}u_{i-1}^{t-1}+\frac{2}{r_i}u_i^{t-1}+\frac{1}{2\Delta r}u_{i+1}^{t-1}\right)\right]$$

$$-\rho_f^a\kappa^a\left[\left(\frac{-1}{2\Delta r}u_{i-1}^{t+1}+\frac{2}{r_i}u_i^{t+1}+\frac{1}{2\Delta r}u_{i+1}^{t+1}\right)-2\left(\frac{-1}{2\Delta r}u_{i-1}^{t}+\frac{2}{r_i}u_i^{t}+\frac{1}{2\Delta r}u_{i+1}^{t}\right)\right.$$

$$\left.+\left(\frac{-1}{2\Delta r}u_{i-1}^{t-1}+\frac{2}{r_i}u_i^{t-1}+\frac{1}{2\Delta r}u_{i+1}^{t-1}\right)\right]=$$

$$\left(\frac{1}{2}\right)\Delta t^2\kappa^a\left[\left(\frac{1}{\Delta r^2}-\frac{1}{r_i\Delta r}\right)p_{i-1}^{a,t+1}-\left(\frac{2}{\Delta r^2}\right)p_i^{a,t+1}+\left(\frac{1}{\Delta r^2}+\frac{1}{r_i\Delta r}\right)p_{i+1}^{a,t+1}\right]$$

$$+\left(\frac{1}{2}\right)\Delta t^2\kappa^a\left[\left(\frac{1}{\Delta r^2}-\frac{1}{r_i\Delta r}\right)p_{i-1}^{a,t}-\left(\frac{2}{\Delta r^2}\right)p_i^{a,t}+\left(\frac{1}{\Delta r^2}+\frac{1}{r_i\Delta r}\right)p_{i+1}^{a,t}\right]+\Delta t^2\overline{s}_{a\to c} \tag{3.48}$$

Rearranging for the nodal values,

$$\left[\rho_f^a\kappa^a-\alpha^a\left(\frac{\Delta t}{2}\right)\right]\left(\frac{1}{2\Delta r}\right)u_{i-1}^{t+1}-\left[\rho_f^a\kappa^a-\alpha^a\left(\frac{\Delta t}{2}\right)\right]\left(\frac{2}{r_i}\right)u_i^{t+1}$$

$$-\left[\rho_f^a\kappa^a-\alpha^a\left(\frac{\Delta t}{2}\right)\right]\left(\frac{1}{2\Delta r}\right)u_{i+1}^{t+1}$$

$$-\left(\frac{1}{2}\right)\Delta t^2\kappa^a\left(\frac{1}{\Delta r^2}-\frac{1}{r_i\Delta r}\right)p_{i-1}^{a,t+1}+\left[\Delta tS_\varepsilon^a+\left(\frac{1}{2}\right)\Delta t^2\kappa^a\left(\frac{2}{\Delta r^2}\right)\right]p_i^{a,t+1}$$

$$-\left(\frac{1}{2}\right)\Delta t^2\kappa^a\left(\frac{1}{\Delta r^2}+\frac{1}{r_i\Delta r}\right)p_{i+1}^{a,t+1}=\rho_f^a\kappa^a\left(\frac{1}{\Delta r}\right)u_{i-1}^t-\rho_f^a\kappa^a\left(\frac{4}{r_i}\right)u_i^t-\rho_f^a\kappa^a\left(\frac{1}{\Delta r}\right)u_{i+1}^t$$

$$+\left(\frac{1}{2}\right)\Delta t^2\kappa^a\left(\frac{1}{\Delta r^2}-\frac{1}{r_i\Delta r}\right)p_{i-1}^{a,t}+\left[\Delta tS_\varepsilon^a-\left(\frac{1}{2}\right)\Delta t^2\kappa^a\left(\frac{2}{\Delta r^2}\right)\right]p_i^{a,t}$$

$$+\left(\frac{1}{2}\right)\Delta t^2\kappa^a\left(\frac{1}{\Delta r^2}+\frac{1}{r_i\Delta r}\right)p_{i+1}^{a,t}-\left[\rho_f^a\kappa^a+\alpha^a\left(\frac{\Delta t}{2}\right)\right]\left(\frac{1}{2\Delta r}\right)u_{i-1}^{t-1}$$

$$+\left[\rho_f^a\kappa^a+\alpha^a\left(\frac{\Delta t}{2}\right)\right]\left(\frac{2}{r_i}\right)u_i^{t-1}+\left[\rho_f^a\kappa^a+\alpha^a\left(\frac{\Delta t}{2}\right)\right]\left(\frac{1}{2\Delta r}\right)u_{i+1}^{t-1}+\Delta t^2\overline{s}_{a\to c} \tag{3.49a}$$

When $t = 0$, we get $u_i^{-1}=u_i^1-2\Delta tV_r^0$, Eqn. (3.45b), and Eqn. (3.46a), and then substitute into and Eqn. (3.49a),

$$2\rho_f^a\kappa^a\left(\frac{1}{2\Delta r}\right)u_{i-1}^1-2\rho_f^a\kappa^a\left(\frac{2}{r_i}\right)u_i^1-2\rho_f^a\kappa^a\left(\frac{1}{2\Delta r}\right)u_{i+1}^1-\left(\frac{1}{2}\right)\Delta t^2\kappa^a\left(\frac{1}{\Delta r^2}-\frac{1}{r_i\Delta r}\right)p_{i-1}^{a,1}$$

$$+\left[\Delta tS_\varepsilon^a+\left(\frac{1}{2}\right)\Delta t^2\kappa^a\left(\frac{2}{\Delta r^2}\right)\right]p_i^{a,1}-\left(\frac{1}{2}\right)\Delta t^2\kappa^a\left(\frac{1}{\Delta r^2}+\frac{1}{r_i\Delta r}\right)p_{i+1}^{a,1}=$$

$$+\rho_f^a\kappa^a\left(\frac{1}{\Delta r}\right)u_{i-1}^0-\rho_f^a\kappa^a\left(\frac{4}{r_i}\right)u_i^0-\rho_f^a\kappa^a\left(\frac{1}{\Delta r}\right)u_{i+1}^0+\left(\frac{1}{2}\right)\Delta t^2\kappa^a\left(\frac{1}{\Delta r^2}-\frac{1}{r_i\Delta r}\right)p_{i-1}^{a,0}$$

$$+\left[\Delta tS_\varepsilon^a-\left(\frac{1}{2}\right)\Delta t^2\kappa^a\left(\frac{2}{\Delta r^2}\right)\right]p_i^{a,0}+\left(\frac{1}{2}\right)\Delta t^2\kappa^a\left(\frac{1}{\Delta r^2}+\frac{1}{r_i\Delta r}\right)p_{i+1}^{a,0}+\Delta t^2\overline{s}_{a\to c} \tag{3.49b}$$

3.2.7.3 Arteriole/Capillary Pressure

Taking Eqn. (3.36c) and using the same process from Eqn. (3.48) to Eqn. (3.49a), we have the nodal values

$$\left[\rho_f^c\kappa^c-\alpha^c\left(\frac{\Delta t}{2}\right)\right]\left(\frac{1}{2\Delta r}\right)u_{i-1}^{t+1}-\left[\rho_f^c\kappa^c-\alpha^c\left(\frac{\Delta t}{2}\right)\right]\left(\frac{2}{r_i}\right)u_i^{t+1}$$

$$-\left[\rho_f^c\kappa^c-\alpha^c\left(\frac{\Delta t}{2}\right)\right]\left(\frac{1}{2\Delta r}\right)u_{i+1}^{t+1}$$

$$-\left(\frac{1}{2}\right)\Delta t^2\kappa^c\left(\frac{1}{\Delta r^2}-\frac{1}{r_i\Delta r}\right)p_{i-1}^{c,t+1}+\left[\Delta tS_\varepsilon^c+\left(\frac{1}{2}\right)\Delta t^2\kappa^c\left(\frac{2}{\Delta r^2}\right)\right]p_i^{c,t+1}$$

$$-\left(\frac{1}{2}\right)\Delta t^2\kappa^c\left(\frac{1}{\Delta r^2}+\frac{1}{r_i\Delta r}\right)p_{i+1}^{c,t+1}=\rho_f^c\kappa^c\left(\frac{1}{\Delta r}\right)u_{i-1}^t-\rho_f^c\kappa^c\left(\frac{4}{r_i}\right)u_i^t-\rho_f^c\kappa^c\left(\frac{1}{\Delta r}\right)u_{i+1}^t$$

$$+\left(\frac{1}{2}\right)\Delta t^2\kappa^c\left(\frac{1}{\Delta r^2}-\frac{1}{r_i\Delta r}\right)p_{i-1}^{c,t}+\left[\Delta tS_\varepsilon^c-\left(\frac{1}{2}\right)\Delta t^2\kappa^c\left(\frac{2}{\Delta r^2}\right)\right]p_i^{c,t}$$

$$+\left(\frac{1}{2}\right)\Delta t^2\kappa^c\left(\frac{1}{\Delta r^2}+\frac{1}{r_i\Delta r}\right)p_{i+1}^{c,t}-\left[\rho_f^c\kappa^c+\alpha^c\left(\frac{\Delta t}{2}\right)\right]\left(\frac{1}{2\Delta r}\right)u_{i-1}^{t-1}$$

$$+\left[\rho_f^c\kappa^c+\alpha^c\left(\frac{\Delta t}{2}\right)\right]\left(\frac{2}{r_i}\right)u_i^{t-1}+\left[\rho_f^c\kappa^c+\alpha^c\left(\frac{\Delta t}{2}\right)\right]\left(\frac{1}{2\Delta r}\right)u_{i+1}^{t-1}$$

$$+\Delta t^2\overline{s}_{c\to a}+\Delta t^2\overline{s}_{c\to v}+\Delta t^2\overline{s}_{c\to e} \tag{3.50a}$$

For the first time step, we use $u_i^{-1}=u_i^1-2\Delta tV_r^0$, Eqn. (3.45b), and Eqn. (3.46b) to substitute into and Eqn. (3.50a),

$$2\rho_f^c\kappa^c\left(\frac{1}{2\Delta r}\right)u_{i-1}^1-2\rho_f^c\kappa^c\left(\frac{2}{r_i}\right)u_i^1-2\rho_f^c\kappa^c\left(\frac{1}{2\Delta r}\right)u_{i+1}^1-\left(\frac{1}{2}\right)\Delta t^2\kappa^c\left(\frac{1}{\Delta r^2}-\frac{1}{r_i\Delta r}\right)p_{i-1}^{c,1}$$

$$+\left[\Delta tS_\varepsilon^c+\left(\frac{1}{2}\right)\Delta t^2\kappa^c\left(\frac{2}{\Delta r^2}\right)\right]p_i^{c,1}-\left(\frac{1}{2}\right)\Delta t^2\kappa^c\left(\frac{1}{\Delta r^2}+\frac{1}{r_i\Delta r}\right)p_{i+1}^{c,1}=$$

$$+\rho_f^c\kappa^c\left(\frac{1}{\Delta r}\right)u_{i-1}^0-\rho_f^c\kappa^c\left(\frac{4}{r_i}\right)u_i^0-\rho_f^c\kappa^c\left(\frac{1}{\Delta r}\right)u_{i+1}^0+\left(\frac{1}{2}\right)\Delta t^2\kappa^c\left(\frac{1}{\Delta r^2}-\frac{1}{r_i\Delta r}\right)p_{i-1}^{c,0}$$

$$+\left[\Delta tS_\varepsilon^c-\left(\frac{1}{2}\right)\Delta t^2\kappa^c\left(\frac{2}{\Delta r^2}\right)\right]p_i^{c,0}+\left(\frac{1}{2}\right)\Delta t^2\kappa^c\left(\frac{1}{\Delta r^2}+\frac{1}{r_i\Delta r}\right)p_{i+1}^{c,0}$$

$$+\Delta t^2\overline{s}_{c\to a}+\Delta t^2\overline{s}_{c\to v}+\Delta t^2\overline{s}_{c\to e} \tag{3.50b}$$

3.2.7.4 Venous Pressure

Taking Eqn. (3.36d) and using the same process from Eqn. (3.48) to Eqn. (3.49a), we have the nodal values

$$\left[\rho_f^v\kappa^v-\alpha^v\left(\frac{\Delta t}{2}\right)\right]\left(\frac{1}{2\Delta r}\right)u_{i-1}^{t+1}-\left[\rho_f^v\kappa^v-\alpha^v\left(\frac{\Delta t}{2}\right)\right]\left(\frac{2}{r_i}\right)u_i^{t+1}$$

$$-\left[\rho_f^v\kappa^v-\alpha^v\left(\frac{\Delta t}{2}\right)\right]\left(\frac{1}{2\Delta r}\right)u_{i+1}^{t+1}$$

$$-\left(\frac{1}{2}\right)\Delta t^2\kappa^v\left(\frac{1}{\Delta r^2}-\frac{1}{r_i\Delta r}\right)p_{i-1}^{v,t+1}+\left[\Delta tS_\varepsilon^v+\left(\frac{1}{2}\right)\Delta t^2\kappa^v\left(\frac{2}{\Delta r^2}\right)\right]p_i^{v,t+1}$$

$$-\left(\frac{1}{2}\right)\Delta t^2\kappa^v\left(\frac{1}{\Delta r^2}+\frac{1}{r_i\Delta r}\right)p_{i+1}^{v,t+1}=\rho_f^v\kappa^v\left(\frac{1}{\Delta r}\right)u_{i-1}^t-\rho_f^v\kappa^v\left(\frac{4}{r_i}\right)u_i^t-\rho_f^v\kappa^v\left(\frac{1}{\Delta r}\right)u_{i+1}^t$$

$$+\left(\frac{1}{2}\right)\Delta t^2\kappa^v\left(\frac{1}{\Delta r^2}-\frac{1}{r_i\Delta r}\right)p_{i-1}^{v,t}+\left[\Delta tS_\varepsilon^v-\left(\frac{1}{2}\right)\Delta t^2\kappa^v\left(\frac{2}{\Delta r^2}\right)\right]p_i^{v,t}$$

$$+\left(\frac{1}{2}\right)\Delta t^2\kappa^v\left(\frac{1}{\Delta r^2}+\frac{1}{r_i\Delta r}\right)p_{i+1}^{v,t}-\left[\rho_f^v\kappa^v+\alpha^v\left(\frac{\Delta t}{2}\right)\right]\left(\frac{1}{2\Delta r}\right)u_{i-1}^{t-1}$$

$$+\left[\rho_f^v\kappa^v+\alpha^v\left(\frac{\Delta t}{2}\right)\right]\left(\frac{2}{r_i}\right)u_i^{t-1}+\left[\rho_f^v\kappa^v+\alpha^v\left(\frac{\Delta t}{2}\right)\right]\left(\frac{1}{2\Delta r}\right)u_{i+1}^{t-1}$$

$$+\Delta t^2\overline{s}_{v\to c}+\Delta t^2\overline{s}_{v\to e} \tag{3.51a}$$

For the first time step, we use $u_i^{-1}=u_i^1-2\Delta tV_r^0$, Eqn. (3.45b), and Eqn. (3.46c) to substitute into and Eqn. (3.51a),

$$2\rho_f^v\kappa^v\left(\frac{1}{2\Delta r}\right)u_{i-1}^1-2\rho_f^v\kappa^v\left(\frac{2}{r_i}\right)u_i^1-2\rho_f^v\kappa^v\left(\frac{1}{2\Delta r}\right)u_{i+1}^1-\left(\frac{1}{2}\right)\Delta t^2\kappa^v\left(\frac{1}{\Delta r^2}-\frac{1}{r_i\Delta r}\right)p_{i-1}^{v,1}$$

$$+\left[\Delta t S_{\varepsilon}^{v}+\left(\frac{1}{2}\right)\Delta t^{2}\kappa^{v}\left(\frac{2}{\Delta r^{2}}\right)\right]p_{i}^{v,1}-\left(\frac{1}{2}\right)\Delta t^{2}\kappa^{v}\left(\frac{1}{\Delta r^{2}}+\frac{1}{r_{i}\Delta r}\right)p_{i+1}^{v,1}=$$

$$+\rho_{f}^{v}\kappa^{v}\left(\frac{1}{\Delta r}\right)u_{i-1}^{0}-\rho_{f}^{v}\kappa^{v}\left(\frac{4}{r_{i}}\right)u_{i}^{0}-\rho_{f}^{v}\kappa^{v}\left(\frac{1}{\Delta r}\right)u_{i+1}^{0}+\left(\frac{1}{2}\right)\Delta t^{2}\kappa^{v}\left(\frac{1}{\Delta r^{2}}-\frac{1}{r_{i}\Delta r}\right)p_{i-1}^{v,0}$$

$$+\left[\Delta t S_{\varepsilon}^{v}-\left(\frac{1}{2}\right)\Delta t^{2}\kappa^{v}\left(\frac{2}{\Delta r^{2}}\right)\right]p_{i}^{v,0}+\left(\frac{1}{2}\right)\Delta t^{2}\kappa^{v}\left(\frac{1}{\Delta r^{2}}+\frac{1}{r_{i}\Delta r}\right)p_{i+1}^{v,0}$$

$$+\Delta t^{2}\overline{s}_{v\to c}+\Delta t^{2}\overline{s}_{v\to e} \tag{3.51b}$$

3.2.7.5 CSF/ISF Pressure

Taking Eqn. (3.36e) and using the same process from Eqn. (3.48) to Eqn. (3.49a), we have the nodal values

$$\left[\rho_{f}^{e}\kappa^{e}-\alpha^{e}\left(\frac{\Delta t}{2}\right)\right]\left(\frac{1}{2\Delta r}\right)u_{i-1}^{t+1}-\left[\rho_{f}^{e}\kappa^{e}-\alpha^{e}\left(\frac{\Delta t}{2}\right)\right]\left(\frac{2}{r_{i}}\right)u_{i}^{t+1}$$

$$-\left[\rho_{f}^{e}\kappa^{e}-\alpha^{e}\left(\frac{\Delta t}{2}\right)\right]\left(\frac{1}{2\Delta r}\right)u_{i+1}^{t+1}$$

$$-\left(\frac{1}{2}\right)\Delta t^{2}\kappa^{e}\left(\frac{1}{\Delta r^{2}}-\frac{1}{r_{i}\Delta r}\right)p_{i-1}^{e,t+1}+\left[\Delta t S_{\varepsilon}^{e}+\left(\frac{1}{2}\right)\Delta t^{2}\kappa^{e}\left(\frac{2}{\Delta r^{2}}\right)\right]p_{i}^{e,t+1}$$

$$-\left(\frac{1}{2}\right)\Delta t^{2}\kappa^{e}\left(\frac{1}{\Delta r^{2}}+\frac{1}{r_{i}\Delta r}\right)p_{i+1}^{e,t+1}=\rho_{f}^{e}\kappa^{e}\left(\frac{1}{\Delta r}\right)u_{i-1}^{t}-\rho_{f}^{e}\kappa^{e}\left(\frac{4}{r_{i}}\right)u_{i}^{t}-\rho_{f}^{e}\kappa^{e}\left(\frac{1}{\Delta r}\right)u_{i+1}^{t}$$

$$+\left(\frac{1}{2}\right)\Delta t^{2}\kappa^{e}\left(\frac{1}{\Delta r^{2}}-\frac{1}{r_{i}\Delta r}\right)p_{i-1}^{e,t}+\left[\Delta t S_{\varepsilon}^{e}-\left(\frac{1}{2}\right)\Delta t^{2}\kappa^{e}\left(\frac{2}{\Delta r^{2}}\right)\right]p_{i}^{e,t}$$

$$+\left(\frac{1}{2}\right)\Delta t^{2}\kappa^{e}\left(\frac{1}{\Delta r^{2}}+\frac{1}{r_{i}\Delta r}\right)p_{i+1}^{e,t}-\left[\rho_{f}^{e}\kappa^{e}+\alpha^{e}\left(\frac{\Delta t}{2}\right)\right]\left(\frac{1}{2\Delta r}\right)u_{i-1}^{t-1}$$

$$+\left[\rho_{f}^{e}\kappa^{e}+\alpha^{e}\left(\frac{\Delta t}{2}\right)\right]\left(\frac{2}{r_{i}}\right)u_{i}^{t-1}+\left[\rho_{f}^{e}\kappa^{e}+\alpha^{e}\left(\frac{\Delta t}{2}\right)\right]\left(\frac{1}{2\Delta r}\right)u_{i+1}^{t-1}$$

$$+\Delta t^{2}\overline{s}_{e\to c}+\Delta t^{2}\overline{s}_{e\to v} \tag{3.52a}$$

For the first time step, we use $u_i^{-1} = u_i^1 - 2\Delta t V_r^0$, Eqn. (3.45b), and Eqn. (3.46d) to substitute into and Eqn. (3.52a),

$$2\rho_f^e\kappa^e\left(\frac{1}{2\Delta r}\right)u_{i-1}^1 - 2\rho_f^e\kappa^e\left(\frac{2}{r_i}\right)u_i^1 - 2\rho_f^e\kappa^e\left(\frac{1}{2\Delta r}\right)u_{i+1}^1 - \left(\frac{1}{2}\right)\Delta t^2\kappa^e\left(\frac{1}{\Delta r^2} - \frac{1}{r_i\Delta r}\right)p_{i-1}^{e,1}$$

$$+\left[\Delta t S_\varepsilon^e + \left(\frac{1}{2}\right)\Delta t^2\kappa^e\left(\frac{2}{\Delta r^2}\right)\right]p_i^{e,1} - \left(\frac{1}{2}\right)\Delta t^2\kappa^e\left(\frac{1}{\Delta r^2} + \frac{1}{r_i\Delta r}\right)p_{i+1}^{e,1} =$$

$$+\rho_f^e\kappa^e\left(\frac{1}{\Delta r}\right)u_{i-1}^0 - \rho_f^e\kappa^e\left(\frac{4}{r_i}\right)u_i^0 - \rho_f^e\kappa^e\left(\frac{1}{\Delta r}\right)u_{i+1}^0 + \left(\frac{1}{2}\right)\Delta t^2\kappa^e\left(\frac{1}{\Delta r^2} - \frac{1}{r_i\Delta r}\right)p_{i-1}^{e,0}$$

$$+\left[\Delta t S_\varepsilon^e - \left(\frac{1}{2}\right)\Delta t^2\kappa^e\left(\frac{2}{\Delta r^2}\right)\right]p_i^{e,0} + \left(\frac{1}{2}\right)\Delta t^2\kappa^e\left(\frac{1}{\Delta r^2} + \frac{1}{r_i\Delta r}\right)p_{i+1}^{e,0}$$

$$+\Delta t^2\overline{s}_{e\to c} + \Delta t^2\overline{s}_{e\to v} \tag{3.52b}$$

3.2.7.6 Discretised Boundary Conditions at the Ventricular Wall

Eqn. (3.37) becomes,

$$(1-\nu)\frac{-3u_1^{t+1} + 4u_2^{t+1} - u_3^{t+1}}{2\Delta r} + 2\nu\frac{u_1^{t+1}}{r_1}$$

$$-\frac{1-2\nu}{2G}\left[\left(\alpha^a - 1\right)p_1^{a,t+1} + \left(\alpha^c - 1\right)p_1^{c,t+1} + \left(\alpha^v - 1\right)p_1^{v,t+1} + \left(\alpha^e - 1\right)p_1^{e,t+1}\right] = 0,$$

Simplified as,

$$\left[\frac{2\nu}{r_1}-\frac{3(1-\nu)}{2\Delta r}\right]u_1^{t+1}+\frac{2(1-\nu)}{\Delta r}u_2^{t+1}-\frac{(1-\nu)}{2\Delta r}u_3^{t+1}-\frac{(\alpha^a-1)(1-2\nu)}{2G}p_1^{a,t+1}$$

$$-\frac{(\alpha^c-1)(1-2\nu)}{2G}p_1^{c,t+1}-\frac{(\alpha^v-1)(1-2\nu)}{2G}p_1^{v,t+1}-\frac{(\alpha^e-1)(1-2\nu)}{2G}p_1^{e,t+1}=0 \qquad (3.53)$$

Eqn. (3.38) becomes,

$$\frac{-3p_1^{c,t+1}+4p_2^{c,t+1}-p_3^{c,t+1}}{2\Delta r}=\frac{Q_{prod}}{R_{cp}^c},$$

and simplified as,

$$-\frac{3}{2}p_1^{c,t+1}+2p_2^{c,t+1}-\frac{1}{2}p_3^{c,t+1}=\frac{Q_{prod}}{R_{c\to vent}^{CP}}\Delta r \qquad (3.54)$$

Eqn. (3.39a) becomes,

$$\frac{-3p_1^{a,t+1}+4p_2^{a,t+1}-p_3^{a,t+1}}{2\Delta r}=0,$$

and simplified as,

$$-\frac{3}{2}p_1^{a,t+1}+2p_2^{a,t+1}-\frac{1}{2}p_3^{a,t+1}=0 \qquad (3.55)$$

Eqn. (3.39b) becomes,

$$\frac{-3p_1^{v,t+1}+4p_2^{v,t+1}-p_3^{v,t+1}}{2\Delta r}=0,$$

and simplified as,

$$-\frac{3}{2}p_1^{v,t+1}+2p_2^{v,t+1}-\frac{1}{2}p_3^{v,t+1}=0 \tag{3.56}$$

Eqn. (3.40) becomes,

$$\frac{\pi d^4}{128\mu^e L}\left(p_1^{e,t+1}-p_N^{e,t+1}\right)-4\pi\kappa^e\left(r_1+u_1^t\right)^2\frac{-3p_1^{e,t+1}+4p_2^{e,t+1}-p_3^{e,t+1}}{2\Delta r}$$

$$+4\pi\left(r_1+u_1^t\right)^2\frac{u_1^{t+1}-u_1^{t-1}}{2\Delta t}=Q_{prod},$$

and simplified as,

$$\frac{1}{2}4\pi\left(r_1+u_1^t\right)^2u_1^{t+1}+\Delta t\left[\frac{\pi d^4}{128\mu^e L}+\frac{4\pi\left(r_1+u_1^t\right)^2\kappa^e}{\Delta r}\left(\frac{3}{2}\right)\right]p_1^{e,t+1}$$

$$-\Delta t\frac{4\pi\left(r_1+u_1^t\right)^2\kappa^e}{\Delta r}\left(\frac{4}{2}\right)p_2^{e,t+1}+\Delta t\frac{4\pi\left(r_1+u_1^t\right)^2\kappa^e}{\Delta r}\left(\frac{1}{2}\right)p_3^{e,t+1}-\Delta t\frac{\pi d^4}{128\mu^e L}p_N^{e,t+1}$$

$$=\Delta tQ_{prod}+\frac{1}{2}4\pi\left(r_1+u_1^t\right)^2u_1^{t-1} \tag{3.57a}$$

For the first time step, we use $u_i^{-1}=u_i^1-2\Delta tV_r^0$, Eqn. (3.45a) and Eqn. (3.45b) to substitute into Eqn. (3.57a),

$$4\pi r_1^2u_1^1+\Delta t\left[\frac{\pi d^4}{128\mu^e L}+\frac{4\pi r^2\kappa^e}{\Delta r}\left(\frac{3}{2}\right)\right]p_1^{e,1}$$

$$-\Delta t\frac{4\pi r_1^2\kappa^e}{\Delta r}\left(\frac{4}{2}\right)p_2^{e,1}+\Delta t\frac{4\pi r_1^2\kappa^e}{\Delta r}\left(\frac{1}{2}\right)p_3^{e,1}-\Delta t\frac{\pi d^4}{128\mu^e L}p_N^{e,1}=\Delta tQ_{prod} \tag{3.57b}$$

3.2.7.7 Discretised Boundary Conditions at the Skull

Eqn. (3.41) and Eqns. (3.42a-b) becomes,

$$u_N^{t+1} = 0 \tag{3.58}$$

$$p_N^{a,t} = p_{ABL} \tag{3.59}$$

$$p_N^{v,t} = p_{VBL} \tag{3.60}$$

Eqn. (3.43) becomes,

$$\frac{3p_N^{c,t+1} - 4p_{N-1}^{c,t+1} + p_{N-2}^{c,t+1}}{2\Delta r} = 0,$$

and simplified as,

$$\frac{3}{2}p_N^{c,t+1} - 2p_{N-1}^{c,t+1} + \frac{1}{2}p_{N-2}^{c,t+1} = 0 \tag{3.61}$$

Eqn. (3.44) becomes,

$$p_N^{e,t+1} = p_{VBL} + \mu^e R_{abs}^{AG} Q_{out} \tag{3.62}$$

Finally, collecting the above discretised equations representations of the system is solved by the FORTRAN 90 solver (**Ax** = **b**, using the LU decomposition subroutine).

3.3 Six-compartmental Multiple-Network Poroelastic Theory

The 4MPET model was introduced in Section 3.2. Apart from the assumptions mentioned above, the 4MPET also makes an implied assumption regarding the "CSF" compartment: this bundles all fluid outside the vascular tree into a single entity. However, this is clearly not the case, since – to start with – we have intracellular and extracellular fluid, but also very distinctive fluid pathways, like the perivascular spaces, which are possibly requiring special treatment and would offer, in return, further sensitization of an MPET model to particular physiological processes.

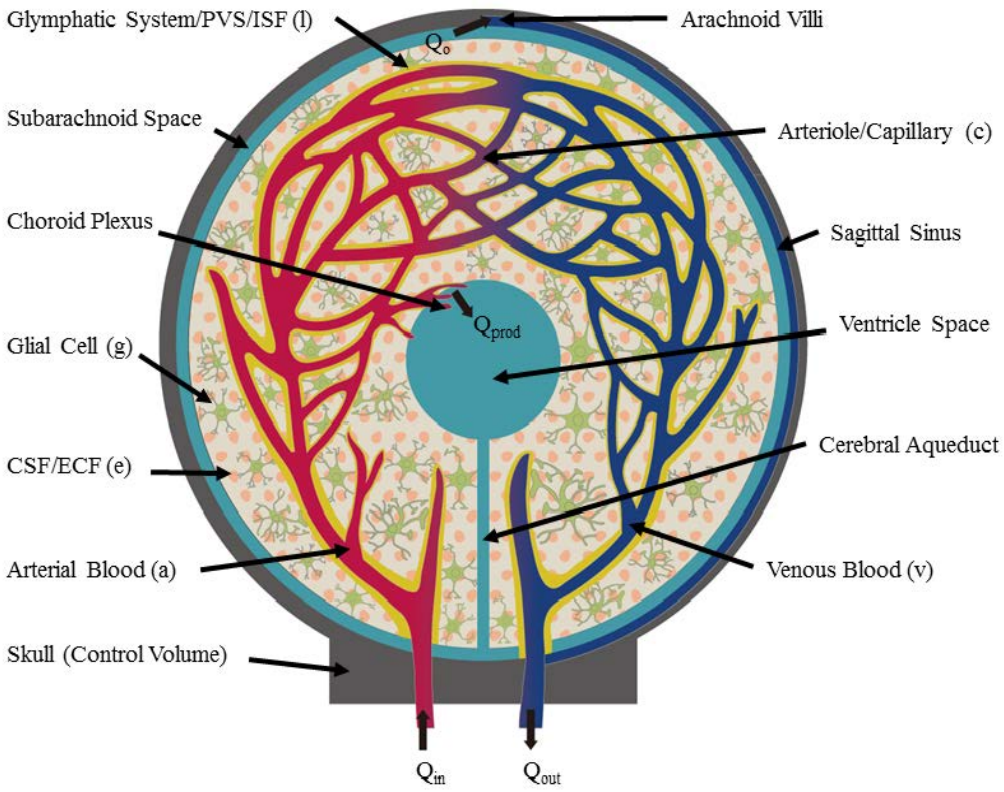


Figure 3.3 Schematic spherical representation of the 1D 6MPET model. The parenchymal tissue for the brain is simplified to a spherical shell. The lumped representation of the cerebral ventricles is connected to the SAS via an idealised representation of the aqueduct of Sylvius. Q_{prod} is the production rate of the fluid, and Q_o is the rate of CSF egress at the skull.

Therefore, to further investigate the fluid transport in the brain, a six-compartment Multiple-network Poroelastic Theory (6MPET) will be demonstrated in this section. This advanced model is based on the newly discovery, glymphatic system [28], and the glial cells with AQP effect as two additional considerations in order to capture more detailed phenomena. These two additional compartments recruit the perivascular space/glymphatic system compartment which generally represents ISF and the glial cells compartment. One of the important processes captured by separating extracellular fluid and fluid inside the glial cells is, of course, the fact that the change in volume of astrocytes results in a change in volume, and therefore porosity and permeability of the extracellular space, i.e. of the "CSF" compartment.

In 4MPET, the CSF/ISF compartment only can show the conflated phenomena that take into account CSF with ISF. This simplification has its limitations. Additionally, according to the literature which was mentioned in chapter one and two, both glial cells and the glymphatic system play an important role in the CNS [27, 66, 69, 89-93, 101, 115, 116, 118, 120, 137, 146, 148, 153-155, 244, 336-340, 343, 344, 371-373]. Therefore, it is necessary to consider the perivascular space/glymphatic system and glial cells as two additional compartments that extend the classical 4MPET system to the novel 6MPET.

Regarding the general assumptions for 6MPET, they are the same as the general assumptions of section 3.2. Nevertheless, 6MPET is assembled from the solid porous matrix representing brain parenchyma with the communicating fluid phases that will be taken into account: arterial blood (a), arteriole/capillary blood (c), venous blood (v), CSF (e), perivascular space/glymphatic system (l), and glial cells (g). Now, extending Eqns. (3.33a) and (3.33b) to represent 6MPET, the general system equations show:

$$\rho\frac{\partial^2\mathbf{u}}{\partial t^2}=G\nabla^2\mathbf{u}+\frac{G}{1-2\nu}\nabla\left(\nabla\cdot\mathbf{u}\right)-\alpha^a\nabla p^a-\alpha^c\nabla p^c-\alpha^v\nabla p^v-\alpha^e\nabla p^e-\alpha^l\nabla p^l-\alpha^g\nabla p^g$$

$$S_\varepsilon^a\frac{\partial p^a}{\partial t}+\alpha^a\frac{\partial\left(\nabla\cdot\mathbf{u}\right)}{\partial t}-\kappa^a\rho^a\frac{\partial^2\left(\nabla\cdot\mathbf{u}\right)}{\partial t^2}=\kappa^a\nabla^2p^a+\overline{s}_{a\to c}+\overline{s}_{a\to v}+\overline{s}_{a\to e}+\overline{s}_{a\to l}+\overline{s}_{a\to g}$$

$$S_\varepsilon^c\frac{\partial p^c}{\partial t}+\alpha^c\frac{\partial\left(\nabla\cdot\mathbf{u}\right)}{\partial t}-\kappa^c\rho^c\frac{\partial^2\left(\nabla\cdot\mathbf{u}\right)}{\partial t^2}=\kappa^c\nabla^2p^c+\overline{s}_{c\to a}+\overline{s}_{c\to v}+\overline{s}_{c\to e}+\overline{s}_{c\to l}+\overline{s}_{c\to g}$$

$$S_\varepsilon^v\frac{\partial p^v}{\partial t}+\alpha^v\frac{\partial\left(\nabla\cdot\mathbf{u}\right)}{\partial t}-\kappa^v\rho^v\frac{\partial^2\left(\nabla\cdot\mathbf{u}\right)}{\partial t^2}=\kappa^v\nabla^2p^v+\overline{s}_{v\to a}+\overline{s}_{v\to c}+\overline{s}_{v\to e}+\overline{s}_{v\to l}+\overline{s}_{v\to g}$$

$$S_\varepsilon^e\frac{\partial p^e}{\partial t}+\alpha^e\frac{\partial\left(\nabla\cdot\mathbf{u}\right)}{\partial t}-\kappa^e\rho^e\frac{\partial^2\left(\nabla\cdot\mathbf{u}\right)}{\partial t^2}=\kappa^e\nabla^2p^e+\overline{s}_{e\to a}+\overline{s}_{e\to c}+\overline{s}_{e\to v}+\overline{s}_{e\to l}+\overline{s}_{e\to g}$$

$$S_\varepsilon^l\frac{\partial p^l}{\partial t}+\alpha^l\frac{\partial\left(\nabla\cdot\mathbf{u}\right)}{\partial t}-\kappa^l\rho^l\frac{\partial^2\left(\nabla\cdot\mathbf{u}\right)}{\partial t^2}=\kappa^l\nabla^2p^l+\overline{s}_{l\to a}+\overline{s}_{l\to c}+\overline{s}_{l\to v}+\overline{s}_{l\to e}+\overline{s}_{l\to g}$$

$$S_\varepsilon^g\frac{\partial p^g}{\partial t}+\alpha^g\frac{\partial\left(\nabla\cdot\mathbf{u}\right)}{\partial t}-\kappa^g\rho^g\frac{\partial^2\left(\nabla\cdot\mathbf{u}\right)}{\partial t^2}=\kappa^g\nabla^2p^g+\overline{s}_{g\to a}+\overline{s}_{g\to c}+\overline{s}_{g\to v}+\overline{s}_{g\to e}+\overline{s}_{g\to l}$$

(3.63a-g)

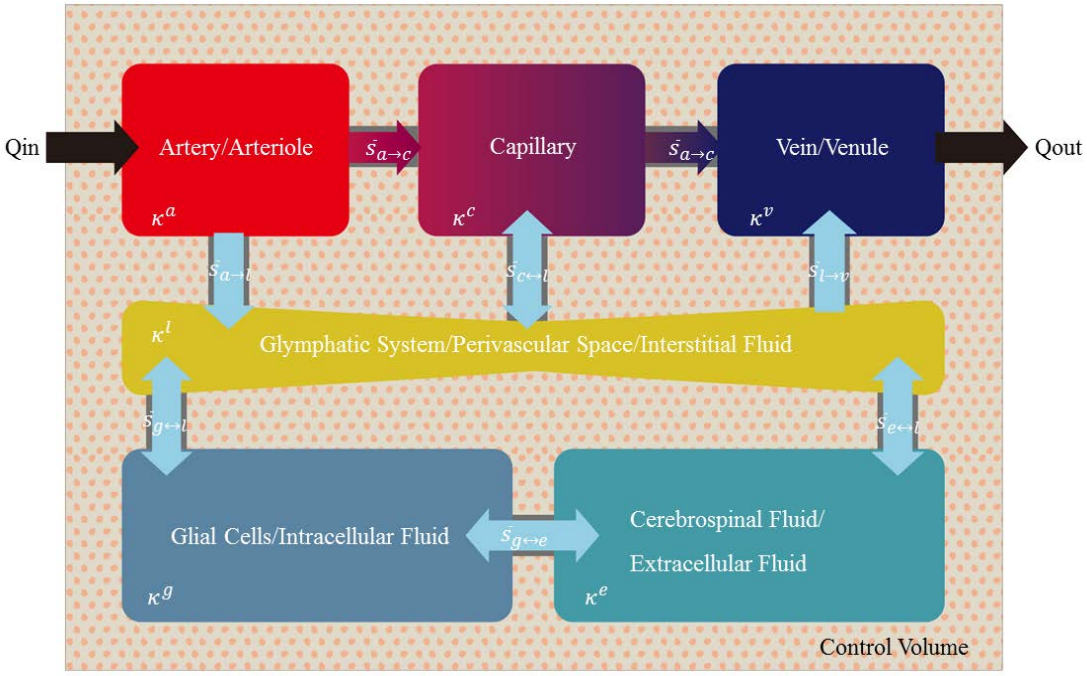


Figure 3.4 The fluid transfer restrictions placed between the six compartments. It can be seen that flow is prohibited between the CSF and cerebrovascular network, and glial cells and cerebrovascular network.

3.3.1 Continuity and Directional Water Transfer

The transfer of fluid among six fluid networks is required to obey the law of continuity for the entire system, but also adequately mimic human cerebral physiology (Figure 3.4). So directionality among fluid compartments must be accurately specified. A summary of the directional fluid restrictions is showed in schematic Figure 3.3 and by illustrating in the following:

$$
\begin{aligned}
&Q_{in} + Q_{acc} = Q_{out} \\
&Q_{acc} = Q_a + Q_c + Q_v + Q_e + Q_l + Q_g \\
&Q_a = -Q_{in} + \overline{s}_{a\to c} + \overline{s}_{a\to l} \\
&Q_c = \overline{s}_{c\to a} + \overline{s}_{c\to v} + \overline{s}_{c\to l} \\
&Q_v = \overline{s}_{v\to c} + \overline{s}_{v\to l} + Q_{out} \\
&Q_e = \overline{s}_{e\to g} + \overline{s}_{e\to l} \\
&Q_l = \overline{s}_{l\to a} + \overline{s}_{l\to c} + \overline{s}_{l\to v} + \overline{s}_{l\to g} + \overline{s}_{l\to e} \\
&Q_g = \overline{s}_{g\to l} + \overline{s}_{g\to e}
\end{aligned}
\qquad \text{(3.64a-h)}
$$

where Q_{in} and Q_{out} are the flux of fluid in and out of the control volume, Q_{acc} is the fluid accumulated in the control volume as a whole, and finally, Q_a, Q_c, Q_v, Q_e, Q_l, and Q_g represent the fluid accumulated in each individual fluid network, namely: arterial/arteriole blood (a), capillary blood (c), venous/venule blood (v), CSF (e), perivascular space/glymphatic system (l), and glial cells (g) network. $\bar{s}_{\Lambda\to\Omega}$ is the interporosity fluxes from network Λ to Ω which have been described in Eqn. (3.31) and it can be both positive and negative. Moreover, regarding the transfer coefficient $\gamma_{\Lambda\Omega}$ in Eqn. (3.31), it can be assembled by the hydraulic conductivity (L_p^{Λ}), the bidirectional constrained specific storage coefficient ($S_{\varepsilon}^{\Lambda}$) and the surface-to-volume ratio$(SA/V)^{\Lambda}$,

$$
\gamma_{\Lambda\Omega} = L_p^{\Lambda} \cdot S_{\varepsilon}^{\Lambda} \cdot \left(\frac{SA}{V}\right)^{\Lambda} \qquad (3.65)
$$

There is another expression, the scaling factor, RF_{AQP}^{Ω}, which represents the level of aquaporin expression. For the glial cells compartment, there are two source terms of the interporosity fluxes, $\bar{s}_{g\to e}$ and $\bar{s}_{g\to l}$. These two interporosity fluxes are considered with AQP effect in mind in this study,

$$\bar{s}_{g\to e} = \gamma_{ge} \cdot RF_{AQP}^{g} \cdot \left(p^{e} - p^{g} \right) \quad ; \quad \bar{s}_{g\to l} = \gamma_{gl} \cdot RF_{AQP}^{g} \cdot \left(p^{l} - p^{g} \right) \qquad (3.66a\text{-}b)$$

According to the studies conducted in Chapter 5 and 6, we suggest the value of RF_{AQP}^{g} between 0.1 to 10.0. The normal case is represented when $RF_{AQP}^{g} = 1.0$. For the case of AQP overexpression, the RF_{AQP}^{g} is considered to set between 1.0 to 0.1. Conversely, the value of the EF_{AQP}^{g} is considered between 1.0 to 10.0 for the AQP deficient case.

Meanwhile, Q_{acc} is equal to zero when averaged over time in the healthy brain, but fluid accumulates in the CSF and ISF space or in the individual blood networks in the symptomatic brain. Based on the physiological observations of the system, there are some assumptions to detail (please refer to Figure 3.4):

i. Directional fluid transport always commences from the arterial/arteriole network and tends towards either the capillary or the perivascular space/glymphatic system network ($\bar{s}_{a\to c} = -\bar{s}_{c\to a} \geq 0$; $\bar{s}_{a\to l} = -\bar{s}_{l\to a} \geq 0$).
ii. Fluid transport from the capillary network will go to either the perivascular space/glymphatic system network ($\bar{s}_{c\to l} = -\bar{s}_{l\to c} \geq 0$) or the venous network ($\bar{s}_{c\to v} = -\bar{s}_{v\to c} \geq 0$).

iii. Fluid transport from the venous/venule network will collect in the perivascular space/glymphatic system network ($\bar{s}_{v\to l} = -\bar{s}_{l\to v} \geq 0$).

iv. Fluid transport from the CSF network will go to either the glial cells network or the perivascular space/glymphatic system network ($\bar{s}_{e\to l} = -\bar{s}_{l\to e} \geq 0$).

v. Fluid transport from the glial cells network will go to either the perivascular space/glymphatic system network ($\bar{s}_{g\to l} = -\bar{s}_{l\to g} \geq 0$) or the CSF network ($\bar{s}_{g\to e} = -\bar{s}_{e\to g} \geq 0$).

According to the physiology, some transfer directions are prohibited:

i. Fluid from the arterial network to venous networks, the CSF network, and glial cells network ($\bar{s}_{a\to v} = \bar{s}_{a\to e} = \bar{s}_{a\to g} = 0$).

ii. Fluid from the arteriole/capillary network to the CSF network and glial cells network ($\bar{s}_{c\to e} = \bar{s}_{c\to g} = 0$).

iii. Fluid from the venous network to the CSF network and glial cells network ($\bar{s}_{v\to e} = \bar{s}_{v\to g} = 0$).

3.3.2 Methodology in One-Dimension

In this section, we show the 1D system equations in the *r*-direction of the spherical coordinate system, reduced from Eqns. (3.63a-g) to,

$$\rho\frac{\partial^2 u_r}{\partial t^2}=\frac{2G(1-\nu)}{1-2\nu}\left(\frac{\partial^2 u_r}{\partial r^2}+\frac{2}{r}\frac{\partial u_r}{\partial r}-\frac{2}{r^2}u_r\right)-\alpha^a\frac{\partial p^a}{\partial r}-\alpha^c\frac{\partial p^c}{\partial r}-\alpha^v\frac{\partial p^v}{\partial r}-\alpha^e\frac{\partial p^e}{\partial r}-\alpha^l\frac{\partial p^l}{\partial r}$$
$$-\alpha^g\frac{\partial p^g}{\partial r}$$

$$S_\varepsilon^a\frac{\partial p^a}{\partial t}+\alpha^a\frac{\partial}{\partial t}\left(\frac{\partial u_r}{\partial r}+\frac{2}{r}u_r\right)-\kappa^a\rho^a\frac{\partial^2}{\partial t^2}\left(\frac{\partial u_r}{\partial r}+\frac{2}{r}u_r\right)=\kappa^a\frac{\partial^2 p^a}{\partial r^2}+\bar{s}_{a\to c}+\bar{s}_{a\to l}$$

$$S_\varepsilon^c\frac{\partial p^c}{\partial t}+\alpha^c\frac{\partial}{\partial t}\left(\frac{\partial u_r}{\partial r}+\frac{2}{r}u_r\right)-\kappa^c\rho^c\frac{\partial^2}{\partial t^2}\left(\frac{\partial u_r}{\partial r}+\frac{2}{r}u_r\right)=\kappa^c\frac{\partial^2 p^c}{\partial r^2}+\bar{s}_{c\to a}+\bar{s}_{c\to v}+\bar{s}_{c\to l}$$

$$S_\varepsilon^v\frac{\partial p^v}{\partial t}+\alpha^v\frac{\partial}{\partial t}\left(\frac{\partial u_r}{\partial r}+\frac{2}{r}u_r\right)-\kappa^v\rho^v\frac{\partial^2}{\partial t^2}\left(\frac{\partial u_r}{\partial r}+\frac{2}{r}u_r\right)=\kappa^v\frac{\partial^2 p^v}{\partial r^2}+\bar{s}_{v\to c}+\bar{s}_{v\to l}$$

$$S_\varepsilon^e\frac{\partial p^e}{\partial t}+\alpha^e\frac{\partial}{\partial t}\left(\frac{\partial u_r}{\partial r}+\frac{2}{r}u_r\right)-\kappa^e\rho^e\frac{\partial^2}{\partial t^2}\left(\frac{\partial u_r}{\partial r}+\frac{2}{r}u_r\right)=\kappa^e\frac{\partial^2 p^e}{\partial r^2}+\bar{s}_{e\to l}+\bar{s}_{e\to g}$$

$$S_\varepsilon^l\frac{\partial p^l}{\partial t}+\alpha^l\frac{\partial}{\partial t}\left(\frac{\partial u_r}{\partial r}+\frac{2}{r}u_r\right)-\kappa^l\rho^l\frac{\partial^2}{\partial t^2}\left(\frac{\partial u_r}{\partial r}+\frac{2}{r}u_r\right)=\kappa^l\frac{\partial^2 p^l}{\partial r^2}+\bar{s}_{l\to a}+\bar{s}_{l\to c}+\bar{s}_{l\to v}+\bar{s}_{l\to e}+\bar{s}_{l\to g}$$

$$S_\varepsilon^g\frac{\partial p^g}{\partial t}+\alpha^g\frac{\partial}{\partial t}\left(\frac{\partial u_r}{\partial r}+\frac{2}{r}u_r\right)-\kappa^g\rho^g\frac{\partial^2}{\partial t^2}\left(\frac{\partial u_r}{\partial r}+\frac{2}{r}u_r\right)=\kappa^g\frac{\partial^2 p^g}{\partial r^2}+\bar{s}_{g\to e}+\bar{s}_{g\to l}$$

(3.67a-g)

where u_r is the displacement in the *r*-direction of the spherical coordinate.

3.3.3 Boundary Conditions at the Ventricular Wall

Since the boundary conditions of the compartments in 4MPET including arterial, arteriole/capillary, venous and CSF, are the same as the boundary conditions of the compartments in 6MPET including arterial, arteriole/capillary, venous and CSF from Eqn. (3.37) to Eqn. (3.40), respectively, we will demonstrate the boundary conditions of the remaining two additional compartments, perivascular space/glymphatic system

compartment and glial cells compartment and the displacement boundary condition at the ventricular wall.

There is no flow into or out of the perivascular space network at the ventricular wall,

$$\frac{\partial p_1^{l,t}}{\partial r} = 0 \tag{3.68}$$

For the glial cells compartment, the normal stress of the solid matrix and the CSF pressure have to be at equilibrium at the ventricular wall,

$$p_1^{g,t} = \frac{p_1^{e,t}}{\alpha^g} + \frac{2G^g}{\alpha^g}\left(\frac{1-\nu^g}{1-2\nu^g}\right)\frac{\partial u_1^t}{\partial r} + \frac{2G^g}{\alpha^g}\left(\frac{2\nu^g}{1-2\nu^g}\right)\frac{u_1^t}{r_1} \tag{3.69}$$[2]

Due to the spherically symmetric shell geometry and assuming the stress must be continuous across the ventricular wall ($r = r_1$),

$$(1-\nu)\frac{\partial u_1^t}{\partial r} + 2\nu\frac{u_1^t}{r_1} = \frac{1-2\nu}{2G}\sum_{\Omega=a,c,v,e,l,g}\left(\alpha^\Omega - 1\right)p_1^{\Omega,t} \tag{3.70}$$

3.3.4 Boundary Conditions at the Skull

As in the section 3.3.2, the remaining boundary conditions of the two additional compartments, perivascular space/glymphatic system compartment and glial cells compartment are as follows:

[2] The mathematic derivation of Eqn (3.69) is available in Appendix (A4).

The SAS pressure is given as a Dirichlet boundary condition for the perivascular space/glymphatic system network at the skull,

$$p_N^{l,t} = p_{SAS} \tag{3.71}$$

There is no flow into or out of the glial cells network at the skull,

$$\frac{\partial p_1^{g,t}}{\partial r} = 0 \tag{3.72}$$

3.3.5 Initial Conditions

Regarding the initial conditions for the displacement and velocity, these are same as the Eqn. (3.45a) and Eqn. (3.45b), respectively. Additionally, setting the steady-state results of the pressure compartments as the initial conditions for the transient model is an alternative way,

$$\begin{aligned} p_r^{a,0} &= \bar{p}^a \\ p_r^{c,0} &= \bar{p}^c \\ p_r^{v,0} &= \bar{p}^v \\ p_r^{e,0} &= \bar{p}^e \\ p_r^{l,0} &= \bar{p}^l \\ p_r^{g,0} &= \bar{p}^g \end{aligned} \tag{3.73a-f}$$

where $\bar{p}^a$, $\bar{p}^c$, $\bar{p}^v$, $\bar{p}^e$, $\bar{p}^l$, $\bar{p}^g$ are the steady-state results in arterial blood compartment, arteriole/capillary blood compartment, venous blood compartment, CSF compartment, perivascular space/glymphatic system compartment, and glial cells compartment respectively.

3.3.6 Numerical Implementation

The 6MPET model is described as a boundary value problem, and finite differences are used to discretise the system equations. The central difference scheme is employed for the spatial discretisation of the equations of motion, and the Crank-Nicolson method is applied to deal with temporal discretisation. Moreover, the second order forward or backward difference schemes are implemented as appropriate for estimating spatial derivatives in the boundary conditions. We have coded a FORTRAN 90 in-house program for this MPET model, by using the following discretised system equations and solve this linear system via the LU decomposition method.

3.3.6.1 Displacement Equation

Eqn. (3.67a) becomes,

$$\frac{u_i^{t+1}-2u_i^t+u_i^{t-1}}{\Delta t^2}=\frac{2G(1-\nu)}{\rho(1-2\nu)}\left(\frac{1}{2}\right)\left[\frac{u_{i+1}^{t+1}-2u_i^{t+1}+u_{i-1}^{t+1}}{\Delta r^2}+\frac{2}{r_i}\left(\frac{u_{i+1}^{t+1}-u_{i-1}^{t+1}}{2\Delta r}\right)-\frac{2}{r_i^2}u_i^{t+1}\right]$$

$$+\frac{2G(1-\nu)}{\rho(1-2\nu)}\left(\frac{1}{2}\right)\left[\frac{u_{i+1}^{t}-2u_i^{t}+u_{i-1}^{t}}{\Delta r^2}+\frac{2}{r_i}\left(\frac{u_{i+1}^{t}-u_{i-1}^{t}}{2\Delta r}\right)-\frac{2}{r_i^2}u_i^{t}\right]$$

$$-\left(\frac{1}{2}\right)\frac{1}{\rho}\sum_{\Omega=a,c,v,e,l,g}\alpha^{\Omega}\left(\frac{p_{i+1}^{\Omega,t+1}-p_{i-1}^{\Omega,t+1}}{2\Delta r}\right)-\left(\frac{1}{2}\right)\frac{1}{\rho}\sum_{\Omega=a,c,v,e,l,g}\alpha^{\Omega}\left(\frac{p_{i+1}^{\Omega,t}-p_{i-1}^{\Omega,t}}{2\Delta r}\right)$$

Rearranging for the nodal values,

$$-\left(\frac{1}{2}\right)\Delta t^2\frac{2G(1-\nu)}{\rho(1-2\nu)}\left(\frac{1}{\Delta r^2}-\frac{1}{r_i\Delta r}\right)u_{i-1}^{t+1}+\left[1+\left(\frac{1}{2}\right)\Delta t^2\frac{2G(1-\nu)}{\rho(1-2\nu)}\left(\frac{2}{r_i^2}+\frac{2}{\Delta r^2}\right)\right]u_i^{t+1}$$

$$-\left(\frac{1}{2}\right)\Delta t^2\frac{2G(1-\nu)}{\rho(1-2\nu)}\left(\frac{1}{\Delta r^2}+\frac{1}{r_i\Delta r}\right)u_{i+1}^{t+1}$$

$$-\left(\frac{1}{2}\right)\frac{\Delta t^2}{\rho 2\Delta r}\sum_{\Omega=a,c,v,e,l,g}\alpha^{\Omega}p_{i-1}^{\Omega,t+1}+\left(\frac{1}{2}\right)\frac{\Delta t^2}{\rho 2\Delta r}\sum_{\Omega=a,c,v,e,l,g}\alpha^{\Omega}p_{i+1}^{\Omega,t+1}=$$

$$\left(\frac{1}{2}\right)\Delta t^2\frac{2G(1-\nu)}{\rho(1-2\nu)}\left(\frac{1}{\Delta r^2}-\frac{1}{r_i\Delta r}\right)u_{i-1}^{t}+\left[2-\left(\frac{1}{2}\right)\Delta t^2\frac{2G(1-\nu)}{\rho(1-2\nu)}\left(\frac{2}{\Delta r^2}+\frac{2}{r_i^2}\right)\right]u_i^{t}$$

$$+\left(\frac{1}{2}\right)\Delta t^2\frac{2G(1-\nu)}{\rho(1-2\nu)}\left(\frac{1}{\Delta r^2}+\frac{1}{r_i\Delta r}\right)u_{i+1}^{t}-u_i^{t-1}$$

$$+\left(\frac{1}{2}\right)\frac{\Delta t^2}{\rho 2\Delta r}\sum_{\Omega=a,c,v,e,l,g}\alpha^{\Omega}p_{i-1}^{\Omega,t}-\left(\frac{1}{2}\right)\frac{\Delta t^2}{\rho 2\Delta r}\sum_{\Omega=a,c,v,e,l,g}\alpha^{\Omega}p_{i+1}^{\Omega,t} \tag{3.74a}$$

When $t = 0$, we have $u_i^{-1} = u_i^1 - 2\Delta t V_r^0$ and Eqn. (3.45b), and then substitute into Eqn. (3.74a),

$$-\left(\frac{1}{2}\right)\Delta t^2\frac{2G(1-\nu)}{\rho(1-2\nu)}\left(\frac{1}{\Delta r^2}-\frac{1}{r_i\Delta r}\right)u_{i-1}^{1}+\left[2+\left(\frac{1}{2}\right)\Delta t^2\frac{2G(1-\nu)}{\rho(1-2\nu)}\left(\frac{2}{r_i^2}+\frac{2}{\Delta r^2}\right)\right]u_i^{1}$$

$$-\left(\frac{1}{2}\right)\Delta t^2\frac{2G(1-\nu)}{\rho(1-2\nu)}\left(\frac{1}{\Delta r^2}+\frac{1}{r_i\Delta r}\right)u_{i+1}^{1}-\left(\frac{1}{2}\right)\frac{\Delta t^2}{\rho 2\Delta r}\sum_{\Omega=a,c,v,e,l,g}\alpha^{\Omega}p_{i-1}^{\Omega,1}$$

$$+\left(\frac{1}{2}\right)\frac{\Delta t^2}{\rho 2\Delta r}\sum_{\Omega=a,c,v,e,l,g}\alpha^{\Omega}p_{i+1}^{\Omega,1}=\left(\frac{1}{2}\right)\Delta t^2\frac{2G(1-\nu)}{\rho(1-2\nu)}\left(\frac{1}{\Delta r^2}-\frac{1}{r_i\Delta r}\right)u_{i-1}^{0}$$

$$+\left[2-\left(\frac{1}{2}\right)\Delta t^2\frac{2G(1-\nu)}{\rho(1-2\nu)}\left(\frac{2}{\Delta r^2}+\frac{2}{r_i^2}\right)\right]u_i^{0}+\left(\frac{1}{2}\right)\Delta t^2\frac{2G(1-\nu)}{\rho(1-2\nu)}\left(\frac{1}{\Delta r^2}+\frac{1}{r_i\Delta r}\right)u_{i+1}^{0}$$

$$+2\Delta t V_r^0+\left(\frac{1}{2}\right)\frac{\Delta t^2}{\rho 2\Delta r}\sum_{\Omega=a,c,v,e,l,g}\alpha^{\Omega}p_{i-1}^{\Omega,0}-\left(\frac{1}{2}\right)\frac{\Delta t^2}{\rho 2\Delta r}\sum_{\Omega=a,c,v,e,l,g}\alpha^{\Omega}p_{i+1}^{\Omega,0} \tag{3.74b}$$

3.3.6.2 Arterial Pressure

Eqn. (3.67b) becomes,

$$\Delta t S_\varepsilon^a \left(p_i^{a,t+1} - p_i^{a,t} \right)$$

$$+\frac{\Delta t}{2}\alpha^a \left[\left(\frac{-1}{2\Delta r} u_{i-1}^{t+1} + \frac{2}{r_i} u_i^{t+1} + \frac{1}{2\Delta r} u_{i+1}^{t+1} \right) - \left(\frac{-1}{2\Delta r} u_{i-1}^{t-1} + \frac{2}{r_i} u_i^{t-1} + \frac{1}{2\Delta r} u_{i+1}^{t-1} \right) \right]$$

$$-\rho_f^a \kappa^a \left[\left(\frac{-1}{2\Delta r} u_{i-1}^{t+1} + \frac{2}{r_i} u_i^{t+1} + \frac{1}{2\Delta r} u_{i+1}^{t+1} \right) - 2\left(\frac{-1}{2\Delta r} u_{i-1}^{t} + \frac{2}{r_i} u_i^{t} + \frac{1}{2\Delta r} u_{i+1}^{t} \right) \right.$$

$$\left. + \left(\frac{-1}{2\Delta r} u_{i-1}^{t-1} + \frac{2}{r_i} u_i^{t-1} + \frac{1}{2\Delta r} u_{i+1}^{t-1} \right) \right] =$$

$$\left(\frac{1}{2}\right)\Delta t^2 \kappa^a \left[\left(\frac{1}{\Delta r^2} - \frac{1}{r_i \Delta r} \right) p_{i-1}^{a,t+1} - \left(\frac{2}{\Delta r^2} \right) p_i^{a,t+1} + \left(\frac{1}{\Delta r^2} + \frac{1}{r_i \Delta r} \right) p_{i+1}^{a,t+1} \right]$$

$$+\left(\frac{1}{2}\right)\Delta t^2 \kappa^a \left[\left(\frac{1}{\Delta r^2} - \frac{1}{r_i \Delta r} \right) p_{i-1}^{a,t} - \left(\frac{2}{\Delta r^2} \right) p_i^{a,t} + \left(\frac{1}{\Delta r^2} + \frac{1}{r_i \Delta r} \right) p_{i+1}^{a,t} \right]$$

$$+\Delta t^2 \overline{s}_{a\to c} + \Delta t^2 \overline{s}_{a\to l} \tag{3.75}$$

Rearranging for the nodal values,

$$\left[\rho_f^a \kappa^a - \alpha^a \left(\frac{\Delta t}{2} \right) \right] \left(\frac{1}{2\Delta r} \right) u_{i-1}^{t+1} - \left[\rho_f^a \kappa^a - \alpha^a \left(\frac{\Delta t}{2} \right) \right] \left(\frac{2}{r_i} \right) u_i^{t+1}$$

$$- \left[\rho_f^a \kappa^a - \alpha^a \left(\frac{\Delta t}{2} \right) \right] \left(\frac{1}{2\Delta r} \right) u_{i+1}^{t+1}$$

$$-\left(\frac{1}{2}\right)\Delta t^2 \kappa^a \left(\frac{1}{\Delta r^2} - \frac{1}{r_i \Delta r} \right) p_{i-1}^{a,t+1} + \left[\Delta t S_\varepsilon^a + \left(\frac{1}{2}\right)\Delta t^2 \kappa^a \left(\frac{2}{\Delta r^2} \right) \right] p_i^{a,t+1}$$

$$-\left(\frac{1}{2}\right)\Delta t^2 \kappa^a \left(\frac{1}{\Delta r^2} + \frac{1}{r_i \Delta r} \right) p_{i+1}^{a,t+1} = \rho_f^a \kappa^a \left(\frac{1}{\Delta r} \right) u_{i-1}^{t} - \rho_f^a \kappa^a \left(\frac{4}{r_i} \right) u_i^{t} - \rho_f^a \kappa^a \left(\frac{1}{\Delta r} \right) u_{i+1}^{t}$$

$$+\left(\frac{1}{2}\right)\Delta t^2 \kappa^a \left(\frac{1}{\Delta r^2} - \frac{1}{r_i \Delta r} \right) p_{i-1}^{a,t} + \left[\Delta t S_\varepsilon^a - \left(\frac{1}{2}\right)\Delta t^2 \kappa^a \left(\frac{2}{\Delta r^2} \right) \right] p_i^{a,t}$$

$$+\left(\frac{1}{2}\right)\Delta t^2 \kappa^a \left(\frac{1}{\Delta r^2} + \frac{1}{r_i \Delta r} \right) p_{i+1}^{a,t} - \left[\rho_f^a \kappa^a + \alpha^a \left(\frac{\Delta t}{2} \right) \right] \left(\frac{1}{2\Delta r} \right) u_{i-1}^{t-1}$$

$$+\left[\rho_f^a\kappa^a+\alpha^a\left(\frac{\Delta t}{2}\right)\right]\left(\frac{2}{r_i}\right)u_i^{t-1}+\left[\rho_f^a\kappa^a+\alpha^a\left(\frac{\Delta t}{2}\right)\right]\left(\frac{1}{2\Delta r}\right)u_{i+1}^{t-1}$$

$$+\Delta t^2\overline{s}_{a\to c}+\Delta t^2\overline{s}_{a\to l} \tag{3.76a}$$

When $t = 0$, we get $u_i^{-1}=u_i^1-2\Delta t V_r^0$, Eqn. (3.45b), and Eqn. (3.73a), and then substitute into and Eqn. (3.76a),

$$2\rho_f^a\kappa^a\left(\frac{1}{2\Delta r}\right)u_{i-1}^1-2\rho_f^a\kappa^a\left(\frac{2}{r_i}\right)u_i^1-2\rho_f^a\kappa^a\left(\frac{1}{2\Delta r}\right)u_{i+1}^1-\left(\frac{1}{2}\right)\Delta t^2\kappa^a\left(\frac{1}{\Delta r^2}-\frac{1}{r_i\Delta r}\right)p_{i-1}^{a,1}$$

$$+\left[\Delta tS_\varepsilon^a+\left(\frac{1}{2}\right)\Delta t^2\kappa^a\left(\frac{2}{\Delta r^2}\right)\right]p_i^{a,1}-\left(\frac{1}{2}\right)\Delta t^2\kappa^a\left(\frac{1}{\Delta r^2}+\frac{1}{r_i\Delta r}\right)p_{i+1}^{a,1}=$$

$$+\rho_f^a\kappa^a\left(\frac{1}{\Delta r}\right)u_{i-1}^0-\rho_f^a\kappa^a\left(\frac{4}{r_i}\right)u_i^0-\rho_f^a\kappa^a\left(\frac{1}{\Delta r}\right)u_{i+1}^0+\left(\frac{1}{2}\right)\Delta t^2\kappa^a\left(\frac{1}{\Delta r^2}-\frac{1}{r_i\Delta r}\right)p_{i-1}^{a,0}$$

$$+\left[\Delta tS_\varepsilon^a-\left(\frac{1}{2}\right)\Delta t^2\kappa^a\left(\frac{2}{\Delta r^2}\right)\right]p_i^{a,0}+\left(\frac{1}{2}\right)\Delta t^2\kappa^a\left(\frac{1}{\Delta r^2}+\frac{1}{r_i\Delta r}\right)p_{i+1}^{a,0}$$

$$+\Delta t^2\overline{s}_{a\to c}+\Delta t^2\overline{s}_{a\to l} \tag{3.76b}$$

3.3.6.3 Arteriole/Capillary Pressure

Taking Eqn. (3.67c) and using the same process from Eqn. (3.75) to Eqn. (3.76a), we have the nodal values

$$\left[\rho_f^c\kappa^c-\alpha^c\left(\frac{\Delta t}{2}\right)\right]\left(\frac{1}{2\Delta r}\right)u_{i-1}^{t+1}-\left[\rho_f^c\kappa^c-\alpha^c\left(\frac{\Delta t}{2}\right)\right]\left(\frac{2}{r_i}\right)u_i^{t+1}$$

$$-\left[\rho_f^c\kappa^c-\alpha^c\left(\frac{\Delta t}{2}\right)\right]\left(\frac{1}{2\Delta r}\right)u_{i+1}^{t+1}$$

$$-\left(\frac{1}{2}\right)\Delta t^2\kappa^c\left(\frac{1}{\Delta r^2}-\frac{1}{r_i\Delta r}\right)p_{i-1}^{c,t+1}+\left[\Delta tS_\varepsilon^c+\left(\frac{1}{2}\right)\Delta t^2\kappa^c\left(\frac{2}{\Delta r^2}\right)\right]p_i^{c,t+1}$$

$$-\left(\frac{1}{2}\right)\Delta t^2\kappa^c\left(\frac{1}{\Delta r^2}+\frac{1}{r_i\Delta r}\right)p_{i+1}^{c,t+1}=\rho_f^c\kappa^c\left(\frac{1}{\Delta r}\right)u_{i-1}^t-\rho_f^c\kappa^c\left(\frac{4}{r_i}\right)u_i^t-\rho_f^c\kappa^c\left(\frac{1}{\Delta r}\right)u_{i+1}^t$$

$$+\left(\frac{1}{2}\right)\Delta t^2\kappa^c\left(\frac{1}{\Delta r^2}-\frac{1}{r_i\Delta r}\right)p_{i-1}^{c,t}+\left[\Delta tS_\varepsilon^c-\left(\frac{1}{2}\right)\Delta t^2\kappa^c\left(\frac{2}{\Delta r^2}\right)\right]p_i^{c,t}$$

$$+\left(\frac{1}{2}\right)\Delta t^2\kappa^c\left(\frac{1}{\Delta r^2}+\frac{1}{r_i\Delta r}\right)p_{i+1}^{c,t}-\left[\rho_f^c\kappa^c+\alpha^c\left(\frac{\Delta t}{2}\right)\right]\left(\frac{1}{2\Delta r}\right)u_{i-1}^{t-1}$$

$$+\left[\rho_f^c\kappa^c+\alpha^c\left(\frac{\Delta t}{2}\right)\right]\left(\frac{2}{r_i}\right)u_i^{t-1}+\left[\rho_f^c\kappa^c+\alpha^c\left(\frac{\Delta t}{2}\right)\right]\left(\frac{1}{2\Delta r}\right)u_{i+1}^{t-1}$$

$$+\Delta t^2\overline{s}_{c\to a}+\Delta t^2\overline{s}_{c\to v}+\Delta t^2\overline{s}_{c\to l} \tag{3.77a}$$

For the first time step, we use $u_i^{-1}=u_i^1-2\Delta tV_r^0$, Eqn. (3.45b), and Eqn. (3.73b) to substitute into and Eqn. (3.77a),

$$2\rho_f^c\kappa^c\left(\frac{1}{2\Delta r}\right)u_{i-1}^1-2\rho_f^c\kappa^c\left(\frac{2}{r_i}\right)u_i^1-2\rho_f^c\kappa^c\left(\frac{1}{2\Delta r}\right)u_{i+1}^1-\left(\frac{1}{2}\right)\Delta t^2\kappa^c\left(\frac{1}{\Delta r^2}-\frac{1}{r_i\Delta r}\right)p_{i-1}^{c,1}$$

$$+\left[\Delta tS_\varepsilon^c+\left(\frac{1}{2}\right)\Delta t^2\kappa^c\left(\frac{2}{\Delta r^2}\right)\right]p_i^{c,1}-\left(\frac{1}{2}\right)\Delta t^2\kappa^c\left(\frac{1}{\Delta r^2}+\frac{1}{r_i\Delta r}\right)p_{i+1}^{c,1}=$$

$$+\rho_f^c\kappa^c\left(\frac{1}{\Delta r}\right)u_{i-1}^0-\rho_f^c\kappa^c\left(\frac{4}{r_i}\right)u_i^0-\rho_f^c\kappa^c\left(\frac{1}{\Delta r}\right)u_{i+1}^0+\left(\frac{1}{2}\right)\Delta t^2\kappa^c\left(\frac{1}{\Delta r^2}-\frac{1}{r_i\Delta r}\right)p_{i-1}^{c,0}$$

$$+\left[\Delta tS_\varepsilon^c-\left(\frac{1}{2}\right)\Delta t^2\kappa^c\left(\frac{2}{\Delta r^2}\right)\right]p_i^{c,0}+\left(\frac{1}{2}\right)\Delta t^2\kappa^c\left(\frac{1}{\Delta r^2}+\frac{1}{r_i\Delta r}\right)p_{i+1}^{c,0}$$

$$+\Delta t^2\overline{s}_{c\to a}+\Delta t^2\overline{s}_{c\to v}+\Delta t^2\overline{s}_{c\to l} \tag{3.77b}$$

3.3.6.4 Venous Pressure

Taking Eqn. (3.67d) and using the same process from Eqn. (3.75) to Eqn. (3.76a), we have the nodal values

$$\left[\rho_f^v\kappa^v-\alpha^v\left(\frac{\Delta t}{2}\right)\right]\left(\frac{1}{2\Delta r}\right)u_{i-1}^{t+1}-\left[\rho_f^v\kappa^v-\alpha^v\left(\frac{\Delta t}{2}\right)\right]\left(\frac{2}{r_i}\right)u_i^{t+1}$$

$$-\left[\rho_f^v\kappa^v-\alpha^v\left(\frac{\Delta t}{2}\right)\right]\left(\frac{1}{2\Delta r}\right)u_{i+1}^{t+1}$$

$$-\left(\frac{1}{2}\right)\Delta t^2\kappa^v\left(\frac{1}{\Delta r^2}-\frac{1}{r_i\Delta r}\right)p_{i-1}^{v,t+1}+\left[\Delta tS_\varepsilon^v+\left(\frac{1}{2}\right)\Delta t^2\kappa^v\left(\frac{2}{\Delta r^2}\right)\right]p_i^{v,t+1}$$

$$-\left(\frac{1}{2}\right)\Delta t^2\kappa^v\left(\frac{1}{\Delta r^2}+\frac{1}{r_i\Delta r}\right)p_{i+1}^{v,t+1}=\rho_f^v\kappa^v\left(\frac{1}{\Delta r}\right)u_{i-1}^t-\rho_f^v\kappa^v\left(\frac{4}{r_i}\right)u_i^t-\rho_f^v\kappa^v\left(\frac{1}{\Delta r}\right)u_{i+1}^t$$

$$+\left(\frac{1}{2}\right)\Delta t^2\kappa^v\left(\frac{1}{\Delta r^2}-\frac{1}{r_i\Delta r}\right)p_{i-1}^{v,t}+\left[\Delta tS_\varepsilon^v-\left(\frac{1}{2}\right)\Delta t^2\kappa^v\left(\frac{2}{\Delta r^2}\right)\right]p_i^{v,t}$$

$$+\left(\frac{1}{2}\right)\Delta t^2\kappa^v\left(\frac{1}{\Delta r^2}+\frac{1}{r_i\Delta r}\right)p_{i+1}^{v,t}-\left[\rho_f^v\kappa^v+\alpha^v\left(\frac{\Delta t}{2}\right)\right]\left(\frac{1}{2\Delta r}\right)u_{i-1}^{t-1}$$

$$+\left[\rho_f^v\kappa^v+\alpha^v\left(\frac{\Delta t}{2}\right)\right]\left(\frac{2}{r_i}\right)u_i^{t-1}+\left[\rho_f^v\kappa^v+\alpha^v\left(\frac{\Delta t}{2}\right)\right]\left(\frac{1}{2\Delta r}\right)u_{i+1}^{t-1}$$

$$+\Delta t^2\overline{s}_{v\to c}+\Delta t^2\overline{s}_{v\to l} \tag{3.78a}$$

For the first time step, we use $u_i^{-1}=u_i^1-2\Delta tV_r^0$, Eqn. (3.45b), and Eqn. (3.73c) to substitute into and Eqn. (3.78a),

$$2\rho_f^v\kappa^v\left(\frac{1}{2\Delta r}\right)u_{i-1}^1-2\rho_f^v\kappa^v\left(\frac{2}{r_i}\right)u_i^1-2\rho_f^v\kappa^v\left(\frac{1}{2\Delta r}\right)u_{i+1}^1-\left(\frac{1}{2}\right)\Delta t^2\kappa^v\left(\frac{1}{\Delta r^2}-\frac{1}{r_i\Delta r}\right)p_{i-1}^{v,1}$$

$$+\left[\Delta tS_\varepsilon^v+\left(\frac{1}{2}\right)\Delta t^2\kappa^v\left(\frac{2}{\Delta r^2}\right)\right]p_i^{v,1}-\left(\frac{1}{2}\right)\Delta t^2\kappa^v\left(\frac{1}{\Delta r^2}+\frac{1}{r_i\Delta r}\right)p_{i+1}^{v,1}=$$

$$+\rho_f^v\kappa^v\left(\frac{1}{\Delta r}\right)u_{i-1}^0-\rho_f^v\kappa^v\left(\frac{4}{r_i}\right)u_i^0-\rho_f^v\kappa^v\left(\frac{1}{\Delta r}\right)u_{i+1}^0+\left(\frac{1}{2}\right)\Delta t^2\kappa^v\left(\frac{1}{\Delta r^2}-\frac{1}{r_i\Delta r}\right)p_{i-1}^{v,0}$$

$$+\left[\Delta tS_\varepsilon^v-\left(\frac{1}{2}\right)\Delta t^2\kappa^v\left(\frac{2}{\Delta r^2}\right)\right]p_i^{v,0}+\left(\frac{1}{2}\right)\Delta t^2\kappa^v\left(\frac{1}{\Delta r^2}+\frac{1}{r_i\Delta r}\right)p_{i+1}^{v,0}$$

$$+\Delta t^2\overline{s}_{v\to c}+\Delta t^2\overline{s}_{v\to l} \tag{3.78b}$$

3.3.6.5 CSF Pressure

Taking Eqn. (3.67e) and using the same process from Eqn. (3.75) to Eqn. (3.76a), we have the nodal values

$$\left[\rho_f^e\kappa^e-\alpha^e\left(\frac{\Delta t}{2}\right)\right]\left(\frac{1}{2\Delta r}\right)u_{i-1}^{t+1}-\left[\rho_f^e\kappa^e-\alpha^e\left(\frac{\Delta t}{2}\right)\right]\left(\frac{2}{r_i}\right)u_i^{t+1}$$

$$-\left[\rho_f^e\kappa^e-\alpha^e\left(\frac{\Delta t}{2}\right)\right]\left(\frac{1}{2\Delta r}\right)u_{i+1}^{t+1}$$

$$-\left(\frac{1}{2}\right)\Delta t^2\kappa^e\left(\frac{1}{\Delta r^2}-\frac{1}{r_i\Delta r}\right)p_{i-1}^{e,t+1}+\left[\Delta tS_\varepsilon^e+\left(\frac{1}{2}\right)\Delta t^2\kappa^e\left(\frac{2}{\Delta r^2}\right)\right]p_i^{e,t+1}$$

$$-\left(\frac{1}{2}\right)\Delta t^2\kappa^e\left(\frac{1}{\Delta r^2}+\frac{1}{r_i\Delta r}\right)p_{i+1}^{e,t+1}=\rho_f^e\kappa^e\left(\frac{1}{\Delta r}\right)u_{i-1}^t-\rho_f^e\kappa^e\left(\frac{4}{r_i}\right)u_i^t-\rho_f^e\kappa^e\left(\frac{1}{\Delta r}\right)u_{i+1}^t$$

$$+\left(\frac{1}{2}\right)\Delta t^2\kappa^e\left(\frac{1}{\Delta r^2}-\frac{1}{r_i\Delta r}\right)p_{i-1}^{e,t}+\left[\Delta tS_\varepsilon^e-\left(\frac{1}{2}\right)\Delta t^2\kappa^e\left(\frac{2}{\Delta r^2}\right)\right]p_i^{e,t}$$

$$+\left(\frac{1}{2}\right)\Delta t^2\kappa^e\left(\frac{1}{\Delta r^2}+\frac{1}{r_i\Delta r}\right)p_{i+1}^{e,t}-\left[\rho_f^e\kappa^e+\alpha^e\left(\frac{\Delta t}{2}\right)\right]\left(\frac{1}{2\Delta r}\right)u_{i-1}^{t-1}$$

$$+\left[\rho_f^e\kappa^e+\alpha^e\left(\frac{\Delta t}{2}\right)\right]\left(\frac{2}{r_i}\right)u_i^{t-1}+\left[\rho_f^e\kappa^e+\alpha^e\left(\frac{\Delta t}{2}\right)\right]\left(\frac{1}{2\Delta r}\right)u_{i+1}^{t-1}$$

$$+\Delta t^2\overline{S}_{e\to g}+\Delta t^2\overline{S}_{e\to l} \tag{3.79a}$$

For the first time step, we use $u_i^{-1}=u_i^1-2\Delta tV_r^0$, Eqn. (3.45b), and Eqn. (3.73d) to substitute into and Eqn. (3.79a),

$$2\rho_f^e\kappa^e\left(\frac{1}{2\Delta r}\right)u_{i-1}^1-2\rho_f^e\kappa^e\left(\frac{2}{r_i}\right)u_i^1-2\rho_f^e\kappa^e\left(\frac{1}{2\Delta r}\right)u_{i+1}^1-\left(\frac{1}{2}\right)\Delta t^2\kappa^e\left(\frac{1}{\Delta r^2}-\frac{1}{r_i\Delta r}\right)p_{i-1}^{e,1}$$

$$+\left[\Delta tS_\varepsilon^e+\left(\frac{1}{2}\right)\Delta t^2\kappa^e\left(\frac{2}{\Delta r^2}\right)\right]p_i^{e,1}-\left(\frac{1}{2}\right)\Delta t^2\kappa^e\left(\frac{1}{\Delta r^2}+\frac{1}{r_i\Delta r}\right)p_{i+1}^{e,1}=$$

$$+\rho_f^e\kappa^e\left(\frac{1}{\Delta r}\right)u_{i-1}^0-\rho_f^e\kappa^e\left(\frac{4}{r_i}\right)u_i^0-\rho_f^e\kappa^e\left(\frac{1}{\Delta r}\right)u_{i+1}^0+\left(\frac{1}{2}\right)\Delta t^2\kappa^e\left(\frac{1}{\Delta r^2}-\frac{1}{r_i\Delta r}\right)p_{i-1}^{e,0}$$

$$+\left[\Delta tS_\varepsilon^e-\left(\frac{1}{2}\right)\Delta t^2\kappa^e\left(\frac{2}{\Delta r^2}\right)\right]p_i^{e,0}+\left(\frac{1}{2}\right)\Delta t^2\kappa^e\left(\frac{1}{\Delta r^2}+\frac{1}{r_i\Delta r}\right)p_{i+1}^{e,0}$$

$$+\Delta t^2\overline{s}_{e\to g}+\Delta t^2\overline{s}_{e\to l} \tag{3.79b}$$

3.3.6.6 Perivascular space/Glymphatic system Pressure

Taking Eqn. (3.67f) and using the same process from Eqn. (3.75) to Eqn. (3.76a), we have the nodal values

$$\left[\rho_f^l\kappa^l-\alpha^l\left(\frac{\Delta t}{2}\right)\right]\left(\frac{1}{2\Delta r}\right)u_{i-1}^{t+1}-\left[\rho_f^l\kappa^l-\alpha^l\left(\frac{\Delta t}{2}\right)\right]\left(\frac{2}{r_i}\right)u_i^{t+1}$$

$$-\left[\rho_f^l\kappa^l-\alpha^l\left(\frac{\Delta t}{2}\right)\right]\left(\frac{1}{2\Delta r}\right)u_{i+1}^{t+1}$$

$$-\left(\frac{1}{2}\right)\Delta t^2\kappa^l\left(\frac{1}{\Delta r^2}-\frac{1}{r_i\Delta r}\right)p_{i-1}^{l,t+1}+\left[\Delta tS_\varepsilon^l+\left(\frac{1}{2}\right)\Delta t^2\kappa^l\left(\frac{2}{\Delta r^2}\right)\right]p_i^{l,t+1}$$

$$-\left(\frac{1}{2}\right)\Delta t^2\kappa^l\left(\frac{1}{\Delta r^2}+\frac{1}{r_i\Delta r}\right)p_{i+1}^{l,t+1}=\rho_f^l\kappa^l\left(\frac{1}{\Delta r}\right)u_{i-1}^t-\rho_f^l\kappa^l\left(\frac{4}{r_i}\right)u_i^t-\rho_f^l\kappa^l\left(\frac{1}{\Delta r}\right)u_{i+1}^t$$

$$+\left(\frac{1}{2}\right)\Delta t^2\kappa^l\left(\frac{1}{\Delta r^2}-\frac{1}{r_i\Delta r}\right)p_{i-1}^{l,t}+\left[\Delta tS_\varepsilon^l-\left(\frac{1}{2}\right)\Delta t^2\kappa^l\left(\frac{2}{\Delta r^2}\right)\right]p_i^{l,t}$$

$$+\left(\frac{1}{2}\right)\Delta t^2\kappa^l\left(\frac{1}{\Delta r^2}+\frac{1}{r_i\Delta r}\right)p_{i+1}^{l,t}-\left[\rho_f^l\kappa^l+\alpha^l\left(\frac{\Delta t}{2}\right)\right]\left(\frac{1}{2\Delta r}\right)u_{i-1}^{t-1}$$

$$+\left[\rho_f^l\kappa^l+\alpha^l\left(\frac{\Delta t}{2}\right)\right]\left(\frac{2}{r_i}\right)u_i^{t-1}+\left[\rho_f^l\kappa^l+\alpha^l\left(\frac{\Delta t}{2}\right)\right]\left(\frac{1}{2\Delta r}\right)u_{i+1}^{t-1}$$

$$+\Delta t^2\overline{s}_{l\to a}+\Delta t^2\overline{s}_{l\to c}+\Delta t^2\overline{s}_{l\to v}+\Delta t^2\overline{s}_{l\to e}+\Delta t^2\overline{s}_{l\to g} \tag{3.80a}$$

For the first time step, we use $u_i^{-1}=u_i^1-2\Delta tV_r^0$, Eqn. (3.45b), and Eqn. (3.73e) to substitute into and Eqn. (3.80a),

$$2\rho_f^l\kappa^l\left(\frac{1}{2\Delta r}\right)u_{i-1}^1-2\rho_f^l\kappa^l\left(\frac{2}{r_i}\right)u_i^1-2\rho_f^l\kappa^l\left(\frac{1}{2\Delta r}\right)u_{i+1}^1-\left(\frac{1}{2}\right)\Delta t^2\kappa^l\left(\frac{1}{\Delta r^2}-\frac{1}{r_i\Delta r}\right)p_{i-1}^{l,1}$$

$$+\left[\Delta tS_\varepsilon^l+\left(\frac{1}{2}\right)\Delta t^2\kappa^l\left(\frac{2}{\Delta r^2}\right)\right]p_i^{l,1}-\left(\frac{1}{2}\right)\Delta t^2\kappa^l\left(\frac{1}{\Delta r^2}+\frac{1}{r_i\Delta r}\right)p_{i+1}^{l,1}=$$

$$+\rho_f^l\kappa^l\left(\frac{1}{\Delta r}\right)u_{i-1}^0-\rho_f^l\kappa^l\left(\frac{4}{r_i}\right)u_i^0-\rho_f^l\kappa^l\left(\frac{1}{\Delta r}\right)u_{i+1}^0+\left(\frac{1}{2}\right)\Delta t^2\kappa^l\left(\frac{1}{\Delta r^2}-\frac{1}{r_i\Delta r}\right)p_{i-1}^{l,0}$$

$$+\left[\Delta tS_\varepsilon^l-\left(\frac{1}{2}\right)\Delta t^2\kappa^l\left(\frac{2}{\Delta r^2}\right)\right]p_i^{l,0}+\left(\frac{1}{2}\right)\Delta t^2\kappa^l\left(\frac{1}{\Delta r^2}+\frac{1}{r_i\Delta r}\right)p_{i+1}^{l,0}$$

$$+\Delta t^2\overline{s}_{l\to a}+\Delta t^2\overline{s}_{l\to c}+\Delta t^2\overline{s}_{l\to v}+\Delta t^2\overline{s}_{l\to e}+\Delta t^2\overline{s}_{l\to g} \tag{3.80b}$$

3.3.6.7 Glial Cells Pressure

Taking Eqn. (3.67g) and using the same process from Eqn. (3.75) to Eqn. (3.76a), we have the nodal values

$$\left[\rho_f^g\kappa^g-\alpha^g\left(\frac{\Delta t}{2}\right)\right]\left(\frac{1}{2\Delta r}\right)u_{i-1}^{t+1}-\left[\rho_f^g\kappa^g-\alpha^g\left(\frac{\Delta t}{2}\right)\right]\left(\frac{2}{r_i}\right)u_i^{t+1}$$

$$-\left[\rho_f^g\kappa^g-\alpha^g\left(\frac{\Delta t}{2}\right)\right]\left(\frac{1}{2\Delta r}\right)u_{i+1}^{t+1}$$

$$-\left(\frac{1}{2}\right)\Delta t^2\kappa^g\left(\frac{1}{\Delta r^2}-\frac{1}{r_i\Delta r}\right)p_{i-1}^{g,t+1}+\left[\Delta tS_\varepsilon^g+\left(\frac{1}{2}\right)\Delta t^2\kappa^g\left(\frac{2}{\Delta r^2}\right)\right]p_i^{g,t+1}$$

$$-\left(\frac{1}{2}\right)\Delta t^2\kappa^g\left(\frac{1}{\Delta r^2}+\frac{1}{r_i\Delta r}\right)p_{i+1}^{g,t+1}=\rho_f^g\kappa^g\left(\frac{1}{\Delta r}\right)u_{i-1}^t-\rho_f^g\kappa^g\left(\frac{4}{r_i}\right)u_i^t-\rho_f^g\kappa^g\left(\frac{1}{\Delta r}\right)u_{i+1}^t$$

$$+\left(\frac{1}{2}\right)\Delta t^2\kappa^g\left(\frac{1}{\Delta r^2}-\frac{1}{r_i\Delta r}\right)p_{i-1}^{g,t}+\left[\Delta tS_\varepsilon^g-\left(\frac{1}{2}\right)\Delta t^2\kappa^g\left(\frac{2}{\Delta r^2}\right)\right]p_i^{g,t}$$

$$+\left(\frac{1}{2}\right)\Delta t^2\kappa^g\left(\frac{1}{\Delta r^2}+\frac{1}{r_i\Delta r}\right)p_{i+1}^{g,t}-\left[\rho_f^g\kappa^g+\alpha^g\left(\frac{\Delta t}{2}\right)\right]\left(\frac{1}{2\Delta r}\right)u_{i-1}^{t-1}$$

$$+\left[\rho_f^g\kappa^g+\alpha^g\left(\frac{\Delta t}{2}\right)\right]\left(\frac{2}{r_i}\right)u_i^{t-1}+\left[\rho_f^g\kappa^g+\alpha^g\left(\frac{\Delta t}{2}\right)\right]\left(\frac{1}{2\Delta r}\right)u_{i+1}^{t-1}$$

$$+\Delta t^2\overline{s}_{g\to e}+\Delta t^2\overline{s}_{g\to l} \tag{3.81a}$$

For the first time step, we use $u_i^{-1}=u_i^1-2\Delta t V_r^0$, Eqn. (3.45b), and Eqn. (3.73f) to substitute into and Eqn. (3.81a),

$$2\rho_f^g\kappa^g\left(\frac{1}{2\Delta r}\right)u_{i-1}^1-2\rho_f^g\kappa^g\left(\frac{2}{r_i}\right)u_i^1-2\rho_f^g\kappa^g\left(\frac{1}{2\Delta r}\right)u_{i+1}^1-\left(\frac{1}{2}\right)\Delta t^2\kappa^g\left(\frac{1}{\Delta r^2}-\frac{1}{r_i\Delta r}\right)p_{i-1}^{g,1}$$

$$+\left[\Delta tS_\varepsilon^g+\left(\frac{1}{2}\right)\Delta t^2\kappa^g\left(\frac{2}{\Delta r^2}\right)\right]p_i^{g,1}-\left(\frac{1}{2}\right)\Delta t^2\kappa^g\left(\frac{1}{\Delta r^2}+\frac{1}{r_i\Delta r}\right)p_{i+1}^{g,1}=$$

$$+\rho_f^g\kappa^g\left(\frac{1}{\Delta r}\right)u_{i-1}^0-\rho_f^g\kappa^g\left(\frac{4}{r_i}\right)u_i^0-\rho_f^g\kappa^g\left(\frac{1}{\Delta r}\right)u_{i+1}^0+\left(\frac{1}{2}\right)\Delta t^2\kappa^g\left(\frac{1}{\Delta r^2}-\frac{1}{r_i\Delta r}\right)p_{i-1}^{g,0}$$

$$+\left[\Delta tS_\varepsilon^g-\left(\frac{1}{2}\right)\Delta t^2\kappa^g\left(\frac{2}{\Delta r^2}\right)\right]p_i^{g,0}+\left(\frac{1}{2}\right)\Delta t^2\kappa^g\left(\frac{1}{\Delta r^2}+\frac{1}{r_i\Delta r}\right)p_{i+1}^{g,0}$$

$$+\Delta t^2\overline{s}_{g\to e}+\Delta t^2\overline{s}_{g\to l} \tag{3.81b}$$

3.3.6.8 Discretised Boundary Conditions at the Ventricular Wall

Eqn. (3.79) becomes,

$$(1-\nu)\frac{-3u_1^{t+1}+4u_2^{t+1}-u_3^{t+1}}{2\Delta r}+2\nu\frac{u_1^{t+1}}{r_1}-\frac{1-2\nu}{2G}\left[\left(\alpha^a-1\right)p_1^{a,t+1}+\left(\alpha^c-1\right)p_1^{c,t+1}\right.$$

$$\left.+\left(\alpha^v-1\right)p_1^{v,t+1}+\left(\alpha^e-1\right)p_1^{e,t+1}+\left(\alpha^l-1\right)p_1^{l,t+1}+\left(\alpha^g-1\right)p_1^{g,t+1}\right]=0,$$

Simplified as,

$$\left[\frac{2\nu}{r_1}-\frac{3(1-\nu)}{2\Delta r}\right]u_1^{t+1}+\frac{2(1-\nu)}{\Delta r}u_2^{t+1}-\frac{(1-\nu)}{2\Delta r}u_3^{t+1}-\frac{(\alpha^a-1)(1-2\nu)}{2G}p_1^{a,t+1}$$

$$-\frac{(\alpha^c-1)(1-2\nu)}{2G}p_1^{c,t+1}-\frac{(\alpha^v-1)(1-2\nu)}{2G}p_1^{v,t+1}-\frac{(\alpha^e-1)(1-2\nu)}{2G}p_1^{e,t+1}$$

$$-\frac{(\alpha^l-1)(1-2\nu)}{2G}p_1^{l,t+1}-\frac{(\alpha^g-1)(1-2\nu)}{2G}p_1^{g,t+1}=0 \qquad (3.82)$$

Eqn. (3.38) becomes,

$$\frac{-3p_1^{c,t+1}+4p_2^{c,t+1}-p_3^{c,t+1}}{2\Delta r}=\frac{Q_{prod}}{R_{cp}^c},$$

and simplified as,

$$-\frac{3}{2}p_1^{c,t+1}+2p_2^{c,t+1}-\frac{1}{2}p_3^{c,t+1}=\frac{Q_{prod}}{R_{c\to vent}^{CP}}\Delta r \qquad (3.83)$$

Eqn. (3.39a) becomes,

$$\frac{-3p_1^{a,t+1}+4p_2^{a,t+1}-p_3^{a,t+1}}{2\Delta r}=0,$$

and simplified as,

$$-\frac{3}{2}p_1^{a,t+1}+2p_2^{a,t+1}-\frac{1}{2}p_3^{a,t+1}=0 \qquad (3.84)$$

Eqn. (3.39b) becomes,

$$\frac{-3p_1^{v,t+1}+4p_2^{v,t+1}-p_3^{v,t+1}}{2\Delta r}=0,$$

and simplified as,

$$-\frac{3}{2}p_1^{v,t+1}+2p_2^{v,t+1}-\frac{1}{2}p_3^{v,t+1}=0 \tag{3.85}$$

Eqn. (3.40) becomes,

$$\frac{\pi d^4}{128\mu^e L}\left(p_1^{e,t+1}-p_N^{e,t+1}\right)-4\pi\kappa^e\left(r_1+u_1^t\right)^2\frac{-3p_1^{e,t+1}+4p_2^{e,t+1}-p_3^{e,t+1}}{2\Delta r}$$

$$+4\pi\left(r_1+u_1^t\right)^2\frac{u_1^{t+1}-u_1^{t-1}}{2\Delta t}=Q_{prod}$$

and simplified as,

$$\frac{1}{2}4\pi\left(r_1+u_1^t\right)^2u_1^{t+1}+\Delta t\left[\frac{\pi d^4}{128\mu^e L}+\frac{4\pi\left(r_1+u_1^t\right)^2\kappa^e}{\Delta r}\left(\frac{3}{2}\right)\right]p_1^{e,t+1}$$

$$-\Delta t\frac{4\pi\left(r_1+u_1^t\right)^2\kappa^e}{\Delta r}\left(\frac{4}{2}\right)p_2^{e,t+1}+\Delta t\frac{4\pi\left(r_1+u_1^t\right)^2\kappa^e}{\Delta r}\left(\frac{1}{2}\right)p_3^{e,t+1}-\Delta t\frac{\pi d^4}{128\mu^e L}p_N^{e,t+1}$$

$$=\Delta tQ_{prod}+\frac{1}{2}4\pi\left(r_1+u_1^t\right)^2u_1^{t-1} \tag{3.86a}$$

For the first time step, we use $u_i^{-1}=u_i^1-2\Delta tV_r^0$, Eqn. (3.45a) and Eqn. (3.45b) to substitute into Eqn. (3.57a),

$$4\pi r_1^2 u_1^1 + \Delta t\left[\frac{\pi d^4}{128\mu^e L} + \frac{4\pi r^2\kappa^e}{\Delta r}\left(\frac{3}{2}\right)\right] p_1^{e,1}$$

$$-\Delta t\frac{4\pi r_1^2\kappa^e}{\Delta r}\left(\frac{4}{2}\right) p_2^{e,1} + \Delta t\frac{4\pi r_1^2\kappa^e}{\Delta r}\left(\frac{1}{2}\right) p_3^{e,1} - \Delta t\frac{\pi d^4}{128\mu^e L}\, p_N^{e,1} = \Delta t Q_{prod} \qquad (3.86b)$$

Eqn. (3.68) becomes,

$$\frac{-3p_1^{l,t+1} + 4p_2^{l,t+1} - p_3^{l,t+1}}{2\Delta r} = 0,$$

and simplified as,

$$-\frac{3}{2}p_1^{l,t+1} + 2p_2^{l,t+1} - \frac{1}{2}p_3^{l,t+1} = 0 \qquad (3.87)$$

Eqn. (3.69) becomes,

$$p_1^{g,t+1} = \frac{p_1^{e,t+1}}{\alpha^g} + \frac{2G^g}{\alpha^g}\left(\frac{1-\nu^g}{1-2\nu^g}\right)\frac{-3u_1^{t+1} + 4u_2^{t+1} - u_3^{t+1}}{2\Delta r} + \frac{2G^g}{\alpha^g}\left(\frac{2\nu^g}{1-2\nu^g}\right)\frac{u_1^{t+1}}{r_1},$$

and simplified as,

$$\frac{2G^g}{\alpha^g}\left[\frac{2\nu^g}{1-2\nu^g}\left(\frac{1}{r_1}\right) - \frac{1-\nu^g}{1-2\nu^g}\left(\frac{3}{2\Delta r}\right)\right]u_1^{t+1} + \frac{2G^g}{\alpha^g}\left(\frac{1-\nu^g}{1-2\nu^g}\right)\left(\frac{2}{\Delta r}\right)u_2^{t+1}$$

$$-\frac{2G^g}{\alpha^g}\left(\frac{1-\nu^g}{1-2\nu^g}\right)\left(\frac{1}{2\Delta r}\right)u_3^{t+1} + \frac{1}{\alpha^g}p_1^{e,t+1} - p_1^{g,t+1} = 0 \qquad (3.88)$$

3.3.6.9 Discretised Boundary Conditions at the Skull

Eqn. (3.41) and Eqns. (3.42a-b) becomes,

$$u_N^{t+1} = 0 \tag{3.89}$$

$$p_N^{a,t} = p_{ABL} \tag{3.90}$$

$$p_N^{v,t} = p_{VBL} \tag{3.91}$$

Eqn. (3.43) becomes,

$$\frac{3p_N^{c,t+1} - 4p_{N-1}^{c,t+1} + p_{N-2}^{c,t+1}}{2\Delta r} = 0,$$

and simplified as,

$$\frac{3}{2}p_N^{c,t+1} - 2p_{N-1}^{c,t+1} + \frac{1}{2}p_{N-2}^{c,t+1} = 0 \tag{3.92}$$

Eqn. (3.44) becomes,

$$p_N^{e,t+1} = p_{VBL} + \mu^e R_{abs}^{AG} Q_{out} \tag{3.93}$$

Eqn. (3.71) becomes,

$$p_N^{l,t} = p_{SAS} = p_{VBL} + \mu^e R_{abs}^{AG} Q_{out} \tag{3.94}$$

Eqn. (3.72) becomes,

$$\frac{3p_N^{g,t+1} - 4p_{N-1}^{g,t+1} + p_{N-2}^{g,t+1}}{2\Delta r} = 0,$$

and simplified as,

$$\frac{3}{2}p_N^{g,t+1} - 2p_{N-1}^{g,t+1} + \frac{1}{2}p_{N-2}^{g,t+1} = 0 \tag{3.95}$$

Finally, collecting the above discretised equations representations of the system is solved by the FORTRAN 90 solver (**Ax** = **b**, using the LU decomposition subroutine).

3.4 Parameter Estimation

In this section, the various parameters are used in 4MPET and 6MPET framework will be introduced. Values will be listed in Tables 3.1 and 3.2 as well. The majority of the parameters for the quasi-steady 4MPET model continue to be used in the fully dynamic version of the 4MPET model. For example, Tully (2010) had performed a careful large scale parametric estimation study on a high performance computing (HPC) facility using the quasi-static 4MPET framework. During this careful large scale parametric estimation study, some parameters within the 4MPET model are surveyed and studied in Tully's works [164, 233].

When the 6MPET model is extended from the 4MPET model, some overlapping compartments are directly employed from the parameters in the 4MPET such as arterial/arteriole compartment, capillary compartment, venous/venule compartment, and CSF compartment. The values of these parameters held by these overlapping compartments are directly recruited from the 4MPET model including total density (ρ), fluid density ($\rho^a, \rho^c, \rho^v, \rho^e$), specific storage coefficient ($S_\varepsilon^a, S_\varepsilon^c, S_\varepsilon^v, S_\varepsilon^e$), shear modulus ($G$), Poisson's ratio ($\nu$), Biot-Willis coefficient ($\alpha^a, \alpha^c, \alpha^v, \alpha^e$), transfer coefficient (γ_{ac}, γ_{cv}) and mobility ($\kappa^a, \kappa^c, \kappa^v, \kappa^e$). Besides, the values of the parameters in the two extra compartments including glial cells compartment and glymphatic system/PVS/ISF compartment in the 6MPET model, such as porosity ($\phi^a, \phi^c, \phi^v, \phi^e, \phi^g, \phi^l$), mobility

(κ^g, κ^l), and transfer coefficient ($\gamma_{al}, \gamma_{cl}, \gamma_{vl}, \gamma_{el}, \gamma_{gl}, \gamma_{eg}$), are considered by the assumptions and some other research works. Regarding the porosity of the two extra compartments, e.g. glial cells compartment and glymphatic system/PVS/ISF compartment, in the 6MPET model, the values are assumed and described in the section 4.3.2 and shown in Table 3.2. For the values of the mobility of the two extra compartments, e.g. glial cells compartment and glymphatic system/PVS/ISF compartment, in the 6MPET model, they will be explained and shown in the section 3.4.2 and Table 3.2, respectively. The transfer coefficients of the two extra compartments, e.g. glial cells compartment and glymphatic system/PVS/ISF compartment, in the 6MPET model are shown in Table 3.2 and the related parameters that are derivable from Eqn. (3.65) are discussed in the section 3.4.3.

One of the contributions in the 6MPET model is that AQP expression levels are controllable via the scaling factor, RF_{AQP}, of the glial cells and the PVS/glymphatic system compartment. The parameter sensitivity analysis is shown in Figure 3.5. This figure depicts the open and severe aqueductal stenosis regarding the varying Biot-Willis constants (compliance: α^c, $\alpha^l$and α^g) with the simultaneous variation in the scaling factor, RF_{AQP}. For the severe aqueductal stenosis (LHS of Figure 3.5), it shows that the largest variation (red curve) occurs when given the larger compliance of the glial cells compartment ($\alpha^g = 0.8$) and given the more AQP deficient expression of the glial cells compartmental ($RF_{AQP} = 10.0$) in the fully dynamic 6MPET model. Meanwhile, when the compliance of the capillary compartment is 0.95 and the AQP scaling factor in the PVS/glymphatic system compartment is 10.0 (more deficient expression), the result (blue curve) displays ventriculomegaly reoccurring after 60 hours.

Regarding the patent aqueduct in the RHS of Figure 3.5, the blue line continues increasing the amount of the compliance of the capillary compartment given 0.95 and the AQP deficient expression in the PVS/glymphatic system compartment given 10.0 ($RF_{AQP} = 10.0$). The setting conditions are the same as that of the severely stenosed aqueduct (blue, LHS of Figure 3.5) but are similar to each other (the largest variation in the compared group). Moreover, if the green curve is given by the AQP overexpression condition till one order magnitude reducing the scaling factor ($RF_{AQP} = 0.1$) in the same case, it is larger than others besides blue curve. Hence, the compliance of the capillary compartment in the fully dynamic 6MPET model should be very sensitive according to the analysis of both cases.

3.4.1 Cerebral Geometry

The radii of the agglomerated ventricular spaces (r_v) and the skull (r_s) are applied from several studies [233, 255, 265, 374, 375]. These radii roughly correspond to values expected for the adult human brain. The parameter of the trans-parenchymal region, *L*, is the difference between the radius of ventricle and skull. Based on our model assumptions, it represents the length of the cerebral aqueduct as well. The parameter, *d*, is the diameter of the cerebral aqueduct. Later, various diameters for this cerebral aqueduct will be considered to represent the varying levels of the obstructive cerebral aqueduct stenosis (obstructive hydrocephalus progression), such as atresia (complete obstruction), severe (severe obstruction), moderate (mild obstruction) and open (health, without obstruction) [233, 265, 269, 303].

3.4.2 Poroelastic Constants

Poisson's ratio value is adopted from Kaczmarek, et al. [252], and Taylor and Miller [376]. The value of Young's modulus is taken from Taylor and Miller because they studied the cerebromechanical properties focusing on HCP simulations [376]. Since the MPET system is assumed to describe a linear homogeneous isotropic material of the porous parenchyma, the elastic moduli, bulk modulus, Young's modulus, shear modulus, Poisson's ratio and Lame's parameter (λ), can be determined by any two moduli among these. Therefore, the shear modulus can be obtained from Young's modulus and Poisson's ratio via linear relationship, $G = E/2(1 + \nu)$. Regarding the total density in MPET, once each compartmental fluid density [377-379] and parenchymal solid density [377] are obtained, it will be able to present via Eqn. (3.31). For the porosities of the compartment, Tully et al. assumed they have the same value, 0.2 [233, 303]. However, this assumption is not satisfied with 6MPET, due to the summation of the six compartments is larger than unity ($6 \times 0.2 > 1$). Hence, we define the new six porosity values for 6MPET and validate these new porosity values in the next two chapters. The Biot-Willis parameter is considered in almost saturated condition. For the mobility in 4MPET model, the same four mobility coefficients are taken from the work of Tully et al. [233, 303]. The mobilities of the remaining two compartments, glymphatic system/perivascular space and glial cells, are obtained from $L_p^{\Omega}/\rho^{\Omega}g$, where L_p^{Ω} is the hydraulic conductivity of the Ω compartment, and $\rho^{\Omega}g$ is the unit weight of the Ω compartment. The parameter, L_p^l, is applied from Rosenberg et al. who measured the hydraulic conductivity of the ISF in the cat [120]. The parameter, L_p^g, is applied from Li et al. who measured the hydraulic conductivity from the endothelial and astrocyte cultures [380].

3.4.3 Coefficients in MPET Source Terms

The transfer coefficients in 4MPET are once again taken from Tully et al. as computed via a careful large-scale parametric study on the high-performance computing (HPC) cluster [233, 303]. However, here we try to employ an alternative way, Eqn. (3.65), to get the transfer coefficients from experimental results and present the results via 6MPET. The hydraulic conductivity of the arterial compartment in 6MPET is obtained from Klanchar and Tarbell [381]. The hydraulic permeability of the capillary compartment in 6MPET is obtained from Mokhtarudin and Payne [268]. Since there are very few papers for venous related studies, values for the hydraulic permeability and hydraulic conductivity are scarce. Therefore, we use the mean value and apply this on the transfer coefficients of arterial and capillary. The justification of using the mean is that it is assumed that the value of the venous transfer coefficient will be between the transfer coefficients of the arterial and capillary. The hydraulic conductivity of the AQP4 is obtained from Gunnarson et al. [372, 382]. The surface-to-volume ratio of the arterial compartment is referred to Wright et al. who investigated brain arterial vasculature via magnetic resonance angiography (MRA) [383].

We also assume the surface-to-volume ratio of the venous compartment is same as the surface-to-volume ratio of the arterial compartment because of the aforementioned reason. For the surface-to-volume ratio of the capillary compartment, we consider the work of Lauwers et al. who studied the morphometry of the human cerebral cortex microcirculation [384]. Regarding the surface-to-volume ratios of the glymphatic system/perivascular space compartment and glial cells compartment, values are employed from Asgari et al. [244]. All of the values relating to the aforementioned parameters are shown in Table 3.2.

Para.	Value	Units	Ref.	Para.	Value	Units	Ref.
r_v	3.0×10^{-02}	m	[233, 255, 304, 375]	μ^{e}	8.9×10^{-04}	Nsm^{-2}	[164, 233, 255, 385]
r_s	1.0×10^{-01}	m	[233, 255, 304, 375]	$\mu^{a,\ c,\ v}$	2.7×10^{-03}	Nsm^{-2}	[164, 233]
L	7.0×10^{-02}	m	[233, 255, 304, 375]	ρ^{e}	1007.0	kgm^{-3}	[377]
d	4.0×10^{-03} 5.0×10^{-04} 2.5×10^{-04} 5.0×10^{-05}	m	[233, 255, 304, 375]	$\rho^{a,\ c,\ v}$	1060.0	kgm^{-3}	[378]
E	584.0	Nm^{-2}	[233, 255, 304, 375, 376]	γ_{ac}	1.5×10^{-19}	$m^2N^{-1}s^{-1}$	[164, 233]
v	0.35		[233, 260, 265, 303, 304, 386]	γ_{cv}	1.5×10^{-19}	$m^2N^{-1}s^{-1}$	[164, 233]
P_{ABL}	1.33×10^{4}	Nm^{-2}	[233, 255, 375, 385]	γ_{ce}	1.0×10^{-22}	$m^2N^{-1}s^{-1}$	[164, 233]
P_{VBL}	6.5×10^{2}	Nm^{-2}	[233, 255, 375, 385]	γ_{ev}	1.0×10^{-13}	$m^2N^{-1}s^{-1}$	[164, 233]
R_{abs}^{AG}	8.5×10^{13}	m^{-3}	[233, 255, 375, 385]	$\kappa^{a,\ c,\ v}$	3.7×10^{-08}	$m^4N^{-1}s^{-1}$	[161, 164, 233, 268]
$R_{c\rightarrow vent}^{CP}$	6.0×10^{-04}	$m^6N^{-1}s^{-1}$	[164, 233]	κ^{e}	1.6×10^{-11}	$m^4N^{-1}s^{-1}$	[233, 255, 304, 375]
Q_o	5.8×10^{-09}	m^3s^{-1}	[233, 255, 375, 385]	$S_{\varepsilon}^{a,c,v,e}$	4.5×10^{-07}	m^2N^{-1}	[161, 322]
Q_{prod}	5.8×10^{-09}	m^3s^{-1}	[233, 255, 375, 385]	$\phi^{a,c,v,e}$	0.2		[164, 233]

Table 3.1 List of the parameter values for 4MPET framework.

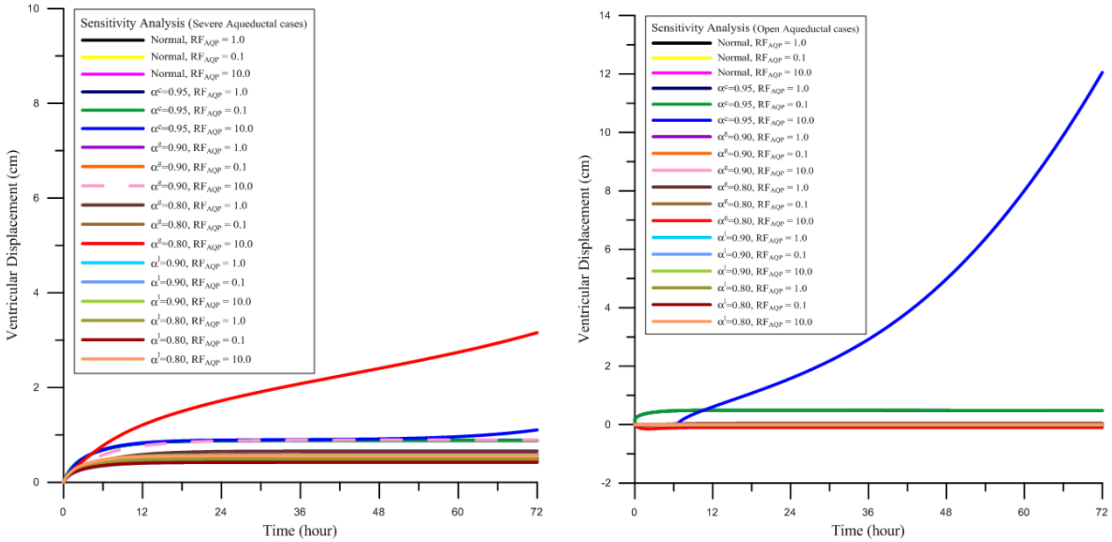


Figure 3.5 Parameters sensitivity for 6MPET by focusing on the compliances (e.g. α^c, $\alpha^l$and α^g) and AQP scaling factor (RF_{AQP}).

Para.	Value	Units	Ref.	Para.	Value	Units	Ref.
ρ^l	1000.0	kgm^{-3}	*	$S_\varepsilon^{l,g}$	4.5×10^{-07}	m^2N^{-1}	*
ρ^g	1150.0	kgm^{-3}	[379]	γ_{ac}, γ_{cv}	1.5×10^{-19}	$m^2N^{-1}s^{-1}$	**
κ^l	2.0×10^{-11}	$m^4N^{-1}s^{-1}$	[387]	γ_{al}	2.8×10^{-14}	$m^2N^{-1}s^{-1}$	**
κ^g	5.1×10^{-08}	$m^4N^{-1}s^{-1}$	[380]	γ_{cl}	7.4×10^{-12}	$m^2N^{-1}s^{-1}$	**
ϕ^a	0.1		*	γ_{vl}	4.5×10^{-13}	$m^2N^{-1}s^{-1}$	**
ϕ^c	0.1		*	γ_{el}	1.4×10^{-19}	$m^2N^{-1}s^{-1}$	**
ϕ^v	0.1		*	γ_{gl}	5.4×10^{-09}	$m^2N^{-1}s^{-1}$	**
ϕ^e	0.2		*	γ_{eg}	5.4×10^{-09}	$m^2N^{-1}s^{-1}$	**
ϕ^l	0.15		*	L_p^c	3.0×10^{-09}	cms^{-1} cmH_2O^{-1}	[268]
ϕ^g	0.15		*	L_p^g	1.4×10^{-07}	cms^{-1} cmH_2O^{-1}	[380]

* Assumed in this dissertation; ** Calculated by Eqn. (3.65)

Table 3.2 List of the parameter values for 6MPET framework.

Chapter 4 Obstructive Hydrocephalus

The Topic of this Chapter

This chapter will provide the quasi-steady state results from the 4MPET and 6MPET models, and compare these results in discretised schemes of varying order according to these two models. Tully et al. quasi-steady state representations in 4MPET will be utilised in this chapter to aid the validation of the in-house FORTRAN 90 code of the fully dynamic 4MPET version. The same validation principle will be applied to the fully dynamic 6MPET later on. Some validation results are shown in the last section. All of the validation being conducted, in addition to the research results presented, are based on obstructive hydrocephalus in the quasi-steady state.

4.1 Quasi-Static Four-Network MPET

Tully et al. utilised a realisation of a 4MPET model to study the CSF transport phenomena in the human brain [164]. They demonstrated the mathematical model of 4MPET and SPET (single network poroelastic theory) in their fully dynamic formulations, however, they used the quasi-static, discretised scheme to deal with research regarding the investigation of cerebral disorders of interest to that study [233, 265]. Here, it is necessary to duplicate the quasi-static 4MPET results in the FORTRAN 90 in-house code in order to confirm the consistency of the results from the C++ in-house code developed by Tully et al. [164, 233, 265, 303], but also show the simulation results based on the different order discretised schemes, such as the first and second order discretised schemes. It seems that the first order discretised scheme is sufficient to present the cerebral water transport disorder via 4MPET based on the aforementioned investigation. However, the second order discretisation scheme is still pursued in this thesis, since the simulation results maintain good consistency in space, from $N = 41$ to $N = 101$ and in time from $\Delta t = 0.01$ *sec* to $\Delta t = 10.0$ *sec* shown from Figure 4.7 to Figure

4.10 in the last section of this chapter. Additionally, since the second order discretisation scheme results of the quasi-static MPET model will be compared with the first order discretisation scheme results of the quasi-static MPET model in the last section, these comparisons suggest that utilising fewer nodal numbers (N = 61) and the larger time marching size (Δt = 10.0 *sec*) via the second order scheme for spatiotemporal discretisation has the same effect that Tully et al. proposed via the first order scheme for spatiotemporal discretised (N = 81, Δt = 0.01 *sec*) [164]. Computational efficiency and numerical consistency are demonstrated in the last section of this chapter as well.

Firstly, the first order discretisation scheme which is identical as that of Tully et al. is employed here to illustrate obstructive HCP in the quasi-steady state [164, 233, 265]. The different levels of aqueductal stenosis (i.e. $4.0 \times 10^{-3} m$, open aqueduct; $5.0 \times 10^{-4} m$, aqueductal moderate stenosis; $2.5 \times 10^{-4} m$, aqueductal severe stenosis; $5.0 \times 10^{-5} m$, aqueductal atresia) which cause obstructive HCP are shown in Figure 4.1, with the ventricular displacement (LHS) and CSF pressure (RHS). The results are proportional to the deterioration of the stenosis condition in the aqueduct of Sylvius. In Figure 4.1, the open cerebral aqueduct which represents the healthy case (blue line) shows that almost no ventricular displacement occurs at the ventricular wall (0.13 μm) and the ventricular CSF pressure keeps the same value (1088.8 *Pa*) as the applied Dirichlet condition during the entire time course. The moderate stenosis of the aqueduct of Sylvius results (green line) in ventricular displacement and CSF pressure in Figure 4.1 (0.40 *mm* and 1103.2 *Pa*, respectively) that are larger than that of the open aqueduct. The results of the severe aqueductal stenosis (red line) show the ventricular displacement and CSF pressure (0.45 *cm* and 1252.3 *Pa*, respectively) during the full development of the solution field. Additionally, the results of the case involving

aqueductal atresia (purple line) demonstrate the ventricular displacement and CSF pressure (1.06 *cm* and 1474.2 *Pa*, respectively) during the full development of the solution field.

Moreover, similar trends as in Figure 4.1 are shown in Figure 4.2, when the second order scheme is applied. Of course, the ventricular displacement and CSF pressure in Figure 4.1 are somewhat different to those in Figure 4.2, a result of the difference in order of the discretisation scheme; however, the differences are small. In Figure 4.2, atresia of the aqueduct of Sylvius has the largest ventricular displacement and CSF pressure (1.01 *cm* and 1471.0 *Pa*, respectively). Severe stenosis of the aqueduct of Sylvius gives rise to a ventricular displacement and CSF pressure of 0.43 *cm* and 1251.2 *Pa*, respectively. Moderate stenosis shows higher ventricular displacement and CSF pressure (0.38 *mm* and 1103.2 *Pa*, respectively) compared to the healthy case (blue line), but lower than the severe aqueductal stenosis case (red line).

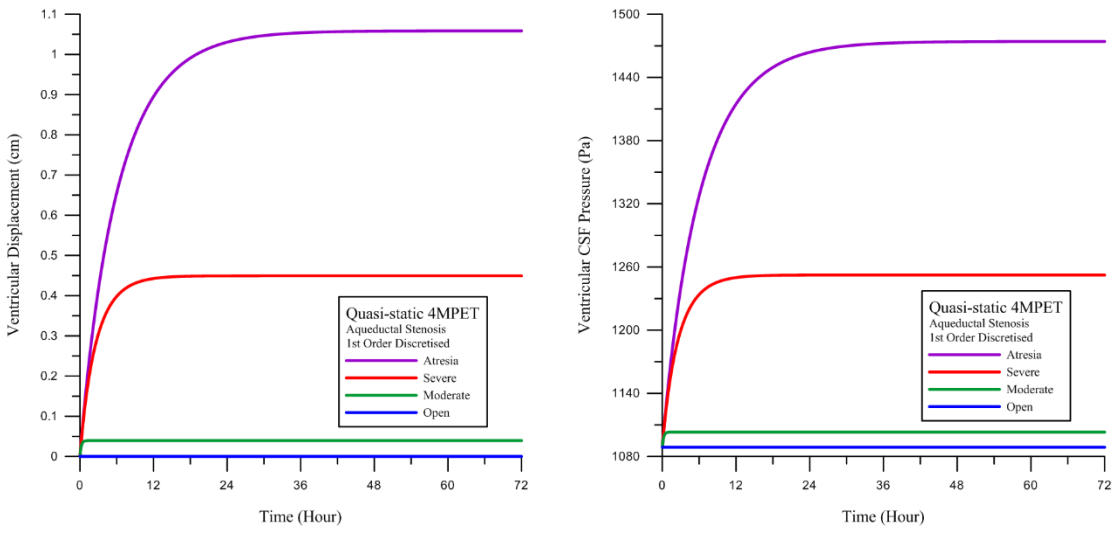


Figure 4.1 The first order discretised scheme of the quasi-static 4MPET model with aqueductal stenosis of varying levels. LHS: Ventricular displacement vs. time course; RHS: Ventricular CSF pressure vs. time course.

Hence, similar results of the ventricular displacement and CSF pressure are demonstrated in Figure 4.1 and 4.2. In the temporal analysis, both of Figure 4.1 and Figure 4.2 show the second order discretised scheme present with somewhat shorter time spans from initiation to full development, compared to that of the first order discretised scheme in all aqueductal stenosis cases of the quasi-static 4MPET model. Meanwhile, according to the varying progression of aqueductal stenosis (atresia, severe, and moderate levels of stenosis) in Figure 4.1 and 4.2, the more severe the stenosis, the more time is needed for the solution fields to arrive at the fully developed level.

The spatial analysis of parenchyma in the radial direction of the displacement and CSF pressure are demonstrated with the evolution of severe stenosis of the aqueduct of Sylvius utilising the second order discretised scheme (see Figure 4.3). The evolution of the parenchymal tissue displacement in the quasi-static 4MPET model does not change any more after 6 hours. This corresponds to the result of the severely stenosed case in Figure 4.2 because Figure 4.2 represents the severe stenosis results of the aqueduct of Sylvius at the ventricle wall (3 *cm*) in Figure 4.3. For the parenchymal tissue displacement in the LHS of Figure 4.3, the distribution of time evolution from 1 minute to 24 hours shows almost linear-like behaviour in the quasi-static 4MPET model. Comparing the parenchymal tissue displacement with the CSF/ECF pressure in Figure 4.3, the distributions of the temporal evolution of the solutions resembles nonlinear behaviour (curved line) for the CSF/ECF pressure in the RHS of Figure 4.3.

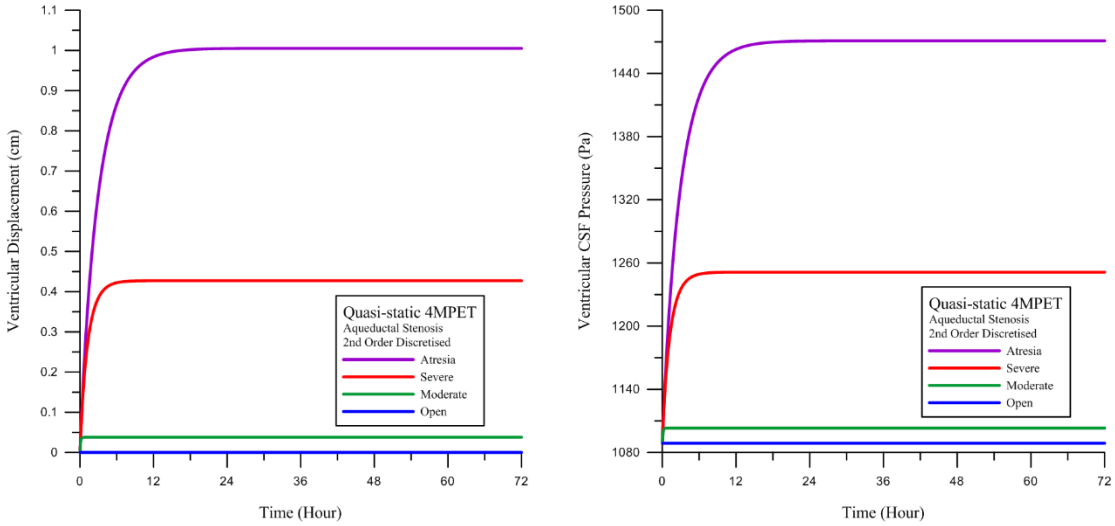


Figure 4.2 The second order discretised scheme on the quasi-static 4MPET model with aqueductal stenosis of varying level. LHS: Ventricular displacement vs. time course; RHS: Ventricular CSF pressure vs. time course.

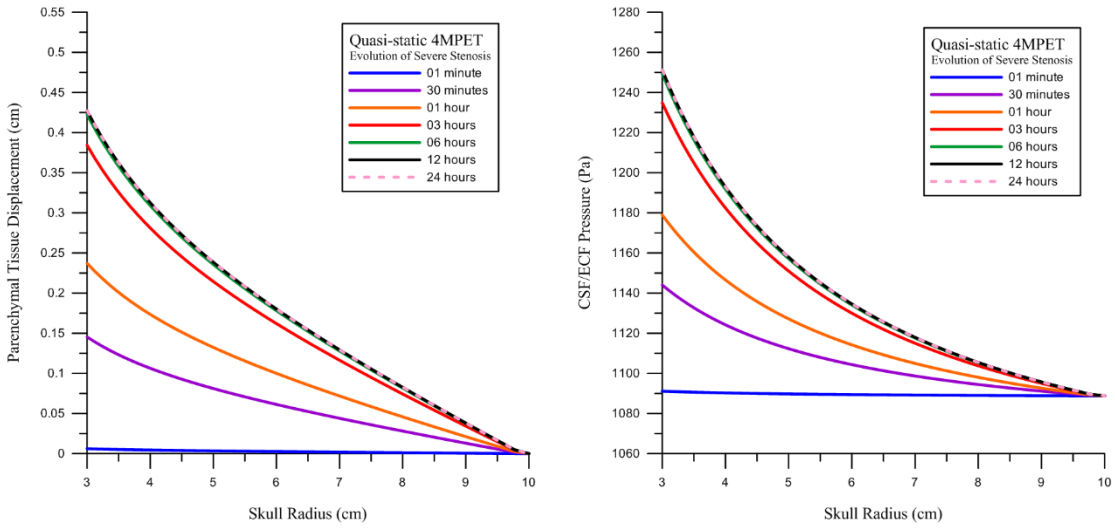


Figure 4.3 The evolution of severe stenosis of the aqueduct of Sylvius utilising the second order discretised scheme on the quasi-static 4MPET model. LHS: Parenchymal tissue displacement vs. skull radius; RHS: CSF/ECF pressure vs. skull radius.

4.2 Quasi-Static Six-Network MPET

In this section, both the results of the various level stenosis of the aqueduct of Sylvius (i.e. $4.0 \times 10^{-3}m$, open aqueduct; $5.0 \times 10^{-4}m$, aqueductal moderate stenosis; $2.5 \times 10^{-4}m$, aqueductal severe stenosis; $5.0 \times 10^{-5}m$, aqueductal atresia) at the ventricle wall and the evolution of the severe stenosis of the aqueduct of Sylvius in the quasi-static 6MPET model will be discussed.

Firstly, the first order discretised scheme of the quasi-static 6MPET model is applied and is shown in Figure 4.4. Although most of the results have a similar trend with the results from the quasi-static 4MPET model in Figure 4.1, there are two significant differences in Figure 4.4.

i. The time span of development (from start to fully development) for each curve (from aqueductal atresia to moderate stenosis) are longer than those in Figure 4.1. For example, the time span of development in the aqueductal atresia case shows quasi-static 4MPET is around 52% of quasi-static 6MPET. The time span of development in aqueductal stenosis (severe) case shows quasi-static 4MPET is around 50% of quasi-static 6MPET. Additionally, the time span of development in aqueductal stenosis (moderate) case shows quasi-static 4MPET is around 60% of quasi-static 6MPET.
ii. The levels of the ventricular displacement and CSF pressure during full development are higher than those in Figure 4.1. For example, the levels of ventricular displacement and ventricular CSF pressure during full development in aqueductal atresia case show during the full development in quasi-static 4MPET are around 73% and 94% of quasi-static 6MPET,

respectively. The amounts of ventricular displacement and CSF pressure during full development in aqueductal stenosis (severe) case show that during the full development in quasi-static 4MPET are around 82% and 98.8% of quasi-static 6MPET, respectively. Additionally, the amounts of ventricular displacement and CSF pressure during full development in aqueductal stenosis (moderate) case show during the full development in quasi-static 4MPET are around 87% and 99% of quasi-static 6MPET, respectively.

The results (purple line) of the atresia condition of the aqueduct of Sylvius in Figure 4.4 shows the largest ventricular displacement, and CSF, glial cells and ISF pressure are generated (1.45 cm; 1561.0 *Pa*, 1561.0 *Pa* and 1283.9 *Pa*, respectively) during the full development of the lumped ventricular system. In Figure 4.4, the open cerebral aqueduct which represents the healthy case (blue line) shows that almost no ventricular displacement occurs at the ventricular wall (14.3 μm), and the ventricular CSF, glial cells and ISF pressures keep the normal value (1088.8 *Pa*, 1088.8 *Pa*, 1089.6 *Pa*) during the entire time course. The moderate stenosis of the aqueduct of Sylvius results (green line) including the ventricular displacement, CSF, glial cells and ISF pressures in Figure 4.4 (0.46 *mm*; 1103.3 *Pa*, 1103.3 *Pa* and 1095.5 *Pa*, respectively) during the full development are larger than the open aqueduct compared with atresia and severe aqueductal stenosis. The results of the severe aqueductal stenosis (red line) including the ventricular displacement, CSF, glial cells and ISF pressure in Figure 4.4 (0.55 *cm*; 1267.8 *Pa*, 1267.8 *Pa* and 1162.8 *Pa*, respectively) during the full development are depicted between atresia and moderate aqueductal stenosis. In the 6MPET framework, the two additional compartments, glymphatic system/PVS/ISF and glial cells, have a similar trend with the CSF compartment in Figure 4.4. This is expected due to the

boundary conditions that were presented in the previous chapter. Moreover, these also correspond to phenomena of cerebral physiology for two reasons. Firstly, the glial cells are surrounded by CSF/ECF, so their pressures can be deemed as being – to a certain extent - at equilibrium in the steady state (especially given the lack of osmosis effects; a simplification we discussed before), and secondly, it is that the ISF pressure is proportional to the CSF pressure due to the same concept dictating glial cells and CSF (glymphatic system/PVS is surrounded by CSF/ECF).

The second order discretised scheme for the quasi-static 6MPET model has a similar trend with the results in Figure 4.2. The time span of the evolution of each curve (from aqueductal atresia to moderate stenosis) are longer than those in Figure 4.2. The amounts of the ventricular displacement and CSF pressure are also higher than those in Figure 4.2. Moreover, the results of the atresia condition of the aqueduct of Sylvius in Figure 4.5 show the largest ventricular displacement, CSF pressure, glial cells and ISF pressure are generated (1.38 cm, 1560.9 *Pa*, 1560.9 *Pa* and 1282.6 *Pa*, respectively) during the full development in the quasi-static 6MPET system. In Figure 4.5, the open cerebral aqueduct which represents the healthy case shows that almost no ventricular displacement occurs at the ventricle wall (13.5 μm), and the ventricular CSF, glial cells and ISF pressures keep their normal value (1088.8 *Pa*, 1088.8 *Pa*, 1089.6 *Pa*) during the entire time course of the simulatons. The moderate stenosis of the aqueduct of Sylvius generates a ventricular displacement, and CSF, glial cells and ISF pressure in Figure 4.5 (0.44 *mm*; 1103.3 *Pa*, 1103.3 *Pa* and 1095.5 *Pa*, respectively) during full development, and these values are larger than the open aqueduct. The results of the severe aqueductal stenosis include ventricular displacement, CSF pressure, glial cells pressure and ISF pressure in Figure 4.5 (0.52 *cm*; 1267.0 *Pa*, 1267.0 *Pa* and 1162.9 *Pa*, respectively) during full development are presented. The results relating to severe

stenosis are between those relating to the moderately stenosed and completely blocked aqueduct (aqueductal atresia).

Comparing Figure 4.4 and 4.5, the second order discretised scheme presents with lower and more consistent values (these are illustrated in the next section 4.3). For example, the ventricular displacement relating to the severely stenosed case in the second order discretised scheme (upper-LHS, Figure 4.5) is lower than the same case in the first order discretised scheme (upper-LHS, Figure 4.4) around 0.1 *cm*. The ventricular CSF pressure of the aforementioned stenosis severity in the second order discretised scheme (upper-RHS, Figure 4.5) is lower than the same case in the first order discretised scheme (upper-RHS, Figure 4.4) by approximately 7 *Pa*. The difference of the pressure of the glial cells is 8 *Pa*. The ISF pressure at the ventricle wall in the second order discretised scheme for severely stenosed case in the lower-RHS of Figure 4.5 is lower than the same case result of the first order discretised scheme (lower-RHS, Figure 4.4) by approximately 33 *Pa*.

Furthermore, comparing the first and second order discretised scheme in the quasi-static 6MPET model, it seems that the time span of the ventricular displacement and pressures (e.g. CSF, glial cells, and ISF) in the first order discretised scheme are longer than in the second order discretised scheme. This suggests that the second order discretised scheme is faster than the first order scheme in reaching the fully developed stage. This suggestion is consistent as that previously mentioned in the last section regarding the comparison of the first and second order discretised scheme in the quasi-static 4MPET model.

Finally, the evolution of severe stenosis of the aqueduct of Sylvius with the second order discretised scheme on the quasi-static 6MPET model are showed in Figure 4.6.

Figure 4.6 gives the variation of parenchymal tissue displacement and other compartmental pressures (e.g. CSF/ECF, glial cells and glymphatic system/PVS/ISF) in the radial direction. The curves of parenchymal tissue displacement (for the severely stenosed response) in the upper-LHS of Figure 4.6 has a temporally evolving sigmoidal characteristic resemblance in the quasi-static 6MPET model. This spatial variation is in contrast to the linear-like variation in the quasi-static 4MPET model (LHS, Figure 4.3). This implies that the quasi-static 6MPET model may be able to characterise more particularised variation of the parenchymal tissue displacement along the radial direction of the cerebral parenchyma than the quasi-static 4MPET model.

However, the distribution of the CSF/ECF pressure in the upper-RHS of Figure 4.6 has the similar pattern with the distribution of the CSF/ECF pressure in the RHS of Figure 4.3. This shows that the behaviour of the CSF/ECF pressure in the quasi-static 4MPET and 6MPET are similar, and a detailed discussion will be presented in the next chapter, the section 5.3. For the pressure of the glial cells along the radial direction of the cerebral parenchyma in the lower-LHS of Figure 4.6, the pressure remains constant throughout the parenchymal tissue, although the magnitude of this pressure does temporally evolve. The results in the lower-LHS quadrant of Figure 4.6 depict the spatially varying glial cells pressure. This family of curves arise as we do not consider effects of osmosis in the current setup (under given boundary conditions for 6MPET). Therefore, future work can be conducted in order to investigate the relationship between glial cells pressure and osmotic pressure in 6MPET.

The glymphatic system/PVS/ISF pressure along the radial direction of the cerebral parenchyma in the quasi-static 6MPET model (Lower-RHS, Figure 4.6) shows that the pressure temporally increases in the periventricular region, and then there is an overall

decrease in the vicinity of the skull. After six hours in the quasi-static 6MPET model, all of the curves reach a point of saturation, such as parenchymal tissue displacement, CSF/ECF pressure, glial cells pressure and glymphatic system/PVS/ISF pressure. The evolution of severe stenosis of the aqueduct of Sylvius with the second order discretisation scheme on the quasi-static 6MPET model are similar to the evolution of severe stenosis of the aqueduct of Sylvius with the second order discretisation scheme on the quasi-static 4MPET model. Hence, comparing results in quasi-static 4MPET and 6MPET, one can imply that the 6MPET model does not only keep the character of 4MPET, but also provides more information from two more compartments, glial cells and glymphatic system/PVS/ISF. 4MPET is considered the composition of water compartments in the cerebral environment as the CSF/ECF compartment and the remaining portion of the cerebrovascular compartments, e.g. arterial/arteriole, capillary and venous/venule. However, this is a general concept to separate the composition of water compartments in a brain. According to a very interesting article in *Trends in Neurosciences* in 2014, the reality under the current neurology understanding is that water in the brain is distributed into four distinct fluid compartments separated by specialised cellular barriers, i.e. the intracellular fluid (glial cells and neurons), ISF (glymphatic system/PVS), CSF, and cerebrovascular compartment [150]. Therefore, the extra two compartments of the 6MPET model are based on this newly concept to be particularly designed. This sophisticated 6MPET model is expected to probe the water transport phenomena in the human brain. The simulation results via 6MPET are demonstrated in chapter 4, 5 and 6 in order to show that 6MPET meets expectations.

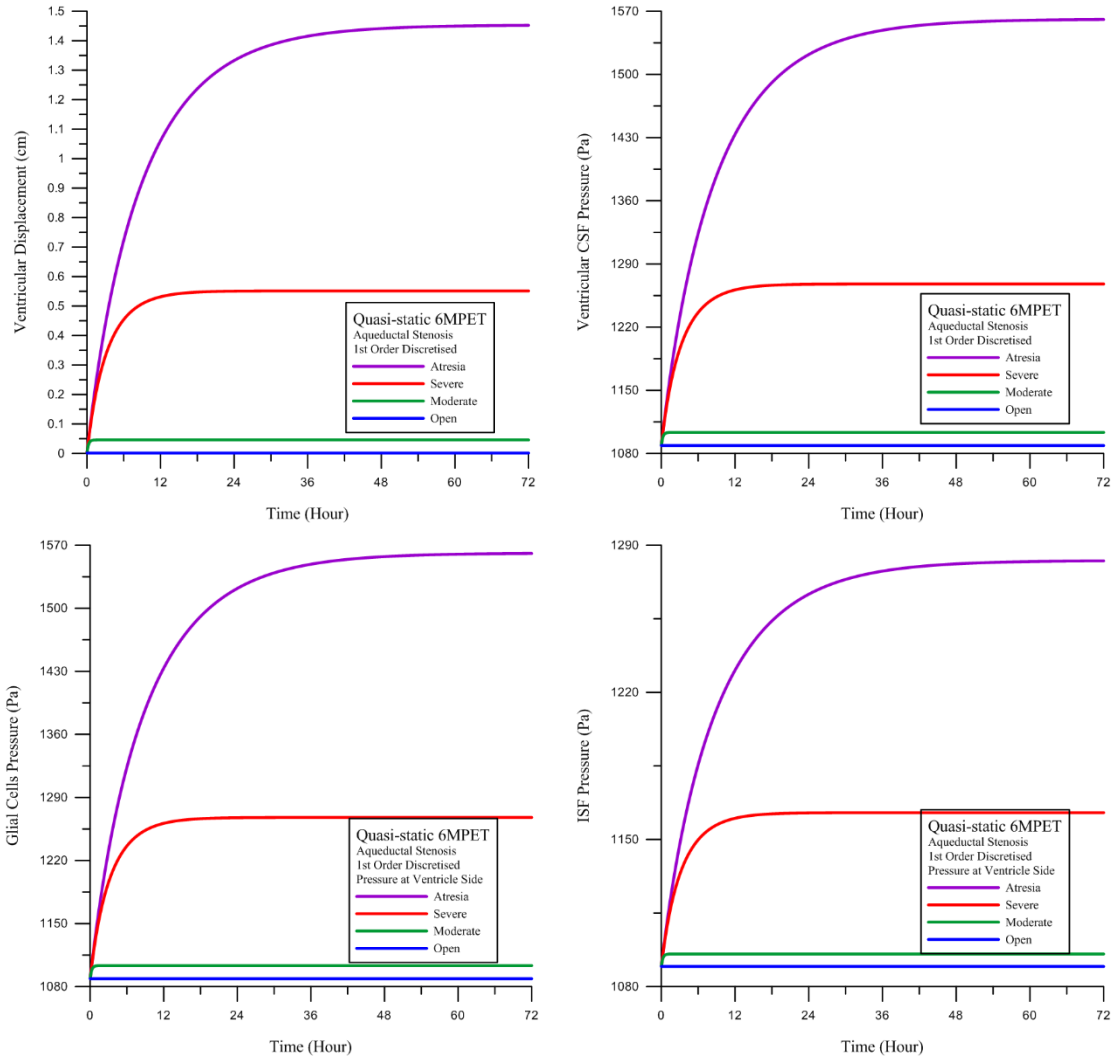


Figure 4.4 The first order discretised scheme on the quasi-static 6MPET model with the aqueductal stenosis in different level. Upper-LHS: Ventricular displacement vs. time course; Upper-RHS: Ventricular CSF pressure vs. time course; Lower-LHS: Glial cells pressure at the ventricle wall vs. time course; Lower-RHS: ISF pressure at the ventricle wall vs. time course.

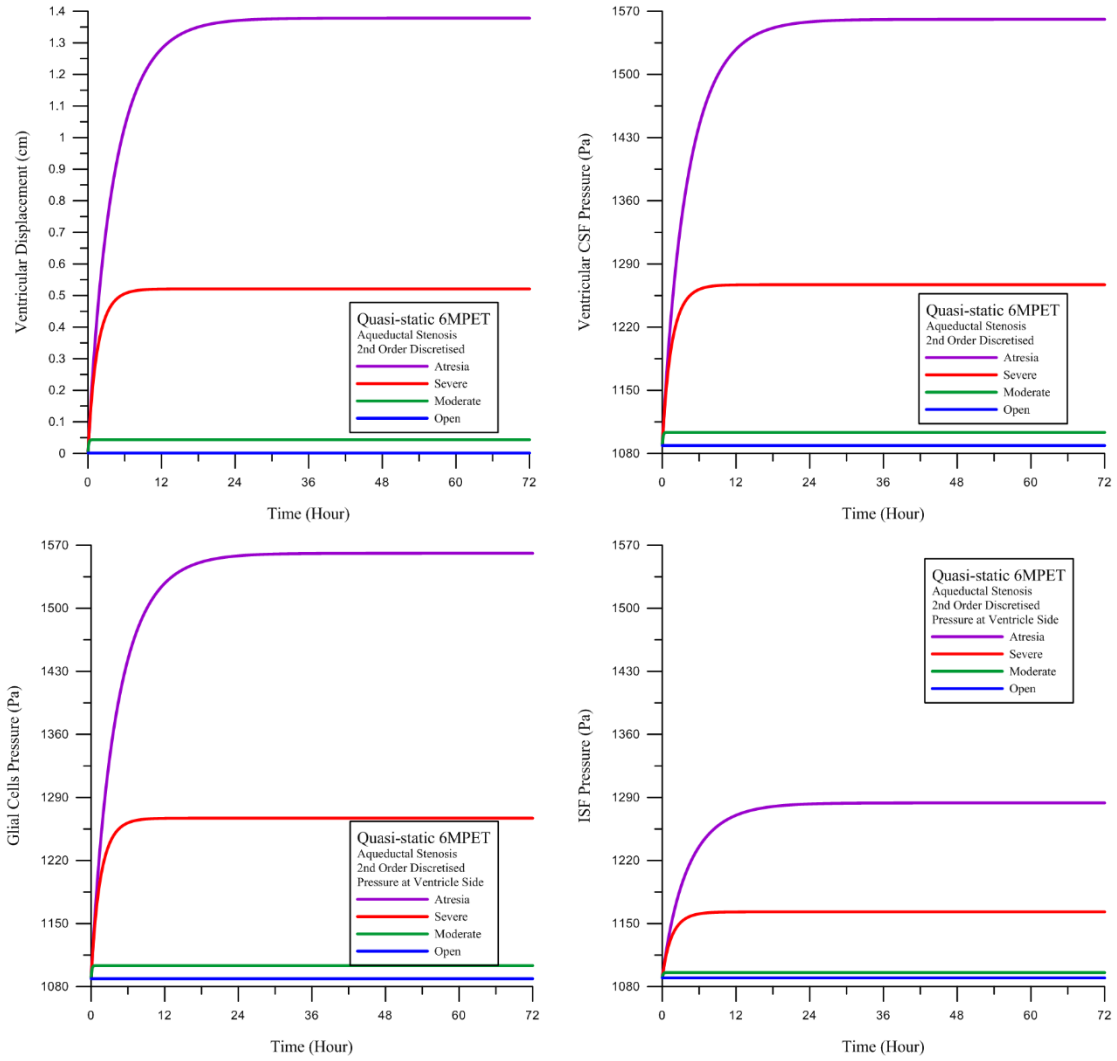


Figure 4.5 The second order discretised scheme on the quasi-static 6MPET model with the aqueductal stenosis in different level. Upper-LHS: Ventricular displacement vs. time course; Upper-RHS: Ventricular CSF pressure vs. time course; Lower-LHS: Glial cells pressure at the ventricle wall vs. time course; Lower-RHS: ISF pressure at the ventricle wall vs. time course.

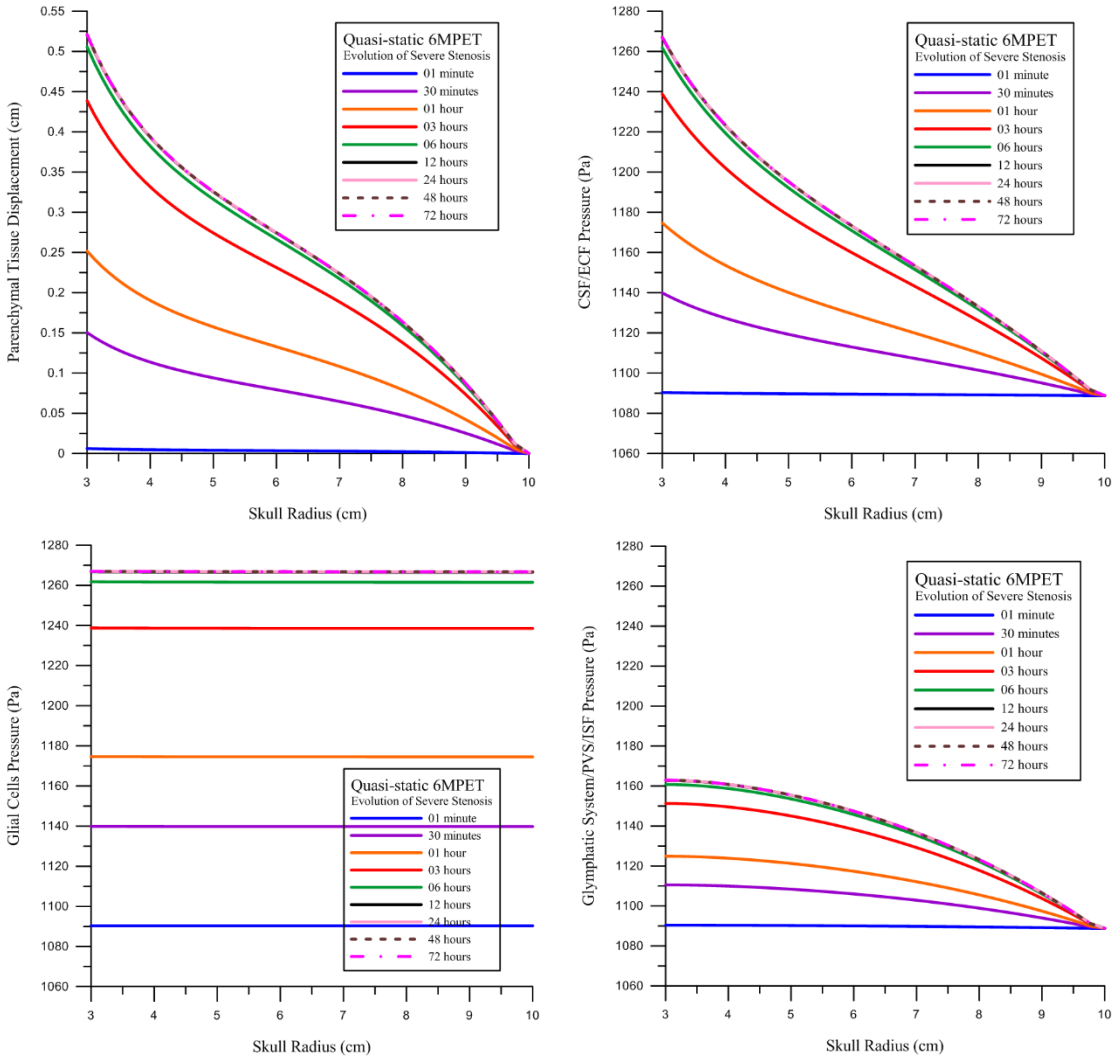


Figure 4.6 The evolution of severe stenosis of the aqueduct of Sylvius with the second order discretised scheme on the quasi-static 6MPET model. Upper-LHS: Parenchymal tissue displacement vs. skull radius; Upper-RHS: CSF/ECF pressure vs. skull radius; Lower-LHS: Glial cells pressure vs. skull radius; Lower-RHS: Glymphatic system/PVS/ISF pressure vs. skull radius.

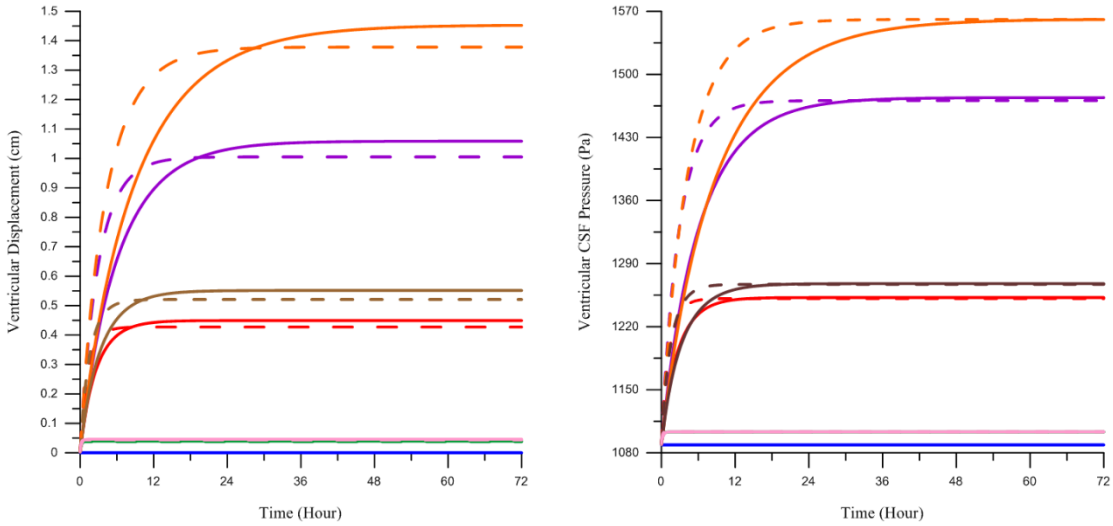


Figure 4.7 The comparison of the first and the second order discretised scheme on the quasi-static 4MPET and 6MPET model with the aqueductal stenosis in the different level. The solid lines represent the first order discretised scheme results and the dashed lines represent the second order discretised scheme results. The orange, brown and pink are the results arising from atresia, severe and moderate aqueductal stenosis via the 6MPET model. The purple, red and green are the results occur from atresia, severe and moderate aqueductal stenosis, respectively, via the 4MPET model.

4.3 Comparison & Validation of the MPET template

In this section, the validation and comparison of the quasi-static and fully dynamic MPET models (e.g. 4MPET and 6MPET) in their respective discretisation schemes (first and second order) will be analysed using the severely stenosed case of the aqueduct of Sylvius. Moreover, the results of the 4MPET model which come from the first order discretisation scheme are followed from Tully et al. [164, 233] as a reference standard in this thesis. The results are shown from the Figure 4.7 to 4.10. The following number of the nodes (n = 41, 61, 81 and 101) and the size of the time steps (Δt = 0.01 and 10.0 *sec*) were used in the spatial analysis and temporal analysis. Subsequently, suggestions on numerical efficiency follow. In sum, the second order discretisation

scheme is more consistent and is, therefore, preferred in the spatiotemporal simulations for both, 4MPET and 6MPET models.

4.3.1 Convergence Analysis for the u-*p* Formulation

In Figure 4.7 (upper-LHS), the convergence results of the first order ventricular displacement based on the number of nodes is shown. When using 101 nodes, and Δt = 0.01 or 10.0 *sec*, the converged result for ventricular displacement is ~0.44 *cm*. For the first order accuracy discretisation scheme, the CSF pressure in insensitive to the size of both temporal and spatial discretisation templates, where a converged result of ~1252 Pa is reached. This insensitivity of the CSF pressure to the size of the discretisation template is also extended to the second order accuracy of the discretisation template, as depicted in Figure 4.7 (lower-RHS), where a converged result of ~1252 Pa is achieved. In addition, the second order accuracy of the discretisation also possesses the added benefit of allowing the ventricular displacement to be independent of the number of nodes used, in addition to the size of the time step – within the range we tested. This is shown in Figure 4.7 (upper-RHS). The convergence results (using the second order accuracy of the discretisation template) for ventricular displacement and CSF pressure are ~0.43 *cm* and 1251 *Pa*, respectively. This implies that the second order accuracy of the discretisation scheme between n = 41 to 101 and Δt = 0.01 to 10.0 *sec* gives consistent results within this spatiotemporal domain.

In Figure 4.8, the trend of each solid and dotted line of the ventricular displacement and CSF pressure in the fully dynamic 4MPET model are shown. The difference between the fully dynamic model and the quasi-static model is that the temporal terms in the system equations (governing equations) are neglected. The same boundary

conditions are used to close the system equations. The values of the convergence results of the first order discretised scheme for ventricular displacement with the number of the nodes (n = 41, 61, 81 and 101) and two values of the time step (Δt = 0.01 and 10.0 *sec*) are shown in Figure 4.8 (Upper-LHS). Specifically, keeping n =101 and using Δt = 0.01 and 10.0 sec, the results are almost the same, at ~0.44 *cm* and ~0.46 *cm*, respectively. The values of the convergence results of the first order discretised scheme for ventricular CSF pressure with the number of the nodes (n = 101) two sizes of the time step (Δt = 0.01 and 10.0 *sec*) have the same value, ~1252 *Pa* (Figure 4.8, Lower-LHS). Moreover, regarding the values of the convergence results of the second order discretised scheme for the ventricular displacement and CSF pressure, all solution curves converge to the results 0.43 *cm* and 1251 *Pa*, respectively. These results are shown in the upper and lower right quadrants in Figure 4.8.

In Figure 4.9, most of the convergence results in the quasi-static 6MPET model are similar to the convergence results in the corresponding 4MPET, e.g. ventricular displacement and ventricular CSF pressure. However, the convergence results of the ISF pressure at the ventricle wall in the quasi-static 6MPET model are increased as the number of nodes, n, increase (Lower-LHS and Lower-RHS, Figure 4.9). The convergence results of the ISF pressure at the ventricle wall between the first and second order discretisation schemes show an interesting response. Increasing the numbers of the nodes that are used will give a higher pressure value at the ventricle wall of the glymphatic system/PVS/ISF compartment. The values of the convergence results of the first order discretised scheme for the different nodal numbers, n = 41 and n = 101, are 1129.6 *Pa* and 1130.7 *Pa*, respectively (Lower-LHS, Figure 4.9). The values of the convergence results of the second order discretisation scheme for the nodal

numbers of n = 41 and n = 101, are 1129.8 *Pa* and 1130.8 *Pa*, respectively (Lower-RHS, Figure 4.9).

The presentation of the convergence results in the Figure 4.10 possesses identical behaviour to the convergence characteristics between the 4MPET and the quasi-static 6MPET model, especially in glymphatic system/PVS/ISF compartment. However, the behaviour of the ISF pressure at the ventricle wall in the fully dynamic 6MPET model has a sizeable difference to the quasi-static 6MPET model. The interesting hook-like curvatures in the fully dynamic 6MPET model are shown here for completeness, but their detailed analysis will be conducted in the next chapter. Comparing the consistency of the results in the quasi-static and fully dynamic 6MPET model, the second order discretization scheme shows more consistent behaviour in the fully dynamic 6MPET model implementation than in the quasi-static 6MPET model. These imply that the second order discretisation scheme that was presented in the previous section can successfully capture the detailed phenomena in the quasi-static and fully dynamic MPET system, especially in the fully dynamic 6MPET system.

4.3.2 Comparison 4MPET with various porosities

The porosity of the quasi-static 4MPET model had been set at 0.2 for each compartment in the previous study [233]. However, the previous porosity settings ($\phi^a = \phi^c = \phi^v = \phi^e =$ 0.2) in the quasi-static 4MPET model are not sufficient for the 6MPET, as Eqn. (3.31) is not satisfied. Comparing 4MPET with 6MPET, there are two extra compartments, glymphatic system/PVS/ISF and glial cells to include in the summation in Eqn. (3.31). The total porosity of the combined fluid networks should keep water comprising approximately 80% of the brain volume ($\sum_{\Omega=a,c,v,e,l,g} \phi^{\Omega} = 0.8$), with the parenchymal

matrix at around 20% (ϕ^p = 0.2), so one adjusts the new porosity values for 6MPET accordingly. Therefore, it is necessary to confirm that the new porosity values (ϕ^a = 0.1, ϕ^c = 0.1, ϕ^v = 0.1, ϕ^e = 0.2, ϕ^l = 0.15, ϕ^g = 0.15) are in fact, reasonable to apply in the 6MPET model.

Firstly, we assume the updated porosity values of the cerebrovascular compartments, including the arterial, capillary, and venous compartment, are similar to the previous porosity values of the cerebrovascular compartments of the 4MPET model, and have the same characteristic porosity. Through this assumption, the new porosity values of the cerebrovascular compartments (ϕ^a = 0.1, ϕ^c = 0.1, ϕ^v = 0.1) are assumed in this research. Moreover, the new porosity value of the CSF compartment considers succeeding to the previous porosity value from 4MPET as 0.2. Both of the new and previous porosity values are tested by 4MPET in order to prove this assumption. The results are discussed in the following:

Figure 4.11 demonstrates the effect of the new porosity setting (ϕ^a = 0.1, ϕ^c = 0.1, ϕ^v = 0.1, ϕ^e = 0.2) on 4MPET (e.g. quasi-static and fully dynamic 4MPET) and utilises the results of the previous porosity values ($\phi^a = \phi^c = \phi^v = \phi^e$ = 0.2) to prove that there is no change (the solid represents the numerical results of the updated porosity values and dotted line represents the numerical results of the previous porosity values) for using these new porosity values. Although the porosity should not be affected in the quasi-static model due to the porosity related term, ρ, in Eqn. (3.33a), the comparison results still include them in order to prove there is no influence from the altered porosity values by the new settings. The numerical results in Figure 4.11 assure no influence when assigning the new porosity values on 4MPET. This implies that either the

previous values or new values work for the 4MPET model. Hence, these new porosity values of the cerebrovascular compartments are incorporated in the 6MPET.

Furthermore, the porosity value of the glial cells compartment ($\phi^g = 0.15$) is assigned from Bertossi et al. [388]. The porosity value of the glymphatic system/PVS/ISF compartment is assumed as 0.15, it could be considered from the mathematical estimate via Eqn. (3.31) or be derived from the physiological idea (equal to the porosity value of the glial cells compartment). On the one hand, according to Eqn. (3.31), the sum of the porosities of the 6MPET compartments should be equal to 0.8 due to the parenchymal porosity setting of 0.2 ($\phi^p = 0.2$). From a physiological perspective, the glymphatic system/PVS/ISF compartment is assumed to portray the fact that it is surrounded by glial cells (as is the case in the cerebral environment), where the astrocytic network is composed of intra/extracellular spaces and capillary basement membranes which construct low resistance fluid pathways. Meanwhile, Nicholson et al. [389] stipulates that the brain interstitial system occupies approximately 15% to 20% of the total brain volume, and it contains interstitial fluid (ISF) and extracellular matrix (ECM).

Considering the porosities for each compartment of the 6MPET system have not been measured via experiments, appropriate assumption is necessary to employ in order to make the fortify the 6MPET system. These new porosity values are proposed to be applied on the 6MPET template, since the comparison results in 6MPET and 4MPET show consistency in the CSF/ECF pressure between the previous porosity values ($\phi^a = \phi^c = \phi^v = \phi^e = 0.2$) and the updated porosity values ($\phi^a = 0.1$, $\phi^c = 0.1$, $\phi^v = 0.1$, $\phi^e = 0.2$, $\phi^l = 0.15$, $\phi^g = 0.15$).

4.3.3 Comparison of the quasi-static 4MPET and 6MPET with various compliances

From a physiological point of view, the Biot - Willis coefficient, α, can be taken as the compliance of the tissue which is the capacity of a porous medium to dilate and increase bulk volume with increasing transmural pressure. Since it is postulated that the altered compliance of the brain tissue may be related to volumetric changes in the vascular network, the results by set from different values of the Biot-Willis coefficient in capillary compartment will be demonstrated in the following [164, 233, 255, 265, 266, 269, 303, 390, 391].

Although Bateman's results showed that HCP patients have lower compliance than the healthy subjects by measuring the superior sagittal sinus and straight sinus volume, varying compliance settings in the quasi-steady state 4MPET model and show interesting results for the obstructive H case. For the parameter to coincide and be able draw comparisons between the quasi-static 4MPET and 6MPET models in Figure 4.12, we present the temporal results of the ventricular displacement for these two combinations of parameters for the capillary compartment (e.g. $\alpha^c = 0.9$, $\alpha^c = 0.8$) two combination parameters for glymphatic system/PVS/ISF compartment (e.g. $\alpha^l = 0.9$, $\alpha^l = 0.8$) and two combination parameters for glial cells compartment (e.g. $\alpha^g = 0.9$, $\alpha^g = 0.8$). Furthermore, the theoretical values ($\alpha^{a,c,v,e} = 1.0$ for 4MPET or $\alpha^{a,c,v,e,l,g} = 1.0$ for 6MPET) can be expected to minimise the influence of any possible compressible characteristics in the brain parenchyma, as the Biot-Willis coefficient, compliance (or inversely elastance), restricts the influence for ventriculomegaly in poroelasticity [233, 271, 332].

The results in Figure 4.12 demonstrate that the larger the capillary compliance, the larger the ventricular displacement. Both combinations for the capillary compartment (α^c = 0.9, α^c = 0.8) in the quasi-static 4MPET model are larger than the equivalent combinations of the compliance for the capillary (α^c = 0.9, α^c = 0.8) compartment in the quasi-static 6MPET model around 0.06 *cm* and 0.22 *cm*, respectively. The same pattern, larger compliance corresponding to higher ventricular displacement, occurs in the compliance of the glial cells compartment and the capillary compartment. However, the larger compliance of the glymphatic system/PVS/ISF compartment has the effect of a smaller ventricular displacement (which is smaller than the ventricular displacement with the theoretical compliance of unity). Moreover, the level of ventriculomegaly of the capillary compliance at $\alpha^{a,c,v,e,l,g}$ = 1.0 is almost the same as the level of ventriculomegaly of the glial cells compliance, where α^g = 0.9. The RHS of Figure 4.12 implies that the higher compliance in glymphatic system/PVS/ISF conducts the reduction of the ventricular displacement.

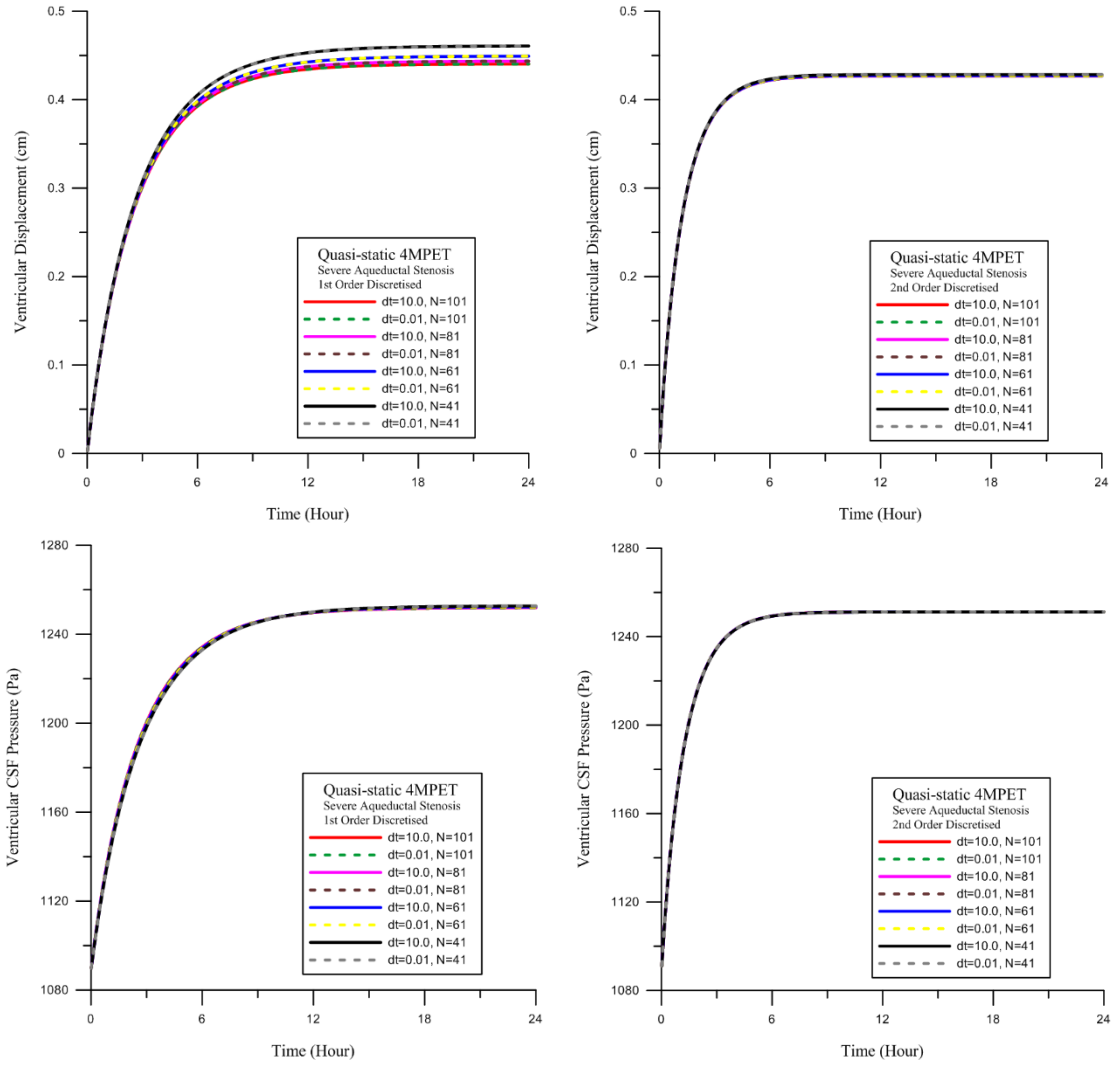


Figure 4.8 Validation results of the first and second order discretised scheme with the severe aqueductal stenosis on the quasi-static 4MPET model. The results of the first order (upper-LHS) and second order (upper-RHS) ventricular displacement, and the results of the first order (lower-LHS) and second order (lower-RHS) ventricular CSF pressure by various nodes along the radial direction and sizes of the time step are demonstrated.

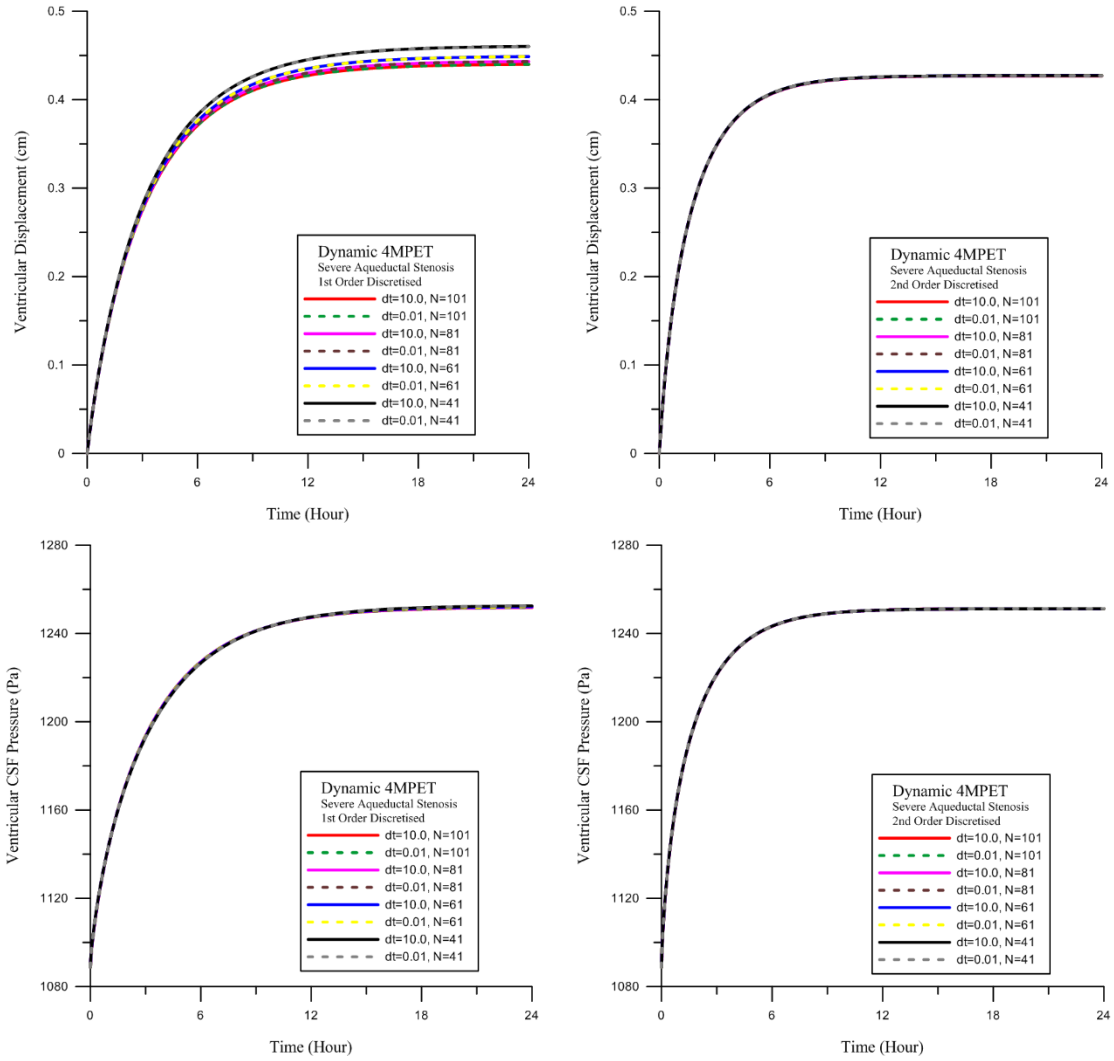


Figure 4.9 Validation results of the first and second order discretised scheme with the severe aqueductal stenosis on the dynamic 4MPET model. The results of the first order (upper-LHS) and second order (upper-RHS) ventricular displacement, and the results of the first order (lower-LHS) and second order (lower-RHS) ventricular CSF pressure by various nodes along the radial direction and sizes of the time step are demonstrated.

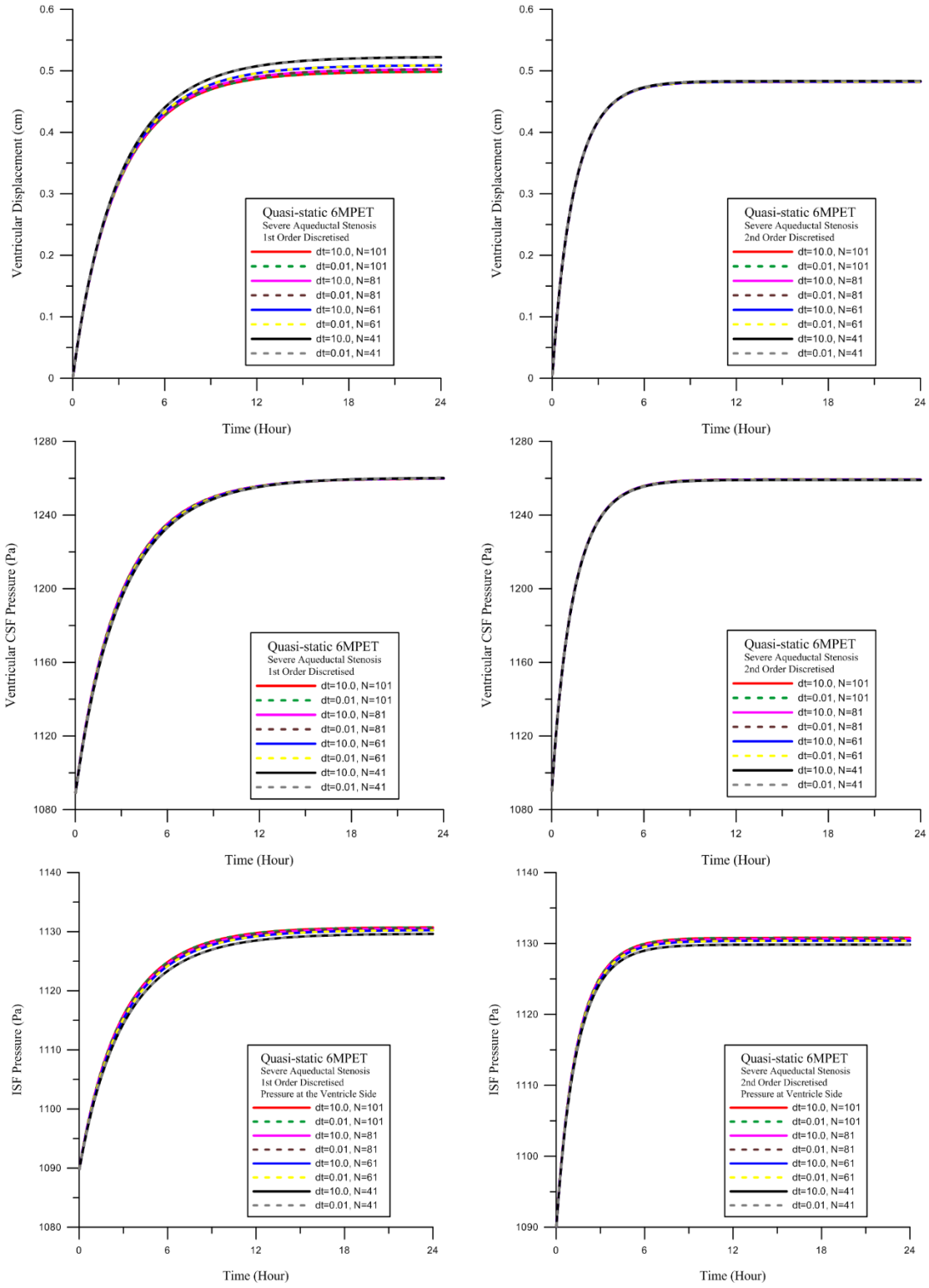


Figure 4.10 Validation results of the first and second order discretised scheme with the severe aqueductal stenosis on the quasi-static 6MPET model. The results of the first order (upper-LHS) and second order (upper-RHS) ventricular displacement, the results of the first order (middle-LHS) and second order (middle-RHS) ventricular CSF pressure and the results of the first order (lower-LHS) and second order (lower-RHS) ISF pressure by various nodes along the radial direction and sizes of the time step are demonstrated.

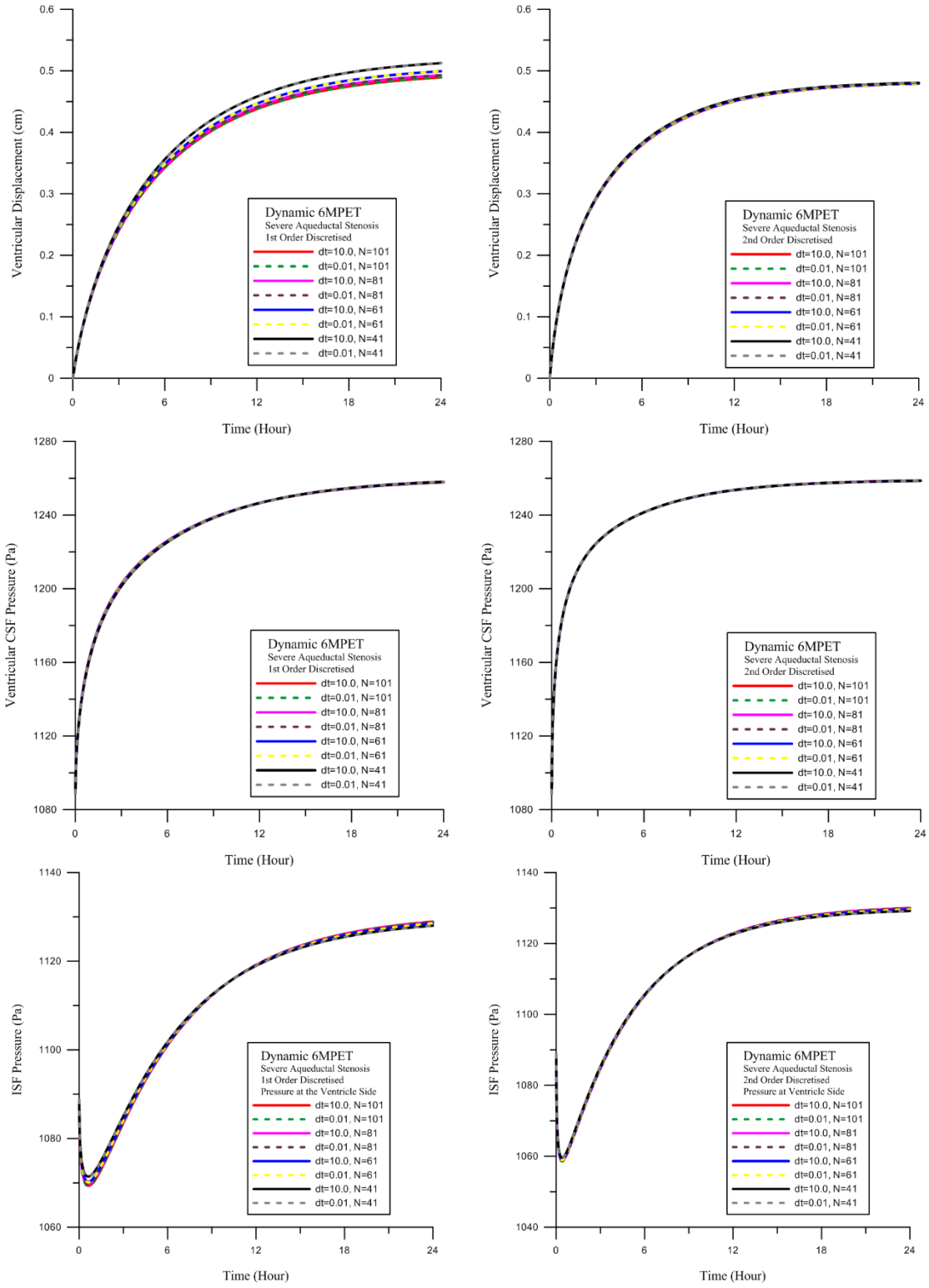


Figure 4.11 Validation results of the first and second order discretised scheme with the severe aqueductal stenosis on the fully dynamic 6MPET model. The results of the first order (upper-LHS) and second order (upper-RHS) ventricular displacement, the results of the first order (middle-LHS) and second order (middle-RHS) ventricular CSF pressure and the results of the first order (lower-LHS) and second order (lower-RHS) ISF pressure by various nodes along the radial direction and sizes of the time step are demonstrated.

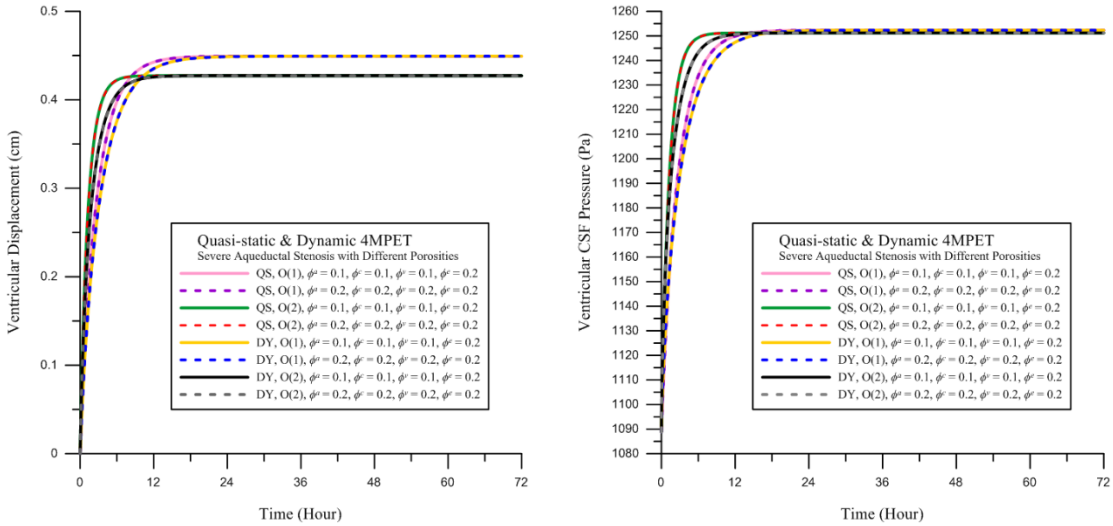


Figure 4.12 Using the different combination porosity to compare the ventricular displacement (LHS) and CSF pressure (RHS) between the quasi-static and dynamic 4MPET model.

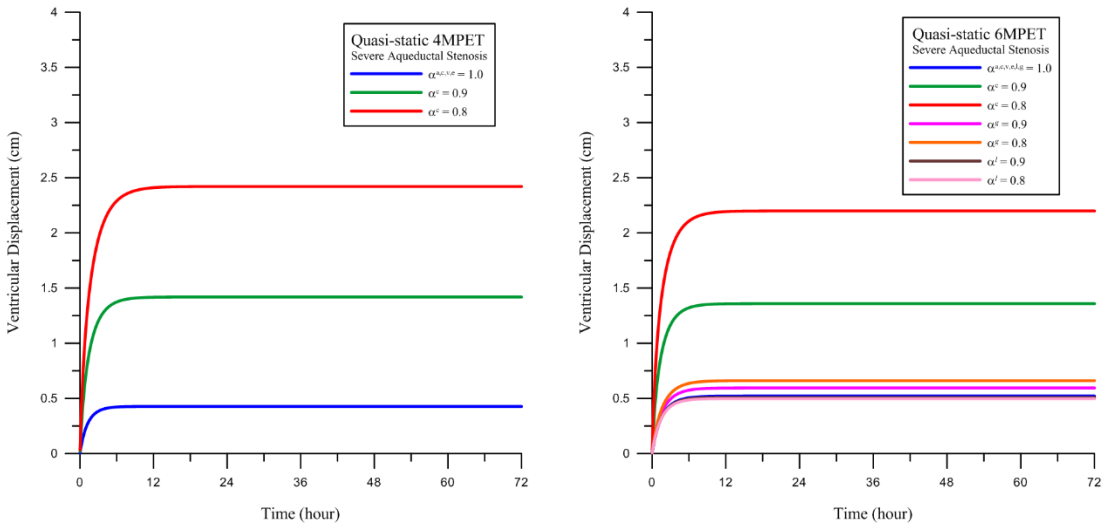


Figure 4.13 Ventricular displacement with various compliances on the quasi-static 4MPET (LHS) and 6MPET (RHS) model.

Chapter 5 Acute Hydrocephalus

The Topic of this Chapter

In order to describe the effect of various levels of stenosis of the aqueduct of Sylvius during acute hydrocephalus, the implementation of the fully dynamic MPET model for 4MPET and 6MPET are proposed in this chapter. The fully dynamic MPET model includes the inertial terms that are usually omitted when slower, chronic disease scale processes are examined. Firstly, the simulation results of the 4MPET model in the fully dynamic version will be presented via a spatiotemporal analysis. Moreover, the same patterns of the analysis will be presented via the more sophisticated 6MPET template. Finally, the comparison between the quasi-static and dynamic MPET model using the second order discretization scheme will be presented in order to demonstrate the 6MPET model in its entirety. Regarding the fully dynamic 4MPET model results which applied on the aqueductal stenosis cases, a reduced version has been published in the Journal of Biomechanics [269].

5.1 Fully Dynamic Four-Network MPET

5.1.1 Results

From Figure 5.1 and 5.2 (the first and second order discretised scheme, respectively) focusing on the steady state results, one can see that both the ventricular displacement and CSF pressure have the largest ventricular displacement (1.06 *cm* and 1.01 *cm*, respectively) and the highest ventricular CSF pressure (1474.1 *Pa* and 1471.0 *Pa*, respectively) in the atresia case of aqueductal stenosis, as expected. There is significant ventricular displacement (0.45 *cm* and 0.43 *cm*, respectively) and high ventricular CSF pressure (1252.3 *Pa* and 1251.2 *Pa*, respectively) in the severe case of aqueductal stenosis. Both of the smaller ventricular displacement (0.040 *cm* and 0.038 *cm*, respectively) and lower ventricular CSF pressure (1103.1 *Pa* and 1103.2 *Pa*, respectively) occur in the moderate case of aqueductal stenosis. However, the

simulation results of the first order discretised scheme are amplified in comparison to the simulation results of the second order discretised scheme, as seen in Figure 5.1 and 5.2. No matter which discretised scheme is used, the open aqueduct (healthy case) develops almost no ventricular displacement, and the constant ventricular CSF pressure (1088.8 *Pa*). Meanwhile, Figure 5.1 and 5.2 show the tracking of ventricular displacement and CSF pressure over the simulation period of 72 hours. As can be seen from the figures, the applications of severe stenosis delay their settlement to approximately 18 and 12 hours for the first and second order discretised scheme, respectively.

Figure 5.3 depicts the evolution of CSF/ECF pressure and parenchymal tissue displacement at seven points in time (t = 1 minute, 30 minutes, 1 hour, 3 hours, 6 hours, 12 hours and 24 hours). CSF/ECF pressure at the ventricles increases from approximately 1094.8 *Pa* to 1251.2 *Pa* over this period. The parenchymal tissue displacement shows an increase in ventricular displacement from approximately 58.8 μm to 0.43 *cm*. The evolution of the parenchymal tissue displacement in the quasi-static 4MPET model does not change anymore after 12 hours. Moreover, Figure 5.4 depicts the results for the CSF/ECF fluid content based on Eqn. (3.9) and parenchymal dilation obtained from the term $\nabla \cdot \mathbf{u}$ in Eqns. (3.34 a-e) adjacent to the ventricles and skull, respectively. There is a substantial increase in the CSF/ECF adjacent to the ventricles with increasing stenosis, whilst the level remains constant at the near-skull region. The dilation of the parenchymal tissue increases substantially near the ventricles with increasing stenosis. The parenchyma also shows gradually increasing compressional characteristics near the skull.

5.1.2 Discussion

The results in Figures 5.1, 5.2, 5.3 and 5.4 show a high qualitative correlation in the magnitude of ventricular displacement and CSF pressure. Similar results have been obtained by Tully & Ventikos [164, 233, 265] and Smillie et al. [255], where the predicted ventricular displacement approached 1 cm after 24 hours of simulation time in both SPET and MPET. The degree of severe aqueductal stenosis between the simulations in this work and that of Tully & Ventikos is matching quite well [233], and the results here correlate favourably to the latter work, in both ventricular displacement and CSF pressure. Therefore, the results in the present work, first of all, demonstrate that the quasi-steady hypothesis adopted in all the previously referenced works, including those involving the MPET formulation, are generally compatible with the solution of the fully transient system.

The RHS of Figure 5.3 depicts the predicted evolution of the CSF pressure between 1 *minute* and 1 *day*. It can be seen that through the use of the fully dynamic MPET model, significant new features of this process can be extracted. For instance, for the tissue region nearest to the skull, the family of CSF pressure curves show a relatively rapid increase in pressure between 1 *minute* and 3 *hours*. The increasing ventricular pressure (complemented with ventriculomegaly, see the LHS of Figure 5.3) is causing the trans-parenchymal tissue region to respond, and this coping mechanism is most attenuated at the regions closest to the skull and the ventricles. After 12 *hours*, the parenchymal tissue shows to be coping well with the additional pressure burden, since both ventriculomegaly and ventricular CSF pressure show small increases between 12 and 24 *hours* (0.425 to 0.427 *cm* and 1250.6 to 1251.2 *Pa* respectively).

In line with previous studies (Smillie et al. [255]; Wirth & Sobey [375]; Wirth & Sobey, [259], Vardakis et al. [303], Vardakis et al. [304]), obtaining the fluid content in the CSF/ISF compartment (Figure 5.4, LHS) provides a possible localized visualisation of periventricular tissue damage, as positive values of fluid content are observed in these regions. The greater the degree of stenosis, the larger the dilation of parenchymal tissue near the ventricles. Near the skull, the trend is reversed, as the parenchymal tissue compresses there and so more fluid is squeezed out of the tissue with increasing stenosis. This metric of comparison is mainly qualitative in nature; as physiologically relevant quantitative comparators are not available. Localised swelling in the periventricular region results in both stretch (adjacent to the ventricles) and compression (adjacent to the skull) of cortical tissue, as seen in the RHS of Figure 5.4. Similar characteristics in the trace of the strain tensor are seen in analytical models of NPH [271]. Periventricular lucency which was first witnessed by Naidich et al. is represented by increased CSF/ISF content in the periventricular regions, and is assumed to result from ependymal surface breakdown which helps alleviate pressure in the ventricles by allowing for CSF extravasation (and oedema formation) [392]. It is speculated that this process could be achieved with the possible assistance of AQP4, which lines the ependymal surface [155].

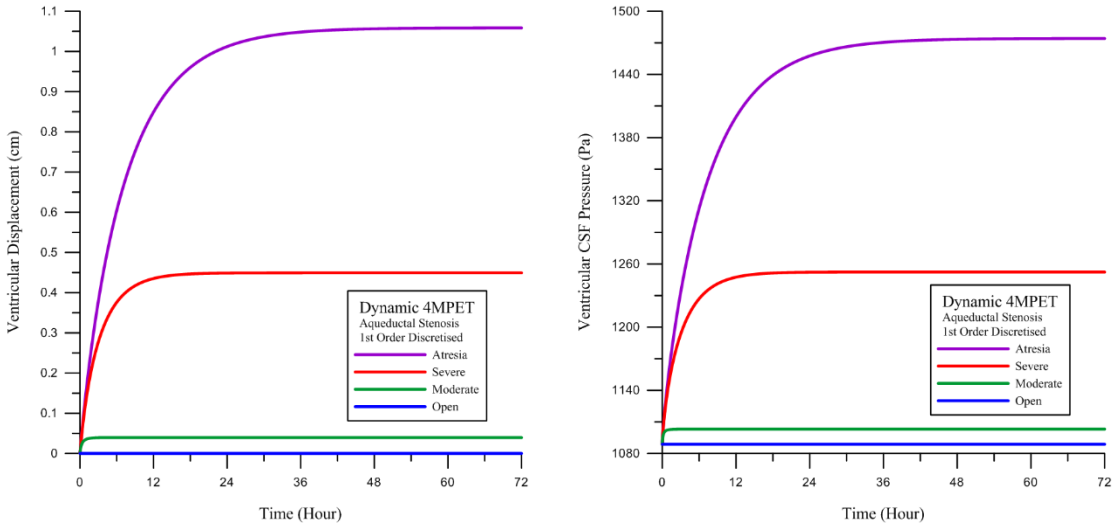


Figure 5.1 First order discretised fully dynamic 4MPET model with different levels of aqueductal stenosis. LHS: Ventricular displacement vs. time course; RHS: Ventricular CSF pressure vs. time course.

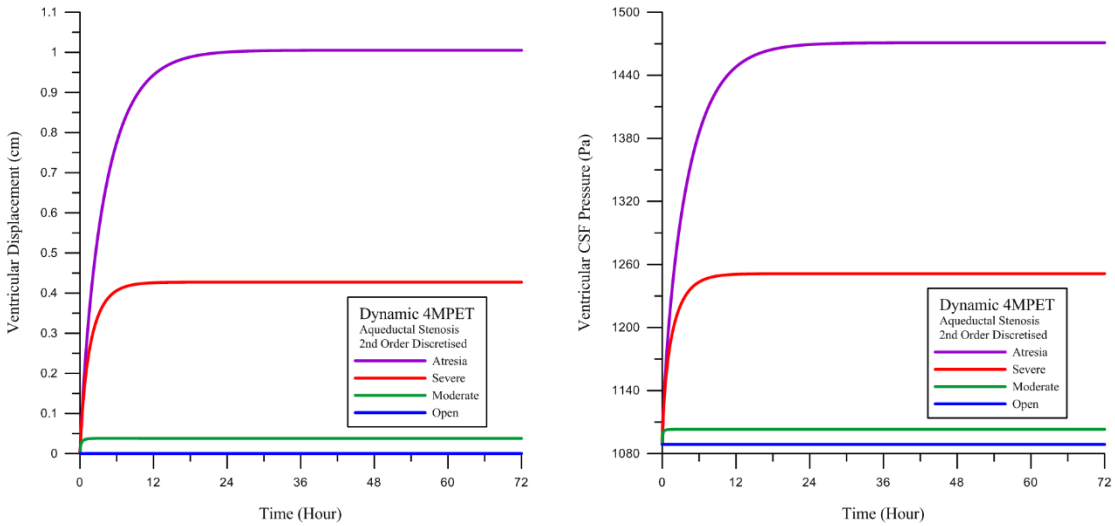


Figure 5.2 Second order discretised fully dynamic 4MPET model with different levels of aqueductal stenosis. LHS: Ventricular displacement vs. time course; RHS: Ventricular CSF pressure vs. time course.

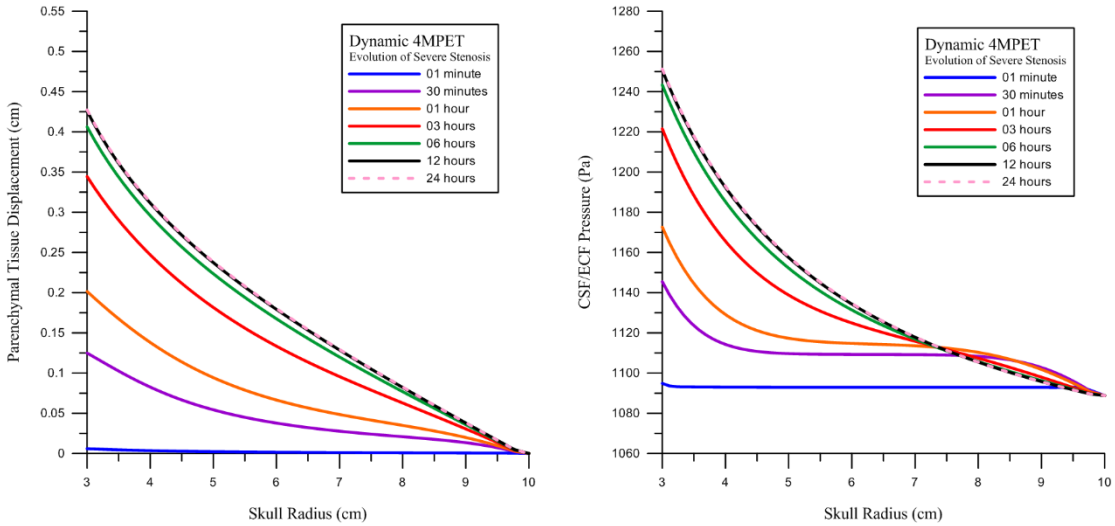


Figure 5.3 Evolution of severe stenosis of the aqueduct of Sylvius - second order discretised scheme of the fully dynamic 4MPET model. LHS: Parenchymal tissue displacement vs. skull radius; RHS: CSF/ECF pressure vs. skull radius.

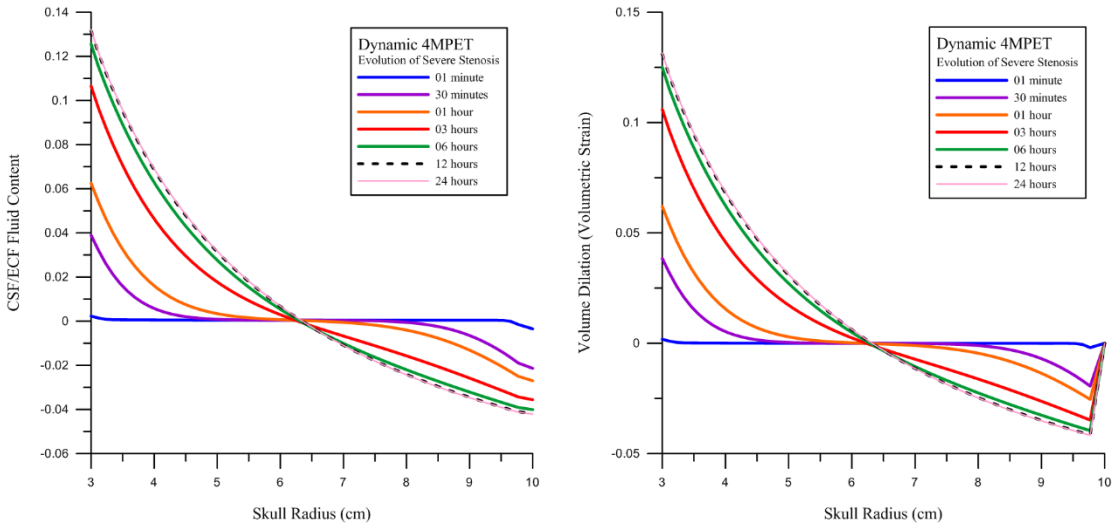


Figure 5.4 Evolution of CSF/ECF fluid content and volume dilation for severe stenosis of the aqueduct of Sylvius with the second order discretised scheme of the fully dynamic 4MPET model. LHS: CSF/ECF fluid content vs. skull radius; RHS: Volume dilation (volumetric strain) vs. skull radius.

5.2 Fully Dynamic Six-Network MPET

From Figure 5.5, it can be seen that, with the second order discretised scheme, the atresia condition of the aqueduct of Sylvius shows the largest ventricular displacement, CSF pressure, glial cells pressure and ISF pressure (1.38 *cm*, 1561.0 *Pa*, 1561.0 *Pa* and 1283.9 *Pa*, respectively); values reached after the full development of the lumped ventricular system. In the same figure, the open cerebral aqueduct which represents the healthy case shows that almost no ventricular displacement occurs at the ventricular wall (13.5 μm) and the ventricular CSF, glial cells and ISF pressure (1088.8 *Pa*, 1088.8 *Pa*, 1089.6 *Pa*) during the entire time course. The moderate stenosis of the aqueduct of Sylvius gives rise to a ventricular displacement, CSF pressure, glial cells pressure and ISF pressure (0.44 *mm*, 1103.3 *Pa*, 1103.3 *Pa* and 1095.6 *Pa*, respectively) during the full time course of the simulation. The results of severe aqueductal stenosis include a ventricular displacement, and CSF pressure, glial cells pressure and ISF pressure of 0.52 *cm*, 1267.0 *Pa*, 1267.0 *Pa* and 1162.9 *Pa*, respectively. Figure 5.5 depicts the tracking of ventricular displacement (upper-LHS), and CSF/ECF (upper-RHS), glial cells (lower-LHS) and glymphatic system/PVS/ISF (lower-RHS) pressure over a simulation period of 72 hours. As can be seen from these Figures 5.5 and 5.6, the application of severe stenosis delays the settlement of ventriculomegaly to approximately 24 hours for the second order discretised scheme.

Moreover, ISF pressures at the ventricle wall present the hook-like shape in the early stage of the simulation period (1 *min* - 1 *hour*). This interesting hook-like shape may illustrate the compensatory response and explain that the trans-ependymal route for water flow indeed exists [155, 393]. Orešković et al. addressed that ICP, CSF formation and absorption are in the balance in the isolated brain ventricles [394]. This

implies that CSF is not only absorbed mainly into the venous sinuses via the AG, but is also absorbed via other routes, such as trans-ependymal flow [109, 113, 395-397] and PVS (glymphatic system) [27] into the cerebral ventricles. Further, the AQP4 expression in ependymal cells and sub-ependymal astrocytes is an important factor for CSF flow across the ventricle-parenchymal tissue interface [101, 146, 339]. Skjolding et al. [343, 344] and Mao et al. [336] discovered that periventricular AQP4 is initially reduced and then elevated and that AQP4 up-regulation represents a compensatory response to maintain water homoeostasis in HCP. If this concept (of periventricular AQP4 is initially reduced and then elevated) is applied on Starling equation by only considering the term of hydrostatic pressure. The behaviour of the hook-like shape at the initial simulation period might be able to explain. Through the relationship of the proportion of the pressure difference to flow flux ($\Delta p \propto J$) from the Starling equation, and of the notion that periventricular AQP4 is initially reduced and then elevated, reduced AQP4 expression will be expected to reduce the amount of flow rate via AQP4 channels. Subsequently, this causes a pressure drop and vice versa. Additionally, the increment of fluid content in the glymphatic system/PVS/ISF compartment (Lower-LHS, Figure 5.7) is able to support a supplementary explanation for compensatory trans-ependymal water flow across the ventricle-parenchymal interface, since the positive value of the fluid content translates into fluid accumulation. Therefore, the hook-like shape behaviour of the ISF pressure at the ventricle wall that occurs in the fully dynamic 6MPET model may assist us to confirm that a compensatory effect exists in acute HCP (as depicted by considering aqueductal stenosis).

Figure 5.6 depicts the evolution of CSF/ECF, glial cells and glymphatic system/PVS/ISF pressure and parenchymal tissue displacement at seven instances in time (t = 1 *minute*, 30 *minutes*, 1 *hour*, 3 *hours*, 6 *hours*, 12 *hours* and 24 *hours*).

CSF/ECF pressure at the ventricle wall increases from approximately 1104.3 *Pa* to 1267.0 *Pa* over this period. Glial cell pressure at the ventricle wall increases from approximately 1104.3 *Pa* to 1267.0 *Pa* over this period. The pressure of the glial cells compartment in spatial behaviour is almost constant and is different to the CSF/ECF compartment and glymphatic system/PVS/ISF compartment in the spatial domain. This nearly consistent behaviour may be caused by the Neumann boundary condition setting and homogeneous assumption in the 6MPET system. Moreover, glymphatic system/PVS/ISF pressure at the ventricle wall increases from approximately 1081.0 *Pa* to 1162.9 *Pa* over this period. Although the overall glymphatic system/PVS/ISF pressure arises during the evolution of acute HCP, there are three colour lines (blue, 1 *minute*; purple, 30 *minutes*; orange, 1 *hour*) presented reducing pressure behaviour (1088.8 *Pa* is assumed to be normal condition, shown in Figure 5.6 by blue line) between the region from 3 cm to 4.75 cm. This behaviour implies that when ventriculomegaly occurs in aqueductal stenosis, the compartment of the glymphatic system/PVS/ISF provides a contributory function to adapt water regulation in this region (3 *cm* to 4.75 *cm*). This contributory function may generate compensatory trans-ependymal water flow due to necessary water homoeostasis between ventricle and parenchyma. For parenchymal tissue displacement, it demonstrates an increase in ventricular displacement from approximately 56.8 μm to 0.52 *cm*. The evolution of the parenchymal tissue displacement in the fully dynamic 6MPET model remains unaltered after 24 hours. Moreover, Figure 5.7 depicts the results for the CSF/ECF, glial cells and glymphatic system/PVS/ISF fluid content based on Eqn. (3.9) and parenchymal dilation adjacent to the ventricles and skull.

5.2.1 The water mobility effect in 6MPET

In Figure 5.8, the simulation results of the different combinations of the water mobility in glymphatic system/PVS/ISF and glial cells compartment at the ventricle wall are demonstrated in order to ascertain the degree of contribution of the 6MPET template in deciphering the characteristics of aqueductal stenosis, since two additional compartments are considered. In Figure 5.8, all of the curves are considered based on the paired response by the water mobility of the glymphatic system and glial cells compartments. The simulation results show that the lines which are altered by water mobility of the glial cells compartment always coincide with the curves which are altered via the water mobility of the glymphatic system/PVS/ISF compartment.

The lower mobility of the glial cells compartment ($\kappa^g = 5.0 \times 10^{-5}, \frac{m^4}{NS}$) always possesses the response of a slightly larger ventricular displacement, as witnessed in the upper-LHS quadrant of Figure 5.8. For example, the mobility pair (κ^l, κ^g) of ($1.75 \times 10^{-8}, 5.0 \times 10^{-5}, \frac{m^4}{NS}$) gives rise to a ventricular displacement of 0.593 *cm* after 72 *hours* of simulation. This is in contrast to the mobility pair ($1.75 \times 10^{-8}, 5.0 \times 10^{-4}, \frac{m^4}{NS}$), which produces a ventricular displacement of 0.598 *cm* after 3 days. The smallest ventricular displacement (0.42 cm at 72 hours) occurs at the highest water mobility of the glymphatic system/PVS/ISF compartment ($\kappa^l = 1.75 \times 10^{-6}, \frac{m^4}{NS}$), where normal water mobility in glymphatic system/PVS/ISF compartment is set as $\kappa^l = 1.75 \times 10^{-5}, \frac{m^4}{NS}$ (Upper-LHS, Figure 5.8). ISF pressure at the ventricle wall does not show any signs of a compensatory behaviour for the lesser ventricular displacement, but does show this behaviour for the other severe ventriculomegaly cases.

Furthermore, the larger the ventricular displacement that is met, the deeper the pressure drop in the early stages, as is shown in the lower-RHS of Figure 5.8. As previously mentioned, the pressure drop within 1 *hour* in the periventricular region provides the ability to generate compensatory trans-ependymal water flow which was confirmed by the experimental work from Skjolding et al. [343, 344] and Mao et al. [336]. They observed that relative periventricular AQP4 density is initially reduced and then elevated and AQP4 up-regulation represents a compensatory response to maintain water homoeostasis in HCP. The periventricular ADC value was raised in a statistically significant way (Kruskal-Wallis, $p < 0.05$) after one and two weeks of HCP. Relative AQP4 density was importantly abated in both cortex and periventricular region after two days and normalised after one week, and was also strongly correlated to lateral ventricular volume. These research results may be indirectly explained by the phenomena shown in the lower-RHS of figure 5.8 via the 6MPET model, due to the aforementioned the hydrostatic pressure relation in the starling equation. However, it should be noted that the altered value to mimic AQP4 expression in the current 6MPET template is only considered as a constant, hence the dynamic variation has been neglected thus far.

The reduced AQP4 expression will be expected to reduce the amount of flow rate via AQP4 channel, and then cause the pressure drop and vice versa. Therefore, the phenomena of the ISF pressure at the ventricle wall which occurs when using the 6MPET model may address the mechanism of periventricular lucency when it meets the most severe cases of aqueductal stenosis based HCP [398]. Although the smallest ventricular displacement is accompanied by the lowest ISF pressure at the ventricle wall, it still has the largest CSF and glial cells pressure (1269 *Pa* at 72 *hours*) attributed to it at the ventricle wall. The difference of the CSF and glial cells pressure between

the smallest and largest ventricular displacement is around 4 *Pa*. It may be speculated that this small pressure difference may provide a window for osmosis to occur; however, it should be noted that the current study does not take osmosis into account. This would be an interesting theme to investigate in the future.

Synopsizing, the increase in water mobility of the glymphatic system/PVS/ISF compartment may mollify the ventriculomegaly in severe aqueductal stenosis. With this conclusion in mind, this additional MPET compartment may be regarded as pivotal in the discussion regarding potential treatment regimes in acute HCP.

5.2.2 The effect of compliance on the fully dynamic 6MPET

In this section, the effect of altered compliance for ventriculomegaly during aqueductal stenosis via the altered compliance of the capillary (α^c = 0.99, green and α^c = 0.95, red solid line), glymphatic system/PVS/ISF (α^l = 0.9, brown and α^l = 0.8, pink solid line) and glial cells (α^g = 0.9, magenta dotted line and α^g = 0.8, orange solid line) compartments are presented (LHS, Figure 5.9). For the condition of severe aqueductal stenosis, the ventricular displacement is 0.52 *cm*. The red line (α^c = 0.95) has the largest ventricular displacement (0.89 *cm*) and the pink line (α^l = 0.8) has the smallest ventricular displacement (0.49 cm) in the LHS of Figure 5.9. All the characteristics in the LHS of Figure 5.9 are similar with the characteristics in the RHS of Figure 4.12. Therefore, the same conclusion from the section 4.3 can be extended here. The higher compliance in the glymphatic system/PVS/ISF compartment might be functionally significant, as it provides a means to reduce ventriculomegaly in aqueductal stenosis-derived HCP.

5.2.3 The AQP4 effect in the fully dynamic 6MPET model

Bloch et al. proposed that AQP4-deficient mice accelerated the progression of kaolin-induced HCP (obstructive hydrocephalus) and revealed a significant phenomenon that trans-ependymal water flow is penetrating the periventricular space from the ventricle into the parenchymal ECS [146]. Regarding the penetrating trans-ependymal water flow, it was already demonstrated and explained that the proposed 6MPET template is able to capture this aforementioned compensatory behaviour. In this section, it is demonstrated that the 6MPET template may also capture the phenomena of the varying levels of AQP4 expression in the system corresponding to the AQP4-deficient expression which can magnify the ventricular displacement, and vice versa (RHS, Figure 5.9).

Since the glymphatic system/PVS/ISF and glial cells compartment are considered in 6MPET, the HCP simulation is able to account for the AQP4 effect via the resistance factor (*RF*) of AQP expression. The transfer coefficient (γ) of 4MPET was mentioned by Tully et al. [164, 233]. In this study, numerous numerical parametric studies were conducted to investigate the acceptable intervals of use of the transfer coefficients. The aforementioned results revealed that the larger transfer coefficients cause the corresponding larger parenchymal tissue displacement [164]. Therefore, the perspective of the resistance factor of AQP expression arises from the large scale parametric study conducted by Tully et al. [164, 233].

Furthermore, it seems that the case relating to overexpression of AQP4 gives rise to the smallest ventricular displacement under the auspice of severe aqueductal stenosis, whilst that relating to AQP4-deficient expression gives rise to the largest

ventriculomegaly. Ventriculomegaly under typical conditions lies in-between the two aforementioned cases. This implies that the overexpression of AQP4 acts as a means to alleviate ventriculomegaly during aqueductal stenosis, and by extension, acute HCP. The reverse is observed for the case of AQP4-deficient expression.

It should be noted that dynamic AQP4 expression is not considered in this thesis. This would form the basis for an interesting future study, since Skjolding et al. [343, 344] claimed that the periventricular AQP4 is initially reduced and then elevated after their spatiotemporal analysis (using an animal model and human subject). Finally, since these results relating to AQP4 effects are successfully captured using the 6MPET template, what follows in the next chapter is an attempt to utilise this important capability to investigate cytotoxic oedema in the brain potentially.

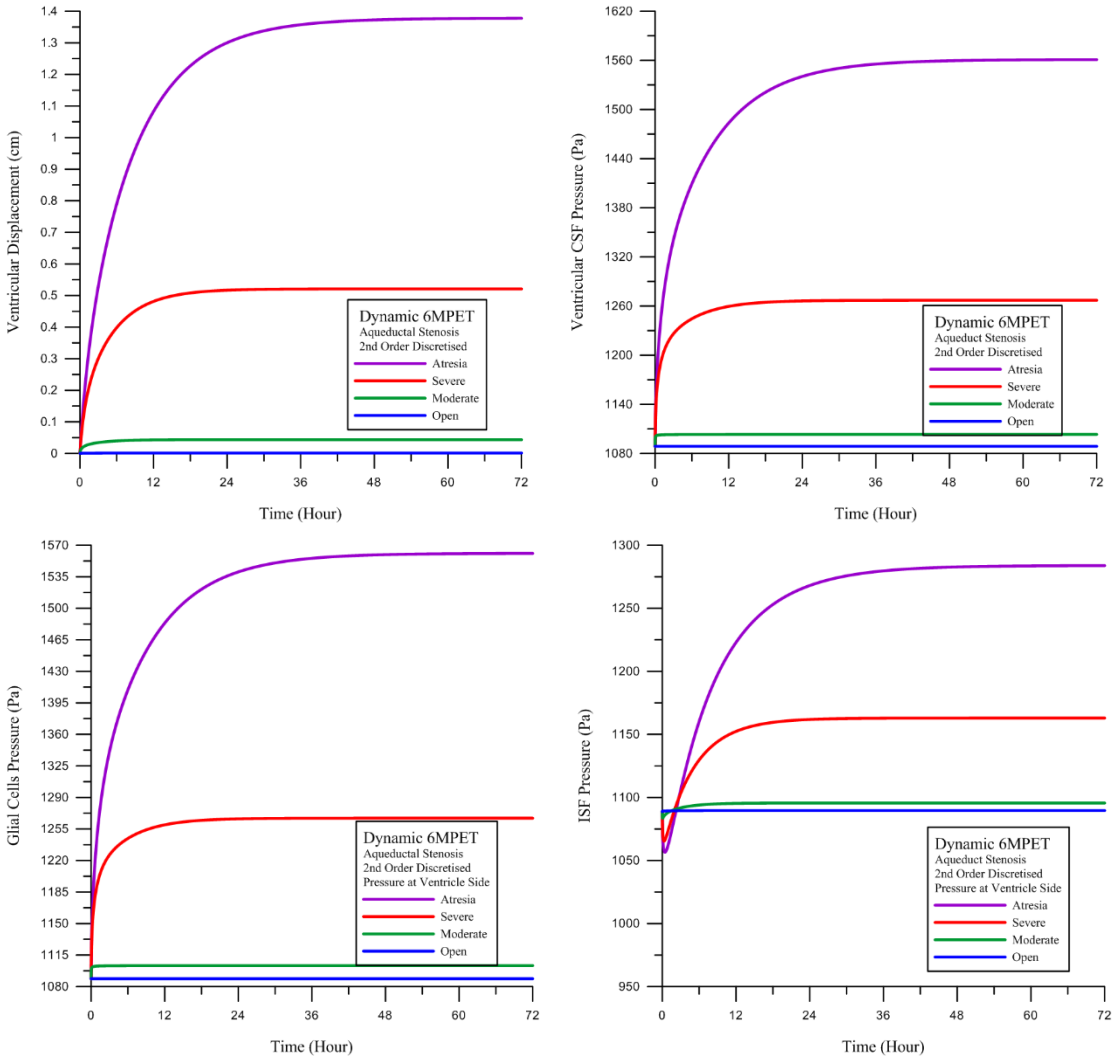


Figure 5.5 Second order discretised scheme applied on the fully dynamic 6MPET model, with varying degrees of aqueductal stenosis. Upper-LHS: Ventricular displacement with time. Upper-RHS: Ventricular CSF pressure with time Lower-LHS: Glial cells pressure at the ventricle wall with time. Lower-RHS: ISF pressure at the ventricle wall with time.

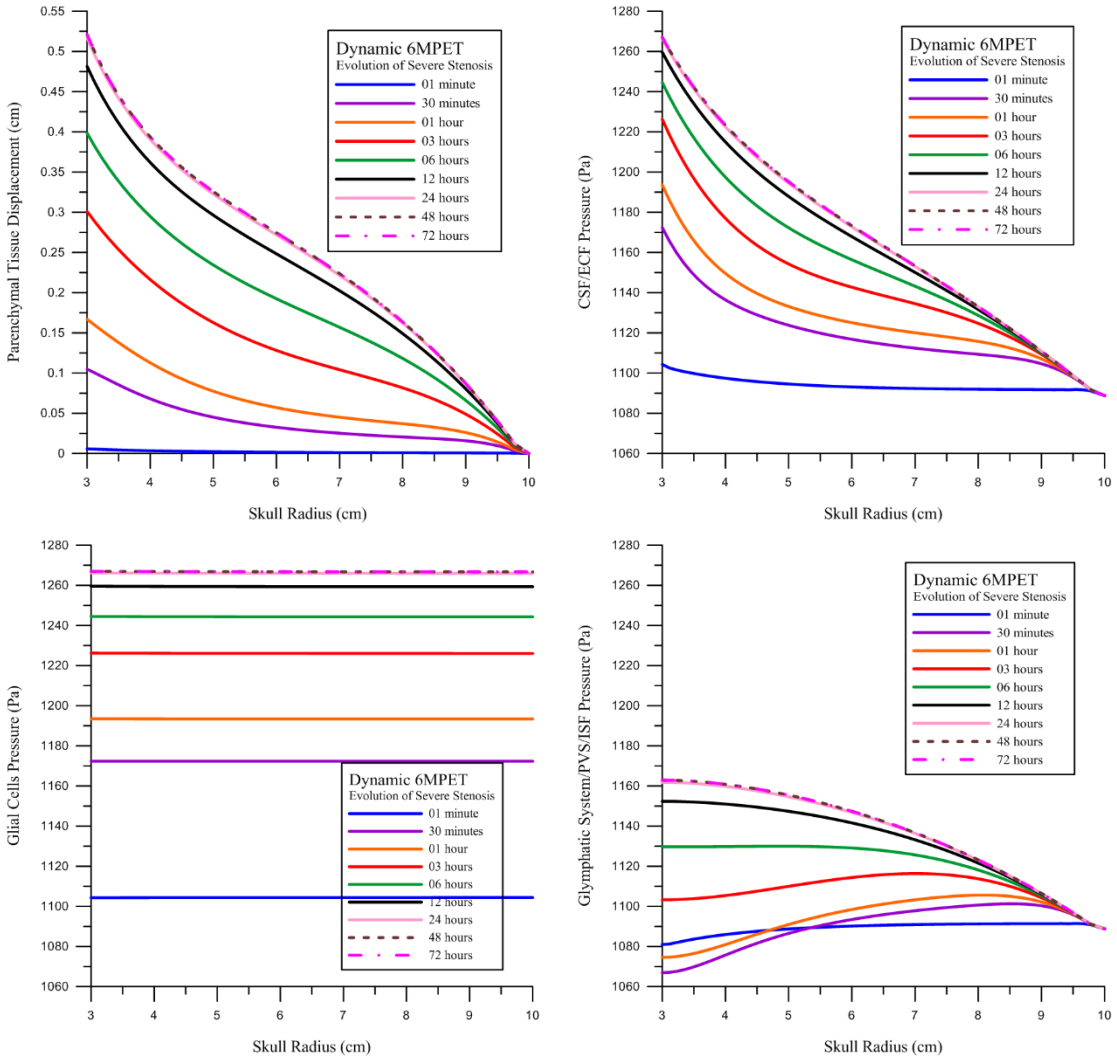


Figure 5.6 Evolution of severe stenosis of the aqueduct of Sylvius with the second order discretised scheme being applied on the fully dynamic 6MPET model. Upper-LHS: Parenchymal tissue displacement as a function of skull radius. Upper-RHS: CSF/ECF pressure as a function of skull radius; Lower-LHS: Glial cells pressure as a function of skull radius; Lower-RHS: Glymphatic system/PVS/ISF pressure as a function of skull radius.

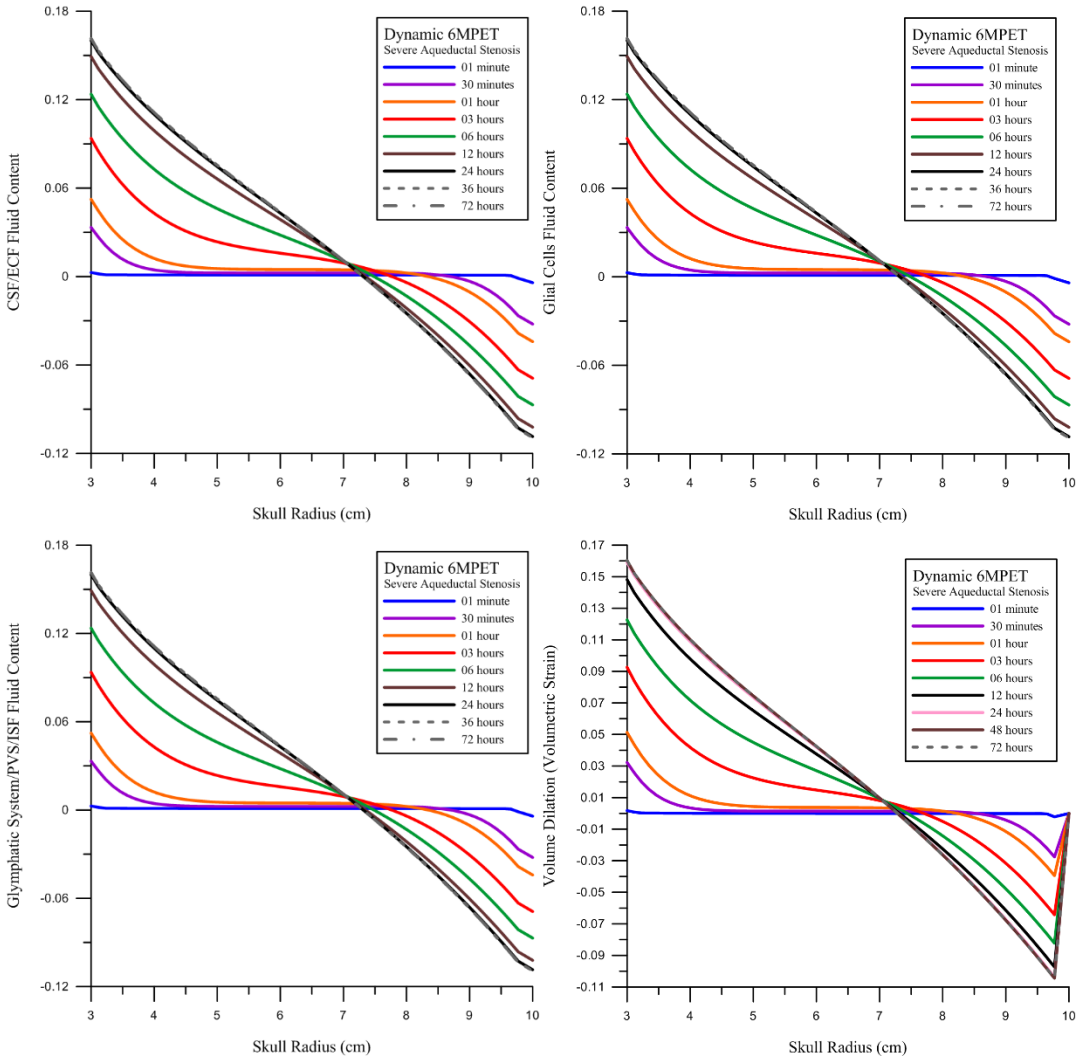


Figure 5.7 Evolution of the fluid content and volume dilation for severe stenosis of the aqueduct of Sylvius with the second order discretised scheme being applied on the fully dynamic 6MPET model. Upper-LHS: CSF/ECF fluid content as a function of skull radius; Upper-RHS: Glial cells fluid content as a function of skull radius; Lower-LHS: Glymphatic system/PVS/ISF fluid content as a function of skull radius; Lower-RHS: Volume dilation (volumetric strain) as a function of skull radius.

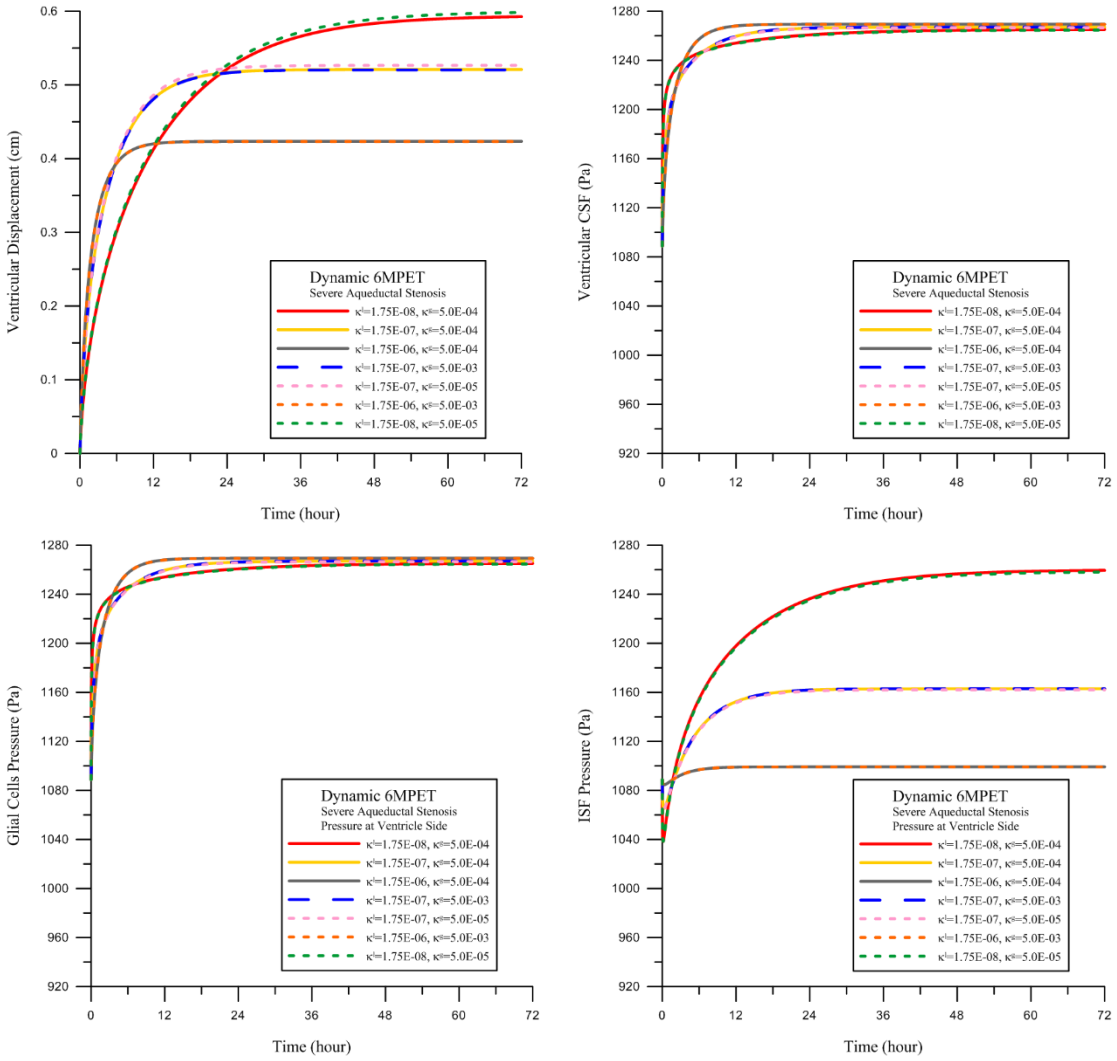


Figure 5.8 Mobility combinations for severe stenosis of the aqueduct of Sylvius with the second order discretised scheme on the fully dynamic 6MPET model. Upper-LHS: Ventricular displacement with time. Upper-RHS: Ventricular CSF pressure with time. Lower-LHS: Glial cells pressure at ventricle the wall with time. Lower-RHS: ISF pressure at the ventricle wall with time.

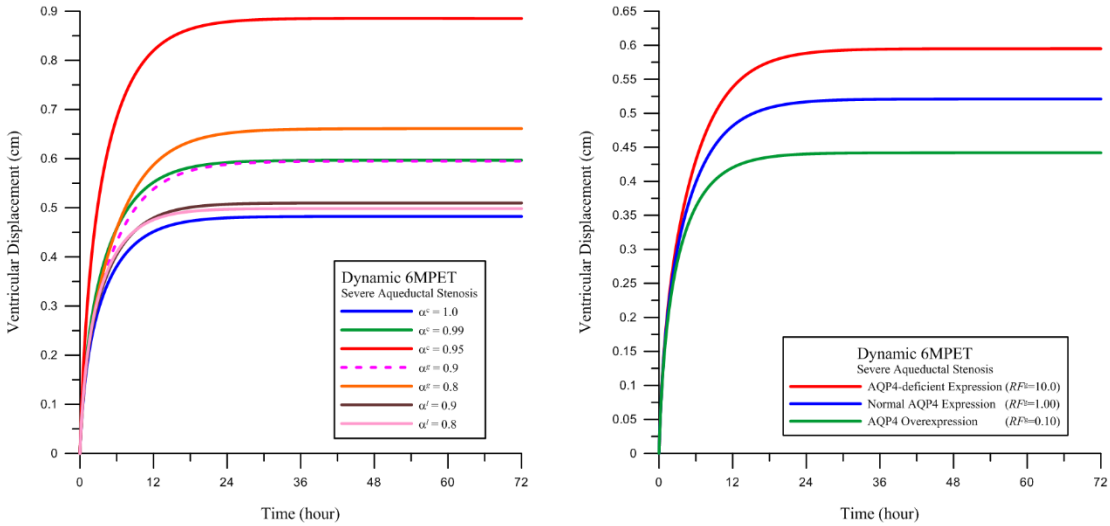


Figure 5.9 Ventricular displacement with various compliances (LHS) and with different AQP4 expression level (RHS) for the severe stenosis of the aqueduct of Sylvius on the fully dynamic 6MPET model.

5.3 Comparison of the Quasi-static & Fully Dynamic MPET

When 4MPET and 6MPET are concerned, there are three cerebrovascular compartments (artery/arteriole, capillary and vein/venule) that are shared between the two templates. The other mutual compartment is the CSF/ECF compartment. Consequently, utilising the ventricular displacement and CSF pressure, one is able to demonstrate the simulation results by comparing the quasi-static with the dynamic models. In Figure 5.10, the case of severe aqueductal stenosis, a comparison of the 4MPET and 6MPET derived time-dependent progression of ventricular displacement (LHS, Figure 5.10) and CSF pressure (RHS, Figure 5.10) is shown. The blue and yellow solid line represent the quasi-static 4MPET model and the fully dynamic 4MPET model. Although both of them use the second order accurate discretisation scheme as the basis to code the two separate routines, the results still converge to the same value of the

ventricular displacement (0.43 *cm*) when both of them arrive the steady state (around 13 *hours*). Moreover, the green and red solid line represent the quasi-static 6MPET model and the fully dynamic 6MPET model. Meanwhile, the ventricular displacement of 6MPET in the quasi-static and dynamic application converge to the same value (0.52 *cm*) when both of them arrive the steady state (around 36 *hours*). Additionally, the ventricular CSF pressure relating to the 4MPET model in the quasi-static and dynamic variations also reaches a convergent value (1251.2 *Pa*). The ventricular CSF pressure of both the quasi-static and dynamic 6MPET models possesses a convergent value (1267.0 *Pa*). In Figure 5.10, it is shown that the quasi-static simulation results, the case of severe aqueductal stenosis condition, overestimate the degree of ventriculomegaly and CSF pressure in the early stages of the simulation. This observation may result from the increased complexity in relaxing the quasi-steady constraint for the MPET system in both solid and liquid phases (has not been considered before), and additionally extends the notion of the mixed hyperbolic-parabolic classical Biot system, which is represented by considering the dynamic equilibrium equation for the poroelastic medium whilst keeping a parabolic representation for the diffusive fluid flow [399]. Volume-distributed external forces are also neglected in this MPET representation. Meanwhile, the ventricular displacement and ventricular CSF pressure using the 6MPET framework are higher than when using the 4MPET framework. This suggests that 4MPET may insufficiently capture the true multiscale phenomena of the cerebral water transport in the human brain due to the lacking consideration for two important compartments in the cerebral environment, specifically the glymphatic system/PVS/ISF and glial cells compartments. Even though 6MPET is suitable for describing water transport phenomena in the cerebral environment, the simulation results show that the quasi-static 6MPET model is not able to capture an important

phenomenon, namely the compensatory response across the ventricle-parenchyma interface, shown in the RHS of Figure 5.11. It is worth noting that similar results have been obtained by Tully & Ventikos [233, 265] and Smillie et al. [255], where the predicted ventricular displacement approached 1 *cm* after 24 hours of simulation time in SPET and MPET with the quasi-static model. The ventricular displacement in 6MPET may be deemed to better approximate these results. This is further evidence to endorse 6MPET as a suitable model for investigating the multiscale water transport phenomena in the brain.

Focusing on the spatiotemporal analyses for the evolution of the severe stenosis case, results are presented in Figure 5.12 to Figure 5.15. Since the detailed analysis has already been addressed in the previous sections, the focus will be on subsequently cross-comparing the quasi-static MPET with the dynamic MPET. The predicted evolution of the parenchymal tissue displacement and CSF/ECF pressure between 1 minute and 24 hours for the 4MPET model, and between 1 minute and 72 hours for 6MPET is observed in Figure 5.12 and 5.13, respectively. The reason why these two different time courses for 4MPET and 6MPET are set originates from the development speed arriving at the fully developed stage (steady state) in each system. It can be seen that through the use of the quasi-static and fully dynamic MPET model, important features of the simulation results are able to be extracted. For example, for the tissue region nearest to the skull, the family of CSF/ECF pressure curves show a relatively rapid increase in pressure between 1 minute and 1 hour through the use of the fully dynamic 4MPET (Lower-RHS, Figure 5.13). Even though this rapidly increasing pressure behaviour in the region nearest to the skull only occurs in the fully dynamic 4MPET model, the increasing pressure shows characteristic diffusive behaviour from the ventricle to skull via 6MPET, especially in the fully dynamic 6MPET model.

Additionally, the predicted evolution of the parenchymal tissue displacement reflects the fact that the increasing ventriculomegaly affects the trans-parenchymal tissue displacement via the intrinsically propagative nature of the 6MPET (fully dynamic 6MPET model). This correlation between displacement and pore pressure can be traced back to the original MPET formulation and is due to the inherent coupling between the two field equations. The predicted evolution of glial cells pressure shows a more even interval when the fully dynamic model is concerned than when the quasi-static model in 6MPET (RHS and LHS, Figure 5.14, respectively). The compensatory response which may be affected by the degree of AQP expression is reflected via the fully dynamic 6MPET model (RHS, Figure 5.15) from one minute to one hour of simulation in the temporal domain, and from the point of the amalgamated ventricles (3 *cm*) until the trans-parenchymal tissue (4.75 *cm*) in the spatial domain. This compensatory response is also not observed in the predicted evolution of glymphatic system/PVS/ISF pressure via the quasi-static 6MPET model (LHS, Figure 5.15).

As previously described and analysed, the fully dynamic 6MPET model is apparently better suited to delineate some critical scenarios, such as parenchymal compensatory response, the effects of AQP4 expression and finally oedema development. Therefore, the fully dynamic 6MPET model will be utilised to simulate cerebral oedema in order to compare the results obtained through these simulations with experimental observations from the literature. These results and observations are discussed in the next chapter.

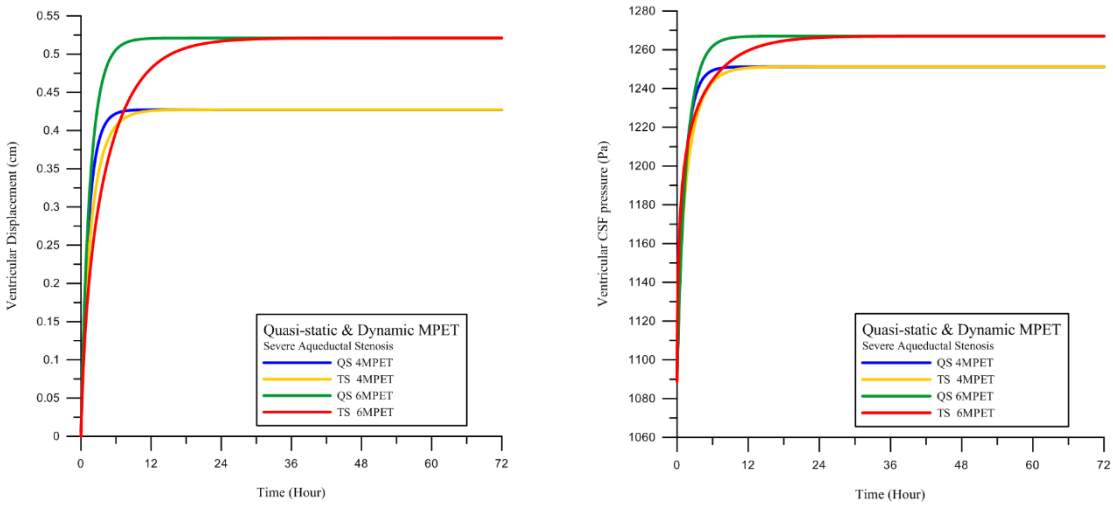


Figure 5.10 Comparison the quasi-static and dynamic model via 4MPET and 6MPET. LHS: ventricular displacement with time; RHS: ventricular CSF pressure with time.The QS and TS in the legend stand for Quasi-Static and Transient.

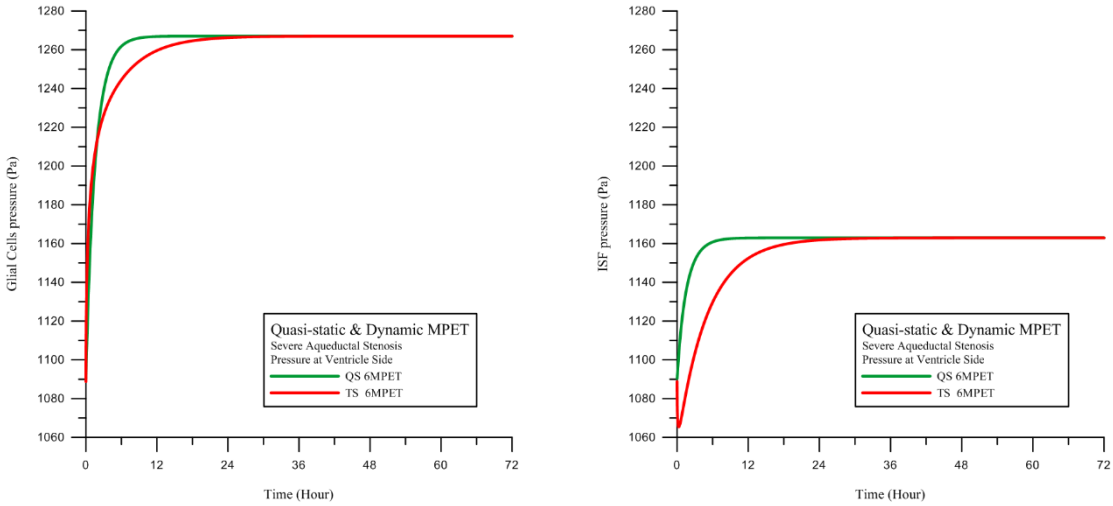


Figure 5.11 Comparison between the quasi-static and dynamic 6MPET models. LHS: glial cells pressure at ventricle wall with time; RHS: ISF pressure at ventricle wall with time. The QS and TS in the legend stand for Quasi-Static and Transient.

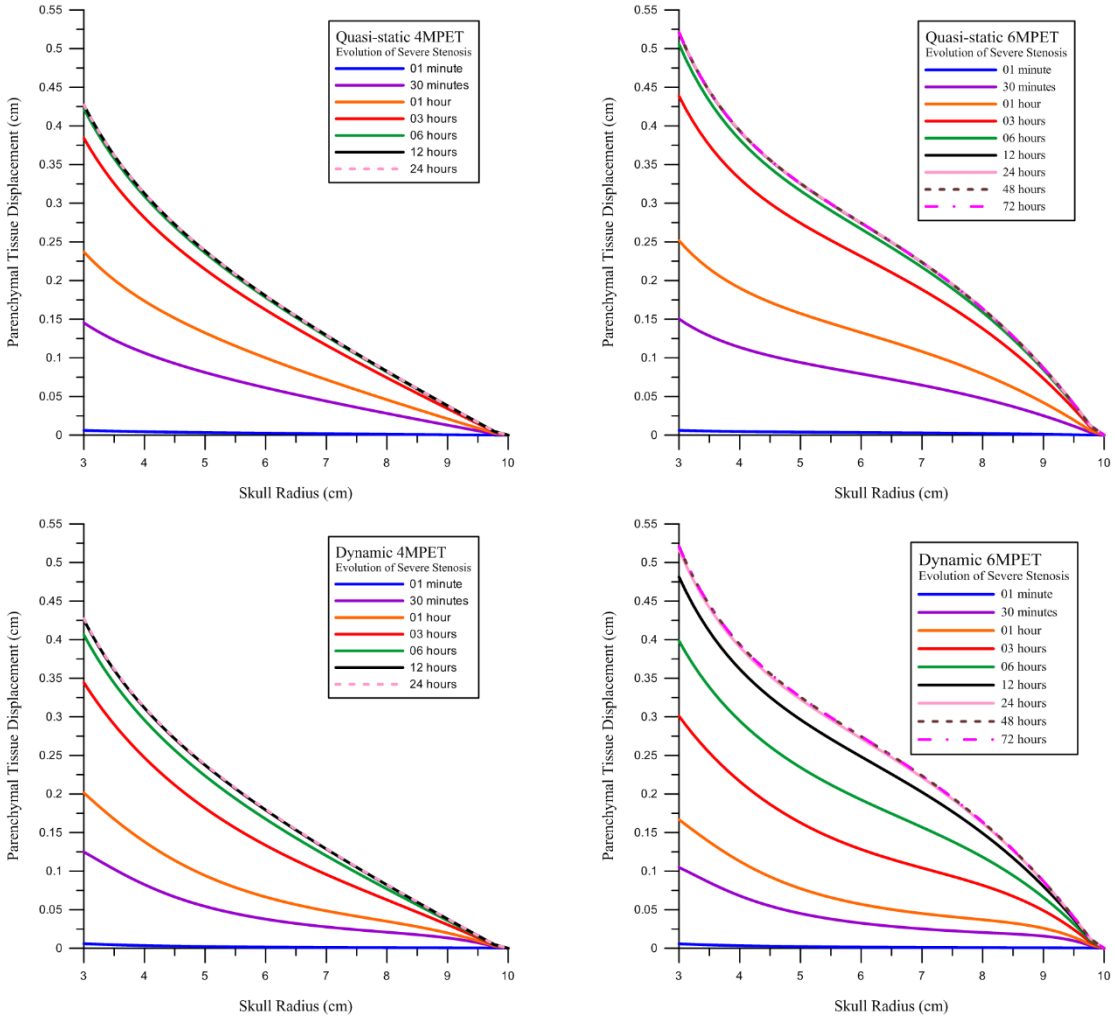


Figure 5.12 Comparison of the parenchymal tissue displacement as a function of skull radius for the quasi-static and dynamic 4MPET and 6MPET models. Upper-LHS: Quasi-static 4MPET; Upper-RHS: Quasi-static 6MPET; Lower-LHS: Dynamic 4MPET; Lower-RHS: Dynamic 6MPET.

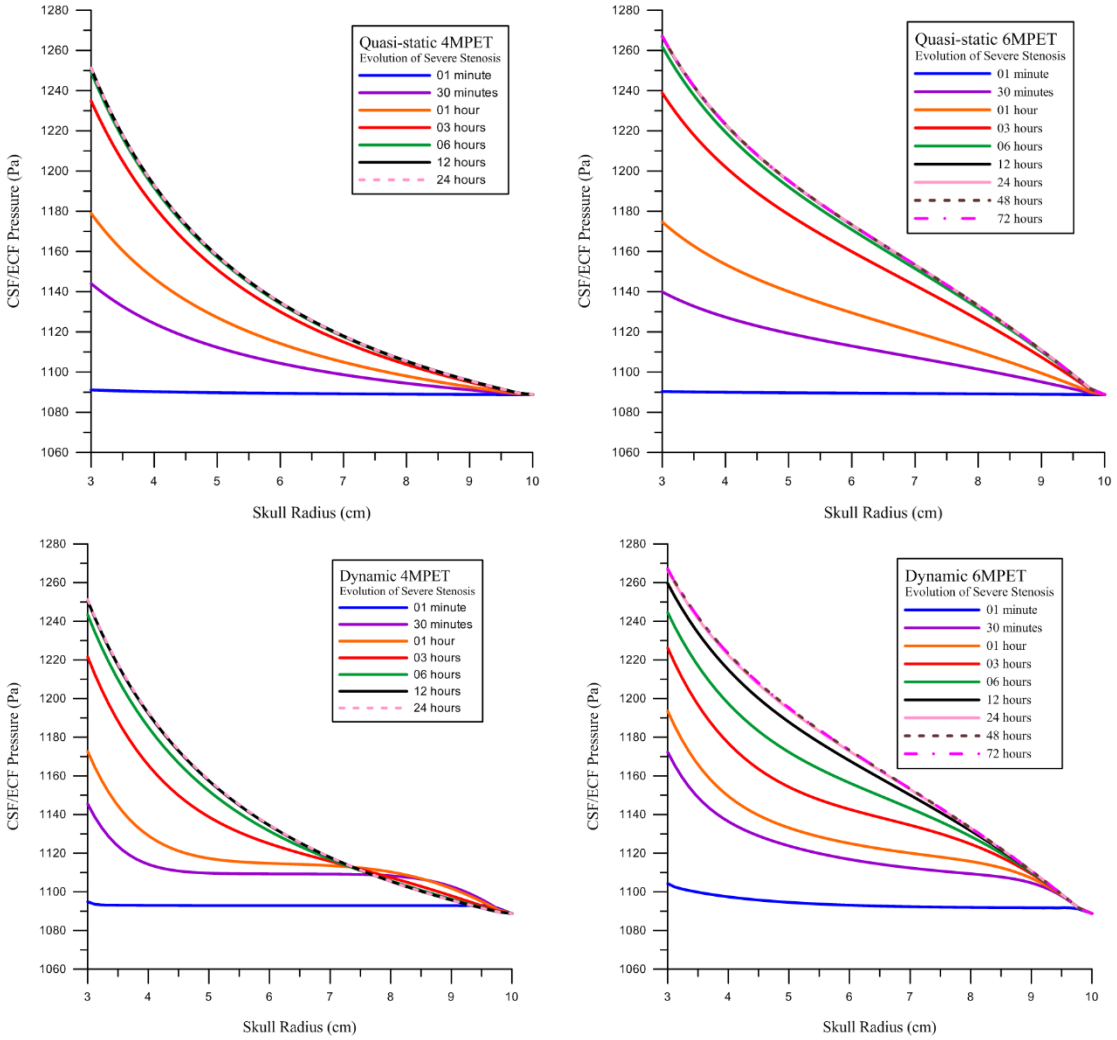


Figure 5.13 Comparison of the CSF/ECF pressure as a function of skull radius for the quasi-static and dynamic MPET model with 4MPET and 6MPET. Upper-LHS: Quasi-static 4MPET; Upper-RHS: Quasi-static 6MPET; Lower-LHS: Dynamic 4MPET; Lower-RHS: Dynamic 6MPET.

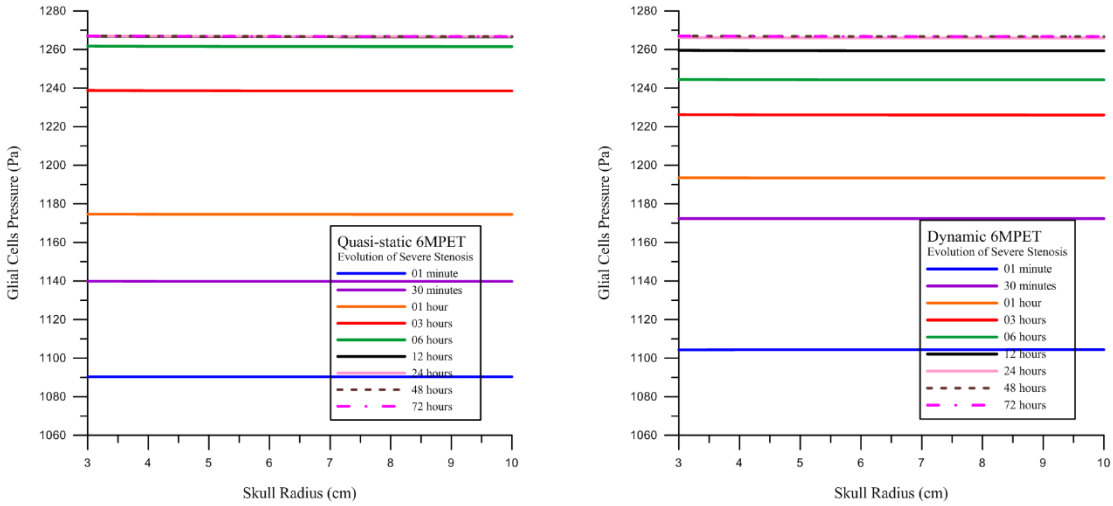


Figure 5.14 Comparison the pressure of the glial cells with a function of skull radius for the quasi-static and dynamic 6MPET model. Upper-LHS: Quasi-static 4MPET; Upper-RHS: Quasi-static 6MPET; Lower-LHS: Dynamic 4MPET; Lower-RHS: Dynamic 6MPET.

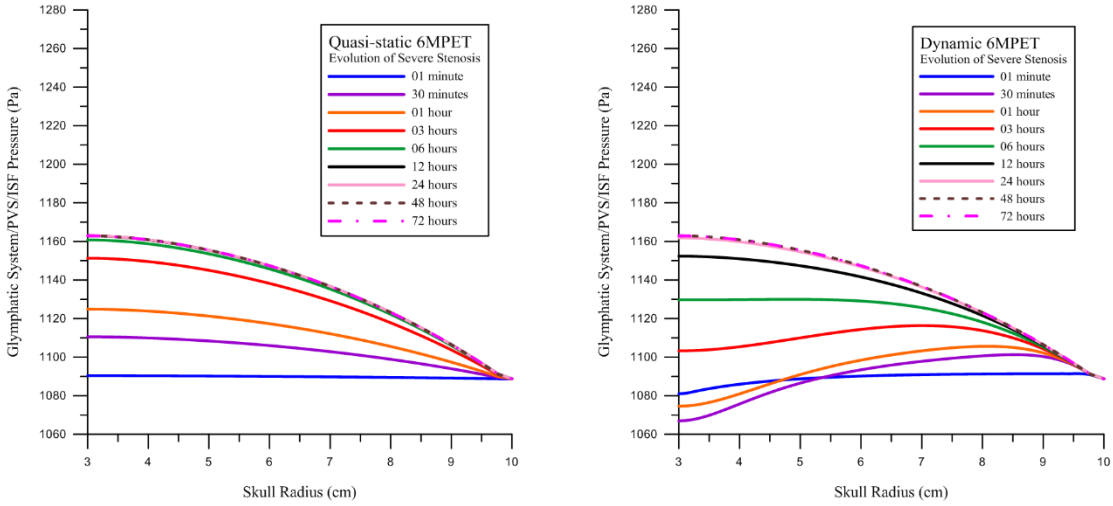


Figure 5.15 Comparison the glymphatic system/PVS/ISF pressure of the evolution of the quasi-static and dynamic 6MPET model. Upper-LHS: Quasi-static 4MPET; Upper-RHS: Quasi-static 6MPET; Lower-LHS: Dynamic 4MPET; Lower-RHS: Dynamic 6MPET.

Chapter 6 Cerebral Oedema

The Topic of this Chapter

For many common neurological disorders, cerebral oedema plays an important role associated with morbidity and death. The typical options of current treatments regimes mainly involve hyperosmolar agents and surgical decompression; these therapies have been utilised for 80 years. Modulating brain water transport via AQP4, which ultimately reduces cerebral oedema, was proposed by Manley et al. in 2000 and was published with experimental results (via a mouse model) in Nature Medicine [137]. In this chapter, an attempt will be made to explore the theme of this ongoing research, namely AQP4 inhibition. It will also be proposed that the compliance and water mobility of the glial cells may provide a new therapeutic perspective for reducing cerebral oedema through the use of the fully dynamic 6MPET model.

Manley et al. employ a well-established model of water intoxication [400], where water movement in the brain via an osmotic gradient generates cellular (cytotoxic) oedema (without disruption to the BBB). This model demonstrates that cerebral oedema decreased by 35% in AQP4-deficient mice. The same condition, water intoxication, will be mimicked by manipulating the compliance and water mobility of the glial cells compartment in the fully dynamic 6MPET model. This will show that the 6MPET model can capture not only elements within acute HCP (aqueductal stenosis) but also cerebral oedema. Specifically, cellular oedema will be investigated in this chapter. In order to set conditions corresponding to cellular oedema, it is assumed that there is no prescribed aqueductal stenosis, which means that a fully patent aqueduct is assumed, and no BBB disruption is enforced, which means the parameters relating to the capillary compartment are fixed, such as water mobility (κ^c), Biot-Willis coefficient (compliance, α^c) and transfer coefficient relating to water transport between the capillary and other compartments, as shown in Figure 3.3 ($\gamma_{a\leftrightarrow c}, \gamma_{v\leftrightarrow c}, \gamma_{l\leftrightarrow c}$). Based on Manley et al.'s conclusion [137], an alleviated cerebral oedema hypothesis, in which purely reducing

the water transport function of glial cells may alleviate cerebral oedema, shall be proposed here and tested via 6MPET. In 6MPET, there are two parameters related to water transport in glial cells compartment, i.e. water mobility (κ^{g}) and AQP4-deficient expression in the glial cells compartment. Since AQP4 on glial cells is highly related with the glymphatic system due to the end-feet regulating water via AQP4 channels [27, 401], the water mobility (κ^{l}) and AQP4-deficient expression in the glymphatic system/PVS/ISF compartment are manipulated as well in order to confirm this alleviated cerebral oedema hypothesis. The simulation results in this chapter are able to address that both the reduction of AQP4 expression (AQP4-deficient expression) and the reduction of water mobility in the glial cells compartment cause more alleviative ventricular shrinking (reduce cerebral oedema), as shown in Figure 6.1 (LHS) and Figure 6.2 (upper-RHS, middle-RHS and lower-RHS). These results are similar to the conclusion that Manley et al. made in Nature Medicine [137] and support the proposed hypothesis here. Furthermore, the detailed evolution of cerebral oedema will be shown in the following three cases:

i. The normal condition, which has normal water mobility in two compartments, glymphatic system/PVS/ISF and glial cells, ($\kappa^{l} = 1.75 \times 10^{-7}, \frac{m^4}{NS}$ and $\kappa^{g} = 5.0 \times 10^{-4}, \frac{m^4}{NS}$ respectively) and higher compliance in the glial cells compartment ($\alpha^{g} = 0.8$) with AQP4-deficient expression ($RF^{g} = 10.0$).
ii. Reducing the water mobility of the glial cells compartmental, normal water mobility in the glymphatic system/PVS/ISF compartment ($\kappa^{l} = 1.75 \times 10^{-7}, \frac{m^4}{NS}$ and $\kappa^{g} = 5.0 \times 10^{-5}, \frac{m^4}{NS}$ respectively). A higher compliance in the glial cells compartment ($\alpha^{g} = 0.8$) with an AQP4-deficient expression ($RF^{g} = 10.0$) is also applied.

iii. Lower water mobility in two compartments, glymphatic system/PVS/ISF and glial cells ($\kappa^l = 1.75 \times 10^{-8}, \frac{m^4}{NS}$ and $\kappa^g = 5.0 \times 10^{-5}, \frac{m^4}{NS}$ respectively), and higher compliance in the glial cells compartment ($\alpha^g = 0.8$) with AQP4-deficient expression ($RF^g = 10.0$), is considered in order to demonstrate the idea that the glial cell's compliance may affect the varying degree of the cerebral oedema as well.

First of all, the negative value of the ventricular displacement signifies that swelling of the brain parenchyma occurs in the vicinity of the ventricle wall. The varying degrees of brain parenchyma swelling were simulated by considering a patent aqueduct on the fully dynamic 6MPET model. The results are shown in the upper-LHS of Figure 6.1. The normal case reveals that there is little evidence of ventriculomegaly; however, the remaining permutations show that brain parenchyma swelling depends on the water mobility and compliance of the glial cells compartment. The lower water mobility of the glial cells compartment we set in the fully dynamic 6MPET model and this corresponded to reduced parenchyma swelling. Meanwhile, it seems that the pink line in the upper-LHS of Figure 6.1 has a sudden numerical jump phenomenon in the very beginning on the temporal scale for three days. However, this is a misinterpretation under closer inspection. Here, an additional inset in Figure 6.1 is provided on the short temporal scale for 120 *sec* to illustrate that this is not a numerical jump phenomenon. Regarding ventricular CSF pressure (upper-RHS, Figure 6.1), it seems that almost no pressure difference occurs in the different combinations of the water mobility and compliance of the glial cells compartment. Although there is negligible pressure difference for CSF at the ventricle wall, ventricular CSF pressure can be grouped using the compliance of the glial cells compartment. There are two groups of pressure values

for ventricular CSF pressure which depend on a pair of compliance values of the glial cells compartment, α^{g} = 0.8 (higher value of the ventricular pressure) and α^{g} = 0.9 (lower value of the ventricular pressure). Moreover, a similar trend of the results shown in the other two pressure compartments, glial cells and glymphatic system/PVS/ISF (lower-LHS and lower-RHS, respectively) is observed. The lower-LHS of Figure 6.1 shows the higher pressure group (~1361 Pa) comes from the larger glial cells compartmental compliance (α^{g} = 0.8), whilst the lower pressure group (~1210 Pa) comes from the smaller glial cells compartmental compliance (α^{g} = 0.9). Under the same glial cells compartmental compliance (α^{g} = 0.8), the lower water mobility of the glial cells compartment ($\kappa^{g} = 5.0 \times 10^{-5}, \frac{m^4}{NS}$) has lower ISF pressure at the ventricle wall (~1328 Pa), whilst the remaining mobilities of the glial cells compartment ($\kappa^{g} = 5.0 \times 10^{-3}, \frac{m^4}{NS}$ and $\kappa^{g} = 5.0 \times 10^{-4}, \frac{m^4}{NS}$) have almost the same ISF pressure at the ventricle wall (~1335 Pa). Generally, the pressure of the glial cells at the ventricle wall is higher than the ISF pressure at the ventricle wall for two groups of the glial cells compartmental compliance (α^{g} = 0.8 and α^{g} = 0.9). Interestingly, the compensatory behaviour is not apparent for the ISF pressure at the ventricle wall in the case involving cerebral oedema (lower-RHS, Figure 6.1). However, it does appear in the previously discussed cases involving aqueductal stenosis (lower-RHS, Figure 5.5 and 5.8) in the section 5.2.

In summary, the larger the glial cells compartmental compliance leads to the larger ventricular displacement according to the upper-LHS of Figure 6.1, obtained via the fully dynamic 6MPET model. These increasing pressure phenomena may be explained by the compensatory capability at the ventricles since the behaviour of the ventricular displacement shows that it is initially decreased and then subsequently increased before

reaching a steady state. The larger the ventricular pressure is showed in the upper-RHS of Figure 6.1, the lower-LHS of Figure 6.1 and the lower-RHS of Figure 6.1; the deeper the well depth (the compensatory capability) is showed in the upper-LHS of Figure 6.1 from the fully dynamic 6MPET model.

In order to clarify the relationship among varying degrees of cerebral oedema and water mobility/compliance under the AQP4-deficient expression condition (for the open aqueduct case on the fully dynamic 6MPET model), simulated results of the ventricular displacement were examined. These were obtained by altering water mobility in the glymphatic system/PVS/ISF and glial cells compartment, in addition to the compliance in the glial cells compartment, as presented in Figure 6.2. The upper-LHS of Figure 6.2 shows the ventricular displacement under the two variations in compartmental mobilities ($\kappa^l = 1.75 \times 10^{-6}, \frac{m^4}{NS}$ and $\kappa^g = 5.0 \times 10^{-3}, \frac{m^4}{NS}$), and the AQP4-deficient expression ($RF^g = 10.0$) accompanied by various compliances ($\alpha^l = 0.8$, $\alpha^l = 0.9$; $\alpha^g = 0.8$, $\alpha^g = 0.9$). The lower-RHS of Figure 6.2 shows the ventricular displacement under the two compartmental mobilities ($\kappa^l = 1.75 \times 10^{-8}, \frac{m^4}{NS}$ and $\kappa^g = 5.0 \times 10^{-5}, \frac{m^4}{NS}$) and the AQP4-deficient expression ($RF^g = 10.0$) accompanied by the various compliances ($\alpha^l = 0.8$, $\alpha^l = 0.9$; $\alpha^g = 0.8$, $\alpha^g = 0.9$). Both of these cases (maximum in upper-LHS and minimum in lower-RHS) are the extreme cases of water mobility in the glymphatic system/PVS/ISF and glial cells compartments considered for simulation. The difference between the LHS and RHS of Figure 6.2 is that in the LHS cases regarding water mobility of the glial cells compartment, there is a larger than the RHS cases of the water mobility of the glial cells compartment. Moreover, the parenchymal swelling at the ventricle wall in the LHS cases with the changing glial cells compartmental compliances is larger than the cerebral parenchyma swelling at the

ventricle wall in the RHS cases with the changing glial cells compartmental compliances. The detail metric values of the ventricular shrinking corresponding to Figure 6.2 are shown in Table 6.1. The smaller swelling phenomena of the cerebral parenchyma occur under the normal water mobility condition of the glymphatic system/PVS/ISF compartment, which is shown in the middle-LHS and middle-RHS of Figure 6.2. Meanwhile, the time span of development of the ventricular displacement in the case of the larger water mobility of the glymphatic system/PVS/ISF compartment ($\kappa^l = 1.75 \times 10^{-6}, \frac{m^4}{NS}$) with various glial cells compartmental compliances (red and green line, upper-LHS; red and green line, upper-RHS, Figure 6.2) are shorter than the time spans of the development of the ventricular displacement in the cases of the smaller water mobility of the glymphatic system/PVS/ISF compartment ($\kappa^l = 1.75 \times 10^{-8}, \frac{m^4}{NS}$) with various glial cells compartmental compliances (red and green line, lower-LHS; red and green line, lower-RHS, Figure 6.2). This larger time span occurs on the lower-RHS of Figure 6.2 may indirectly imply that the lower water permeability of the glymphatic system/PVS/ISF compartment and glial cells compartment try to protect itself against the cerebral oedema due to the tug of war between intracellular compartment and extracellular compartment via the mechanism of cerebral oedema [147, 402]. For the case where the mobilities are set as $\kappa^l = 1.75 \times 10^{-8}, \frac{m^4}{NS}$ and $\kappa^g = 5.0 \times 10^{-5}, \frac{m^4}{NS}$, along with the two glial cells compartmental compliances of $\alpha^{\mathrm{g}} = 0.8$ and $\alpha^{\mathrm{g}} = 0.9$, the cerebral parenchyma at the ventricle wall shows shrinkage behaviour in the beginning of 14 *minutes* and 12 *minutes*, respectively.

According to the simulation results in Figure 6.2 and Table 6.1, all of these may support the aforementioned hypothesis regarding the alleviated cerebral oedema. There

are two reasons that support this assertion. Firstly, the RHS column of Table 6.1 shows that altering the mobility of the glymphatic system/PVS/ISF compartment with AQP4-deficient expression does not significantly affect the ventricular shrinkage. For example, when only altering the mobility of the glymphatic system/PVS/ISF compartment, is an order of magnitude larger or an order of magnitude smaller than the normal case which is $\kappa^l = 1.75 \times 10^{-7}, \frac{m^4}{NS}$ (e.g. $\kappa^l = 1.75 \times 10^{-8}, \frac{m^4}{NS}$ and $\kappa^l = 1.75 \times 10^{-6}, \frac{m^4}{NS}$, respectively), the red line ($\alpha^g = 0.8$, $RF^g = 10.0$) cases in the RHS column of Table 6.1 are 0.216 *cm* and 0.217 *cm*, respectively. This implies that the glymphatic system/PVS/ISF compartment does not contribute to the function of reducing cerebral oedema. Secondly, three row cases in Table 6.1 show the same result, which the ventricular shrinkage is alleviated when the mobility of the glymphatic system/PVS/ISF compartment is fixed and the mobility of the glial cells compartment is decreased with AQP4-deficient expression condition. This implies that decreasing the mobility of the glial cells compartment has alleviated ventricular shrinkage. Therefore, the aforementioned hypothesis which states that purely reducing the water transport function of glial cells may alleviate the cerebral oedema could be supported based on the aforementioned reasons.

$\kappa^l = 1.75 \times 10^{-6}$, $\kappa^g = 5.00 \times 10^{-3}$ (m^4/NS)		$\kappa^l = 1.75 \times 10^{-6}$, $\kappa^g = 5.00 \times 10^{-5}$ (m^4/NS)	
α^g =0.8, RF^g= 10.0 (red line)	0.288 (cm)	α^g =0.8, RF^g= 10.0 (red line)	0.216 (cm)
α^g =0.9, RF^g= 10.0 (green line)	0.134 (cm)	α^g =0.9, RF^g= 10.0 (green line)	0.092 (cm)
α^l =0.8, RF^g= 10.0 (brown line)	0.000 (cm)	α^l =0.8, RF^g= 10.0 (brown line)	0.000 (cm)
α^l =0.8, RF^g= 10.0 (magenta line)	0.000 (cm)	α^l =0.8, RF^g= 10.0 (magenta line)	0.000 (cm)
$\alpha^{l,g}$=1.0, RF^g= 10.0 (orange line)	0.000 (cm)	$\alpha^{l,g}$=1.0, RF^g= 10.0 (orange line)	0.000 (cm)
$\alpha^{l,g}$=1.0, RF^g= 1.0 (blue line)	0.000 (cm)	$\alpha^{l,g}$=1.0, RF^g= 1.0 (blue line)	0.000 (cm)
$\kappa^l = 1.75 \times 10^{-7}$, $\kappa^g = 5.00 \times 10^{-4}$ (m^4/NS)		$\kappa^l = 1.75 \times 10^{-7}$, $\kappa^g = 5.00 \times 10^{-5}$ (m^4/NS)	
α^g =0.8, RF^g= 10.0 (red line)	0.096 (cm)	α^g =0.8, RF^g= 10.0 (red line)	0.046 (cm)
α^g =0.9, RF^g= 10.0 (green line)	0.063 (cm)	α^g =0.9, RF^g= 10.0 (green line)	0.033 (cm)
α^l =0.8, RF^g= 10.0 (brown line)	0.000 (cm)	α^l =0.8, RF^g= 10.0 (brown line)	0.000 (cm)
α^l =0.8, RF^g= 10.0 (magenta line)	0.000 (cm)	α^l =0.8, RF^g= 10.0 (magenta line)	0.000 (cm)
$\alpha^{l,g}$=1.0, RF^g= 10.0 (orange line)	0.000 (cm)	$\alpha^{l,g}$=1.0, RF^g= 10.0 (orange line)	0.000 (cm)
$\alpha^{l,g}$=1.0, RF^g= 1.0 (blue line)	0.000 (cm)	$\alpha^{l,g}$=1.0, RF^g= 1.0 (blue line)	0.000 (cm)
$\kappa^l = 1.75 \times 10^{-8}$, $\kappa^g = 5.00 \times 10^{-3}$ (m^4/NS)		$\kappa^l = 1.75 \times 10^{-8}$, $\kappa^g = 5.00 \times 10^{-5}$ (m^4/NS)	
α^g =0.8, RF^g= 10.0 (red line)	0.274 (cm)	α^g =0.8, RF^g= 10.0 (red line)	0.217 (cm)
α^g =0.9, RF^g= 10.0 (green line)	0.146 (cm)	α^g =0.9, RF^g= 10.0 (green line)	0.114 (cm)
α^l =0.8, RF^g= 10.0 (brown line)	0.000 (cm)	α^l =0.8, RF^g= 10.0 (brown line)	0.000 (cm)
α^l =0.8, RF^g= 10.0 (magenta line)	0.000 (cm)	α^l =0.8, RF^g= 10.0 (magenta line)	0.000 (cm)
$\alpha^{l,g}$=1.0, RF^g= 10.0 (orange line)	0.000 (cm)	$\alpha^{l,g}$=1.0, RF^g= 10.0 (orange line)	0.000 (cm)
$\alpha^{l,g}$=1.0, RF^g= 1.0 (blue line)	0.000 (cm)	$\alpha^{l,g}$=1.0, RF^g= 1.0 (blue line)	0.000 (cm)

Table 6.1 Values of ventricular shrinking corresponding to Figure 6.2.

6.1 The evolution of the brain oedema

In this section, three cases, including CASE (A): the normal water mobility of both glymphatic system/PVS/ISF and glial cells compartment, CASE (B): the normal water mobility of the glymphatic system/PVS/ISF compartment but lower water mobility of the glial cells compartment, and CASE (C): the lower water mobility of both glymphatic system/PVS/ISF and glial cells compartment, are considered for analysis. The reason why it is pertinent to compare CASE (A) and (B) is that there may be a link between reducing water mobility of the glial cells compartment, which may assist to alleviate cerebral oedema especially based on the previous analysis via 6MPET, according to our hypothesis of alleviated cerebral oedema [137, 382, 402, 403]. Intuitively speaking, this idea arises from the two red curves (α^g = 0.8, RF^g = 10.0) of

the middle-LHS and middle-RHS in Figure 6.2. From the red line ($\alpha^g = 0.8$, $RF^g = 10.0$) of the middle-LHS to the red line ($\alpha^g = 0.8$, $RF^g = 10.0$) of the middle-RHS in Figure 6.2, we could argue that parenchyma shrinking at the ventricle wall depends on reducing the water mobility of the glial cells compartment. However, this only addresses the shrinking phenomena at the ventricle wall. Hence, CASE (A) (Figure 6.3 and 6.4) and (B) (Figure 6.5 and 6.6) show further spatiotemporal analysis for displacement, pressure and increment of fluid content in order to prove that reducing the water mobility of the glial cells compartment may assist to alleviate brain oedema.

In Figure 6.3, upper-LHS, the evolution of the parenchymal tissue displacement along the radial direction is shown. The parenchymal region in the vicinity of the ventricles (3.0 *cm* to ~3.5 *cm*) exhibits ventricular shrinkage. In other words, the parenchymal tissue is stretched which causes ventricular shrinkage in the periventricular region. As already mentioned, the brain parenchyma initially swells toward the centre point of the ventricle. However, it then shrinks in the proximal periventricular region (~4.0 cm to 5.0 cm).

The parenchymal tissue displacement reaches a steady-state after 24 hours in the upper-LHS of Figure 6.3. The distribution of the CSF/ECF pressure along the radial direction presents the trend of the increasing parabola-open-downward shape with two fixed pressure points (ventricle wall and skull) on the upper-RHS of Figure 6.3. These curves illustrate that the CSF/ECF pressure increases within the brain parenchyma with time, but does not fluctuate at the ventricle wall. On the lower-LHS of Figure 6.3, the pressure of the glial cells is gradually decreased from the ventricle wall (3.0 *cm*) to the skull (10.0 *cm*), but the difference of the pressure of the glial cells at these two points is not substantial (~ 2 *Pa*). The glymphatic system/PVS/ISF pressure arises from the

proximal periventricular region to the ventricle wall on the lower-RHS of Figure 6.3. The starting point of the raising pressure migrates from around 4.5 *cm* to 5.0 *cm*, and the starting point of the pressure drop migrates 9.5 *cm* to 7.0 *cm* with the time. Between these two points, the pressure almost keeps a constant value before the glymphatic system/PVS/ISF pressure reaches a steady state (~ 6 hours). Moreover, the increment of fluid content for CSF/ECF, glial cells, and glymphatic system/PVS/ISF (upper-LHS, upper-RHS and lower-LHS; Figure 6.4, respectively) show overlapping characteristics. The only difference among these three cases of fluid content is that the magnitude of the glial cells fluid content is the lowest. Fluid drainage occurs in the periventricular region and the region at the skull from 8.25 *cm* to 10 *cm*, depending on time evolution. Regarding the evolution of the volumetric strain results on the lower-RHS of Figure 6.4, the reason why a sharp jump is visible near the skull is that the boundary condition for displacement at the skull sets to zero for the adult's brain, shown in Eqn. (3.41).

Different results can be seen on the lower-LHS of Figure 6.5 which represent the evolution of the pressure of the glial cells, whilst the upper-LHS of Figure 6.5 represents the evolution of the parenchymal tissue displacement. Regarding the hook-like shapes are observed in the upper-LHS of Figure 6.1, these phenomena at the ventricular side may be illustrated by the compensatory capability as previously mentioned. Since this behaviour occurs at the ventricular side, it also affects the behaviour of the parenchymal tissue displacement around the periventricular space shown in the upper-LHS of Figure 6.5. Therefore, we may speculate that the compensatory capability should have a buffer region which is the periventricular space. Furthermore, the pressure difference for each curve between ventricle and skull is larger than those on the lower-LHS of Figure 6.3 due to the reduced water mobility of the glial cells compartment. The spatial pressure behaviour on the lower-LHS of Figure 6.5 may

be able to explain the formation of cytotoxic oedema. One of the causes of cytotoxic oedema formation is that extracellular Na+ and other cations enter into glial cells and accumulate intracellularly. This, as mentioned in the section 1.2.4.1 [136, 404], could be the result of the intracellular pressure of the glial cells being lower than the extracellular pressure. Hence, this phenomenon may be explained by the spatial glial cells pressure with lower water mobility of the glial cells compartment on the lower-LHS of Figure 6.5, which is generally lower than the spatial glial cells pressure with the normal condition of the water mobility of glial cells compartment on the lower-LHS of Figure 6.3. The swelling level of the brain parenchyma at the ventricle wall means the ventricular shrinkage around the periventricular region on the upper-LHS of Figure 6.5 is lower than those on the upper-LHS of Figure 6.3. In other words, this alleviated ventricle shrinkage condition is caused by the lower water mobility of the glial cells compartment. This reduced ability of water movement through the porous media of glial cells may indirectly play a role in diminishing the ions to protect the cerebral parenchyma [136, 337, 405]. Therefore, these two differences, e.g. the ventricular shrinkage and the spatial glial cells pressure behaviour, imply that the lower water mobility of the glial cells not only affects the swelling level of the brain parenchyma in the periventricular region, but also affects the magnitude of the pressure gradient of the glial cells along the radial direction of the brain. This causes more water accumulation in glial cells at the ventricle wall than at the skull, due to the spatial glial cells pressure rise toward the ventricle wall.

Although the different time evolutions of the swelling parenchyma in the periventricular region (from blue to magenta line, upper-LHS, Figure 6.7) are larger than the swelling observed in CASE (A) and (B) (upper-LHS, Figure 6.3; upper-LHS, Figure 6.5, respectively), the expansion of the brain parenchyma between 5.25 *cm* to

10 *cm* for each time evolution (from blue to magenta line, upper-LHS, Figure 6.7) are smaller than the expansion of the brain parenchyma around the same region in CASE (A) and (B). The pressure of the glial cells in CASE (C) (lower-LHS, Figure 6.7) shows a smaller pressure difference between the ventricle wall and skull in the steady state, but larger pressure differences between the ventricle wall and skull continue to occur before six hours. The CSF/ECF pressure in CASE (C) (upper-RHS, Figure 6.7) also present a parabola-open-downward shape which is more symmetric than other two CSF/ECF pressure in CASE (A) and (B) (upper-RHS, Figure 6.3 and 6.5, respectively). The glymphatic system/PVS/ISF pressure still possesses the rising pressure from the proximal periventricular region to the ventricle wall, but the central region (from 4.5 *cm* to 8.5 *cm*) does not show the constant pressure type anymore during the transient stages, seen on the lower-RHS of Figure 6.7. However, constant pressure occurs from 3.0 cm to 8.5 cm when they are in the steady state. This distribution of the pressure in the steady state is totally different to those on the lower-RHS of Figure 6.3 and 6.5 which are gradually decreasing. This constant glymphatic/PVS/ISF pressure behaviour on the RHS of Figure 6.7 results from the reducing water mobility of the glymphatic system/PVS/ISF compartment and implies that the bulk flow in this region could not work well due to almost no pressure difference to drive it and the swelling interstitial space [401].

In short, both reducing water mobility and compliance in glial cells compartment can be major conditions alleviating oedema in the human brain according to the simulation results shown in Figure 6.1 and 6.2 under the same condition of the AQP4-deficient expression ($RF^{g} = 10$). The above observations imply that when slowing the water transport through the cellular compartment, there is a reduction in the cell compliance of the glial cells and increasing the inhibition for AQP4 in human brain

may be a potential direction for drug design to provide an alternative way to solve cerebral oedema in the future, thereby decreasing the morbidity and death associated with many common neurological disorders. This suggestion is not only similar to some previous research results, (AQP4 inhibitors might slow the accumulation of oedema in the brain [91, 137, 147, 337, 402, 403, 405]), but also supports the hypothesis of alleviated cerebral oedema that we proposed above.

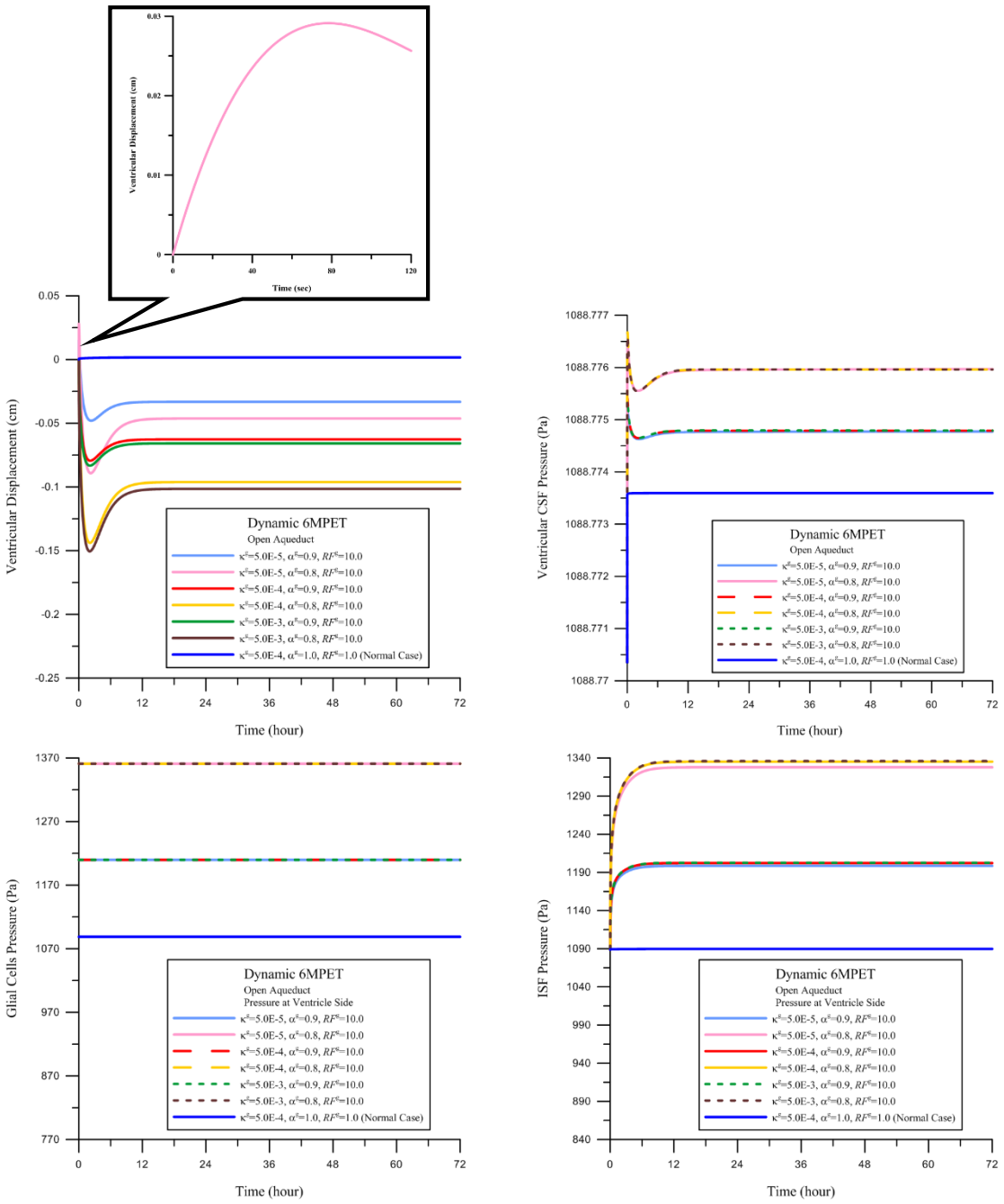


Figure 6.1 The progressing oedema level is mainly alleviated by the AQP4-deficient expression, the reducing water mobility and compliance of the glial cells compartment. The comparison of the ventricular displacement (Upper-LHS) and CSF pressure (Upper-RHS), and the pressure of the glial cells (Lower-LHS) and ISF pressure (Lower-RHS) at the ventricle side using various values of the water mobility (κ^g) and compliance (α^g) in the glial cells compartment with AQP4-deficient expression of the glial cells (RF^g) vs. time course.

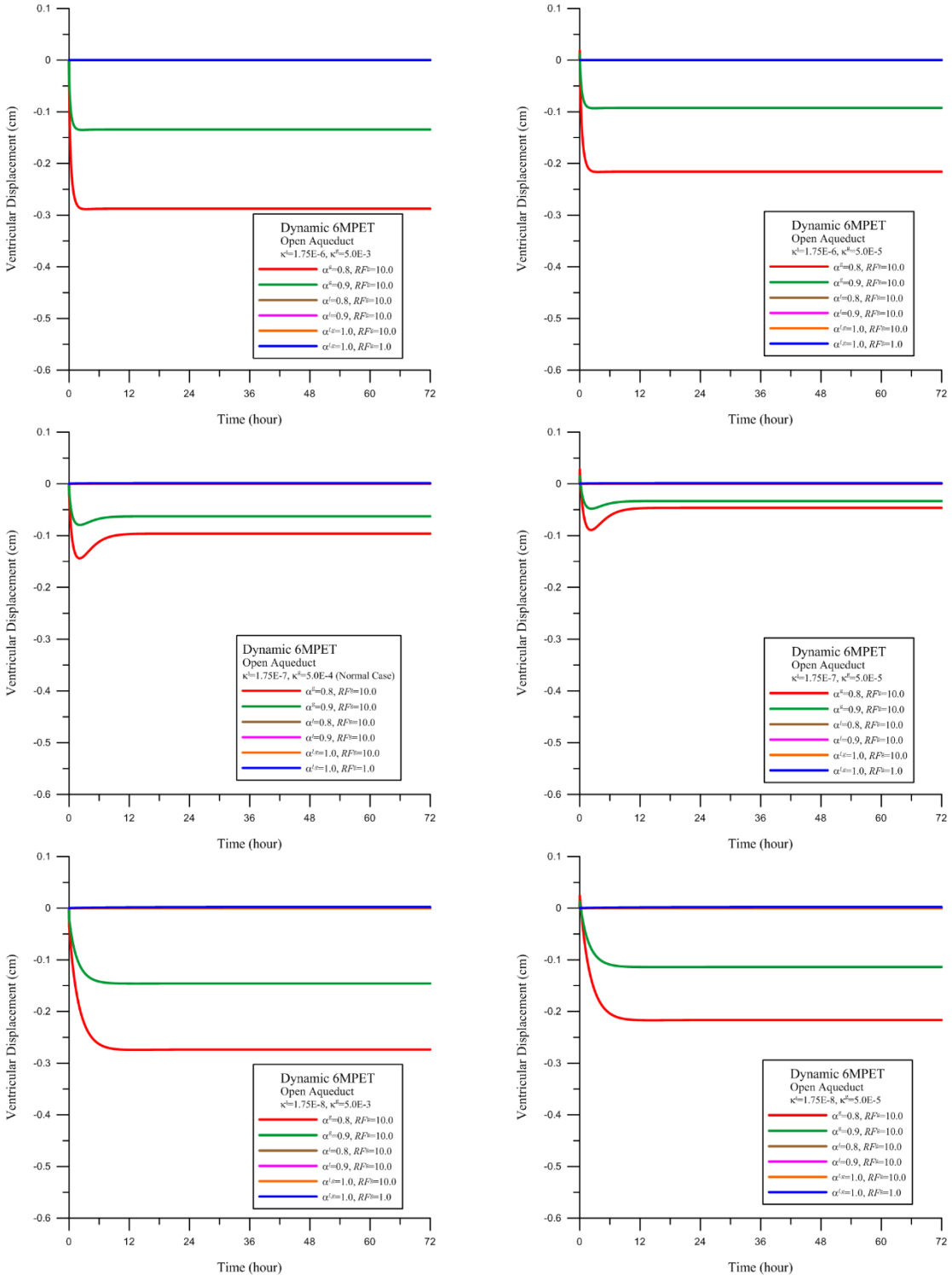


Figure 6.2 Ventricular displacement of the open aqueduct case, using different combinations of two compartmental mobilities and various compliances of the glial cells compartment with the AQP4-deficient expression for the open aqueduct on the fully dynamic 6MPET model.

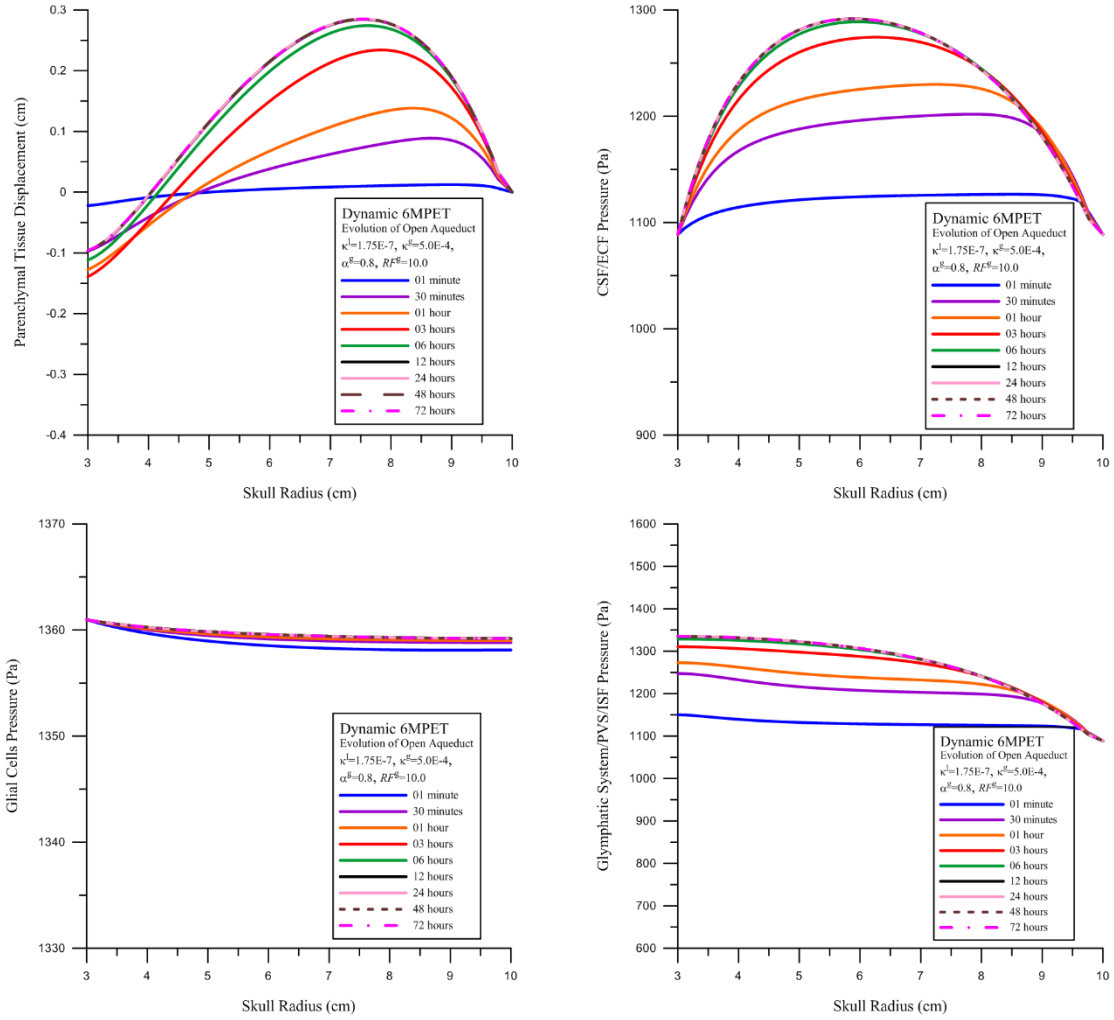


Figure 6.3 CASE (A): Evolution of the open aqueduct with the second order discretised scheme on the fully dynamic 6MPET model. Upper-LHS: Parenchymal tissue displacement vs. skull radius; Upper-RHS: CSF/ECF pressure vs. skull radius. Lower-LHS: Glial cells pressure vs. skull radius; Lower-RHS: Glymphatic system/PVS/ISF pressure vs. skull radius.

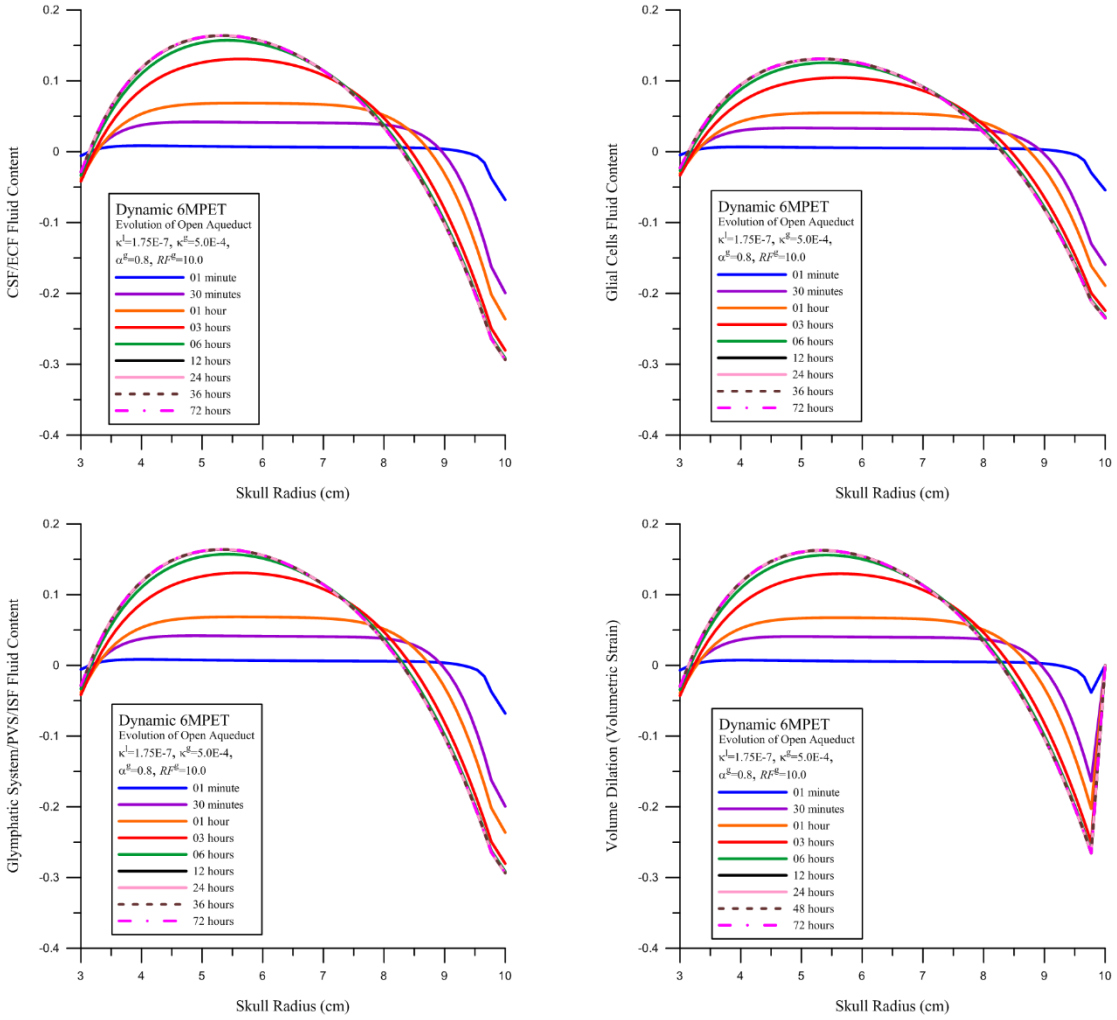


Figure 6.4 CASE (A): Evolution of the fluid content and volume dilation for the open aqueduct with the second order discretised scheme on the fully dynamic 6MPET model. Upper-LHS: CSF/ECF fluid content vs. skull radius; Upper-RHS: Glial cells fluid content vs. skull radius; Lower-LHS: Glymphatic system/PVS/ISF fluid content vs. skull radius; Lower-RHS: volume dilation (volumetric strain) vs. skull radius.

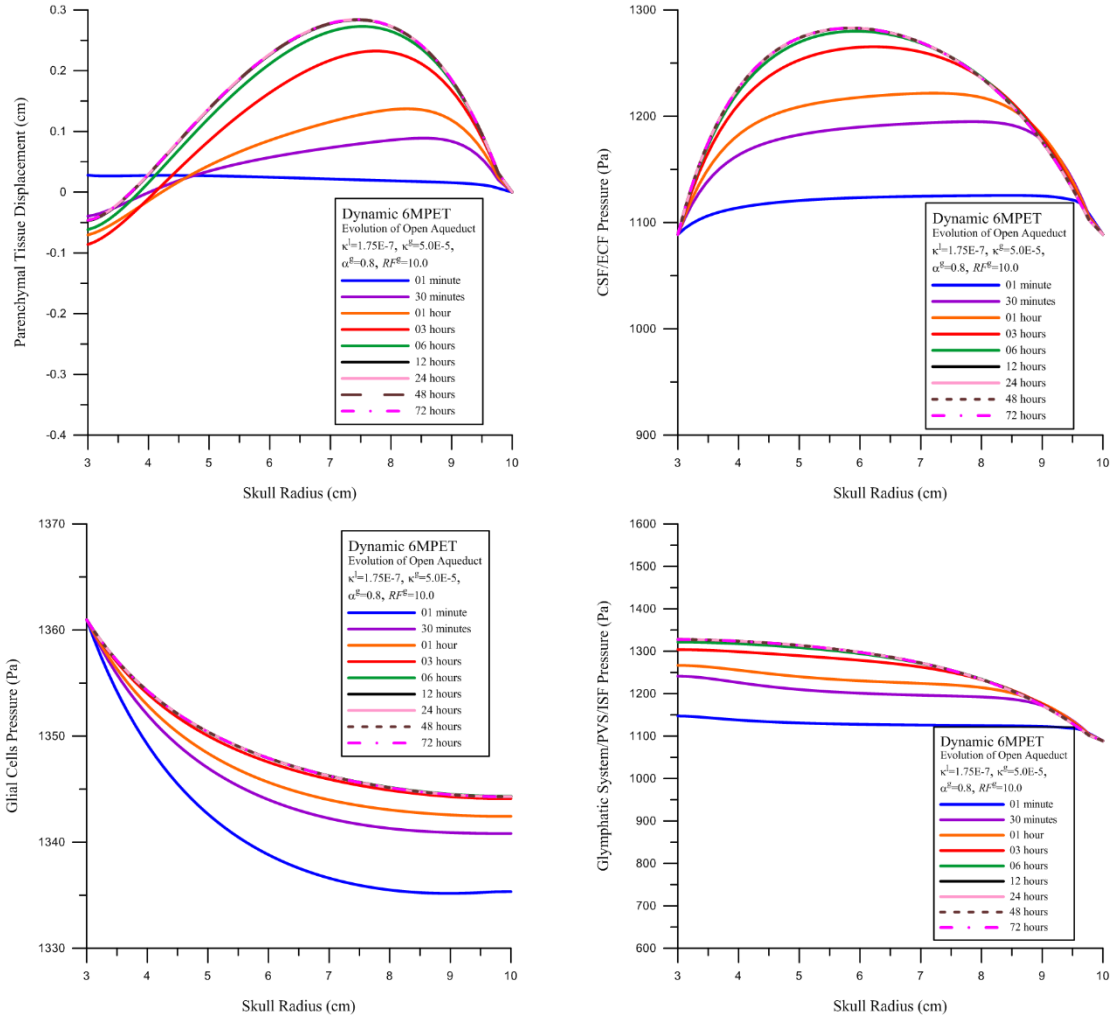


Figure 6.5 CASE (B): Evolution of the open aqueduct case, with the second order discretised scheme on the fully dynamic 6MPET model. Upper-LHS: Parenchymal tissue displacement vs. skull radius; Upper-RHS: CSF/ECF pressure vs. skull radius; Lower-LHS: Glial cells pressure vs. skull radius; Lower-RHS: Glymphatic system/PVS/ISF pressure vs. skull radius.

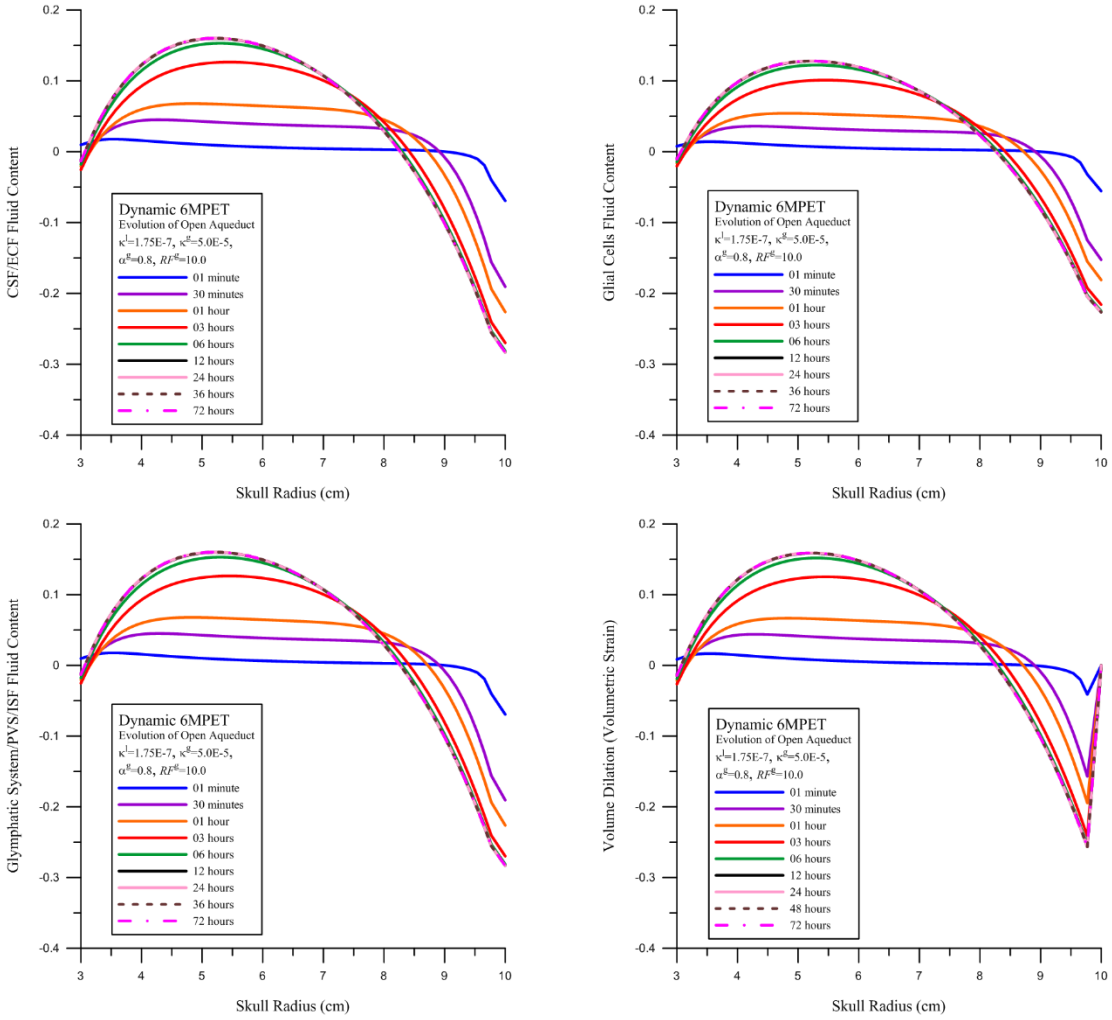


Figure 6.6 CASE (B): Evolution of fluid content and volume dilation for the open aqueduct with the second order discretised scheme on the fully dynamic 6MPET model. Upper-LHS: CSF/ECF fluid content vs. skull radius; Upper-RHS: Glial cells fluid content vs. skull radius; Lower-LHS: Glymphatic system/PVS/ISF fluid content vs. skull radius; Lower-RHS: Volume dilation (volumetric strain) vs. skull radius.

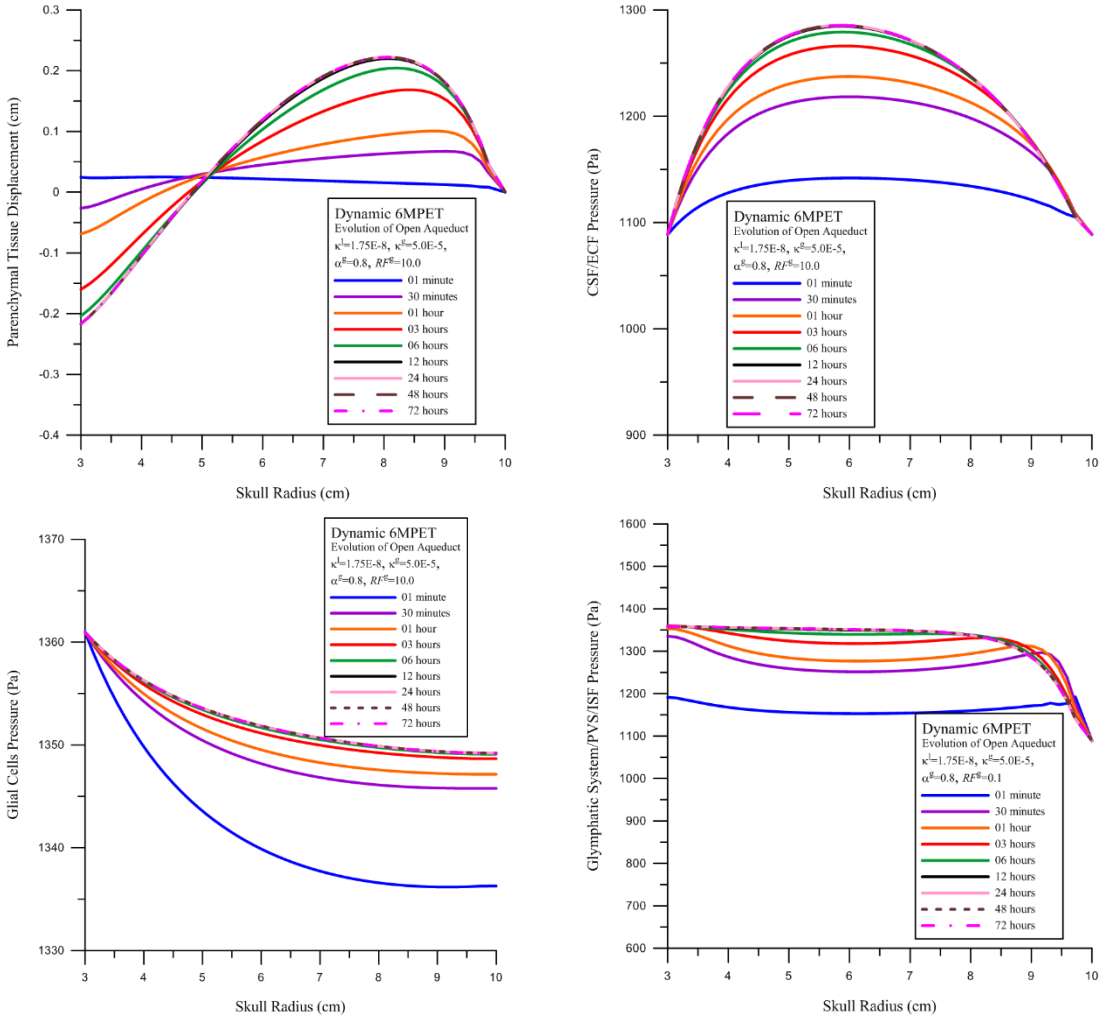


Figure 6.7 CASE (C): Evolution of the open aqueduct with the second order discretised scheme on the fully dynamic 6MPET model. Upper-LHS: Parenchymal tissue displacement vs. skull radius; Upper-RHS: CSF/ECF pressure vs. skull radius; Lower-LHS: Glial cells pressure vs. skull radius; Lower-RHS: Glymphatic system/PVS/ISF pressure vs. skull radius.

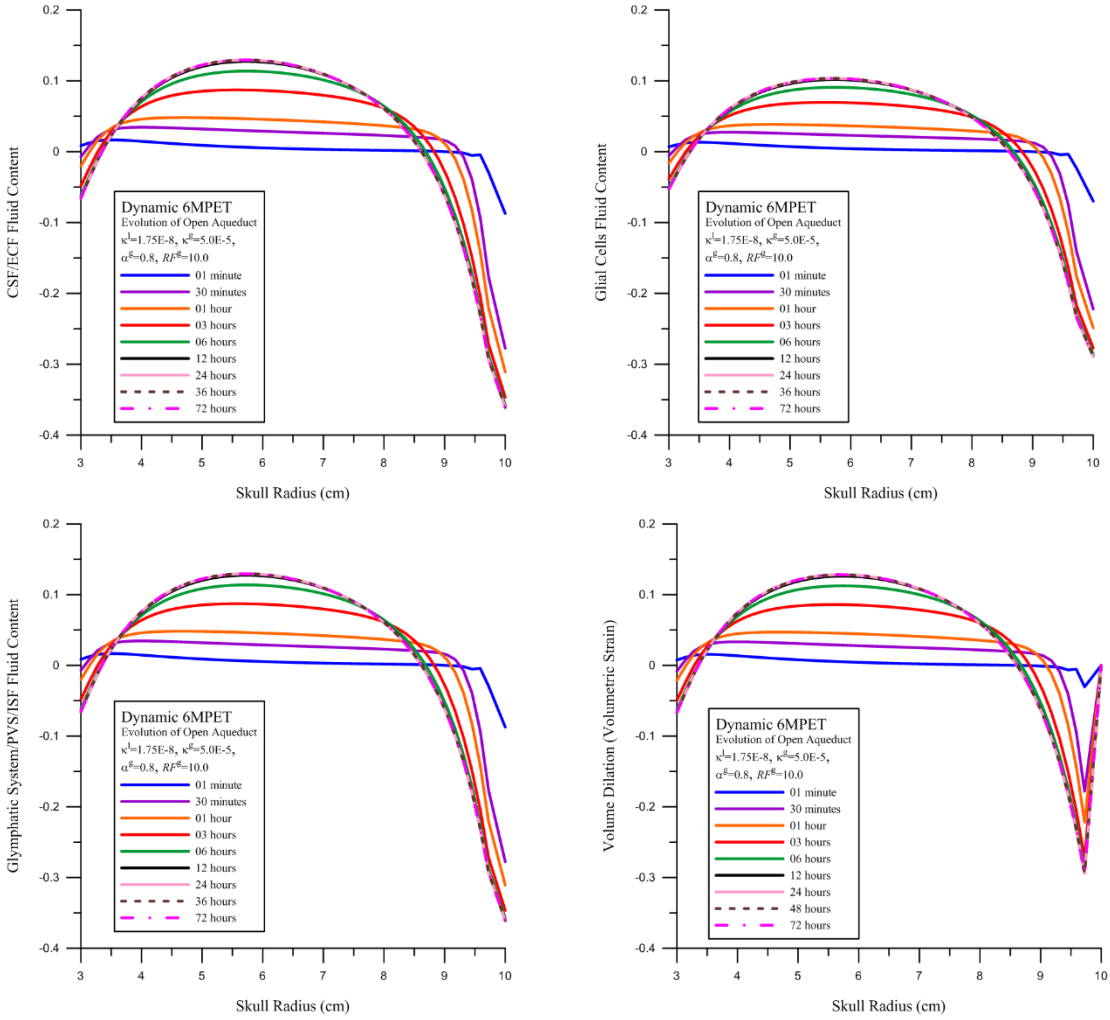


Figure 6.8 CASE (C): Evolution of the fluid content and volume dilation for the open aqueduct with the second order discretised scheme on the fully dynamic 6MPET model. Upper-LHS: CSF/ECF fluid content vs. skull radius; Upper-RHS: Glial cells fluid content vs. skull radius; Lower-LHS: Glymphatic system/PVS/ISF fluid content vs. skull radius; Lower-RHS: Volume dilation (volumetric strain) vs. skull radius.

Chapter 7 Conclusions and Future Work

The Topic of this Chapter

It has been shown that both 4MPET and 6MPET may depict acute hydrocephalus and oedema formation in the brain. It was also concluded that the 6MPET is better suited for capturing more intricate aspects of the multiscale fluid exchange. Poroelasticity theory had been well recognised to deal with porous media in biological problems, due to its ability to provide meaningful spatiotemporal information deriving from both physics and the relevant physiology. This chapter will present conclusions and possibilities for future work.

7.1 Conclusions

The aim of this dissertation was to compare simulation results obtained through the fully dynamic 4MPET extension to Tully's original formulation [164, 233, 265], and to propose a novel model, the 6MPET, which is more aptly suited for describing the multiscale water transport phenomena in the cerebral environment. Tully's original work for the 4MPET model contributed the quasi-steady state results and a careful large scale parametric estimation study seeking the suitable transfer coefficients range for compartmental communication to each other at the source term of the system equations. Therefore, the further contribution in this dissertation for the 4MPET model is based on Tully's work to move forward to realise the ultimate consequence of 4MPET which is fully considering the spatiotemporal terms in whole system equations with the inertial terms of each compartment [269]. Moreover, the extension of 6MPET to the more intricate understanding of the glymphatic pathway is developed through the addition of compartments in order to better mimic the parenchymal volume [27]. Glial cell water pressure-flux relationships are also being developed in collaboration with experiments

as a means of informing the macroscopic MPET framework. This allows for the possibility to decipher some of the underlying complexities of neurological disorders, such as those evident in HCP. It is necessary to evaluate the advantages and disadvantages of the approaches propose, before drawing any conclusions in this chapter (shown in Table 7.1). For investigating cerebral disorders, the 4MPET model adequately captures the essential phenomena of aqueductal stenosis. 6MPET is generated for the specific purpose of providing an alternative way to do further investigative research regarding HCP and cerebral oedema. The simulation results of 6MPET were demonstrated in previous chapters and compared with 4MPET in order to assure the conclusions drawn are reliable via the quasi-static 4MPET model which was already published by Tully et al. [233]. The conclusions reliability argument means that the trends of the quasi-static 6MPET model correspond well to the trends of the quasi-static 4MPET model. We believe this holds, due to three main reasons:

i. The quasi-static 4MPET model provides the steady-state results in the cerebral parenchyma, as well as evolution results on the boundary (the ventricular wall and ventricular pressure behaviour). Based on the quasi-static results of the 4MPET model from Tully works [164, 233], the quasi-static 6MPET model in the overlap compartments, i.e. arterial/arteriole blood (*a*), capillary blood (*c*), vein/venule blood (*v*) and the CSF/ISF (*e*) space, should produce similar results to 4MPET. This expectation is met, as discussed previously.

ii. Regarding the overlap compartments from the quasi-static 4MPET and 6MPET models, their differences are on the source terms due to different conceptual transfer routes in the cerebral environment, e.g. 6MPET makes the glymphatic system/PVS/ISF compartment as a hub and other

compartments are the spokes, but 4MPET does not have this compartment. Although these differences exist in each compartment's equation, both of these models (4MPET and 6MPET) should produce comparable results for the common compartments. This expectation is also mostly met.

iii. As mentioned before in the section 3.4.3, Tully et al. via a careful large-scale parametric study on the HPC cluster analysed transfer coefficients and identified suitable and physiologically relevant/importance ranges of those coefficients for the 4MPET quasi-steady model [164, 233]. The transfer coefficients in 6MPET (mentioned in the section 3.4.3 as well) are deduced from some related experimental data and then assembled by Eqn. (3.65) [244, 268, 372, 381-384]. Due to these two different ways to obtain the transfer coefficients for 4MPET and 6MPET, results of the overlap compartments that demonstrate compatibility lend further confidence in supporting the suitability of these models to mimic the cerebral transport processes.

Although 6MPET is better suited than 4MPET to explore the enigma of neurological disorders in cerebral environment, 4MPET is still a suitable model in the initial stage of research at the scale of the organ – possibly not just the brain but also renal oedema in the urinary system, pulmonary oedema in the respiratory system and chemosis (conjunctival oedema) [406-412]. The reason why 4MPET is a suitable model for general organ level research is that most of the organ systems in the human body are fundamentally assembled by four compartments, e.g. arterial/arteriole compartment, capillary compartment, venous/venule compartment and CSF/ISF compartment, which are similar with the compartments in the 4MPET described in this work. Alternatively, when the model would like to consider the lymphatic system, it is expandable to include

the extra compartment, the lymphatic compartment, as the 5MPET model. Therefore, choosing 4MPET, 5MPET or 6MPET to be the modelling tool of choice should be dependent on the specific investigation at hand. Even though 6MPET is promoted here, there are some limitations and disadvantages that have persisted. The computational expense is one of the challenging issues connected with 6MPET. Since two more compartments are added in 6MPET, the system matrix of 6MPET ($[N \times 6 \times N \times 6][N \times 6] = [N \times 6]$) is substantially larger than the system matrix of 4MPET ($[N \times 4 \times N \times 4][N \times 4] = [N \times 4]$). Future work will entail dealing specifically with sparse matrices, in order to reduce the overall computational expense. The consistency of the results which are shown in the section 4.3 between the first and second accurate discretisation schemes demonstrate that using fewer nodes and larger time step size via the second order accurate discretisation scheme is able to obtain results with acceptable convergence, as compared to more nodes and a smaller time step via the first order accurate discretisation scheme. Hence, the second order accurate discretisation scheme was used in this work. The numerical consistency was demonstrated in the section 4.3 in order to prove that fewer nodal points are employed and less computational run time is necessary to obtain similar and reasonable simulation results comparing Tully's results (using 81 nodal points) [164].

The limitations surrounding the proposed MPET models include the use of a linear stress-strain relationship and various mechanical properties (e.g. shear modulus and Poisson's ratio) as well as other parameters (e.g. CP production rate, CSF absorption rate via AG, specific storage coefficient, Biot-Willis coefficient, mobility, transfer coefficient and AQP4 expression factor) which are considered to be constant. All these simulation results must be assessed with more assumptions in mind like the reduction of the system to a spherical geometry, assigning material properties does not come from

the same research sources and the pulsatility of the fluid compartments –importantly the arterial one – is ignored.

Some important mechanisms have been confirmed via the 6MPET model, and shown in the previous chapters, including compensatory trans-ependymal flow response in chapter 6 (indirectly confirmed with glymphatic system/PVS/ISF pressure compartment based on the assumption of the altered water channels expression, AQPs, via the starling force relation), AQP4 overexpression with applied severe aqueductal stenosis (directly confirmed the conclusion from Bloch et al [146] with the simulation results at the RHS of Figure 5.9) in chapter 6 and AQP4-deficient expression with a patent aqueduct (healthy, no obstructive mechanism) directly confirmed the conclusion from Manley et al. [137] with the simulation results in Figure 6.1 and 6.2). Likewise, the fully dynamic 4MPET model can potentially be a powerful tool that may be applied on research at organ level for a variety of organs, as mentioned earlier. Some possible avenues for future work in the next section may be considered in order to potentially mould more powerful and realistic 4MPET and 6MPET templates for assisting to probe some enigmatic problems in medicine and biology.

Model	Advantages	Defects
Quasi-static 4MPET	• Easier to have analytic solutions • Allow a thorough investigation of properties over the time scale • Good for startup in the first stage of the research	• Transient behaviour is ignored • More insufficient details for cerebral environment, e.g. temporal insensitivity, no glial cells, no AQPs effect, no fluid content
Fully Dynamic 4MPET	• Computational efficiency • Transient behaviour is observed • Good for general system study	• Harder to have analytic solutions • Insufficient detail for cerebral environment, e.g. no glial cells, no AQPs effect

Quasi-static 6MPET	• Easy to have analytic solutions • Specific design for brain study • Multiscale modelling • Specific design for brain study	• Computationally expensive • Transient behaviour is ignored
Fully Dynamic 6MPET	• Multiscale modelling • Specific design for brain study	• Hardest to have analytic solutions • Computationally expensive

Table 7.1 The advantages and disadvantages for the MPET templates.

7.2 Future Work

Since some limitations which will be mentioned in the following exist in 4MPET and 6MPET at the current stage of research, these limitations create a space allowing one to move forward in terms of model improvement. Additionally, with the extension from 4MPET to 6MPET in this thesis, it is shown that a highly extensible model, MPET, has some strongly exploratory applications (not necessarily restricted to the biomedical engineering field). In this section, some improvements and research will be listed in order map possible avenues for future work.

7.2.1 Model Improvements

According to Table 7.1, it seems that reducing a heavy burden of the calculation is one of the major issues for the next step before attempting to tackle the three-dimensional model. Since the matrix (not treated as sparse) in the one-dimensional fully dynamic MPET model already created a heavy calculation loading which has been explained in the previous section 7.1 depending on the number compartments of the network in MPET, e.g. 6MPET are more cumbersome than 4MPET, it is necessary to introduce specialised algorithms for solving MPET. From this point of view, using Boundary

Element Method (BEM) or Boundary Integral Equations (BIE) to exhibit MPET may be considered as an alternative way for facing the real three-dimensional patient-specific case because of the complex three-dimensional geometry resulted in huge numbers of the mesh node. Although using BIE will meet the nearly singular points problem due to the surface of the cortex composed of ridges (gyri) and grooves (sulci), it should still be kept in mind (for reducing the calculation burden) as an advantage when dealing with the patient-specific subjects. Moreover, seeking analytic solutions of 4MPET and 6MPET is another research direction in order to profoundly understand the mathematical behaviour of these models. The expectable benefits on the numerical approach for obtaining analytic solutions are not only for the accuracy validation, but also for the numerical stability analysis. Meanwhile, the values of the parameters in 6MPET can be further confirmed via validation, such as specific storage coefficients, compliances, water mobilities and transfer coefficients for the healthy human case, but also for patient-specific subjects and for each compartment of 6MPET.

Besides the computational cost issue, system validation and stability mentioned above, the pulsatile boundary condition for fluid compartments, e.g. cerebrovascular, CSF, and glymphatic system/PVS/ISF compartment, should be considered for improved 6MPET setup in the future. The pulsatile nature of CSF flow through the open aqueduct confirmed in vivo by MRI can be related to the change in cerebrovascular volume via the heartbeat [242, 413], breathing and other slower variations. With this concept, data from MRI giving physical parameters to computational models can be considered [292, 295, 414-416].

In addition to the pulsatile nature of CSF flow and cerebrovascular volume via the heartbeat, PVS and glymphatic system are another essential flow route for ISF and

solute transport associated with the heartbeat [417, 418]. Some theoretical models have been proposed, though limited [387, 419, 420]. Therefore, this is another beneficial conduit for future work in order to supply these proposed model and may be able to discover the enigma which was addressed by Smith and his colleagues using conventional understanding shown in Figure 7.1, specifically, to challenge the glymphatic system hypothesis in Trends in Neuroscience in 2015 [119].

Combining MPET with CFD is also another critical step forward for future work to investigate the two-way coupling of fluid-structure interaction (FSI) phenomena. Additionally, it is important for altering some currently constant parameters to dynamic functions, in order to make the MPET better resemble realistic conditions, such as the dynamic pressure-dependent AQP4 expression and the dynamic strain-dependent (non-linear) mobility. In earlier work, some of the authors already utilised non-linear (strain-dependent) permeability to investigate cerebral and arterial in hydromechanics under steady state condition via poromechanics, such as Kaczmarek et al. [374]; Klachnar & Tarbell [421], respectively. More recently, Sobey and Wirth used non-linear (strain-dependent) permeability to probe HCP and apply non-linear permeability in a small strain poroelastic framework [385]. The shape change of the ventricle which is able to associate with a characteristic feature of the non-linear (strain-dependent) permeability was proposed in this research work. Moreover, they also applied the strain-dependent (non-linear) permeability on an axisymmetric and fully 3D poroelastic model to investigate the HCP problem and proposed two conclusions related to the non-linear strain-dependent permeability, i.e. an important step towards realistic simulations of HCP evolution and treatment and associated with NPH [375].

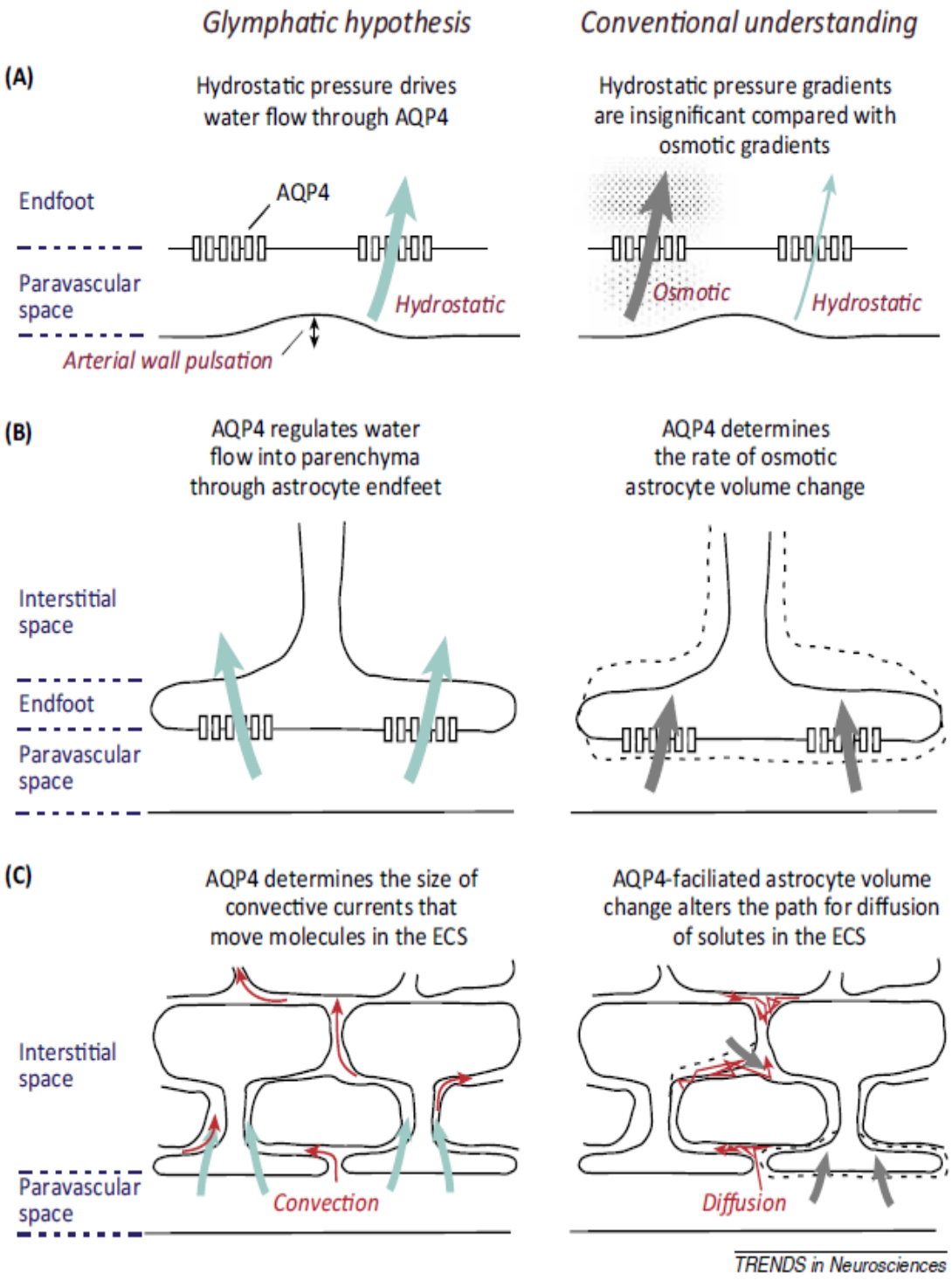


Figure 7.1 The glymphatic hypothesis and conventional understanding of the AQP4 role in brain water movement. (A) The glymphatic hypothesis proposes the hydrostatic pressure driven water flow via the endfeet of the glial cells; transmembrane flow in response to the hydrostatic pressure is smaller than the osmotic pressure gradients in conventional understanding. (B) For the glymphatic hypothesis, water flows via AQP4 of the endfeet on the glial cells to drive convection in the parenchyma; water flow results in cell swelling (or shrinking) until osmosis reaching steady-state in conventional understanding. (C) For the glymphatic hypothesis, AQP4-facilitated convective water flow drives solutes; conventionally, AQP4 regulates diffusion effects in ECS [119].

7.2.2 Other MPET Applications

Since the inter-communicating compartments within the MPET system lie at the heart of this formulation, the different avenues that can be investigated should have a number of MPET compartments that best highlight the character of the research in question. For example, the lithium battery can be designed as three compartments MPET model, since the lithium battery is comprised of three parts, e.g. positive (anode) and negative (cathode) electrodes and separator [422, 423]. Therefore, for analysing some other organ systems in human, it is recommended that using 4MPET as the first step would be the most suitable strategy.

An important comment to make here is that the 6MPET has an inertial force term that can be utilised (this term does not show in the traditional poroelasticity formulation), and therefore some interesting research can be proposed with dealing with this inertial term. Firstly, NASA is developing the capabilities needed to send humans to Mars in the 2030s [424]. For humans to be able to survive and function long-term in a micro-gravity environment, it is important to study its effect on cerebral physiology. Therefore, 6MPET is a suitable model that can be used to assist in possible proposals in aiding in the discovery the cerebral physiology in the micro-gravity environment [425-428]. Secondly, traumatic brain injury (TBI) occurs when an external force injures the brain. This circumstance may integrate into MPET in order to investigate the influence of TBI [429, 430]. The research may apply for the New Car Assessment Programme (NCAP) and military applications to estimate the damage when the human brain suffers impact [430-432]. Thirdly, 6MPET may assist handset manufacturers to confirm the influence of the electromagnetic effect in human brain due to manipulating the body force term by electromagnetic body force [433-435].

Finally, the boundary conditions of 6MPET can be manipulated to link with the portable devices which are able to detect the physiological signals and to combine 6MPET with the Internet of Things (IoT), as a means of being a more powerful analysis tool. One of the IoT concepts is the portable or wearable devices embedded with electronics, software, sensors, and network connectivity that enables to collect and exchange data in order to apply in healthcare related applications [436-438]. Therefore, MPET can be considered as a platform to gather the physiological signals through network connectivity, e.g. internet or iBeancon, as the boundary conditions which are recorded as real-time data, e.g. pulsatile blood pressure and blood vessel stiffness via sensors, in order to predict or estimate the subject's state [439-445]. This is another interesting topic for research and business in the future.

References

1. *UN projects world population to reach 8.4 billion by 2030, driven by growth in developing countries*. Retrieved July 30, 2015; Available from: http://www.un.org/apps/news/story.asp?NewsID=51526#.VqTaDPl95D8.

2. *World Population Ageing 1950-2050*. 2015: Population Division, DESA, United Nations.

3. *World Population Prospects*. 2008: Department of Economic and Social Affairs, Population Division, United Nations

4. Hindle, J.V., *Ageing, neurodegeneration and Parkinson's disease.* Age and Ageing, 2010. **39**(2): p. 156-161.

5. *World Alzheimer Report 2015*. 2015: Alzheimer's Disease International.

6. *Neurological disorders: public health challenges.* 2014: World Health Organization

7. Ng J.B., T.M., Hakim A.M., *Heart disease as a risk factor for dementia.* Clinical Epidemiology, 2013. **5**(1): p. 135-145.

8. Blumenthal, J.A., et al., *Can lifestyle modification improve neurocognition? Rationale and design of the ENLIGHTEN clinical trial.* Contemporary Clinical Trials, 2013. **34**(1): p. 60-69.

9. *The Epidemiology and Impact of Dementia: Current State and Futrue Trends*. 2015, World Health Organization: http://www.who.int/mental_health/neurology/dementia/en/.

10. *Policy Brief for G8 Heads of Government. The Global Impact of Dementia 2013-2050*. 2013, Alzheimer's Disease International: London.

11. Nepal, B., L.J. Brown, and K.J. Anstey, *Rising midlife obesity will worsen future prevalence of dementia.* PLoS One, 2014. **9**(9): p. e99305.

12. Van Mierlo, L.D., et al., *Personalized dementia care: proven effectiveness of psychosocial interventions in subgroups.* Ageing Res Rev, 2010. **9**(2): p. 163-83.

13. Van Mierlo, L.D., et al., *Towards personalized integrated dementia care: a qualitative study into the implementation of different models of case management.* BMC Geriatr, 2014. **14**: p. 84.

14. Fenner, J.W., et al., *The EuroPhysiome, STEP and a roadmap for the virtual physiological human.* Philos Trans A Math Phys Eng Sci, 2008. **366**(1878): p. 2979-99.

15. Viceconti, M., G. Clapworthy, and S. Van Sint Jan, *The Virtual Physiological Human - a European initiative for in silico human modelling.* J Physiol Sci, 2008. **58**(7): p. 441-6.

16. Clapworthy, G., et al., *The virtual physiological human: building a framework for computational biomedicine I. Editorial.* Philos Trans A Math Phys Eng Sci, 2008. **366**(1878): p. 2975-8.

17. Deng, Q.K., *[A novel model of the medical instrumentation--an overview of wearable sensors and systems]*. Zhongguo Yi Liao Qi Xie Za Zhi, 2006. **30**(5): p. 327-9.

18. Gargiulo, G., et al., *Wearable dry sensors with bluetooth connection for use in remote patient monitoring systems.* Stud Health Technol Inform, 2010. **161**: p. 57-65.

19. Bonato, P., *Wearable sensors and systems. From enabling technology to clinical applications.* IEEE Eng Med Biol Mag, 2010. **29**(3): p. 25-36.

20. Marschollek, M., et al., *Wearable sensors in healthcare and sensor-enhanced health information systems: all our tomorrows?* Healthc Inform Res, 2012. **18**(2): p. 97-104.

21. Bonato, P., *Wearable sensors/systems and their impact on biomedical engineering.* IEEE Eng Med Biol Mag, 2003. **22**(3): p. 18-20.

22. Nickerson, D.P., et al., *Standards and tools supporting collaborative development of the virtual physiological human.* Conf Proc IEEE Eng Med Biol Soc, 2013. **2013**: p. 5541-4.

23. Viceconti, M. and P. Kohl, *The virtual physiological human: computer simulation for integrative biomedicine I.* Philos Trans A Math Phys Eng Sci, 2010. **368**(1920): p. 2591-4.

24. Kohl, P. and M. Viceconti, *The virtual physiological human: computer simulation for integrative biomedicine II.* Philos Trans A Math Phys Eng Sci, 2010. **368**(1921): p. 2837-9.

25. De Deyn, P.P., *Dementia: Cerebrospinal fluid biomarkers in dementias.* Nat Rev Neurol, 2015. **11**(10): p. 549-50.

26. Ahmed, R.M., et al., *Biomarkers in dementia: clinical utility and new directions.* J Neurol Neurosurg Psychiatry, 2014. **85**(12): p. 1426-34.

27. Iliff, J.J., et al., *A paravascular pathway facilitates CSF flow through the brain parenchyma and the clearance of interstitial solutes, including amyloid beta.* Sci Transl Med, 2012. **4**(147): p. 147ra111.

28. Xie, L., et al., *Sleep drives metabolite clearance from the adult brain.* Science, 2013. **342**(6156): p. 373-7.

29. VPH-DARE@IT. *Virtual Physiological Human: DementiA Research Enabled by IT*. 2013.

30. Sen, P.N. and P.J. Basser, *Modeling diffusion in white matter in the brain: a composite porous medium.* Magn Reson Imaging, 2005. **23**(2): p. 215-20.

31. Woerly, S., et al., *Neural tissue formation within porous hydrogels implanted in brain and spinal cord lesions: ultrastructural, immunohistochemical, and diffusion studies.* Tissue Eng, 1999. **5**(5): p. 467-88.

32. Brunker, C. and S. Shah, *Systems and diseases. Exploring normal anatomy and physiology. Nervous system 11: Brain tumours.* Nurs Times, 2001. **97**(26): p. 43-6.

33. Kaplan, H.A., *Vascular anatomy and physiology of brain.* N Y State J Med, 1966. **66**(8): p. 951-3.

34. Heidrich, R., *[On the anatomy and physiology of the subarachnoid space of the brain and spinal cord]*. Z Arztl Fortbild (Berl), 1963. **57**: p. 433-42.

35. Conn, P.M. and SpringerLink (Online service), *Neuroscience in Medicine*. 2008, Humana Press : Imprint: Humana Press,: Totowa, NJ. p. 1 online resource (XIII, 816 p.

36. Blumenfeld, H., *Neuroanatomy through clinical cases*. 2002, Sunderland, Mass.: Sinauer Associates. xxii, 951 p.

37. Colbert, B.J., J. Ankney, and K.T. Lee, *Anatomy, physiology & disease*. Third edition. ed. 2015, Boston, Massachusetts: Pearson. xxiv, 866 pages.

38. *Anatomy and Physiology*. 2014 Textbook Equity Edition ed. Vol. 2. 2014: Textbook Equity.

39. Zhang, E.T., C.B. Inman, and R.O. Weller, *Interrelationships of the pia mater and the perivascular (Virchow-Robin) spaces in the human cerebrum.* J Anat, 1990. **170**: p. 111-23.

40. Morris, A.W., et al., *Vascular basement membranes as pathways for the passage of fluid into and out of the brain.* Acta Neuropathol, 2016. **131**(5): p. 725-36.

41. Salzman, K.L., et al., *Giant tumefactive perivascular spaces.* AJNR Am J Neuroradiol, 2005. **26**(2): p. 298-305.

42. Pollock, H., et al., *Perivascular spaces in the basal ganglia of the human brain: their relationship to lacunes.* J Anat, 1997. **191 (Pt 3)**: p. 337-46.

43. Engelhardt, B., P. Vajkoczy, and R.O. Weller, *The movers and shapers in immune privilege of the CNS.* Nat Immunol, 2017. **18**(2): p. 123-131.

44. Damkier, H.H., P.D. Brown, and J. Praetorius, *Cerebrospinal fluid secretion by the choroid plexus.* Physiol Rev, 2013. **93**(4): p. 1847-92.

45. Inoue, T., et al., *Observation of the Ciliary Movement of Choroid Plexus Epithelial Cells Ex Vivo.* J Vis Exp, 2015(101): p. e52991.

46. Dandy, W.E., *Where is cerebrospinal fluid absorbed?* Journal of the American Medical Association, 1929. **92**(24): p. 2012-2014.

47. van Baalen, A. and U. Stephani, *Flexible and floating choroid plexus cyst of the third ventricle: an ultrasonographic video documentation.* Childs Nerv Syst, 2007. **23**(2): p. 259-61.

48. Johanson, C.E., et al., *Multiplicity of cerebrospinal fluid functions: New challenges in health and disease.* Cerebrospinal Fluid Res, 2008. **5**: p. 10.

49. Bradbury, M.W., *Physiopathology of the blood-brain barrier.* Adv Exp Med Biol, 1976. **69**: p. 507-16.

50. Abbott, N.J., *Evidence for bulk flow of brain interstitial fluid: significance for physiology and pathology.* Neurochem Int, 2004. **45**(4): p. 545-52.

51. Neff, S. and R.P. Subramaniam, *Monro-Kellie doctrine.* J Neurosurg, 1996. **85**(6): p. 1195.

52. Mokri, B., *The Monro-Kellie hypothesis: applications in CSF volume depletion.* Neurology, 2001. **56**(12): p. 1746-8.

53. Takahashi, H., et al., *Variation in supratentorial cerebrospinal fluid production rate in one day: measurement by nontriggered phase-contrast magnetic resonance imaging.* Jpn J Radiol, 2011. **29**(2): p. 110-5.

54. Rubenstein, E., *Relationship of senescence of cerebrospinal fluid circulatory system to dementias of the aged.* Lancet, 1998. **351**(9098): p. 283-5.

55. Silverberg, G.D., et al., *Alzheimer's disease, normal-pressure hydrocephalus, and senescent changes in CSF circulatory physiology: a hypothesis.* Lancet Neurol, 2003. **2**(8): p. 506-11.

56. Pasternak, O., et al., *Excessive extracellular volume reveals a neurodegenerative pattern in schizophrenia onset.* J Neurosci, 2012. **32**(48): p. 17365-72.

57. Szczepek, E., et al., *Analysis of intracranial volume ratios by means of cerebrospinal fluid deployment indicators.* Folia Neuropathol, 2015. **53**(2): p. 121-7.

58. Filippi, M., M. Rovaris, and G. Comi, *Neurodegeneration in multiple sclerosis*. Topics in neuroscience. 2007, Milan ; New York: Springer. xi, 236 p.

59. Black, P.M., et al., *The emerging field of third circulation research.* Clin Neurosurg, 2007. **54**: p. 129-33.

60. Cushing, H., *Studies in intracranial physiology & surgery : the third circulation, the hypophysics, the gliomas*. Oxford medical publications. 1926, London: H. Milford, Oxford university press. xii, 146 p.

61. Oreskovic, D., M. Klarica, and M. Vukic, *The formation and circulation of cerebrospinal fluid inside the cat brain ventricles: a fact or an illusion?* Neurosci Lett, 2002. **327**(2): p. 103-6.

62. Vladic, A., et al., *Homeostatic role of the active transport in elimination of [3H]benzylpenicillin out of the cerebrospinal fluid system.* Life Sci, 2000. **67**(19): p. 2375-85.

63. Milhorat, T.H., *The third circulation revisited.* J Neurosurg, 1975. **42**(6): p. 628-45.

64. Pardridge, W.M., *Drug transport in brain via the cerebrospinal fluid.* Fluids Barriers CNS, 2011. **8**(1): p. 7.

65. By OpenStax https://cnx.org/contents/FPtK1zmh@8.25:fEI3C8Ot@10/Preface, C.B., https://commons.wikimedia.org/w/index.php?curid=30147960, *the Textbook OpenStax Anatomy and Physiology*. 2016.

66. Brinker, T., et al., *A new look at cerebrospinal fluid circulation.* Fluids Barriers CNS, 2014. **11**: p. 10.

67. Davson, H. and W.H. Oldendorf, *Symposium on membrane transport. Transport in the central nervous system.* Proc R Soc Med, 1967. **60**(4): p. 326-9.

68. McLaurin, R.L., *Brain electrolytes and fluid metabolism.* JAMA, 1973. **226**(11): p. 1362-1362.

69. Rennels, M.L., et al., *Evidence for a 'paravascular' fluid circulation in the mammalian central nervous system, provided by the rapid distribution of tracer protein throughout the brain from the subarachnoid space.* Brain Res, 1985. **326**(1): p. 47-63.

70. Nolte, J., *Essentials of the human brain*. 2010, Philadelphia: Mosby/Elsevier. ix, 243 p.

71. Louveau, A., et al., *Structural and functional features of central nervous system lymphatic vessels.* Nature, 2015. **523**(7560): p. 337-41.

72. Bradstreet, J.J., M. Ruggiero, and S. Pacini, *Commentary: Structural and functional features of central nervous system lymphatic vessels.* Front Neurosci, 2015. **9**: p. 485.

73. Pfeffer, W., *Osmotische Untersuchungen*. 1877, Leipzig: W. Engelmann.

74. Nernst, W., *Zur Theorie des elektrischen Reizes.* Pflügers Archiv European Journal of Physiology, 1908. **122**(7): p. 275-314.

75. Paganelli, C.V. and A.K. Solomon, *The rate of exchange of tritiated water across the human red cell membrane.* J Gen Physiol, 1957. **41**(2): p. 259-77.

76. Agre, P., et al., *Purification and partial characterization of the Mr 30,000 integral membrane protein associated with the erythrocyte Rh(D) antigen.* Journal of Biological Chemistry, 1987. **262**(36): p. 17497-17503.

77. Denker, B.M., et al., *Identification, purification, and partial characterization of a novel Mr 28,000 integral membrane protein from erythrocytes and renal tubules.* J Biol Chem, 1988. **263**(30): p. 15634-42.

78. Preston, G.M. and P. Agre, *Isolation of the cDNA for erythrocyte integral membrane protein of 28 kilodaltons: member of an ancient channel family.* Proc Natl Acad Sci U S A, 1991. **88**(24): p. 11110-4.

79. Smith, B.L. and P. Agre, *Erythrocyte Mr 28,000 transmembrane protein exists as a multisubunit oligomer similar to channel proteins.* J Biol Chem, 1991. **266**(10): p. 6407-15.

80. Agre, P., S. Sasaki, and M.J. Chrispeels, *Aquaporins: a family of water channel proteins.* Am J Physiol, 1993. **265**(3 Pt 2): p. F461.

81. Preston, G.M., et al., *Appearance of water channels in Xenopus oocytes expressing red cell CHIP28 protein.* Science, 1992. **256**(5055): p. 385-7.

82. Sabolic, I., et al., *Localization of the CHIP28 water channel in rat kidney.* Am J Physiol, 1992. **263**(6 Pt 1): p. C1225-33.

83. Zeidel, M.L., et al., *Reconstitution of functional water channels in liposomes containing purified red cell CHIP28 protein.* Biochemistry, 1992. **31**(33): p. 7436-40.

84. Harvey Lodish; Arnold Berk, C.A.K., Monty Krieger, Anthony Bretscher, Hidde Ploegh, Angelika Amon, Matthew P. Scott, *Molecular Cell Biology*. 7th ed. 2012, United States of America: W. H. Freeman and Company. 482.

85. Amiry-Moghaddam, M. and O.P. Ottersen, *The molecular basis of water transport in the brain.* Nat Rev Neurosci, 2003. **4**(12): p. 991-1001.

86. Borgnia, M., et al., *Cellular and molecular biology of the aquaporin water channels.* Annu Rev Biochem, 1999. **68**: p. 425-58.

87. Agre, P., et al., *Aquaporin water channels--from atomic structure to clinical medicine*. J Physiol, 2002. **542**(Pt 1): p. 3-16.

88. Schrier, R.W. and M.A. Cadnapaphornchai, *Renal aquaporin water channels: from molecules to human disease*. Prog Biophys Mol Biol, 2003. **81**(2): p. 117-31.

89. Carson, M.J., J.C. Thrash, and B. Walter, *The cellular response in neuroinflammation: The role of leukocytes, microglia and astrocytes in neuronal death and survival.* Clin Neurosci Res, 2006. **6**(5): p. 237-245.

90. Hostenbach, S., et al., *Astrocyte loss and astrogliosis in neuroinflammatory disorders.* Neurosci Lett, 2014. **565**: p. 39-41.

91. Zador, Z., et al., *Role of aquaporin-4 in cerebral edema and stroke.* Handb Exp Pharmacol, 2009(190): p. 159-70.

92. Graber, D.J., et al., *Neuromyelitis optica pathogenesis and aquaporin 4.* J Neuroinflammation, 2008. **5**: p. 22.

93. Papadopoulos, M.C. and A.S. Verkman, *Aquaporin 4 and neuromyelitis optica.* Lancet Neurol, 2012. **11**(6): p. 535-44.

94. Javot, H. and C. Maurel, *The role of aquaporins in root water uptake.* Ann Bot, 2002. **90**(3): p. 301-13.

95. Maurel, C., et al., *Molecular physiology of aquaporins in plants.* Int Rev Cytol, 2002. **215**: p. 105-48.

96. Badaut, J., et al., *Aquaporins in brain: distribution, physiology, and pathophysiology.* J Cereb Blood Flow Metab, 2002. **22**(4): p. 367-78.

97. Badaut, J., J.F. Brunet, and L. Regli, *Aquaporins in the brain: from aqueduct to "multi-duct".* Metab Brain Dis, 2007. **22**(3-4): p. 251-63.

98. Gunnarson, E., M. Zelenina, and A. Aperia, *Regulation of brain aquaporins.* Neuroscience, 2004. **129**(4): p. 947-55.

99. Rojek, A., et al., *A current view of the mammalian aquaglyceroporins.* Annu Rev Physiol, 2008. **70**: p. 301-27.

100. Longatti, P., et al., *Aquaporin(s) expression in choroid plexus tumours.* Pediatr Neurosurg, 2006. **42**(4): p. 228-33.

101. Filippidis, A.S., M.Y. Kalani, and H.L. Rekate, *Hydrocephalus and aquaporins: the role of aquaporin-4.* Acta Neurochir Suppl, 2012. **113**: p. 55-8.

102. Albertini, R. and R. Bianchi, *Aquaporins and glia.* Curr Neuropharmacol, 2010. **8**(2): p. 84-91.

103. Aspelund, A., et al., *A dural lymphatic vascular system that drains brain interstitial fluid and macromolecules.* J Exp Med, 2015. **212**(7): p. 991-9.

104. Bradbury, M.W., H.F. Cserr, and R.J. Westrop, *Drainage of cerebral interstitial fluid into deep cervical lymph of the rabbit.* Am J Physiol, 1981. **240**(4): p. F329-36.

105. Pepper, M.S. and M. Skobe, *Lymphatic endothelium: morphological, molecular and functional properties.* J Cell Biol, 2003. **163**(2): p. 209-13.

106. Wiig, H. and M.A. Swartz, *Interstitial fluid and lymph formation and transport: physiological regulation and roles in inflammation and cancer.* Physiol Rev, 2012. **92**(3): p. 1005-60.

107. Shayan, R., M.G. Achen, and S.A. Stacker, *Lymphatic vessels in cancer metastasis: bridging the gaps.* Carcinogenesis, 2006. **27**(9): p. 1729-38.

108. Aspelund, A., et al., *A dural lymphatic vascular system that drains brain interstitial fluid and macromolecules.* Journal of Experimental Medicine, 2015. **212**(7): p. 991-999.

109. Cserr, H.F., *Physiology of the choroid plexus.* Physiol Rev, 1971. **51**(2): p. 273-311.

110. Nicholson, C. and J.M. Phillips, *Ion diffusion modified by tortuosity and volume fraction in the extracellular microenvironment of the rat cerebellum.* J Physiol, 1981. **321**: p. 225-57.

111. Jin, B.J., A.J. Smith, and A.S. Verkman, *Spatial model of convective solute transport in brain extracellular space does not support a "glymphatic" mechanism.* Journal of General Physiology, 2016. **148**(6): p. 489-501.

112. Asgari, M., D. de Zelicourt, and V. Kurtcuoglu, *Glymphatic solute transport does not require bulk flow.* Sci Rep, 2016. **6**: p. 38635.

113. Bulat, M. and M. Klarica, *Recent insights into a new hydrodynamics of the cerebrospinal fluid.* Brain Research Reviews, 2011. **65**(2): p. 99-112.

114. Iliff, J.J. and M. Nedergaard, *Is there a cerebral lymphatic system?* Stroke, 2013. **44**(6 Suppl 1): p. S93-5.

115. Cserr, H.F., et al., *Convection of Cerebral Interstitial Fluid and Its Role in Brain Volume Regulation.* Annals of the New York Academy of Sciences, 1986. **481**: p. 123-134.

116. Johnston, M., et al., *Evidence of connections between cerebrospinal fluid and nasal lymphatic vessels in humans, non-human primates and other mammalian species.* Cerebrospinal Fluid Res, 2004. **1**(1): p. 2.

117. Murtha, L.A., et al., *Cerebrospinal fluid is drained primarily via the spinal canal and olfactory route in young and aged spontaneously hypertensive rats.* Fluids Barriers CNS, 2014. **11**: p. 12.

118. Hawkes, C.A., et al., *Perivascular drainage of solutes is impaired in the ageing mouse brain and in the presence of cerebral amyloid angiopathy.* Acta Neuropathol, 2011. **121**(4): p. 431-43.

119. Smith, A.J., B.J. Jin, and A.S. Verkman, *Muddying the water in brain edema?* Trends Neurosci, 2015. **38**(6): p. 331-2.

120. Rosenberg, G.A., W.T. Kyner, and E. Estrada, *Bulk flow of brain interstitial fluid under normal and hyperosmolar conditions.* Am J Physiol, 1980. **238**(1): p. F42-9.

121. Papadopoulos, M.C., J.K. Kim, and A.S. Verkman, *Extracellular space diffusion in central nervous system: anisotropic diffusion measured by elliptical surface photobleaching.* Biophys J, 2005. **89**(5): p. 3660-8.

122. Iliff, J.J., et al., *A Paravascular Pathway Facilitates CSF Flow Through the Brain Parenchyma and the Clearance of Interstitial Solutes, Including Amyloid beta.* Science Translational Medicine, 2012. **4**(147).

123. Milhorat, T.H., *Classification of the Cerebral Edemas with Reference to Hydrocephalus and Pseudotumor Cerebri.* Childs Nervous System, 1992. **8**(6): p. 301-306.

124. Ho, M.L., R. Rojas, and R.L. Eisenberg, *Cerebral Edema.* American Journal of Roentgenology, 2012. **199**(3): p. W258-W273.

125. Chodobski, A., B.J. Zink, and J. Szmydynger-Chodobska, *Blood-brain barrier pathophysiology in traumatic brain injury.* Transl Stroke Res, 2011. **2**(4): p. 492-516.

126. Holtmannspotter, M., et al., *Intracranial hypertension influences the resolution of vasogenic brain edema following intracerebral hemorrhage.* Acta Neurochir Suppl, 2000. **76**: p. 497-9.

127. Holmin, S. and T. Mathiesen, *Intracerebral administration of interleukin-1beta and induction of inflammation, apoptosis, and vasogenic edema.* J Neurosurg, 2000. **92**(1): p. 108-20.

128. Baldwin, S.A., et al., *Blood-brain barrier breach following cortical contusion in the rat.* J Neurosurg, 1996. **85**(3): p. 476-81.

129. Shapira, Y., et al., *Blood-brain barrier permeability, cerebral edema, and neurologic function after closed head injury in rats.* Anesth Analg, 1993. **77**(1): p. 141-8.

130. Baskaya, M.K., et al., *The biphasic opening of the blood-brain barrier in the cortex and hippocampus after traumatic brain injury in rats.* Neurosci Lett, 1997. **226**(1): p. 33-6.

131. Raslan, A. and A. Bhardwaj, *Medical management of cerebral edema.* Neurosurg Focus, 2007. **22**(5): p. E12.

132. Creasy, J.L., *The General Appearance of Edema and Hemorrhage on CT, MR and US (Including a General Introduction to CT, MR and US Scanning)*, in *Dating Neurological Injury:: A Forensic Guide for Radiologists, Other Expert Medical Witnesses, and Attorneys*, L.J. Creasy, Editor. 2011, Springer New York: New York, NY. p. 43-58.

133. Heo, J.H., S.W. Han, and S.K. Lee, *Free radicals as triggers of brain edema formation after stroke.* Free Radic Biol Med, 2005. **39**(1): p. 51-70.

134. Sweeney, M.I., et al., *Cellular mechanisms involved in brain ischemia.* Can J Physiol Pharmacol, 1995. **73**(11): p. 1525-35.

135. Simard, J.M., et al., *Newly expressed SUR1-regulated NC(Ca-ATP) channel mediates cerebral edema after ischemic stroke.* Nat Med, 2006. **12**(4): p. 433-40.

136. Kahle, K.T., et al., *Molecular mechanisms of ischemic cerebral edema: role of electroneutral ion transport.* Physiology (Bethesda), 2009. **24**: p. 257-65.

137. Manley, G.T., et al., *Aquaporin-4 deletion in mice reduces brain edema after acute water intoxication and ischemic stroke.* Nat Med, 2000. **6**(2): p. 159-63.

138. Papadopoulos, M.C. and A.S. Verkman, *Aquaporin-4 gene disruption in mice reduces brain swelling and mortality in pneumococcal meningitis.* J Biol Chem, 2005. **280**(14): p. 13906-12.

139. Le Bars, E., et al., *Delayed progression of cytotoxic oedema in focal cerebral ischemia after treatment with a torasemide derivative: a diffusion-weighted magnetic resonance imaging study.* Neurosci Lett, 1996. **213**(2): p. 123-6.

140. Shapiro, K., et al., *Hydrocephalic Edema: Accessory CSF Absorption or Passive Response to Ventricular Enlargement*, in *Intracranial Pressure VI: Proceedings of the Sixth International Symposium on Intracranial Pressure Held in Glasgow, Scotland, June 9–13, 1985*, J.D. Miller, et al., Editors. 1986, Springer Berlin Heidelberg: Berlin, Heidelberg. p. 428-432.

141. Lux, W.E., Jr., et al., *Periventricular water content. Effect of pressure in experimental chronic hydrocephalus.* Arch Neurol, 1970. **23**(5): p. 475-9.

142. Milhorat, T.H., et al., *Structural, ultrastructural, and permeability changes in the ependyma and surrounding brain favoring equilibration in progressive hydrocephalus.* Arch Neurol, 1970. **22**(5): p. 397-407.

143. Braun, K.P., et al., *Cerebral ischemia and white matter edema in experimental hydrocephalus: a combined in vivo MRI and MRS study.* Brain Res, 1997. **757**(2): p. 295-8.

144. Lascelles, P.T., *Cerebrospinal Fluid in Diseases of the Nervous System.* Journal of Clinical Pathology, 1981. **34**(4): p. 453-453.

145. Hiratsuka, H., et al., *Evaluation of periventricular hypodensity in experimental hydrocephalus by metrizamide CT ventriculography.* J Neurosurg, 1982. **56**(2): p. 235-40.

146. Bloch, O., et al., *Accelerated progression of kaolin-induced hydrocephalus in aquaporin-4-deficient mice.* J Cereb Blood Flow Metab, 2006. **26**(12): p. 1527-37.

147. Papadopoulos, M.C. and A.S. Verkman, *Aquaporin-4 and brain edema.* Pediatr Nephrol, 2007. **22**(6): p. 778-84.

148. Zador, Z., et al., *Aquaporins: role in cerebral edema and brain water balance.* Prog Brain Res, 2007. **161**: p. 185-94.

149. Wang, T., et al., *Reduction of brain edema and expression of aquaporins with acute ethanol treatment after traumatic brain injury.* J Neurosurg, 2013. **118**(2): p. 390-6.

150. Thrane, A.S., V. Rangroo Thrane, and M. Nedergaard, *Drowning stars: reassessing the role of astrocytes in brain edema.* Trends Neurosci, 2014. **37**(11): p. 620-8.

151. Goriely, A., et al., *Mechanics of the brain: perspectives, challenges, and opportunities.* Biomech Model Mechanobiol, 2015. **14**(5): p. 931-65.

152. Donkin, J.J. and R. Vink, *Mechanisms of cerebral edema in traumatic brain injury: therapeutic developments.* Curr Opin Neurol, 2010. **23**(3): p. 293-9.

153. Fukuda, A.M. and J. Badaut, *Aquaporin 4: a player in cerebral edema and neuroinflammation.* J Neuroinflammation, 2012. **9**: p. 279.

154. Fukuda, A.M., et al., *Delayed increase of astrocytic aquaporin 4 after juvenile traumatic brain injury: possible role in edema resolution?* Neuroscience, 2012. **222**: p. 366-78.

155. Papadopoulos, M.C. and A.S. Verkman, *Aquaporin water channels in the nervous system.* Nat Rev Neurosci, 2013. **14**(4): p. 265-77.

156. Rekate, H.L., *A contemporary definition and classification of hydrocephalus.* Semin Pediatr Neurol, 2009. **16**(1): p. 9-15.

157. Thompson, D.N.P., *Hydrocephalus.* Surgery - Oxford International Edition, 2009. **27**(3): p. 130-134.

158. Stagno, V., et al., *Management of hydrocephalus around the world.* World Neurosurg, 2013. **79**(2 Suppl): p. S23 e17-20.

159. Nielsen, N. and A. Breedt, *Hydrocephalus*, in *Nursing Care of the Pediatric Neurosurgery Patient*, C.C. Cartwright and C.D. Wallace, Editors. 2013, Springer Berlin Heidelberg: Berlin, Heidelberg. p. 37-84.

160. Rekate, H.L., *The definition and classification of hydrocephalus: a personal recommendation to stimulate debate.* Cerebrospinal Fluid Res, 2008. **5**: p. 2.

161. Vardakis, I.C., *Multicompartmental poroelasticity for the integrative modelling of fluid transport in the brain*. 2014, University of Oxford. p. xvii, 172 leaves.

162. Daroff, R.B. and W.G. Bradley, *Bradley's neurology in clinical practice*. 6th ed. 2012, Philadelphia, PA: Elsevier/Saunders.

163. Sivagnanam, M.a.J., N. K., *Hydrocephalus: An Overview, Hydrocephalus, Dr Sadip Pant (Ed.)*. 2012, InTech.

164. Tully, B.J. and Y. Ventikos, *Allostasis of cerebral water : modelling the transport of cerebrospinal fluid*. 2010, University of Oxford. p. xxiii, 206 .

165. Greitz, D., *Paradigm shift in hydrocephalus research in legacy of Dandy's pioneering work: rationale for third ventriculostomy in communicating hydrocephalus.* Childs Nerv Syst, 2007. **23**(5): p. 487-9.

166. Greitz, D., *Radiological assessment of hydrocephalus: new theories and implications for therapy.* Neurosurg Rev, 2004. **27**(3): p. 145-65; discussion 166-7.

167. Armao, D., et al., *Colloid cyst of the third ventricle: imaging-pathologic correlation.* AJNR Am J Neuroradiol, 2000. **21**(8): p. 1470-7.

168. Anegawa, S., et al., *Dilated fourth ventricle in Arnold-Chiari malformation type II: isolated fourth ventricle as sequelae of shunt?--Case report.* Neurol Med Chir (Tokyo), 1993. **33**(8): p. 575-8.

169. Suzuki, K., et al., *Dilated fourth ventricle on brain computed tomography scan in the diagnosis of Chiari I malformation with syringomyelia.* Intern Med, 2008. **47**(3): p. 185-6.

170. Spennato, P., et al., *Hydrocephalus in Dandy-Walker malformation.* Childs Nerv Syst, 2011. **27**(10): p. 1665-81.

171. Bourneville, S.a.N., J. *Hydrocephalie*. in *Prog Med*. 1900. Paris.

172. Abbati, S., *Images in clinical medicine. Idiopathic aqueductal stenosis.* N Engl J Med, 2012. **367**(21): p. e30.

173. Deavin, E., et al., *Idiopathic aqueductal stenosis.* Clin Med (Lond), 2012. **12**(5): p. 491.

174. Vannemreddy, P., et al., *Congenital Chiari malformations.* Neurol India, 2010. **58**(1): p. 6-14.

175. O'Brien, M.S. and M.M. Schechter, *Arteriovenous malformations involving the Galenic system.* Am J Roentgenol Radium Ther Nucl Med, 1970. **110**(1): p. 50-5.

176. Schreml, S., et al., *Neurocutaneous melanosis in association with Dandy-Walker malformation: case report and literature review.* Clin Exp Dermatol, 2008. **33**(5): p. 611-4.

177. Fukumizu, M., S. Takashima, and L.E. Becker, *Neuropathology and immunohistochemistry of the brain-stem in neonates with congenital hydrocephalus: comparative studies between aqueductal stenosis and Arnold-Chiari malformation.* Acta Paediatr Jpn, 1994. **36**(5): p. 472-9.

178. Fryns, J.P., et al., *X linked complicated spastic paraplegia, MASA syndrome, and X linked hydrocephalus owing to congenital stenosis of the aqueduct of Sylvius: variable expression of the same mutation at Xq28.* J Med Genet, 1991. **28**(6): p. 429-31.

179. Noetzel, H., *Stenosis or atresia of the aqueduct of Sylvius as a cause of congenital hydrocephalus.* Dev Med Child Neurol Suppl, 1970. **22**: p. Suppl 22:123+.

180. Ortiz-Gonzalez, J.M., et al., *[Comment in relation to a case of congenital neurological malformations: agenesia of the corpus callosum, hydrocephalus due to aqueduct stenosis and lumbosacral MENINGOCELE].* Arch Neurobiol (Madr), 1968. **31**(2): p. 206-10.

181. Reinthaller, A. and J. Deutinger, *[X chromosome recessively transmitted hydrocephalus with congenital aqueduct stenosis].* Z Geburtshilfe Perinatol, 1985. **189**(5): p. 244-6.

182. Van Landingham, M., et al., *Risk factors of congenital hydrocephalus: a 10 year retrospective study.* J Neurol Neurosurg Psychiatry, 2009. **80**(2): p. 213-7.

183. Thompson, J.A., *Mumps: A cause of acquired aqueductal stenosis.* J Pediatr, 1979. **94**(6): p. 923-4.

184. Simon, T.D., et al., *Association of intraventricular hemorrhage secondary to prematurity with cerebrospinal fluid shunt surgery in the first year following initial shunt placement.* J Neurosurg Pediatr, 2012. **9**(1): p. 54-63.

185. Hirsch, J.F., et al., *Stenosis of the aqueduct of Sylvius. Etiology and treatment.* J Neurosurg Sci, 1986. **30**(1-2): p. 29-39.

186. *Observations on the Pathology of Hydrocephalus. By Dorothy S. Russell, SC.D., M.D., F.R.C.P. Pp. 138 + vi. 1949. Issued by the Medical Research Council. London: H.M.S.O. 6s.* British Journal of Surgery, 1949. **37**(145): p. 126-126.

187. Oberson, R. and E. Gessaga, *Forking of the aqueduct in an adult.* Acta Radiol Diagn (Stockh), 1972. **13**(1): p. 441-8.

188. Jellinger, G., *Anatomopathology of non-tumoral aqueductal stenosis.* J Neurosurg Sci, 1986. **30**(1-2): p. 1-16.

189. I. M. Turnbull and C. G. Drake, *Membranous Occlusion of the Aqueduct of Sylvius.* Journal of Neurosurgery, 1966. **24**(1): p. 24-34.

190. Mallucci, C. and S. Sgouros, *Cerebrospinal fluid disorders*. 2010, New York: Informa Healthcare USA. xv, 574 p.

191. Brage, D., et al., *[Partial and Congenital Stenosis of the Aqueduct of Sylvius by Gliosis. (Clinical, Surgical and Anatomo-Pathological Observation)]*. Rev Neurol (Paris), 1963. **108**: p. 979-83.

192. McHugh, P.R., *Hydrocephalic dementia.* Bull N Y Acad Med, 1966. **42**(10): p. 907-17.

193. McHugh, P.R., *Occult Hydrocephalus.* Q J Med, 1964. **33**: p. 297-308.

194. Adams, R.D., et al., *Symptomatic Occult Hydrocephalus with "Normal" Cerebrospinal-Fluid Pressure.A Treatable Syndrome.* N Engl J Med, 1965. **273**: p. 117-26.

195. Shprecher, D., J. Schwalb, and R. Kurlan, *Normal pressure hydrocephalus: diagnosis and treatment.* Curr Neurol Neurosci Rep, 2008. **8**(5): p. 371-6.

196. Yamada, S., et al., *Current and emerging MR imaging techniques for the diagnosis and management of CSF flow disorders: a review of phase-contrast and time-spatial labeling inversion pulse.* AJNR Am J Neuroradiol, 2015. **36**(4): p. 623-30.

197. Bradley, W.G., *Cerebrospinal fluid dynamics and shunt responsiveness in patients with normal-pressure hydrocephalus.* Mayo Clin Proc, 2002. **77**(6): p. 507-8.

198. Bradley, W.G., Jr., K.E. Kortman, and B. Burgoyne, *Flowing cerebrospinal fluid in normal and hydrocephalic states: appearance on MR images.* Radiology, 1986. **159**(3): p. 611-6.

199. Yamada, S., et al., *Visualization of cerebrospinal fluid movement with spin labeling at MR imaging: preliminary results in normal and pathophysiologic conditions.* Radiology, 2008. **249**(2): p. 644-52.

200. Relkin, N., et al., *Diagnosing idiopathic normal-pressure hydrocephalus.* Neurosurgery, 2005. **57**(3 Suppl): p. S4-16; discussion ii-v.

201. Gallia, G.L., D. Rigamonti, and M.A. Williams, *The diagnosis and treatment of idiopathic normal pressure hydrocephalus.* Nat Clin Pract Neurol, 2006. **2**(7): p. 375-81.

202. Evans, W.A. and Jr, *AN encephalographic ratio for estimating ventricular enlargement and cerebral atrophy.* Archives of Neurology & Psychiatry, 1942. **47**(6): p. 931-937.

203. Luetmer, P.H., et al., *Measurement of cerebrospinal fluid flow at the cerebral aqueduct by use of phase-contrast magnetic resonance imaging: technique validation and utility in diagnosing idiopathic normal pressure hydrocephalus.* Neurosurgery, 2002. **50**(3): p. 534-43; discussion 543-4.

204. Tullberg, M., et al., *Normal pressure hydrocephalus: vascular white matter changes on MR images must not exclude patients from shunt surgery.* AJNR Am J Neuroradiol, 2001. **22**(9): p. 1665-73.

205. Sasaki, M., et al., *Narrow CSF space at high convexity and high midline areas in idiopathic normal pressure hydrocephalus detected by axial and coronal MRI.* Neuroradiology, 2008. **50**(2): p. 117-22.

206. Bradley, W.G., *Normal pressure hydrocephalus: new concepts on etiology and diagnosis.* AJNR Am J Neuroradiol, 2000. **21**(9): p. 1586-90.

207. Pople, I.K., *Hydrocephalus and shunts: what the neurologist should know.* J Neurol Neurosurg Psychiatry, 2002. **73 Suppl 1**: p. i17-22.

208. Krauss, J.K., et al., *Evaluation of gait in normal pressure hydrocephalus before and after shunting.* Adv Neurol, 2001. **87**: p. 301-10.

209. Yang, F., et al., *Quantitative evaluation of changes in gait after extended cerebrospinal fluid drainage for normal pressure hydrocephalus.* J Clin Neurosci, 2016.

210. Leschey, W.H., Jr. and A.P. Iverson, Jr., *Normal pressure hydrocephalus and urinary incontinence.* J Maine Med Assoc, 1976. **67**(6): p. 152-8.

211. Campos-Juanatey, F., et al., *Assessment of the urodynamic diagnosis in patients with urinary incontinence associated with normal pressure hydrocephalus.* Neurourol Urodyn, 2015. **34**(5): p. 465-8.

212. Behrens, A., et al., *A computerized neuropsychological test battery designed for idiopathic normal pressure hydrocephalus.* Fluids Barriers CNS, 2014. **11**: p. 22.

213. Behrman, S., et al., *Dementia and normal-pressure hydrocephalus.* Lancet, 1971. **1**(7690): p. 137.

214. Turner, D.A. and R.E. McGeachie, *Normal pressure hydrocephalus and dementia--evaluation and treatment.* Clin Geriatr Med, 1988. **4**(4): p. 815-30.

215. Daou, B., et al., *Revisiting secondary normal pressure hydrocephalus: does it exist? A review.* Neurosurg Focus, 2016. **41**(3): p. E6.

216. Shenkin, H.A., J.O. Greenberg, and C.B. Grossman, *Ventricular size after shunting for idiopathic normal pressure hydrocephalus.* J Neurol Neurosurg Psychiatry, 1975. **38**(9): p. 833-7.

217. Shukla, D., B.M. Singh, and R.J. Strobos, *Hypertensive cerebrovascular disease and normal pressure hydrocephalus.* Neurology, 1980. **30**(9): p. 998-1000.

218. Newton, H., J.D. Pickard, and R.O. Weller, *Normal pressure hydrocephalus and cerebrovascular disease: findings of postmortem.* J Neurol Neurosurg Psychiatry, 1989. **52**(6): p. 804.

219. Earnest, M.P., et al., *Normal pressure hydrocephalus and hypertensive cerebrovascular disease.* Arch Neurol, 1974. **31**(4): p. 262-6.

220. Haidri, N.H. and S.M. Modi, *Normal pressure hydrocephalus and hypertensive cerebrovascular disease.* Dis Nerv Syst, 1977. **38**(11): p. 918-21.

221. Akai, K., et al., *Normal pressure hydrocephalus. Neuropathological study.* Acta Pathol Jpn, 1987. **37**(1): p. 97-110.

222. Boon, A.J., et al., *Dutch Normal-Pressure Hydrocephalus Study: the role of cerebrovascular disease.* J Neurosurg, 1999. **90**(2): p. 221-6.

223. Bech, R.A., et al., *Shunting effects in patients with idiopathic normal pressure hydrocephalus; correlation with cerebral and leptomeningeal biopsy findings.* Acta Neurochir (Wien), 1999. **141**(6): p. 633-9.

224. Bateman, G.A., *Vascular compliance in normal pressure hydrocephalus.* AJNR Am J Neuroradiol, 2000. **21**(9): p. 1574-85.

225. Bateman, G.A., et al., *The venous manifestations of pulse wave encephalopathy: windkessel dysfunction in normal aging and senile dementia.* Neuroradiology, 2008. **50**(6): p. 491-7.

226. Graff-Radford, N.R., et al., *Do systolic BP and pulse pressure relate to ventricular enlargement?* Eur J Neurol, 2013. **20**(4): p. 720-4.

227. Krauss, J.K., et al., *Vascular risk factors and arteriosclerotic disease in idiopathic normal-pressure hydrocephalus of the elderly.* Stroke, 1996. **27**(1): p. 24-9.

228. *What is Hydrocephalus?* 2015.

229. Bateman, G.A., *The pathophysiology of idiopathic normal pressure hydrocephalus: cerebral ischemia or altered venous hemodynamics?* AJNR Am J Neuroradiol, 2008. **29**(1): p. 198-203.

230. Bradley, W.G., Jr., *Idiopathic normal pressure hydrocephalus: new findings and thoughts on etiology.* AJNR Am J Neuroradiol, 2008. **29**(1): p. 1-3.

231. Bradley, W.G., Jr., G. Bahl, and J.F. Alksne, *Idiopathic normal pressure hydrocephalus may be a "two hit" disease: benign external hydrocephalus in infancy followed by deep white matter ischemia in late adulthood.* J Magn Reson Imaging, 2006. **24**(4): p. 747-55.

232. McComb, J.G., et al., *Is a large hat size hazardous to your health?* AJNR Am J Neuroradiol, 2004. **25**(9): p. 1454-5; author reply 1455.

233. Tully, B. and Y. Ventikos, *Cerebral water transport using multiple-network poroelastic theory: application to normal pressure hydrocephalus.* Journal of Fluid Mechanics, 2011. **667**: p. 188-215.

234. Monro, A., *Observations on the structure and functions of the nervous system.* 1783, Edinburgh,: Printed for, and sold by, W. Creech. 176 p.

235. Madsen, J.R., M. Egnor, and R. Zou, *Cerebrospinal fluid pulsatility and hydrocephalus: the fourth circulation.* Clin Neurosurg, 2006. **53**: p. 48-52.

236. Ransohoff, J., K. Shulman, and R.A. Fishman, *Hydrocephalus: a review of etiology and treatment.* J Pediatr, 1960. **56**: p. 399-411.

237. Guinane, J.E., *Equivalent Circuit Analysis of Cerebrospinal-Fluid Hydrodynamics.* American Journal of Physiology, 1972. **223**(2): p. 425-&.

238. Marmarou, A., K. Shulman, and R.M. Rosende, *Non-Linear Analysis of Cerebrospinal-Fluid System and Intracranial-Pressure Dynamics.* J Neurosurg, 1978. **48**(3): p. 332-344.

239. Sklar, F.H. and I. Elashvili, *Pressure-Volume Function of Brain Elasticity - Physiological Considerations and Clinical Applications.* Journal of Neurosurgery, 1977. **47**(5): p. 670-679.

240. Sklar, F.H., et al., *Brain Elasticity Changes with Ventriculomegaly.* Journal of Neurosurgery, 1980. **53**(2): p. 173-179.

241. Spertell, R.B., *The Response of Brain to Transient Elevations in Intraventricular Pressure.* Journal of the Neurological Sciences, 1980. **48**(3): p. 343-352.

242. Egnor, M., A. Rosiello, and L. Zheng, *A model of intracranial pulsations.* Pediatr Neurosurg, 2001. **35**(6): p. 284-98.

243. Egnor, M., et al., *A model of pulsations in communicating hydrocephalus.* Pediatr Neurosurg, 2002. **36**(6): p. 281-303.

244. Asgari, M., D. de Zelicourt, and V. Kurtcuoglu, *How astrocyte networks may contribute to cerebral metabolite clearance.* Sci Rep, 2015. **5**: p. 15024.

245. Jannin, P. and X. Morandi, *Surgical models for computer-assisted neurosurgery.* Neuroimage, 2007. **37**(3): p. 783-91.

246. Biot, M.A., *General Theory of Three-Dimensional Consolidation.* Journal of Applied Physics, 1941. **12**(2): p. 155-164.

247. Biot, M.A., *Theory of Deformation of a Porous Viscoelastic Anisotropic Solid.* Journal of Applied Physics, 1956. **27**(5): p. 459-467.

248. Biot, M.A., *General Solutions of the Equations fo Elasticity and Consolidation for a Porous Material.* Journal of Applied Mechanics, 1956: p. 91-96.

249. Berryman, J.G., *Extension of poroelastic analysis to double-porosity materials: New technique in microgeomechanics.* Journal of Engineering Mechanics-Asce, 2002. **128**(8): p. 840-847.

250. McGarry, M.D., et al., *Suitability of poroelastic and viscoelastic mechanical models for high and low frequency MR elastography.* Med Phys, 2015. **42**(2): p. 947-57.

251. Nagashima, T., et al., *Biomechanics of Hydrocephalus - a New Theoretical-Model.* Neurosurgery, 1987. **21**(6): p. 898-904.

252. Kaczmarek, M., R.P. Subramaniam, and S.R. Neff, *The hydromechanics of hydrocephalus: Steady-state solutions for cylindrical geometry*. Bulletin of Mathematical Biology, 1997. **59**(2): p. 295-323.

253. Levine, D.N., *The pathogenesis of normal pressure hydrocephalus: A theoretical analysis.* Bulletin of Mathematical Biology, 1999. **61**(5): p. 875-916.

254. Levine, D.N., *Ventricular size in pseudotumor cerebri and the theory of impaired CSF absorption.* J Neurol Sci, 2000. **177**(2): p. 85-94.

255. Smillie, A., I. Sobey, and Z. Molnar, *A hydroelastic model of hydrocephalus.* Journal of Fluid Mechanics, 2005. **539**: p. 417-443.

256. Sivaloganathan, S., et al., *Biomechanics of the brain: A theoretical and numerical study of Biot's equations of consolidation theory with deformation-dependent permeability.* International Journal of Non-Linear Mechanics, 2005. **40**(9): p. 1149-1159.

257. Wirth, B. and I. Sobey, *An axisymmetric and fully 3D poroelastic model for the evolution of hydrocephalus.* Mathematical Medicine and Biology-a Journal of the Ima, 2006. **23**(4): p. 363-388.

258. Sobey, I. and B. Wirth, *Effect of non-linear permeability in a spherically symmetric model of hydrocephalus.* Mathematical Medicine and Biology-a Journal of the Ima, 2006. **23**(4): p. 339-361.

259. Wirth, B. and I. Sobey, *Analytic solution during an infusion test of the linear unsteady poroelastic equations in a spherically symmetric model of the brain.* Math Med Biol, 2009. **26**(1): p. 25-61.

260. Clatz, O., et al., *Dynamic model of communicating hydrocephalus for surgery simulation.* IEEE Trans Biomed Eng, 2007. **54**(4): p. 755-8.

261. Momjian, S. and D. Bichsel, *Nonlinear poroplastic model of ventricular dilation in hydrocephalus.* J Neurosurg, 2008. **109**(1): p. 100-7.

262. Narsilio, G., et al., *Hydrocephalus: A Realistic Porous-Media Model with Geometry Based on Neuroimaging*, in *Advances in Cognitive Neurodynamics ICCN 2007: Proceedings of the International Conference on Cognitive Neurodynamics. ICCN 2007 Proceedings*, R. Wang, E. Shen, and F. Gu, Editors. 2008, Springer Netherlands: Dordrecht. p. 565-569.

263. Linninger, A.A., B. Sweetman, and R. Penn, *Normal and hydrocephalic brain dynamics: the role of reduced cerebrospinal fluid reabsorption in ventricular enlargement.* Ann Biomed Eng, 2009. **37**(7): p. 1434-47.

264. Liu, F., et al., *Model-based estimation of ventricular deformation in the cat brain.* Med Image Comput Comput Assist Interv, 2009. **12**(Pt 2): p. 308-15.

265. Tully, B. and Y. Ventikos, *Coupling Poroelasticity and CFD for Cerebrospinal Fluid Hydrodynamics.* Ieee Transactions on Biomedical Engineering, 2009. **56**(6): p. 1644-1651.

266. Sobey, I.E., A. Wirth, B. Czosnyka, M., *Simulation of Cerebral Infusion Tests Using a Poroelastic Model.* International Journal of Numerical Analysis and Modeling, Series B, 2012. **3**(1): p. 52-64.

267. Wirth, B., I. Sobey, and A. Eisentrager, *Conditions for choking in a poroelastic flow model.* Ima Journal of Applied Mathematics, 2014. **79**(2): p. 254-273.

268. Mohamed Mokhtarudin, M.J. and S.J. Payne, *Mathematical model of the effect of ischemia-reperfusion on brain capillary collapse and tissue swelling.* Math Biosci, 2015. **263**: p. 111-20.

269. Chou, D., et al., *A fully dynamic multi-compartmental poroelastic system: Application to aqueductal stenosis.* J Biomech, 2015.

270. Shahim, K., et al., *Finite element analysis of normal pressure hydrocephalus: influence of CSF content and anisotropy in permeability.* Applied Bionics and Biomechanics, 2010. **7**(3): p. 187-197.

271. Shahim, K., et al., *Ventricle Equilibrium Position in Healthy and Normal Pressure Hydrocephalus Brains Using an Analytical Model.* Journal of Biomechanical Engineering-Transactions of the Asme, 2012. **134**(4).

272. Wilkie, K.P., G. Nagra, and M. Johnston, *A Mathematical Analysis of Physiological and Molecular Mechanisms That Modulate Pressure Gradients and Facilitate Ventricular Expansion in Hydrocephalus.* Int J Numer Anal Model B, 2012. **316**: p. 65-81.

273. A. H. S. Holbourn, *The Mechanics of Trauma with Special Reference to Herniation of Cerebral Tissue.* Journal of Neurosurgery, 1944. **1**(3): p. 190-200.

274. Sivaloganathan, S., et al., *A viscoelastic approach to the modelling of hydrocephalus.* Applied Mathematics and Computation, 2005. **163**(3): p. 1097-1107.

275. Sivaloganathan, S., et al., *A viscoelastic model of the brain parenchyma with pulsatile ventricular pressure.* Applied Mathematics and Computation, 2005. **165**(3): p. 687-698.

276. Drapaca, C.S., et al., *A quasi-linear viscoelastic constitutive equation for the brain: Application to hydrocephalus.* Journal of Elasticity, 2006. **85**(1): p. 65-83.

277. Libertiaux, V. and F. Pascon, *Viscoelastic Modeling of Brain Tissue: A Fractional Calculus-Based Approach*, in *Mechanics of Microstructured Solids: Cellular Materials, Fibre Reinforced Solids and Soft Tissues*, J.F. Ganghoffer and F. Pastrone, Editors. 2009, Springer Berlin Heidelberg: Berlin, Heidelberg. p. 81-90.

278. Miller, K. and K. Chinzei, *Constitutive modelling of brain tissue: Experiment and theory.* Journal of Biomechanics, 1997. **30**(11-12): p. 1115-1121.

279. Miller, K. and K. Chinzei, *Mechanical properties of brain tissue in tension.* Journal of Biomechanics, 2002. **35**(4): p. 483-490.

280. Miller, K., et al., *Mechanical properties of brain tissue in-vivo: experiment and computer simulation.* Journal of Biomechanics, 2000. **33**(11): p. 1369-1376.

281. Ommaya, A.K., *Mechanical properties of tissues of the nervous system.* J Biomech, 1968. **1**(2): p. 127-38.

282. Galford, J.E. and J.H. McElhaney, *A viscoelastic study of scalp, brain, and dura.* J Biomech, 1970. **3**(2): p. 211-21.

283. Pamidi, M.R. and S.H. Advani, *Non-Linear Constitutive Relations for Human-Brain Tissue.* Journal of Biomechanical Engineering-Transactions of the Asme, 1978. **100**(1): p. 44-48.

284. Bilston, L.E., Z. Liu, and N. Phan-Thien, *Linear viscoelastic properties of bovine brain tissue in shear.* Biorheology, 1997. **34**(6): p. 377-85.

285. Donnelly, B.R. and J. Medige, *Shear properties of human brain tissue.* J Biomech Eng, 1997. **119**(4): p. 423-32.

286. Miller, K., *Constitutive model of brain tissue suitable for finite element analysis of surgical procedures.* Journal of Biomechanics, 1999. **32**(5): p. 531-537.

287. Kohandel, M., et al., *The constitutive properties of the brain parenchyma Part 1. Strain energy approach.* Medical Engineering & Physics, 2006. **28**(5): p. 449-454.

288. Davis, G.B., et al., *The constitutive properties of the brain paraenchyma Part 2. Fractional derivative approach.* Medical Engineering & Physics, 2006. **28**(5): p. 455-459.

289. Mehrabian, A. and Y. Abousleiman, *General solutions to poroviscoelastic model of hydrocephalic human brain tissue.* J Theor Biol, 2011. **291**: p. 105-18.

290. Fin, L. and R. Grebe, *Three dimensional modeling of the cerebrospinal fluid dynamics and brain interactions in the aqueduct of sylvius.* Comput Methods Biomech Biomed Engin, 2003. **6**(3): p. 163-70.

291. Kurtcuoglu, V., et al., *Reconstruction of cerebrospinal fluid flow in the third ventricle based on MRI data.* Med Image Comput Comput Assist Interv, 2005. **8**(Pt 1): p. 786-93.

292. Kurtcuoglu, V., D. Poulikakos, and Y. Ventikos, *Computational modeling of the mechanical behavior of the cerebrospinal fluid system.* J Biomech Eng, 2005. **127**(2): p. 264-9.

293. Kurtcuoglu, V., et al., *Computational investigation of subject-specific cerebrospinal fluid flow in the third ventricle and aqueduct of Sylvius.* J Biomech, 2007. **40**(6): p. 1235-45.

294. Kurtcuoglu, V., *Computational Fluid Dynamics for the Assessment of Cerebrospinal Fluid Flow and Its Coupling with Cerebral Blood Flow*, in *Biomechanics of the Brain*, K. Miller, Editor. 2011, Springer New York: New York, NY. p. 169-188.

295. Linninger, A.A., et al., *Pulsatile cerebrospinal fluid dynamics in the human brain.* IEEE Trans Biomed Eng, 2005. **52**(4): p. 557-65.

296. Hakim, S., J.G. Venegas, and J.D. Burton, *The physics of the cranial cavity, hydrocephalus and normal pressure hydrocephalus: mechanical interpretation and mathematical model.* Surg Neurol, 1976. **5**(3): p. 187-210.

297. Linninger, A.A., et al., *Cerebrospinal fluid flow in the normal and hydrocephalic human brain.* IEEE Trans Biomed Eng, 2007. **54**(2): p. 291-302.

298. Howden, L., et al., *Three-dimensional cerebrospinal fluid flow within the human ventricular system.* Computer Methods in Biomechanics and Biomedical Engineering, 2008. **11**(2): p. 123-133.

299. Gupta, S., et al., *Three-dimensional computational modeling of subject-specific cerebrospinal fluid flow in the subarachnoid space.* J Biomech Eng, 2009. **131**(2): p. 021010.

300. Pope, W., *External ventriculostomy: a practical application for the acute care nurse.* J Neurosci Nurs, 1998. **30**(3): p. 185-90.

301. Sweetman, B., et al., *Three-dimensional computational prediction of cerebrospinal fluid flow in the human brain.* Comput Biol Med, 2011. **41**(2): p. 67-75.

302. Bouzerar, R., et al., *Dynamics of hydrocephalus: a physical approach.* J Biol Phys, 2012. **38**(2): p. 251-66.

303. Vardakis, J.C., B.J. Tully, and Y. Ventikos, *Exploring the efficacy of endoscopic ventriculostomy for hydrocephalus treatment via a multicompartmental poroelastic model of CSF transport: a computational perspective.* PLoS One, 2013. **8**(12): p. e84577.

304. Vardakis, J.C., et al., *Investigating cerebral oedema using poroelasticity.* Med Eng Phys, 2016. **38**(1): p. 48-57.

305. Kurtcuoglu, V., D. Poulikakos, and Y. Ventikos, *Computational modeling of the mechanical behavior of the cerebrospinal fluid system.* Journal of Biomechanical Engineering-Transactions of the Asme, 2005. **127**(2): p. 264-269.

306. Kurtcuoglu, V., et al., *Computational investigation of subject-specific cerebrospinal fluid flow in the third ventricle and aqueduct of Sylvius.* Journal of Biomechanics, 2007. **40**(6): p. 1235-1245.

307. Linninger, A.A., et al., *Pulsatile cerebrospinal fluid dynamics in the human brain.* Ieee Transactions on Biomedical Engineering, 2005. **52**(4): p. 557-565.

308. Linninger, A.A., et al., *Cerebrospinal fluid flow in the normal and hydrocephalic human brain.* Ieee Transactions on Biomedical Engineering, 2007. **54**(2): p. 291-302.

309. Linninger, A.A., B. Sweetman, and R. Penn, *Normal and Hydrocephalic Brain Dynamics: The Role of Reduced Cerebrospinal Fluid Reabsorption in Ventricular Enlargement.* Annals of Biomedical Engineering, 2009. **37**(7): p. 1434-1447.

310. Loth, F., M.A. Yardimci, and N. Alperin, *Hydrodynamic modeling of cerebrospinal fluid motion within the spinal cavity.* Journal of Biomechanical Engineering-Transactions of the Asme, 2001. **123**(1): p. 71-79.

311. Miller, K., et al., *Modelling brain deformations for computer-integrated neurosurgery.* International Journal for Numerical Methods in Biomedical Engineering, 2010. **26**(1): p. 117-138.

312. Ursino, M. and C.A. Lodi, *A simple mathematical model of the interaction between intracranial pressure and cerebral hemodynamics.* Journal of Applied Physiology, 1997. **82**(4): p. 1256-1269.

313. Wirth, B. and I. Sobey, *Analytic solution during an infusion test of the linear unsteady poroelastic equations in a spherically symmetric model of the brain.* Mathematical Medicine and Biology-a Journal of the Ima, 2009. **26**(1): p. 25-61.

314. Holbourn, A.H.S., *MECHANICS OF HEAD INJURIES.* The Lancet. **242**(6267): p. 438-441.

315. Fallenst.Gt, V.D. Hulce, and J.W. Melvin, *Dynamic Mechanical Properties of Human Brain Tissue.* Journal of Biomechanics, 1969. **2**(3): p. 217-&.

316. Metz, H., Mcelhane.J, and A.K. Ommaya, *A Comparison of Elasticity of Live, Dead, and Fixed Brain Tissue.* Journal of Biomechanics, 1970. **3**(4): p. 453-&.

317. Donnelly, B.R. and J. Medige, *Shear properties of human brain tissue.* Journal of Biomechanical Engineering-Transactions of the Asme, 1997. **119**(4): p. 423-432.

318. Galford, J.E. and Mcelhane.Jh, *A Viscoelastic Study of Scalp, Brain, and Dura.* Journal of Biomechanics, 1970. **3**(2): p. 211-&.

319. Velardi, F., F. Fraternali, and M. Angelillo, *Anisotropic constitutive equations and experimental tensile behavior of brain tissue.* Biomechanics and Modeling in Mechanobiology, 2006. **5**(1): p. 53-61.

320. Prevost, T.P., et al., *Biomechanics of brain tissue.* Acta Biomaterialia, 2011. **7**(1): p. 83-95.

321. Sanborn, B., et al., *Inertia effects on characterization of dynamic response of brain tissue.* Journal of Biomechanics, 2012. **45**(3): p. 434-439.

322. Li, X., H. von Holst, and S. Kleiven, *Influences of brain tissue poroelastic constants on intracranial pressure (ICP) during constant-rate infusion.* Comput Methods Biomech Biomed Engin, 2013. **16**(12): p. 1330-43.

323. Urbanczyk, C.A., M.L. Palmeri, and C.R. Bass, *Material characterization of in vivo and in vitro porcine brain using shear wave elasticity.* Ultrasound Med Biol, 2015. **41**(3): p. 713-23.

324. Nicolas, E., S. Callé, and J.-P. Remenieras, *Generating Shear Waves in the Human Brain for Ultrasound Elastography: A new Approach.* Physics Procedia, 2015. **70**: p. 1255-1259.

325. Manduca, A., et al., *Visualization of tissue elasticity by magnetic resonance elastography.* Visualization in Biomedical Computing, 1996. **1131**: p. 63-68.

326. Kruse, S.A., et al., *Magnetic resonance elastography of the brain.* Neuroimage, 2008. **39**(1): p. 231-7.

327. Sack, I., et al., *Non-invasive measurement of brain viscoelasticity using magnetic resonance elastography.* NMR Biomed, 2008. **21**(3): p. 265-71.

328. Marlin, A.E., et al., *On the movement of fluid through the brain of hydrocephalic cats.* Neurology, 1976. **26**(12): p. 1159-63.

329. Collins, P., *Experimental obstructive hydrocephalus in the rat: a scanning electron microscopic study.* Neuropathol Appl Neurobiol, 1979. **5**(6): p. 457-68.

330. Aarabi, B. and D.M. Long, *Dynamics of cerebral edema. The role of an intact vascular bed in the production and propagation of vasogenic brain edema.* J Neurosurg, 1979. **51**(6): p. 779-84.

331. Borgesen, S.E. and F. Gjerris, *Relationships between intracranial pressure, ventricular size, and resistance to CSF outflow.* J Neurosurg, 1987. **67**(4): p. 535-9.

332. McCormick, J.M., et al., *Time course of intraventricular pressure change in a canine model of hydrocephalus: its relationship to sagittal sinus elastance.* Pediatr Neurosurg, 1992. **18**(3): p. 127-33.

333. Kuroiwa, T., et al., *Biomechanical characteristics of brain edema: the difference between vasogenic-type and cytotoxic-type edema.* Acta Neurochir Suppl (Wien), 1994. **60**: p. 158-61.

334. Johnson, M.J., et al., *Development and characterization of an adult model of obstructive hydrocephalus.* J Neurosci Methods, 1999. **91**(1-2): p. 55-65.

335. Kostopoulos, V., et al., *A new method for the early diagnosis of brain edema/brain swelling. An experimental study in rabbits.* J Biomech, 2006. **39**(16): p. 2958-65.

336. Mao, X., T.L. Enno, and M.R. Del Bigio, *Aquaporin 4 changes in rat brain with severe hydrocephalus.* Eur J Neurosci, 2006. **23**(11): p. 2929-36.

337. Bloch, O. and G.T. Manley, *The role of aquaporin-4 in cerebral water transport and edema.* Neurosurg Focus, 2007. **22**(5): p. E3.

338. Tourdias, T., et al., *Aquaporin 4 correlates with apparent diffusion coefficient and hydrocephalus severity in the rat brain: a combined MRI-histological study.* Neuroimage, 2009. **47**(2): p. 659-66.

339. Feng, X., et al., *Sporadic obstructive hydrocephalus in Aqp4 null mice.* J Neurosci Res, 2009. **87**(5): p. 1150-5.

340. Paul, L., et al., *Expression of aquaporin 1 and 4 in a congenital hydrocephalus rat model.* Neurosurgery, 2011. **68**(2): p. 462-73.

341. Shen, X.Q., et al., *Expression of the water-channel protein aquaporin 4 in the H-Tx rat: possible compensatory role in spontaneously arrested hydrocephalus.* J Neurosurg, 2006. **105**(6 Suppl): p. 459-64.

342. McAllister, J.P., 2nd and J.M. Miller, *Aquaporin 4 and hydrocephalus.* J Neurosurg, 2006. **105**(6 Suppl): p. 457-8; discussion 458.

343. Skjolding, A.D., et al., *Hydrocephalus induces dynamic spatiotemporal regulation of aquaporin-4 expression in the rat brain.* Cerebrospinal Fluid Res, 2010. **7**: p. 20.

344. Skjolding, A.D., et al., *Differences in distribution and regulation of astrocytic aquaporin-4 in human and rat hydrocephalic brain.* Neuropathol Appl Neurobiol, 2013. **39**(2): p. 179-91.

345. Geertsma, J., *Problems of Rock Mechanics In Petroleum Production Engineering*. International Society for Rock Mechanics.

346. Terzaghi, K., *Theoretical soil mechanics*. 1943, London, New York: Chapman and Hall ; Wiley. xvii, 510 p.

347. Biot, M.A., *General Theory of Three-Dimensional Consolidation.* Journal of Applied Physics, 1941. **12**(2): p. 155-164.

348. Biot, M.A., *Theory of Propagation of Elastic Waves in a Fluid-Saturated Porous Solid. I. Low-Frequency Range.* The Journal of the Acoustical Society of America, 1956. **28**(2): p. 168-178.

349. Biot, M.A., *Theory of Propagation of Elastic Waves in a Fluid-Saturated Porous Solid. II. Higher Frequency Range.* The Journal of the Acoustical Society of America, 1956. **28**(2): p. 179-191.

350. Aifantis, E.C., *Continuum Basis for Diffusion in Regions with Multiple Diffusivity.* Journal of Applied Physics, 1979. **50**(3): p. 1334-1338.

351. Aifantis, E.C. and J.M. Hill, *On the Theory of Diffusion in Media with Double Diffusivity .1. Basic Mathematical Results.* Quarterly Journal of Mechanics and Applied Mathematics, 1980. **33**(Feb): p. 1-21.

352. Hill, J.M. and E.C. Aifantis, *On the Theory of Diffusion in Media with Double Diffusivity .2. Boundary-Value-Problems.* Quarterly Journal of Mechanics and Applied Mathematics, 1980. **33**(Feb): p. 23-41.

353. Bai, M., *On equivalence of dual-porosity poroelastic parameters.* Journal of Geophysical Research-Solid Earth, 1999. **104**(B5): p. 10461-10466.

354. Bai, M., et al., *Dual-porosity poroelastic modeling of generalized plane strain.* International Journal of Rock Mechanics and Mining Sciences, 1999. **36**(8): p. 1087-1094.

355. Chen, M., M. Bai, and J.C. Roegiers, *Permeability tensors of anisotropic fracture networks.* Mathematical Geology, 1999. **31**(4): p. 355-373.

356. Barenblatt, G.I., I.P. Zheltov, and I.N. Kochina, *Basic concepts in the theory of seepage of homogeneous liquids in fissured rocks [strata].* Journal of Applied Mathematics and Mechanics, 1960. **24**(5): p. 1286-1303.

357. Bai, M., D. Elsworth, and J.C. Roegiers, *Multiporosity Multipermeability Approach to the Simulation of Naturally Fractured Reservoirs.* Water Resources Research, 1993. **29**(6): p. 1621-1633.

358. Verruijt, A., *Theory and Problems of Poroelasticity*. 2015, Delft University of Technology.

359. Detournay, E. and A.H.D. Cheng, *5 - Fundamentals of Poroelasticity A2 - FAIRHURST, CHARLES*, in *Analysis and Design Methods*. 1993, Pergamon: Oxford. p. 113-171.

360. Gan, Q., et al., *Breakdown pressures due to infiltration and exclusion in finite length boreholes.* Journal of Petroleum Science and Engineering, 2015. **127**: p. 329-337.

361. Martins, J.B. and SpringerLink (Online service), *Numerical Methods in Geomechanics Proceedings of the NATO Advanced Study Institute, University of Minho, Braga, Portugal, held at Vimeiro, August 24 - September 4, 1981*, in *NATO Advanced Study Institutes Series, Series C - Mathematical and Physical Sciences Proceedings of the Advanced Study Institute Programme, which aims at the dissemination of advanced knowledge and the formation of contacts among scientists from different countries,*. 1982.

362. Zienkiewicz, O.C. and T. Shiomi, *Dynamic Behavior of Saturated Porous-Media - the Generalized Biot Formulation and Its Numerical-Solution.* International Journal for Numerical and Analytical Methods in Geomechanics, 1984. **8**(1): p. 71-96.

363. Zienkiewicz, O.C., et al., *Static and Dynamic Behavior of Soils - a Rational Approach to Quantitative Solutions .1. Fully Saturated Problems.* Proceedings of the Royal Society of London Series a-Mathematical Physical and Engineering Sciences, 1990. **429**(1877): p. 285-309.

364. Zienkiewicz, O.C., et al., *Static and Dynamic Behavior of Soils - a Rational Approach to Quantitative Solutions .2. Semi-Saturated Problems.* Proceedings of the Royal Society of London Series a-Mathematical Physical and Engineering Sciences, 1990. **429**(1877): p. 311-321.

365. Biot, M.A., *Theory of Propagation of Elastic Waves in a Fluid-Saturated Porous Solid .1. Low-Frequency Range.* Journal of the Acoustical Society of America, 1956. **28**(2): p. 168-178.

366. Biot, M.A., *Theory of Propagation of Elastic Waves in a Fluid-Saturated Porous Solid .2. Higher Frequency Range.* Journal of the Acoustical Society of America, 1956. **28**(2): p. 179-191.

367. Zienkiewicz, O.C., C.T. Chang, and P. Bettess, *Drained, Undrained, Consolidating and Dynamic Behavior Assumptions in Soils.* Geotechnique, 1980. **30**(4): p. 385-395.

368. Brown, S.F., *Soil mechanics-transient and cyclic loads (constitutive relations and numerical treatment), edited by G. N. Pande and 0. C. Zienkiewicz, Wiley, Chichester, 1982. No. of pages: 627. Price: £34.50.* Earthquake Engineering & Structural Dynamics, 1983. **11**(3): p. 439-439.

369. Bukhman, E.V., et al., *Spectral-Analysis of Acoustic Vibrations on the Surface of the Human-Body.* Acoustical Physics, 1995. **41**(1): p. 41-48.

370. Press, W.H., *Numerical recipes : the art of scientific computing*. 3rd ed. 2007, Cambridge: Cambridge University Press. xxi, 1235 p.

371. Bechmann, I., et al., *Turnover of rat brain perivascular cells.* Experimental Neurology, 2001. **168**(2): p. 242-249.

372. Gunnarson, E., et al., *Lead induces increased water permeability in astrocytes expressing aquaporin 4.* Neuroscience, 2005. **136**(1): p. 105-14.

373. Iadecola, C. and M. Nedergaard, *Glial regulation of the cerebral microvasculature.* Nature Neuroscience, 2007. **10**(11): p. 1369-1376.

374. Kaczmarek, M., R.P. Subramaniam, and S.R. Neff, *The hydromechanics of hydrocephalus: steady-state solutions for cylindrical geometry*. Bull Math Biol, 1997. **59**(2): p. 295-323.

375. Wirth, B. and I. Sobey, *An axisymmetric and fully 3D poroelastic model for the evolution of hydrocephalus.* Math Med Biol, 2006. **23**(4): p. 363-88.

376. Taylor, Z. and K. Miller, *Reassessment of brain elasticity for analysis of biomechanisms of hydrocephalus.* J Biomech, 2004. **37**(8): p. 1263-9.

377. Barber, T.W., J.A. Brockway, and L.S. Higgins, *The density of tissues in and about the head.* Acta Neurol Scand, 1970. **46**(1): p. 85-92.

378. Herscovitch, P. and M.E. Raichle, *What is the correct value for the brain--blood partition coefficient for water?* J Cereb Blood Flow Metab, 1985. **5**(1): p. 65-9.

379. Corbin, E.A., et al., *Measuring physical properties of neuronal and glial cells with resonant microsensors.* Anal Chem, 2014. **86**(10): p. 4864-72.

380. Li, G., et al., *Permeability of endothelial and astrocyte cocultures: in vitro blood-brain barrier models for drug delivery studies.* Ann Biomed Eng, 2010. **38**(8): p. 2499-511.

381. Klanchar, M. and J.M. Tarbell, *Modeling Water-Flow through Arterial Tissue.* Bulletin of Mathematical Biology, 1987. **49**(6): p. 651-669.

382. Gunnarson, E., et al., *Erythropoietin modulation of astrocyte water permeability as a component of neuroprotection.* Proc Natl Acad Sci U S A, 2009. **106**(5): p. 1602-7.

383. Wright, S.N., et al., *Digital reconstruction and morphometric analysis of human brain arterial vasculature from magnetic resonance angiography.* Neuroimage, 2013. **82**: p. 170-81.

384. Lauwers, F., et al., *Morphometry of the human cerebral cortex microcirculation: general characteristics and space-related profiles.* Neuroimage, 2008. **39**(3): p. 936-48.

385. Sobey, I. and B. Wirth, *Effect of non-linear permeability in a spherically symmetric model of hydrocephalus.* Math Med Biol, 2006. **23**(4): p. 339-61.

386. Lefever, J.A., J. Jaime Garcia, and J.H. Smith, *A patient-specific, finite element model for noncommunicating hydrocephalus capable of large deformation.* J Biomech, 2013. **46**(8): p. 1447-53.

387. Wang, P. and W.L. Olbricht, *Fluid mechanics in the perivascular space.* J Theor Biol, 2011. **274**(1): p. 52-7.

388. Bertossi, M., et al., *Ultrastructural and morphometric investigation of human brain capillaries in normal and peritumoral tissues.* Ultrastruct Pathol, 1997. **21**(1): p. 41-9.

389. Nicholson, C., P. Kamali-Zare, and L. Tao, *Brain Extracellular Space as a Diffusion Barrier.* Comput Vis Sci, 2011. **14**(7): p. 309-325.

390. Bateman, G.A., *Vascular compliance in normal pressure hydrocephalus.* American Journal of Neuroradiology, 2000. **21**(9): p. 1574-1585.

391. Bateman, G.A., *Magnetic resonance imaging quantification of compliance and collateral flow in late-onset idiopathic aqueductal stenosis: venous pathophysiology revisited.* J Neurosurg, 2007. **107**(5): p. 951-8.

392. Naidich, T.P., et al., *Evaluation of pediatric hydrocephalus by computed tomography.* Radiology, 1976. **119**(2): p. 337-45.

393. Eide, P.K. and G. Ringstad, *MRI with intrathecal MRI gadolinium contrast medium administration: a possible method to assess glymphatic function in human brain.* Acta Radiol Open, 2015. **4**(11): p. 2058460115609635.

394. Oreskovic, D., P.S. Whitton, and V. Lupret, *Effect of intracranial pressure on cerebrospinal fluid formation in isolated brain ventricles.* Neuroscience, 1991. **41**(2-3): p. 773-7.

395. Brightman, M.W., *The intracerebral movement of proteins injected into blood and cerebrospinal fluid of mice.* Prog Brain Res, 1968. **29**: p. 19-40.

396. Bulat, M., et al., *Transventricular and transpial absorption of cerebrospinal fluid into cerebral microvessels.* Coll Antropol, 2008. **32 Suppl 1**: p. 43-50.

397. Hopkins, L.N., et al., *Demonstration of transventricular CSF absorption by computerized tomography.* Acta Neurochir (Wien), 1977. **39**(3-4): p. 151-7.

398. Murata, T., et al., *The Significance of Periventricular Lucency on Computed-Tomography - Experimental-Study with Canine Hydrocephalus.* Neuroradiology, 1980. **20**(5): p. 221-227.

399. Showalter, R.E., *Diffusion in poro-elastic media.* Journal of Mathematical Analysis and Applications, 2000. **251**(1): p. 310-340.

400. Gullans, S.R. and J.G. Verbalis, *Control of brain volume during hyperosmolar and hypoosmolar conditions.* Annu Rev Med, 1993. **44**: p. 289-301.

401. Thrane, A.S., et al., *Filtering the muddied waters of brain edema.* Trends Neurosci, 2015. **38**(6): p. 333-5.

402. Verkman, A.S., et al., *Three distinct roles of aquaporin-4 in brain function revealed by knockout mice.* Biochim Biophys Acta, 2006. **1758**(8): p. 1085-93.

403. Yang, B., Z. Zador, and A.S. Verkman, *Glial cell aquaporin-4 overexpression in transgenic mice accelerates cytotoxic brain swelling.* J Biol Chem, 2008. **283**(22): p. 15280-6.

404. Siemen, D. and J.K.J. Hescheler, *Nonselective cation channels : pharmacology, physiology and biophysics*. Experientia Supplementum. 1993, Basel ; Boston: Birkhäuser. xiii, 316 p.

405. Liang, D., et al., *Cytotoxic edema: mechanisms of pathological cell swelling.* Neurosurg Focus, 2007. **22**(5): p. E2.

406. Shantha, E., S. Ruhoy, and E. Esparza, *Persistent chemosis and periorbital edema.* Int J Dermatol, 2016.

407. Blasi, A., et al., *A new case of acute pulmonary edema secondary to phenylephrine administered on the conjunctiva in cataract surgery.* Rev Esp Anestesiol Reanim, 1998. **45**(5): p. 210.

408. Ridenti, F.A., *Neurogenic pulmonary edema: a current literature review.* Rev Bras Ter Intensiva, 2012. **24**(1): p. 91-6.

409. Schoene, R.B., *Pulmonary edema at high altitude. Review, pathophysiology, and update.* Clin Chest Med, 1985. **6**(3): p. 491-507.

410. IaA, L. and S. Ia, *On the pathogenesis of pulmonary edema: review.* Sov Med, 1960. **24**: p. 97-105.

411. Fanestil, D.D., *Pulmonary edema: a study of its pathogenesis and review of the literature.* J Kans Med Soc, 1957. **58**(5): p. 328; passim.

412. Said, S., et al., *Hypertension, renal failure, and edema in a 38-year-old man: light chain deposition disease; a case report and review of the literature.* J Nephropathol, 2014. **3**(2): p. 63-8.

413. Stoquart-ElSankari, S., et al., *Aging effects on cerebral blood and cerebrospinal fluid flows.* J Cereb Blood Flow Metab, 2007. **27**(9): p. 1563-72.

414. Kurtcuoglo, V., *Computational modeling of the cerebral ventricular cerebrospinal fluid system*. 2006, ETH: Zürich. p. 151 S.

415. Loth, F., M.A. Yardimci, and N. Alperin, *Hydrodynamic modeling of cerebrospinal fluid motion within the spinal cavity.* J Biomech Eng, 2001. **123**(1): p. 71-9.

416. Lundervold, A., et al., *Volume distribution of cerebrospinal fluid using multispectral MR imaging.* Med Image Anal, 2000. **4**(2): p. 123-36.

417. Iliff, J.J., et al., *Cerebral arterial pulsation drives paravascular CSF-interstitial fluid exchange in the murine brain.* J Neurosci, 2013. **33**(46): p. 18190-9.

418. Hadaczek, P., et al., *The "perivascular pump" driven by arterial pulsation is a powerful mechanism for the distribution of therapeutic molecules within the brain.* Mol Ther, 2006. **14**(1): p. 69-78.

419. Bilston, L.E., et al., *Arterial pulsation-driven cerebrospinal fluid flow in the perivascular space: a computational model.* Comput Methods Biomech Biomed Engin, 2003. **6**(4): p. 235-41.

420. Schley, D., et al., *Mechanisms to explain the reverse perivascular transport of solutes out of the brain.* J Theor Biol, 2006. **238**(4): p. 962-74.

421. Klanchar, M. and J.M. Tarbell, *Modeling water flow through arterial tissue.* Bulletin of Mathematical Biology. **49**(6): p. 651-669.

422. Ramadesigan, V., et al., *Modeling and Simulation of Lithium-Ion Batteries from a Systems Engineering Perspective.* Journal of The Electrochemical Society, 2012. **159**(3): p. R31-R45.

423. Gor, G.Y., et al., *A Model for the Behavior of Battery Separators in Compression at Different Strain/Charge Rates.* Journal of The Electrochemical Society, 2014. **161**(11): p. F3065-F3071.

424. Administration, N.A.a.S., *NASA's Journey to Mars: Pioneering Next Steps in Space Exploration* NASA, Editor. 2015: http://www.nasa.gov/sites/default/files/atoms/files/journey-to-mars-next-steps-20151008_508.pdf.

425. Lakin, W.D., S.A. Stevens, and P.L. Penar, *Modeling Intracranial Pressures in Microgravity: The Influence of the Blood-Brain Barrier.* Aviation, Space, and Environmental Medicine, 2007. **78**(10): p. 932-936.

426. Stevens, S.A., W.D. Lakin, and P.L. Penar, *Modeling Steady-State Intracranial Pressures in Supine, Head-Down Tilt and Microgravity Conditions.* Aviation, Space, and Environmental Medicine, 2005. **76**(4): p. 329-338.

427. Li, K., et al., *Effect of Simulated Microgravity on Human Brain Gray Matter and White Matter ? Evidence from MRI.* PLoS ONE, 2015. **10**(8): p. e0135835.

428. Tsybko, A.S., et al., *Effect of microgravity on glial cell line-derived neurotrophic factor and cerebral dopamine neurotrophic factor gene expression in the mouse brain.* Journal of Neuroscience Research, 2015. **93**(9): p. 1399-1404.

429. McAllister, T.W., *Neurobiological consequences of traumatic brain injury.* Dialogues in Clinical Neuroscience, 2011. **13**(3): p. 287-300.

430. Goriely, A., et al., *Mechanics of the brain: perspectives, challenges, and opportunities.* Biomechanics and Modeling in Mechanobiology, 2015. **14**(5): p. 931-965.

431. Misra, J.C. and S. Chakravarty, *A poroelastic spheroidal shell model for studying the problem of head injury.* Journal of Mathematical Analysis and Applications, 1984. **103**(2): p. 332-343.

432. Li, X.G., et al., *Three Dimensional Poroelastic Simulation of Brain Edema: Initial Studies on Intracranial Pressure*, in *World Congress on Medical Physics and Biomedical Engineering, September 7 - 12, 2009, Munich, Germany: Vol. 25/4 Image Processing, Biosignal Processing, Modelling and Simulation, Biomechanics*, O. Dössel and W.C. Schlegel, Editors. 2010, Springer Berlin Heidelberg: Berlin, Heidelberg. p. 1478-1481.

433. Marino, A.A. and S. Carrubba, *The Effects of Mobile-Phone Electromagnetic Fields on Brain Electrical Activity: A Critical Analysis of the Literature.* Electromagnetic Biology and Medicine, 2009. **28**(3): p. 250-274.

434. Choi, H.-s., I.-h. Park, and S.-H. Lee, *Electromagnetic body force calculation based on virtual air gap.* Journal of Applied Physics, 2006. **99**(8): p. 08H903.

435. *The Electromagnetic Body Force in Magnetohydrodynamics.* Journal of the Aerospace Sciences, 1962. **29**(3): p. 347-348.

436. Konstantinidis, E.I., et al., *Internet of things for an age-friendly healthcare.* Stud Health Technol Inform, 2015. **210**: p. 587-91.

437. Schreier, G., *The internet of things for personalized health.* Stud Health Technol Inform, 2014. **200**: p. 22-31.

438. Monares, A., et al., *Modeling IoT-based solutions using human-centric wireless sensor networks.* Sensors (Basel), 2014. **14**(9): p. 15687-713.

439. Partsch, H. and G. Mosti, *Comparison of three portable instruments to measure compression pressure.* Int Angiol, 2010. **29**(5): p. 426-30.

440. Salvi, P., et al., *Validation of a new non-invasive portable tonometer for determining arterial pressure wave and pulse wave velocity: the PulsePen device.* J Hypertens, 2004. **22**(12): p. 2285-93.

441. Andreu-Perez, J., et al., *From Wearable Sensors to Smart Implants--Toward Pervasive and Personalized Healthcare.* IEEE Trans Biomed Eng, 2015. **62**(12): p. 2750-62.

442. Wysham, N.G., A.P. Abernethy, and C.E. Cox, *Setting the vision: applied patient-reported outcomes and smart, connected digital healthcare systems to improve patient-centered outcomes prediction in critical illness.* Curr Opin Crit Care, 2014. **20**(5): p. 566-72.

443. Wang, X., et al., *Enabling smart personalized healthcare: a hybrid mobile-cloud approach for ECG telemonitoring.* IEEE J Biomed Health Inform, 2014. **18**(3): p. 739-45.

444. Vashist, S.K., E.M. Schneider, and J.H. Luong, *Commercial Smartphone-Based Devices and Smart Applications for Personalized Healthcare Monitoring and Management.* Diagnostics (Basel), 2014. **4**(3): p. 104-28.

445. Oh, S.Y., et al., *Recent trends in convergence-based smart healthcare service.* Technol Health Care, 2014.

Appendices

A series of transformations and boundary conditions in the derivation of MPET will be presented.

A1 Mathematical Transformations

The standard transformations of del (∇) in the radial distance of a spherical coordinate system,

$$\nabla_r = \frac{\partial}{\partial r}\vec{r} \tag{A1.1}$$

$$\nabla \cdot \mathbf{u_r} = \frac{1}{r^2}\frac{\partial(r^2 u_r)}{\partial r} = \frac{\partial u_r}{\partial r} + \frac{2}{r}u_r \tag{A1.2}$$

$$\nabla_r^2 = \frac{\partial^2}{\partial r^2} + \frac{2}{r}\frac{\partial}{\partial r} \tag{A1.3}$$

$$\nabla^2 u_r = \frac{1}{r^2}\frac{\partial}{\partial r}\left(r^2\frac{\partial u_r}{\partial r}\right) = \frac{\partial^2 u_r}{\partial r^2} + \frac{2}{r}\frac{\partial u_r}{\partial r} \tag{A1.4}$$

$$\nabla_r^2 \mathbf{u} = \left[\nabla^2 u_r - \frac{2}{r^2}u_r\right]\vec{r} = \left(\frac{\partial^2 u_r}{\partial r^2} + \frac{2}{r}\frac{\partial u_r}{\partial r} - \frac{2}{r^2}u_r\right)\vec{r} \tag{A1.5}$$

$$\nabla(\nabla \cdot \mathbf{u}) = \left(\frac{\partial^2 u_r}{\partial r^2} + \frac{2}{r}\frac{\partial u_r}{\partial r} - \frac{2}{r^2}u_r\right)\vec{r} \tag{A1.6}$$

$$\nabla^2 p = \nabla \cdot \nabla p = \frac{\partial^2 p}{\partial r^2} + \frac{2}{r}\frac{\partial p}{\partial r} \tag{A1.7}$$

A2 Stress as a Function of Displacement

$$\sigma'_{ij} = \frac{2G\upsilon}{1-2\upsilon}\delta_{ij}\varepsilon_{kk} + 2G\varepsilon_{ij} \tag{A2.1}$$

$$\varepsilon_{ij} = \frac{1}{2}\left(u_{i,j} + u_{j,i}\right) = \frac{1}{2}\left(\frac{\partial u_i}{\partial x_j} + \frac{\partial u_j}{\partial x_i}\right) \tag{A2.2}$$

$$\varepsilon_{kk} = \frac{\partial u_j}{\partial u_j} = \delta_{ji}\frac{\partial u_i}{\partial u_j} \tag{A2.3}$$

$$\sigma'_{ij,j} = \frac{\partial}{\partial x_j}\left(\frac{2G\upsilon}{1-2\upsilon}\delta_{ij}\varepsilon_{kk} + 2G\varepsilon_{ij}\right) = \frac{\partial}{\partial x_j}\left\{\frac{2G\upsilon}{1-2\upsilon}\delta_{ij}\varepsilon_{kk} + 2G\left[\frac{1}{2}\left(\frac{\partial u_i}{\partial x_j} + \frac{\partial u_j}{\partial x_i}\right)\right]\right\}$$

$$= \frac{2G\upsilon}{1-2\upsilon}\delta_{ij}u_{k,kj} + Gu_{i,jj} + Gu_{j,ij} = \left(\frac{2G\upsilon}{1-2\upsilon}u_{j,ji} + Gu_{j,ij}\right) + Gu_{i,jj}$$

$$= \frac{G}{1-2\upsilon}u_{j,ij} + Gu_{i,jj} = \frac{G}{1-2\upsilon}\frac{\partial}{\partial x_j}u_{i,i} + G\frac{\partial}{\partial x_j}u_{i,j} = \frac{G}{1-2\upsilon}\nabla(\nabla\cdot\mathbf{u}) + G\nabla^2\mathbf{u} \tag{A2.4}$$

A3 Boundary Condition Derivation at Ventricle Wall, Displacement

Total stress of the cerebral parenchyma at the ventricle wall is equal to the sum of each compartmental pressure at the ventricle wall in the MPET system,

$$-\sum_{\Omega=a,c,v,e} p^{\Omega} = \sigma_{ii} \tag{A3.1}$$

The negative sign arises from the standard convention of taking tensile stresses to be positive. Eqn. (A3.1) can be expressed in terms of the deformation with the aid of:

$$\sigma_{ii} = 2G\varepsilon_{ii} + \frac{2G\upsilon}{1-2\upsilon}\varepsilon_{kk} - \sum_{\Omega=a,c,v,e}\alpha^{\Omega}p^{\Omega} \tag{A3.2}$$

When combining (A3.1) with (A3.2) gives:

$$-\sum_{\Omega=a,c,v,e} p_{vent}^{\Omega,t} = 2G\varepsilon_{ii} + \frac{2G\upsilon}{1-2\upsilon}\varepsilon_{kk} - \sum_{\Omega=a,c,v,e} \alpha^{\Omega} p^{\Omega} \qquad \text{(A3.3)}$$

For the 1D spherically symmetric geometry therefore, we have:

$$\frac{2G}{1-2\upsilon}\left[(1-\upsilon)\frac{\partial u_r}{\partial r}\bigg|_{r=r_1} + 2\upsilon\frac{u_r}{r}\bigg|_{r=r_1}\right] = \sum_{\Omega=a,c,v,e}(\alpha^{\Omega}-1)p_1^{\Omega} \qquad \text{(A3.4)}$$

A4 Boundary Condition Derivation at Ventricle Wall, Glial Cells

For continuity of stresses, the pressure exerted by the CSF inside the ventricles and on the ventricle wall of the glial cells compartment specifically, must balance the poroelastic stress in the brain tissue. Denoting the unit outward normal to the ventricle wall by **n**

$$-p^{e} = \sigma_{ij}^{g} \cdot \mathbf{n} \qquad \text{(A4.1)}$$

The negative sign arises from the standard convention of taking tensile stresses to be positive. The above equation already comprises three boundary conditions, and can be expressed in terms of the deformation with the aid of:

$$\sigma_{ij}^{g} = 2G^{g}\varepsilon_{ij} + \frac{2G^{g}\upsilon^{g}}{1-2\upsilon^{g}}\varepsilon_{kk}\delta_{ij} - \alpha^{g}p^{g} \qquad \text{(A4.2)}$$

When combining (A4.1) with (A4.2) gives:

$$-p^{e} = 2G^{g}\varepsilon_{ii} + \frac{2G^{g}\upsilon^{g}}{1-2\upsilon^{g}}\varepsilon_{kk} - \alpha^{g}p^{g}$$

$$\rightarrow p^g = \frac{p^e}{\alpha^g} + \frac{2G^g}{\alpha^g}\varepsilon_r + \frac{2G^g v^g}{\alpha^g(1-2v^g)}\left(\varepsilon_r + \varepsilon_\theta + \varepsilon_\phi\right)$$

$$= \frac{p^e}{\alpha^g} + \frac{2G^g(1-v^g)}{\alpha^g(1-2v^g)}\frac{\partial u_r}{\partial r} + \frac{2G^g v^g}{\alpha^g(1-2v^g)}\frac{2u_r}{r} \qquad \text{(A4.3)}$$